2000

Investigations on electrode materials for lithium-ion batteries

Guoxiu Wang
University of Wollongong

Investigations on Electrode Materials for Lithium-ion Batteries

A thesis submitted in fulfillment of the requirements for the award of the degree

Doctor of Philosophy

from

University of Wollongong

by

Guoxiu Wang, M. Eng., B. Eng.

Institute for Superconducting & Electronic Materials, Faculty of Engineering

2000

Declaration

I hereby declare that the research work presented in this thesis is original and was performed by the candidate in the laboratories in Institute for Superconducting & Electronic Materials and in the Faculty of Engineering at the University of Wollongong, New South Wales, Australia. This thesis has not been submitted for a degree to any other University or Institution.

Guoxiu Wang

Dedicated to

My Parents

My wife, Jane Yao

My lovely daughter, Mandy Wang

Acknowledgements

I would like to express my sincere gratitude and appreciation to my supervisors, Professor H. K. Liu, Professor Doug Bradhurst and Professor S. X. Dou for their consistent academic supervision, guidance and encouragement as well as financial support throughout my Ph. D project.

I wish to thank technical officers, Mr. Carlo Rossi, Mr. N. Mackie and Mr. G. Tillman for their invaluable help with my experimental procedures. My sincere thanks should also go to Dr. M. Ionescu and Dr. S. Zhong for their technical support and suggestions in carrying out all of my experimental work. Furthermore, I would like to thank Dr. Shane J. Kennedy at ANSTO for assistance with neutron diffraction measurements on some of the electrode materials.

I deeply appreciate Australian DEET for providing me the OPRS Scholarship, the Institute for Superconducting & Electronic Materials for providing the Energy Storage Materials Matching Scholarship.

Finally, I would like to express my grateful acknowledgement to my parents and parents-in-law for their encouragement and support. Specially, I wish to give my deepest gratitude and great appreciation to my wife Jane Yao and my daughter Mandy Wang for their love, understanding and patience.

ABSTRACT

This Ph. D project aims to prepare and study the preparations of advanced electrode materials with high capacity and long cycle life for rechargeable lithium batteries. The structural, physical and electrochemical properties of the electrode materials determine the energy density and performance of lithium ion batteries. Therefore, new electrode materials are critical for developing high energy density lithium ion batteries.

A thorough literature review has been made in order to provide a detailed description of the status of current research and development in rechargeable lithium ion battery systems. In particular, many different electrode materials used for lithium ion batteries are described.

A variety of cathode materials have been investigated. Some of them have shown good electrochemical performance when used as electrode materials in lithium ion cells. The $LiM_xMn_{2-x}O_4$ spinels doped with different metal ions were prepared using either solid state reaction or other chemical methods. The structural characteristics of the doped spinels were determined by neutron diffraction. The best dopant effects were found with Co^{3+} and Cr^{3+} ions, in terms of stabilising the spinel structure, improving the cycle life and alleviating the self-discharge when the electrode was charged to the highly charged state. A series of layered $LiM_\delta Ni_{1-\delta}O_2$ compounds were synthesised to improve the cyclability of the $LiNiO_2$ electrode. These compounds have many advantages over commercial $LiCoO_2$ cathode material in terms of capacity and cost, but they are required to be synthesized in an oxygen atmosphere. An innovative orthorhombic $LiMnO_2$ was also synthesised to explore the feasibility of utilising inexpensive $LiMnO_2$ as cathode material for lithium-ion batteries. In general, dopant effects were found to have a

positive impact on the improvement of the structural and electrochemical stability as well as rechargeability of the layered electrode materials.

Also, in this project, various different types of anode materials were prepared and their electrochemical properties were tested. $Li_4Ti_5O_{12}$ compound demonstrated a very stable cyclability with a voltage plateau at 1.5 V vs. Li/Li^+. It can be used as an anode coupled with high potential cathodes such as $LiMn_2O_4$ or $LiCoO_2$ to construct lithium ion cells.

Lithium ions can reversibly insert/extract in the $La_{0.33}NbO_3$ perovskite and $LiTi_2(PO_4)_3$ with NASICON-type structure. Through the analysis of the structure of these materials, new lithium insertion materials could be identified.

The intermetallic alloys are emerging as new generation anode materials with high lithium storage capacity. Nano-crystalline alloys Cu_6Sn_5, NiSi, FeSi and NiSn were produced by mechanical ball milling. These alloy anodes delivered large capacities in the range of 800 – 1400 mAh/g, but their cycle life still needs further improvement.

A series of $La_{(0.57-2x/3)}SrLi_{0.3}TiO_3$ solid-state electrolytes have been investigated. The maximum Li-ion conductivity observed at room temperature is about $1.12 \times 10\text{-}3\ Scm^{-1}$ for a Sr dopant level of x = 0.08. This Sr doped perovskite could be a candidate material as an electrolyte for solid-state lithium batteries.

The synthesised electrode materials were characterized by x-ray diffraction, SEM, TEM or HREM, through which the phase composition and microstructure were observed. Charge/discharge cycling tests were performed using CR2032 coin cells. The capacity and cycle life of the electrode materials were obtained from these tests. The kinetic characteristics and kinetic parameters of lithium ion insertion and extraction

within the electrode materials were determined by a. c. impedance spectroscopy, cyclic voltammograms and galvanostatic intermittent titration technique (GITT).

In summary, the investigations in this project have produced several types of cathode and anode materials with high capacity and long cycle life. The mechanisms of the electrochemical reaction in lithium ion cell were theoretically analyzed and then experimentally determined by various techniques. All of these studies provide a fundamental basis for the development of high energy density lithium ion batteries.

CONTENTS

Chapter 1 Introduction

Lithium-ion batteries are state-of-the-art rechargeable battery systems for modern portable electronic devices. They have higher energy density and longer cycle life than the existing Ni-Cd and Ni-MH rechargeable batteries. The overall electrochemical performance of lithium-ion batteries is determined by the properties of the cathode and anode materials. Therefore, this study is motivated by the need to improve the electrochemical properties of electrode materials and to synthesise new electrode materials for lithium-ion batteries. In practical terms, the battery performance also relates to the electrolyte, the preparation of the electrodes and manufacturing of the battery. The commercial electrolytes were used to assemble the test cells.

Chapter 2 gives an overview of the lithium-ion battery system, based on the literature survey. First, the operation principle of lithium-ion batteries is presented. The operation of the lithium-ion batteries relies on Li-ion "rocking" between cathode and anode hosts. Some early reports described lithium-ion batteries as "rocking chair" batteries. Some common cathode materials such as $LiMn_2O_4$ spinel, layered $LiNiO_2$ and $LiCoO_2$ as well as orthorhombic $LiMnO_2$ have been reviewed in terms of their advantages, disadvantages and existing problems to be overcome. Next, carbon materials and intermetallic alloys as anode materials for lithium-ion batteries are discussed. Finally, electrolyte systems including polymer electrolyte are also briefly reviewed.

In chapter 3, the materials and chemicals used in this project are described. The experimental methods and procedures are described in details.

Chapter 4 presents the synthesis, structures of $LiMn_2O_4$ and doped $LiM_xMn_{2-x}O_4$. These spinels are unstable at high temperature with oxygen evolution from their structure. Doping these spinels with Co and Cr can increase their high temperature

stability and cyclability. The inverse spinel $LiNiVO_4$ has a high operating potential of 4.8 V versus lithium.

Chapter 5 presents the results of a systematic investigation of the layered $LiMO_2$ (M=Ni, Co and Al) compounds and orthorhombic $LiMnO_2$ cathodes. The electrochemical properties of $LiNiO_2$ are sensitive to the synthesis conditions, which are believed to relate to the decomposition of $LiNiO_2$ to the electrochemically non-active compounds. Improvement of the electrochemical properties and structural stability of $LiNiO_2$ by doping with Al and Co are demonstrated. The kinetic parameters for lithium insertion in these compounds were obtained based on a.c. impedance measurements. The electrochemical behavior of orthorhombic $LiMnO_2$ as cathode in lithium-ion cell was studied in this investigation.

Nano-crystalline intermetallic alloys are new emerging anode materials for the next generation of lithium-ion batteries with high energy density and improved safety. In chapter 6, an investigation of several nano-crystalline alloys including η-Cu_6Sn_5, NiSi and FeSi is described. The reaction mechanisms of these alloys with lithium in lithium-ion cells were explored and discussed. In order to utilise the good cyclability of graphite and the high lithium storage capacity of Sn, a series of C-Sn composites were prepared by ball-milling. Their electrochemical performance as anodes in lithium cells was tested.

Chapter 7 identifies some new anode candidates for the lithium-ion battery based on their structural analysis. These anode materials are $Li[Li_{1/3}Ti_{5/3}]O_4$ spinel, $La_{0.33}NbO_3$ perovskite and $LiTi_2(PO_4)_3$ with NASICON-type structure. All of these materials demonstrated a certain lithium storage capacity.

Chapter 8 discusses the lithium-ion conductivity of $La_{(0.57-2x/3)}Sr_xLi_{0.3}TiO_3$ solid-state electrolyte. The optimum Sr composition with maximum Li-ion conductivity was identified.

Finally, in the summary session, the major conclusions from this study are presented and some suggestions for future study are proposed.

Chapter 2 Literature Review

2.1 Introduction to Lithium-ion Batteries

Lithium-ion batteries have the highest energy density and the highest operation voltage (3.6 V) among all rechargeable battery systems. They are the state-of-the-art power sources for modern consumer electronics such as camcorders, laptop computers and cellular phones (so-called 3Cs). Fig. 2-1 compares the energy densities of the different types of rechargeable batteries. As shown, lithium-ion batteries deliver the highest energy density. Furthermore, there is no memory effect for lithium-ion batteries. Large scale lithium-ion batteries also have great potential for electric vehicles and stationary

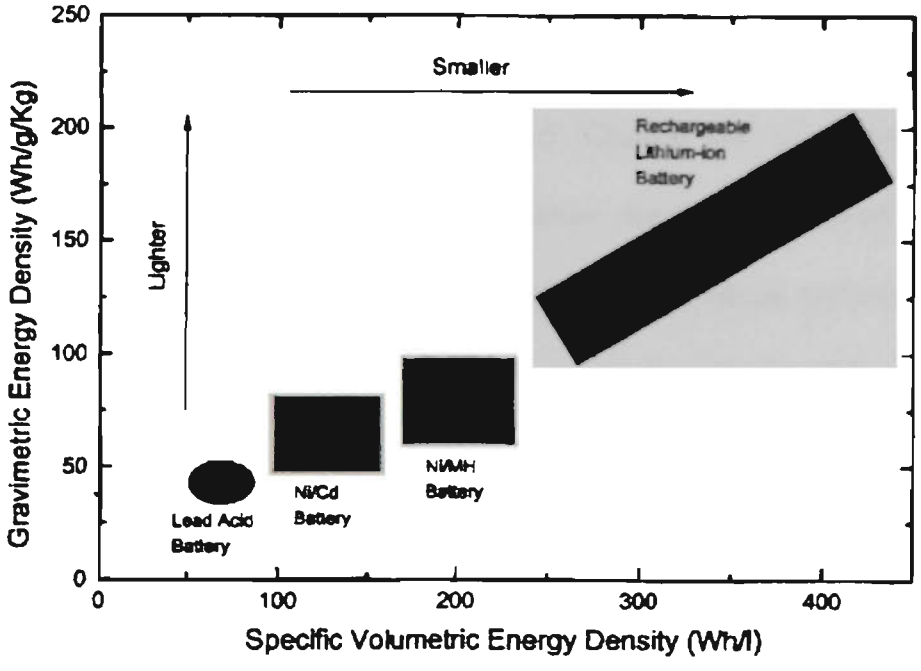

Fig. 2-1 The comparison of the energy density of different types of rechargeable batteries.

energy storage systems. Intensive research activities have been carried out worldwide to improve the energy density, cycle life and safety of lithium ion batteries. Today, lithium-ion batteries dominate the rechargeable battery market due to their excellent performance.

2.1.1 The Development History of Lithium-ion Batteries

The first paper in terms of rechargeable lithium batteries was presented at the Electrochemical Society Fall Meeting in Boston in 1962 by Chilton Jr. and Cook [1]. The goal was to build a high energy density and long cycle life battery to increase the mission lifetime of satellites. After almost 30 years, Sony successfully commercialized rechargeable lithium-ion batteries in 1990 [2].

Many difficulties have been met during the early development of rechargeable lithium batteries. A stable electrolyte medium containing lithium had to be identified. The electrolyte must be some lithium salts dissolved in organic solvent. A reversible positive electrode materials needed to be found. Chilton and Cook used a metallic positive electrode (Ag, Cu or Ni), and formed lithium deposited *in situ* on Ni during the first charge from a LiCl-$AlCl_3$ electrolyte dissolved in propylene carbonate. However, the formation of soluble complexes like $CuCl^{2-}$, caused an irreversible self-discharge. The large volume changes of the electrode during cycling led to a short cycle life of such systems.

In the early seventies, the insertion compounds were developed, which brought a decisive solution to the search for electrode materials for rechargeable lithium batteries [3]. The insertion materials host lithium ions inside their crystalline structure. The lithium ions can be reversibly inserted and extracted in the hosts. This so-called topotactical electrochemical reaction could occur reversibly without a major phase

change and with no damage of the material structure. From that time, a new electrochemistry for energy storage started to spring up, involving more and more solid state chemistry.

Lithium metal was initially used as the negative electrode in the rechargeable lithium battery system. However, lithium dendrites usually grow up during repeated charge/discharge cycling, resulting in short cycle life and cell shorting. The short circuit could cause serious safety problems such as fire and explosion, and eventually led to the abandonment of lithium metal as the anode material in rechargeable lithium batteries.

Dey [4] demonstrated the possibility of electrochemical formation of lithium alloys in organic electrolytes in 1971. Since then, many lithium alloys have been developed as alternative anode materials. The energy densities of lithium alloys normally are reduced by a factor of two or three, compared to pure lithium metals [5-10]. Unfortunately, the volume changes related to the insertion/extraction of Li into/from alloy matrices are quite substantial (200 – 600 %). This causes a fast disintegration of the alloy anodes by cracking and crumbling. As a result, short cycle life and low cycling efficiency are induced, preventing the commercial application of lithium alloys as anode materials for lithium-ion battery. Fortunately, the graphitic carbon was found to be dimensionally stable for lithium insertion and extraction. Intercalation of lithium ions corresponding to the composition LiC_6 results in only about a 10% increase in the layer distance [11]. Therefore, graphite became the choice of anode materials for the lithium-ion battery in place of lithium metal and lithium alloys.

The search for cathode hosts has been continued for more than two decades. The lithium cobalt oxide, $LiCoO_2$ was first reported by Mizushima and Goodenough et al. in 1980 [12]. $LiCoO_2$ is currently the dominant cathode material in commercial lithium ion battery production. The compound $LiNiO_2$ was also proposed, which can deliver higher

actual capacity than that of $LiCoO_2$. However, it is difficult to synthesize an ordered layer structure and stoichiometric materials because nickel tends to form Ni^{2+} [13]. Considerable investigations have been focused on characterization and optimization of the lithiated manganese oxides. Among of them, $LiMn_2O_4$ spinel is the most attractive cathode material. Although its theoretical capacity is lower than that of $LiCoO_2$ and $LiNiO_2$, it is inexpensive and less toxic. The electrochemical properties of $LiMn_2O_4$ spinel have been improved through a world-wide effort. Recently, it has been used in commercial lithium ion battery production.

The electrochemical performance of the lithium-ion battery is strongly dependent on the electrolyte. Many solutions were proposed, from well-known Propylene carbonates (PC) and Ethylene carbonate (EC) to ether-based solutions 1,3-dioxolane or 3-MeTHF [14, 15]. In general, the electrolytes for the lithium-ion battery are based on organic systems, which consist of organic solvents and lithium salts. The moisture is strictly controlled to avoid any side reaction. Polymer electrolytes have also been developed to construct so-called all-solid-state lithium-ion batteries. Such a system provides the fundamental safeguard for battery operation since no liquid electrolyte is present inside the battery.

The combination of intercalation anode host and cathode host as well as appropriate organic electrolyte has been emerging in lithium-ion battery technology since 1990. Following Sony [2], more than ten Japanese companies are currently producing lithium-ion batteries. Now, the commercial production can be seen worldwide. Lithium-ion batteries are becoming the dominant power sources for consumer electronics, military applications, aerospace and especially for wireless telecommunication.

2.1.2 The Principle of Lithium ion Battery Operation

Lithium metal free lithium batteries were originally termed "rocking chair" batteries (RCB) by Armand [16]. The basic concept of operation for the RCB's system was partially derived from concentration cells which consists of essentially identical electrodes containing different reactant concentrations [17]. After the RCB concept was revealed, this concept was demonstrated using transition metal compound anodes and cathodes [18-20]. Later, new names for this technology appeared: lithium ion, Shuttlecock and Swing Electrode System, etc.. But the fundamental concept remained the same.

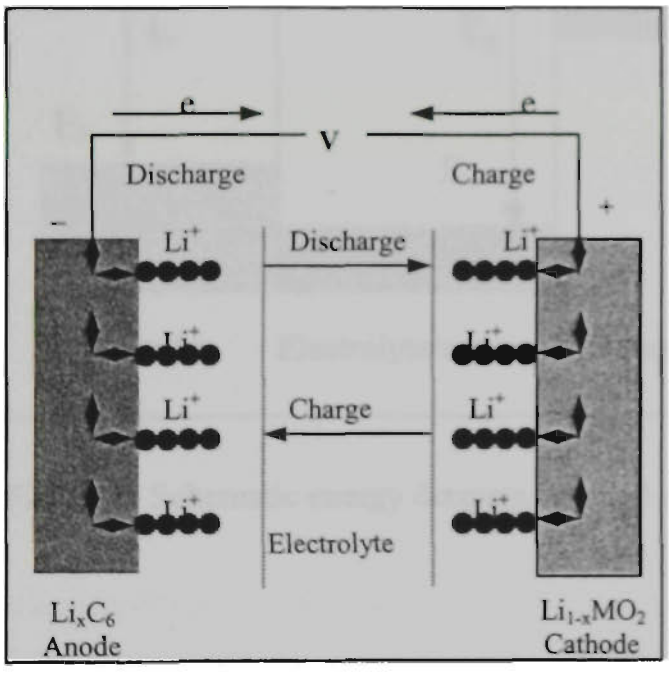

Fig. 2-2 The charge and discharge processes of a lithium ion battery.

In a lithium-ion cell, the Li^+ ions shuttle between the cathode and anode hosts during the discharge and charge processes. The principles of lithium-ion battery operation are shown in Fig. 2-2. Lithium ions are extracted from the cathode, go through electrolyte and separator and insert into the anode structure. The reverse process happens during discharging. In order to achieve high cycling efficiency and

long cycle life, the movement of Li ions in anode and cathode hosts should not change or damage the host crystal structure. The design of a lithium-ion battery system requires careful selection of electrode pairs to obtain a high operating voltage (V_c).

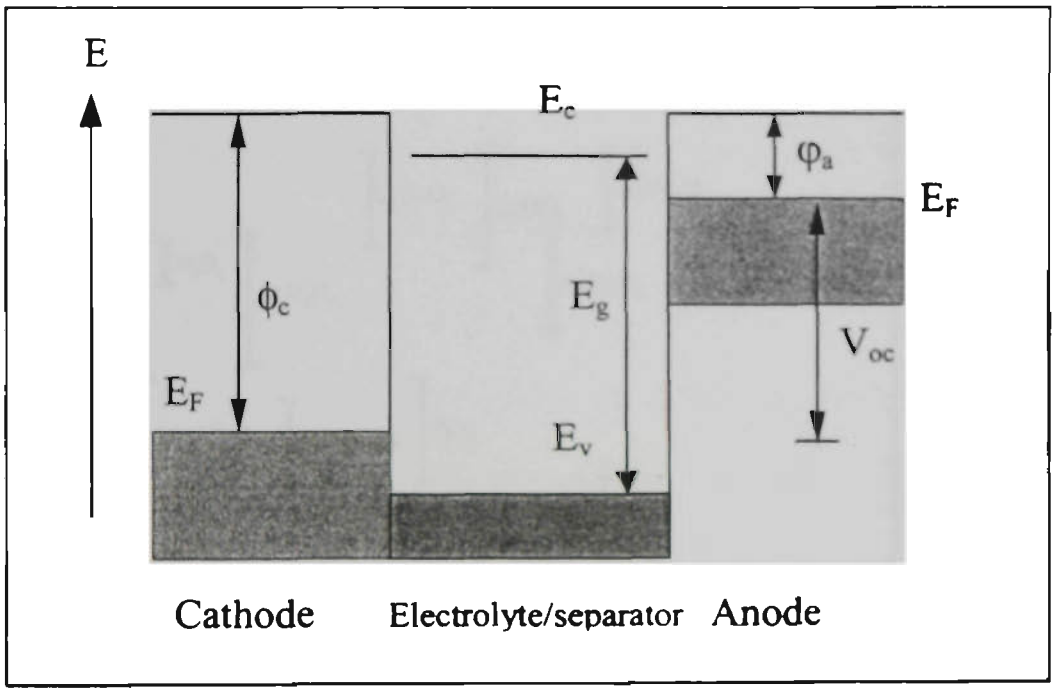

Fig. 2-3 Schematic energy diagram of a cell at open circuit

A high V_c can be realized with anode and cathode that have respectively, smaller and larger work functions ϕ_a and ϕ_c. The open-circuit voltage V_{oc} of the cell can be calculated from the following formula:

$$V_{oc} = (\phi_c - \phi_a) / e \qquad (2.1)$$

Where e is the electronic charge. The schematic energy level diagram showing the work functions is shown in Fig. 2-3.

The Fermi energies (E_F) of the anode and cathode must lie within the band gap (Eg) of the electrolyte. Therefore, the anode and cathode materials are thermodynamically stable in contact with electrolyte, and there will be no side reduction or oxidation of the electrolyte.

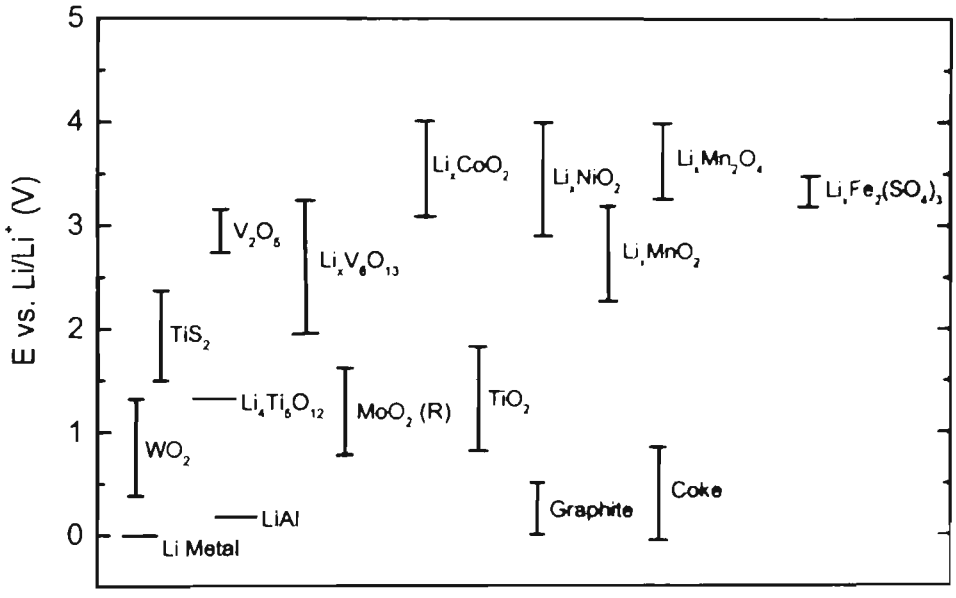

Fig. 2-4 Electrochemical potentials of some lithium-insertion materials versus Li/Li^+.

The electrochemical potentials of some electrode materials are illustrated in Fig. 2-4. Carbon (hard carbon and graphitized carbon) with a potential of 0 – 1 V versus lithium metal is the major choice as the anode material for lithium ion batteries. The cathode materials can be chosen from the spinel $LiMn_2O_4$, layered $LiCoO_2$ and $LiNiO_2$, which have discharge potentials around 4 V versus lithium metal. A battery with the

combination of high potential cathode materials and low potential anode materials can deliver a voltage of 3.6 ~ 3.8 V, which is 3 times that of Ni-Cd or Ni-MH batteries.

2.2 Cathode Materials for Lithium-ion Batteries

In rechargeable lithium batteries, the cathode host provides the lithium ion source for the intercalation reaction. So, the physical, structural and electrochemical properties of the cathode materials are critical to the performance of the whole battery. When insertion materials were proposed as the best solution for rechargeable non-aqueous batteries, the first materials proposed were the chalcogenides. The layered compound TiS_2 was extensively studied. It provides a stable layered structure, electronic conductivity, high drain capability and good reversibility [21, 22]. It was used by Exxon as the positive electrode material in the first marketed rechargeable lithium battery coupling with LiAl as negative electrode. This was a coin cell providing 2-2.5 V voltage. TiS_2 stood for a long time as the standard positive electrode material. The metal oxides such as MoO_3 and WO_3 were proposed as reversible insertion electrodes in 1971 [23]. A large number of materials were investigated such as chromium oxides and vanadium oxides [24, 25]. However, the number of different compounds which are suitable as cathode hosts for lithium-ion batteries is quite limited due to the critical requirements such as high energy density, good cycleability and safety. They can be arbitrarily divided into layered $LiMO_2$ (e.g $LiCoO_2$, $LiNiO_2$ and $LiMnO_2$) compounds, manganese oxides (e.g $LiMn_2O_4$ spinel) and other materials. Lithium ions reversibly intercalate into and de-intercalate from these compounds above 3 V versus Li/Li^+. The properties of these materials and the preparation procedure will be summarized as follows.

2.2.1 Layered Lithium Cobalt Oxide and Lithium Nickel Oxide

The potentials of the $LiMO_2$ compounds of the heavier transition metals are generally lower than 2 V versus Li. Therefore, they are not suitable to be used as cathode materials for rechargeable lithium batteries.

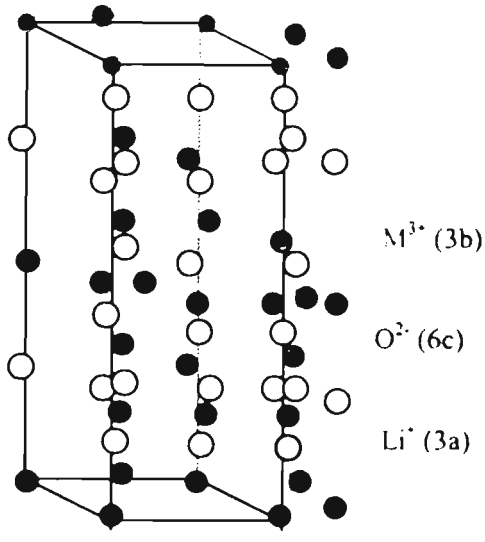

Fig. 2-5 The structure of layered $LiMO_2$ (M = Co, Ni) compound.

The layered $LiMO_2$ compounds (where M = Co or Ni) have a rhombohedral structure, in which lithium and transition metal atoms are ordered alternate (111) planes in a distorted cubic-close-packed oxygen ion lattice. A schematic diagram of the structure of layered $LiMO_2$ is shown in Fig. 2-5. The structure has trigonal (R3m) symmetry; the unit cell parameters are usually defined in terms of the hexagonal setting. The layered framework provides a two dimensional interstitial site which allows for relatively facile extraction and insertion of lithium ions.

2.2.1.1 $LiCoO_2$ compound

The $LiCoO_2$ compound was first described by Mizushima et. al [12] in 1980. $LiCoO_2$ currently is the dominant cathode material in commercial lithium-ion batteries. T. Ohzuku investigated the mechanism of the reaction of $LiCoO_2$ electrode in lithium cells using *in situ* XRD and concluded that the reaction of $LiCoO_2$ electrode in lithium cells can be divided into three regions. In the region $0< x < 1$ in $Li_{1-x}CoO_2$, the coexistence of two hexagonal phases was observed. The reaction in terms of lithium insertion and extraction in this region is a topotactic two-phase reaction. In the region $1/4 < x < 3/4$ in $Li_{1-x}CoO_2$, the reaction is a single phase reaction as a whole. In the region $3/4 < x < 1$, the reaction is a two-phase reaction [26]. Removal of lithium corresponding to 1 mole Li per formula $LiCoO_2$ delivers a theoretical capacity of about 274 mAh/g. However, only part of the lithium can be reversibly extracted and inserted due to structural restriction [27]. Good electrochemical performance can be obtained up to 4.2 - 4.25 V versus Li/Li^+, providing about 150 mAh/g capacity. The $LiCoO_2$ cathode may be reversibly cycled over 1000 charge-discharge cycles without appreciable specific capacity loss.

Many synthesis methods can be used to prepare electrochemically active $LiCoO_2$ compounds. The conventional solid-state reaction was commonly used by sintering the mixture of cobalt oxide (cobalt carbonate) and lithium carbonate (or lithium hydroxide) at high temperature. Some solution approaches such as sol-gel or organo-chemical synthesis for the $LiCoO_2$ compound have also been reported [28, 29]. In general, the different synthesis methods using high temperature sintering have no significant impact on the electrochemical performance of the $LiCoO_2$ electrode. However, the $LiCoO_2$ material synthesized at low temperature demonstrated a high specific capacity in the initial few cycles but only a limited cycle number [30].

During charge/discharge cycling, an interfacial layer usually is formed on the surface of the $LiCoO_2$ electrode. The formation of this interfacial film, caused by the reaction between the electrolyte and $LiCoO_2$ compound, has an important influence on the electrochemical properties of the $LiCoO_2$ electrode. The characterization of this interfacial film has been conducted by many researchers via a.c. impedance and electron microscopy [31, 32].

The use of $LiCoO_2$ as the cathode material in large scale lithium prototype batteries has been demonstrated by several institutions. Cylindrical 1.5 - 2 Ah and 8 Ah cells, having a flat plate construction inside were assembled and tested [33]. Cylindrical "C" size cells showed high capacity and a cycle life of more than 100 cycles. Although $LiCoO_2$ compound has excellent electrochemical properties as a cathode materials in lithium ion batteries, some drawbacks have to be addressed and cannot be ignored. The major drawback is the high cost for $LiCoO_2$ due to the high price and limited resource of Co. Another problem is the toxicity of Co, which causes come environmental impact when batteries are disposed of. These two factors forbid the application of $LiCoO_2$ as the cathode materials in any large batteries.

2.2.1.2 $LiNiO_2$ compound

Layered $LiNiO_2$ is an attractive cathode candidate for lithium ion batteries because of the relatively abundant natural resources of nickel, and because this compound is environmentally benign. The theoretical capacity of $LiNiO_2$ is close to that of the $LiCoO_2$ compound ie. 275 mAh/g. In practice, it can deliver a specific capacity between 185 to 210 mAh/g by charging up to 4.1 - 4.2 V versus Li/Li^+, which is much higher than that of $LiCoO_2$. However, $LiNiO_2$ electrodes have a higher fading rate of capacity

on cycling. Furthermore, the thermal stability of the $LiNiO_2$ compound is lower than that of $LiCoO_2$.

$LiNiO_2$ has the same structure as $LiCoO_2$ with a space group R3m in which nickel and lithium ions are located at octahedral 3(a) and 3(b) sites in a cubic-close-packed oxygen array. The dimensions of the $LiNiO_2$ unit cells (a_h = 2.9 Å, c_h = 14.2 Å ; c_h/a_h = 4.9 in hexagonal setting) are very close to the corresponding values for $LiCoO_2$. This suggests that the displacement of nickel and lithium ions occurs easily without a dimensional mismatch compared to $LiCoO_2$, which makes the preparation of electrochemical active $LiNiO_2$ difficult [34].

According to the reports [35, 36], the structural disorder due to the displacement of nickel ions at 3(a) sites and lithium ions at 3(b) sites in $LiNiO_2$ can severely affect the electrochemical properties such as specific capacity, average charge/discharge voltage and the shape of the differential chronopotentiometric curve etc. When there is a 50% displacement of nickel ions at 3(a) sites and lithium ions at 3(b) sites, a rock-salt type $LiNiO_2$ with a space group Fm3m could be generated, which is electrochemically inactive because of the immobile lithium ions at octahedral sites [37]. This presents a challenge for the preparation of structurally ordered $LiNiO_2$ compound with good electrochemical performance.

The $LiNiO_2$ compound tends to decompose to nonstoichiometric $Li_{1-x}Ni_{1+x}O_2$ during the sintering process of preparation. In the structure of $Li_{1-x}Ni_{1+x}O_2$, the extra nickel ions occupy the lithium ion sites and block the movement of lithium ions, leading to a poor electrochemical performance: a small amount of lithium extracted (low specific capacity) and poor reversibility of electrochemical process. Therefore, the optimization of the synthesis process is needed to suppress the decomposition of $LiNiO_2$ and achieve low x values of less than 1 - 2% in $Li_{1-x}Ni_{1+x}O_2$ [38-42]. The second problem to be

overcome is the capacity fading with cycling. The poor cycleability of $LiNiO_2$ electrode has been reported, but the cycle life of the $LiNiO_2$ electrode is greatly influenced by the way the compound was prepared. If properly synthesized, the cycle life of $LiNiO_2$ can be improved to an acceptable level. No evolution of the structure of the $LiNiO_2$ compound was observed even after 1200 cycles. Solid-state reactions are generally used to synthesize the $LiNiO_2$ compound under appropriate temperature and strongly oxidizing conditions. Unlike to $LiCoO_2$, which can be prepared by sintering a mixture of almost any Li, Co and O sources, the precursors for the preparation of $LiNiO_2$ have to be carefully chosen. The typical approach is to heat the mixtures of hydroxides (eg. Nickel hydroxide and lithium hydroxide), nickel hydroxide and lithium nitride, nickel oxide and lithium hydroxide [43-45] or by the use of Na_2O_2 and Ni sources, followed by ion exchange with $LiNO_3$ at elevated temperature [46]. With the careful control of all of the above factors, the $LiNiO_2$ compound with good electrochemical performance as cathode materials for lithium batteries could be obtained. The Li/$LiNiO_2$ and C/$LiNiO_2$ cells have been assembled using liquid electrolyte. The results using PAN based hybrid polymer electrolyte were also obtained [47]. Long cycle life, excellent high temperature performance and low self-discharge rate have been demonstrated using $LiNiO_2$/coke cells [38].

2.2.1.3 $LiMO_2$ (M = Co, Ni, Al or other metal elements) Derivatives

Many efforts have been made to improve the electrochemical performance of $LiNiO_2$, and decrease the cost and toxicity of $LiCoO_2$ by partial substitution of Co or Ni, with other metal elements such as Mg, Al, Mn, Cr, Fe and Ti respectively [48-50]. $LiNi_xCo_yO_2$ compounds were most investigated, because Ni and Co can substitute for each other to form solid solutions of any percentage and without disturbance of the

layered structure. Typical $LiNi_xCo_yO_2$ compounds include $LiNi_{0.5}Co_{0.5}O_2$, $LiNi_{0.8}Co_{0.2}O_2$ and $LiNi_{0.75}Co_{0.25}O_2$, which are commercially available. T. Ozuku [51] has reported a detailed investigation of the structural change of the $LiNi_{0.5}Co_{0.5}O_2$ compound during the insertion/extraction of lithium ions. The behavior of $LiNi_{0.5}Co_{0.5}O_2$ is the same as the $LiCoO_2$ compound upon the insertion/extraction of lithium ions. A study of a phenomenological expression of solid-state redox potentials shows that the solid-state electrochemical reaction of $LiNi_xCo_yO_2$ consists of three redox systems characterized by E = 4.50, 4.18 and 3.91 V versus Li/Li^+ for $LiCoO_2$; 4.23, 3.93 and 3.63 V for $LiNiO_2$; and 4.58, 4.05 and 3.58 V for $LiNi_{0.5}Co_{0.5}O_2$ [52]. The influence of particle morphology on the electrochemical properties of $LiNi_{1-x}Co_xO_2$ powders was explored by Li and Currie [53]. With proper control of the morphology and crystal size, $LiNi_{1-x}Co_xO_2$ ($0.1 < x < 0.3$) has excellent electrochemical performance, including low fade rate both at room temperature and high temperature and good rate capacities as well as long cycle life.

The addition of Al^{3+} ions in $LiNiO_2$ can stabilize the structure of the $LiNiO_2$ compound. It is already known that there is a two-phase reaction when a Li_xNiO_2 electrode is charged to $0.75 < x \leq 1$, which includes ca. 0.3 Å shrinkage in the interlayer distance. Such interlayer change has a damaging effect to the layered structure of $LiNiO_2$. Therefore, the rechargeability in the two-phase region in Li_xNiO_2 ($0.75 < x \leq 1$) is expected to be poor. To circumvent this problem, doping $LiNiO_2$ with Al^{3+} ions is an ideal approach. Because $LiAlO_2$ is isostructural with $LiNiO_2$, it can form solid solutions with $LiNiO_2$. For example, by synthesizing $LiAl_{0.25}Ni_{0.75}O_2$, the following topotatic reaction would be expected:

$$LiAl_{0.25}Ni_{0.75}O_2 \rightleftharpoons \square_{0.75}Li_{0.25}Al_{0.25}Ni_{0.75}O_2 + 0.75Li^+ + 0.75e^- \qquad (2.2)$$

Since Al must remain 3+ in oxidation state, when all the Ni ions are oxidized to the Ni^{4+} state, the maximum quantity of Li ions extracted is 0.75 mole per mole $LiAl_{0.25}Ni_{0.75}O_2$. This prevents the overcharge of the electrode [54]. $LiAl_xNi_{1-x}O_2$ solid solutions have been thoroughly investigated by many groups. DSC measurements have shown that $LiAl_{0.25}Ni_{0.75}O_2$ is much safer than $LiNiO_2$ in the charged state. The thermal behavior of $LiNiO_2$ in the charged state is a haystack-type reaction associated with thermal run away. The thermal behavior of the fully charged $LiAl_{0.25}Ni_{0.75}O_2$ is quite different, in which the reaction is much milder [55, 56]. The lithium intercalation into and deintercalation from $LiAl_{1/4}Ni_{3/4}O_2$ electrode was investigated by using a current transient technique [57]. No potential plateau was observed in the charge/discharge curve, indicating that lithium ion diffusion proceeds in a single phase region, thus favoring good reversibility and extended cycle life.

Apart from Ni/Co, Ni/Al combination, it is generally known that substitution with other transition metals results in materials with lower capacities and less reversible insertion/extraction reactions. The single phase of $Li_xCr_yCo_{1-y}O_2$ and $Li_xCr_yNi_{1-y}O_2$ compounds have been successfully prepared. The electrochemical tests indicated that as y increased, specific capacity declined [58]. Very good thermal stability was obtained by co-substitution of titanium and magnesium [59].

Doping $LiNiO_2$ is a subject of increasing interest and has produced a large number of papers and patents. Many elements from the periodic table have been investigated, including Ti, V, Cr, Fe, Co, Mn, Cu, Zn, Cd, Sn, Al, B, Mg, Ga, Ca and Na. The general trend is now oriented on multiple substitution, with each element bringing some peculiar advantage on reversibility, fading or thermal stability for safety.

The layered $LiMO_2$ (M = Co, Ni) compounds and their derivatives as cathode materials are used in approximately 90% of commercial lithium-ion battery production. Their preparation and their electrochemical performance are summarized in table 2-1.

Table 2-1 The Synthesis and electrochemical performance of layered $LiMO_2$ compounds

# Compound	synthesis	Current (mA/cm^2)	Counter electrode	Electrolyte	Cycle capacity (mAh g) / •	
1 $LiCoO_2$	Li_2CO_3 + $CoCO_3$, 850°C, air	0.17	Nature graphite	1M $LiClO_4$ EC DME 1:1	140	[60]
2 $LiCoO_2$	$LiNO_3$ + $Co(NO_3)_2$ Spray dry 400°C	C/100	Li	1M $LiClO_4$ PC EC 1:1	118	[61]
3 $LiCoO_2$	$LiOH.H_2O$ + $CoCO_3$, 850°C, air	C/100	Li	1M $LiClO_4$ PC EC 1:1	148	[61]
4 $LiCoO_2$	Co_2O_3 + LiOH 700°C, O_2	1	Li	$LiAsF_6$ in proprietary solvent	126	[46]
5 $LiCoO_2$	$Co(NO_3)_2$ + LiOH + organic acid	0.25	Li	1M $LiPF_6$ PC DEC 1:4	145	[62]
6 $LiCoO_2$	Li_2CO_3 + $CoCO_3$ 800°C, air	0.2	Li	$LiClO_4$ PC	137	[63]
7 $LiCoO_2$	Li_2CO_3 + Co_3O_4 900°C, Ar	<0.2	Li	$LiClO_4$ PC	137	[64]
8 $LiCoO_2$	Li_2CO_3 + $CoCO_3$ 850°C, O_2	0.25	Li	N/A	150	[65]
9 $LiCoO_2$	Li_2CO_3 + Co_3O_4 900°C, Ar	0.06	Li	Li_3PO_4-Li_2S-SiS_2	90/4	[45]
10 $LiCoO_2$ (LT)	LiOH + NH_4OH + $Co(NO_3)_2$ 400°C	N/A	Li	1M $LiClO_4$	110	[48]
11 $LiCoO_2$ (LT)	Co acetate + Li acetate, 550°C, air	C/5	Li	1M $LiClO_4$ PC EC DME 1:1:2	N/A	[66]
12 $LiNiO_2$	LiOH + $Ni(OH)_2$ 675°C, O_2	0.1	Li	1M $LiN(CF_3SO_3)_2$ PC/DME 1:1	150	[67]
13 $LiNiO_2$	Pyro, alcoholate 720 °C, O_2	0.4	Li	N/A	150 16	[68]
14 $LiNiO_2$	$LiNO_3$ + $NiCO_3$ 600°C, O_2	0.17	Nature graphite	1M $LiClO_4$ EC DME 1:1	>150	[34]
15 $LiNiO_2$	$LiNO_3$ + $Ni(OH)_2$	0.17	graphite	1M $LiClO_4$/PC	>200	[34]
16 $LiNiO_2$	NiO + LiOH 700°C, O_2	1	Li	$LiAsF_6$ in proprietary solvent	140	[46]
17 $LiNiO_2$	$NiCO_3$ + $LiNO_3$ 750°C, O_2	0.17	Li	1M $LiClO_4$/PC	190	[37]
18 $LiNiO_2$	$LiOH.H_2O$ + $Ni(OH)_2$	C/100	Li	1M $LiPF_6$ EC/PC 1:1	173	[49]
19 $LiNiO_2$	$LiNO_3$ + $Ni(OH)_2$ 750, O_2	0.48	Li	1M $LiClO_4$ EC PC	152 50	[50]
20 $LiNi_{0.5}Co_{0.5}O_2$	Li_2CO_3 + $CoCO_3$ +	0.17	Nature	1M $LiClO_4$	140 100	[60]

	$NiCO_3$, 850°C		graphite	EC DME 1:1		
21 $LiNi_{0.7}Co_{0.3}O_2$	Li_2CO_3 + NiO + Co_3O_4, O_2 800-1000°C	0.07	Li	1M $LiClO_4$ PC	154	[69]
22 $LiNi_{0.8}Co_{0.2}O_2$	Li_2CO_3 + NiO + Co_3O_4, O_2 800-1000°C	0.07	Li	1M $LiClO_4$ PC	148	[69]
23 $Li_{1.1}Mn_{0.1}Ni_{0.9}O_2$	LiOH + NiO+MnO	C/100	Li	1M $LiClO_4$ EC PC 1:1	148	[70]
24 $LiAl_{0.05}Ni_{0.95}O_2$	LiOH + NiO + Al	C/50	Li	1M $LiAsF_6$ PC DME	180	[71]

*The numbers in this column represent cycling capacity after the number of cycles given after "/". If no cycle number is given, the capacity is the first recharge capacity.

2.2.2 $LiMn_2O_4$ Spinel and its derivatives

The spinel-type oxide $LiMn_2O_4$ and its derivatives have been studied for more than a decade as cathode materials for lithium ion batteries. The lithium insertion and extraction in $LiMn_2O_4$ spinel provides an average voltage of 4 V versus Li/Li^+, which is similar to $LiCoO_2$ and $LiNiO_2$. Significant efforts have been made to extend the capacity of the 4 V plateau to the 3 V plateau without compromising the specific capacity. Spinel $LiMn_2O_4$ has the advantages over Co- and Ni- containing systems of being inexpensive, environmentally benign and having a larger thermal stability domain especially when overcharged. However, the theoretical capacity of $LiMn_2O_4$ is only 148 mAh/g. The high rate of capacity fading on cycling is another serious drawback for $LiMn_2O_4$ spinel electrodes. Fortunately, the problems related to the capacity fading can be circumvented by doping Mn with other transition metals M to suppress the Jahn-Teller (Mn^{3+}) effect. Therefore, $LiMn_2O_4$ spinel is still an attractive cathode candidate for lithium ion batteries. Some doped $LiM_xMn_{2-x}O_4$ spinels have already been used in commercial production.

2.2.2.1 The Structural Characteristics of Spinel Lithium Manganese Oxides

The spinel $LiMn_2O_4$ belongs to the cubic system with a space group of Fd3m, in which Li^+, $Mn^{3+/4+}$ and O^{2-} ions occupy tetragonal 8a, octahedral 16d and 32e position in the cubic-closed-packed (ccp) oxygen array. The spinel structure is shown in Fig. 2-6. This structure provides a three dimensional network of face-sharing tetrahedral and octahedra for lithium ion diffusion. In the $[M_2]O_4$ spinel framework, 75% of the metal cations occupy alternate layers between the ccp oxygen planes; the remaining 25% of the metal cations are located in the adjacent layers. Therefore, sufficient metal M cations exist in every layer to provide a sufficiently high binding energy to maintain an ideal ccp oxygen array when lithium ions are extracted from the structure. The unit cell of the spinel structure expands and contracts isotropically [72]. The electrodes with such structure are likely to be more stable to electrochemical cycling than those in which there is a large anisotropic expansion or contraction of the lattice parameters. For example, the spinels $Li[M_{1.67}Li_{0.33}]O_4$ (M = Mn, Ti) are extremely tolerant to cycling because the volume variation of the cubic unit cell is less than 1% within controlled compositional limits [73, 74].

The $LiMn_2O_4$ spinel electrode offers a 4 V voltage versus lithium in the compositional range $0 \leq x \leq 1$ in $Li_xMn_2O_4$. Lithium ions can further insert into $LiMn_2O_4$ to form $Li_{1+x}Mn_2O_4$ at 3 V against lithium. For $Li_{1+x}Mn_2O_4$, the electrode consists of two phases: a cubic phase $LiMn_2O_4$, and a tetragonal phase $Li_2Mn_2O_4$. The tetragonal phase grows at the expense of the cubic phase. In the $LiMn_2O_4$ spinel structure, the strong Mn-O bond maintains the structural integrity of the electrode during lithium ion insertion and extraction. However, the Jahn-Teller distortion effect starts at $Mn^{n+} = 3.5$ (c/a = 1) and reaches a maximum at the valence of $Mn^{3+} = 3$ (c a = 1.16), which reduces the symmetry of the cubic spinel phase to tetragonal phase

$Li_2Mn_2O_4$ and increases c/a to 1.16 concomitantly. Such distortion accompanying the volume change of the unit cell would cause the crystal structure of the electrode to degrade and the electrochemical properties to deteriorate.

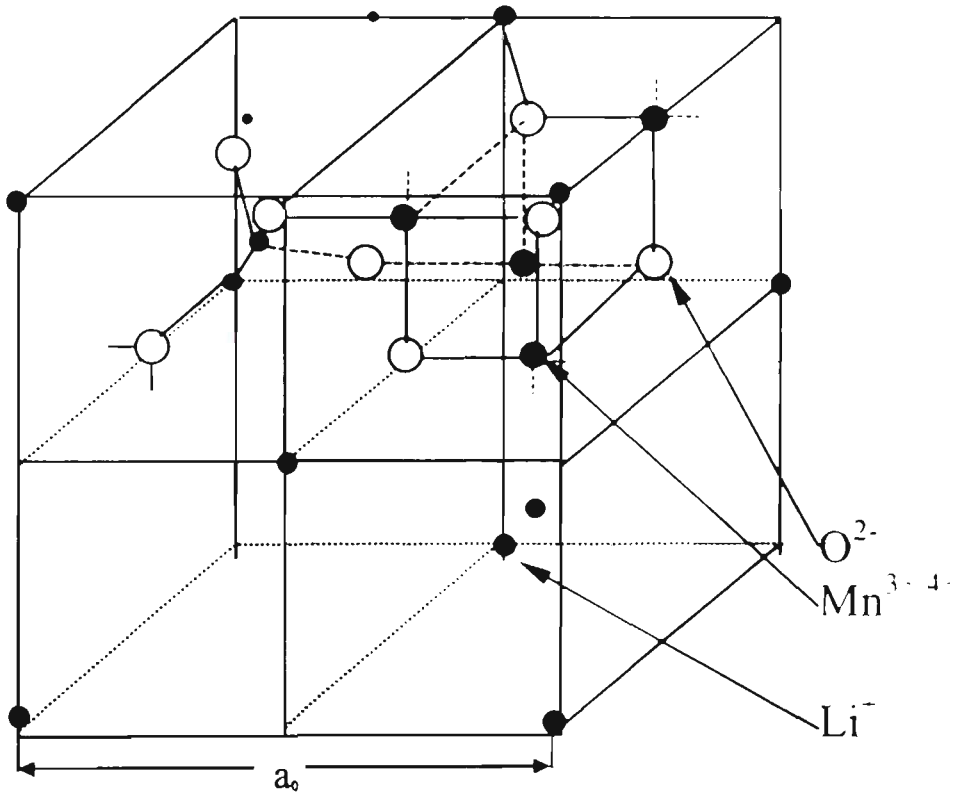

Fig. 2-6 The structure of spinel $LiMn_2O_4$.

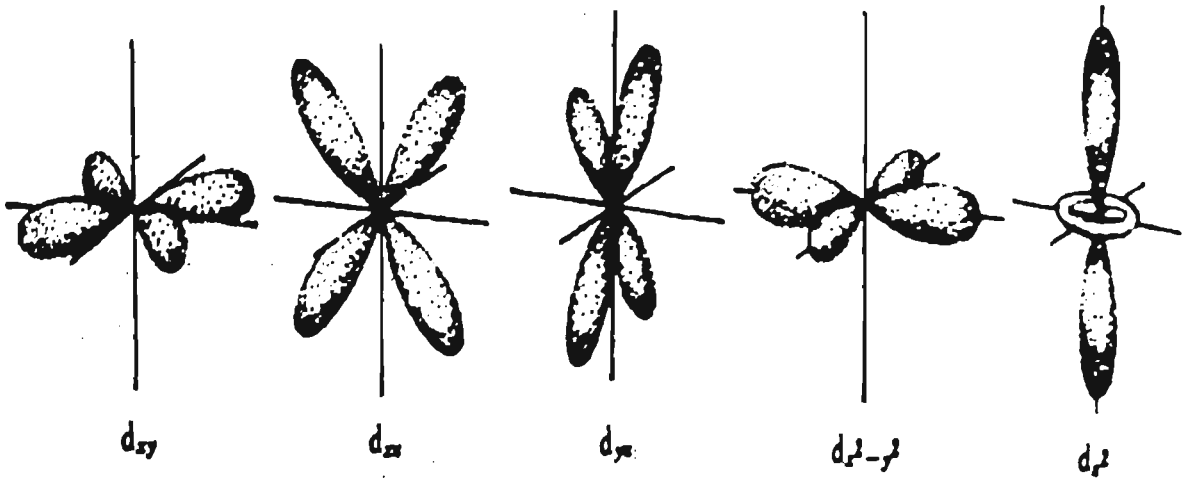

Fig. 2-7 The space distribution of d orbitals.

It is generally known that there are five d orbitals in the d electron shell. As shown in Fig. 2-7, the three orbitals d_{xy}, d_{xz} and d_{yz} are oriented in space such that their distribution maxima fall into the region between the coordinate axes. The remaining two orbitals d_z^2 and $d_x^2{}_{-y}^2$ have their lobes oriented symetrically along the axes. Each orbital can accommodate a pair of electrons with the opposite spinning. The five d orbitals have the same energy level in the free atom (or ion). When the cations are in the crystal field, they will split into different energy level. Under the octahedral field of the ligands, the five d states are divided into two groups of states, with different energies, expressed as denotation of Mulliken:

$$^2D \longrightarrow {}^2T_{2g} + {}^2E_g \qquad (2.3)$$

Taking into account that the ligands have negative charges (ligand-dipoles are oriented with the negative pole to the central atom), we can easily come to the conclusion that in octahedral complexes: the $d_x^2{}_{-y}^2$ and d_z^2 electron is subject to a stronger electrostatic repulsion from the ligands than the electrons in d_{xy}, d_{xz} and d_{yz} orbitals. Hence, the

electron energies of these two states, under the electrostatic influence of the ligands, become different: the E_g energy level is higher than T_{2g} level. All three T_{2g} states are fully equivalent with respect to the six ligands, the same as for all two E_g states. The ligand numeration in octahedral complex and the splitting of d states are shown in Fig. 2-8 [75].When the d shell has a configuration of d_0, d_3, d_5, d_{10}, the orbitals occupied by electrons overlap to form an O_h symmetry, which is stable in the crystal field. If the d shell has a configuration of d_4 or d_9, the electron distribution will not be O_h symmetry. Such transition metal cations will be unstable in an octahedral field, and their d orbitals will split and induce the distortion of the crystal structure to make the central cations stable. This effect is called Jahn-Teller distortion [76].

Mn^{3+} cation has a d state of d_4, in which 4 electrons occupy the 3d shell. In an octahedral field, four 3d electrons distribute as $T_{2g}3E_g$ e.g. three electron in the T_{2g} energy level and one electron in the E_g energy level, which is subject to a Jahn-Teller distortion. Because of the odd number of E_g electrons, this distortion should be appreciable. Indeed, a considerable elongation of two trans bonds with little difference in the lengths of the other four has been observed in many Mn^{3+} compounds such as the tetragonal elongation in $Li_2Mn_2O_4$.

The valence of Mn in stoichiometric $LiMn_2O_4$ is 3.5. The reaction of the $LiMn_2O_4$ spinel electrode in lithium cells proceeds as follow:

$$LiMn_2O_4 \rightleftharpoons Li^+ + Mn_2O_4 + e^- \qquad (2.4)$$

When lithium is extracted, the valence of Mn increases up to +4; On lithiation, the Mn valence decreases to +3.5. So, it seems Jahn-Teller distortion is unlikely to occur. However, in practice, the situation is different from the theoretical aspect. Battery

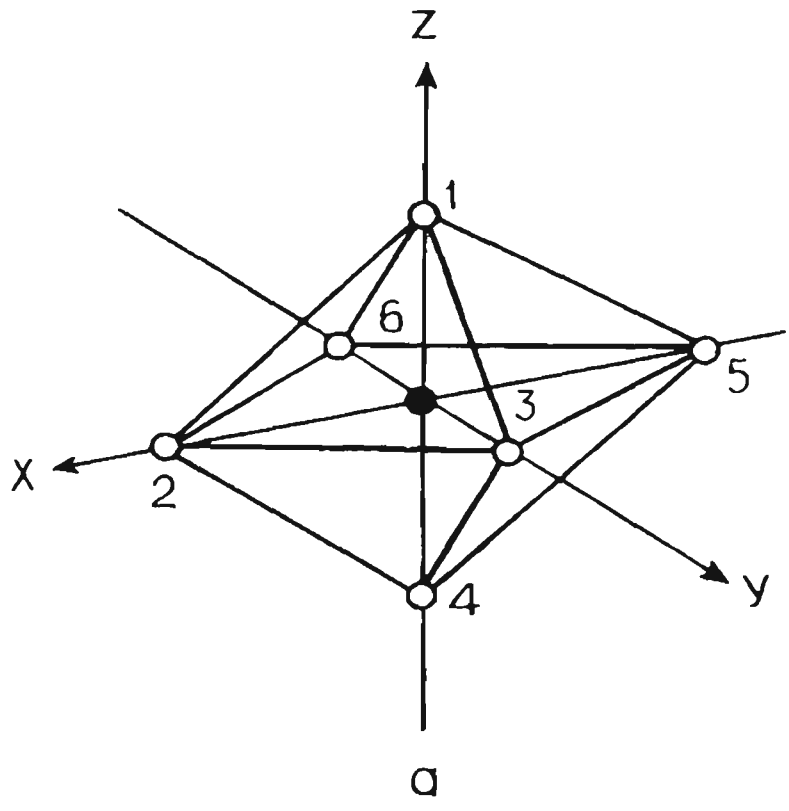

(a)

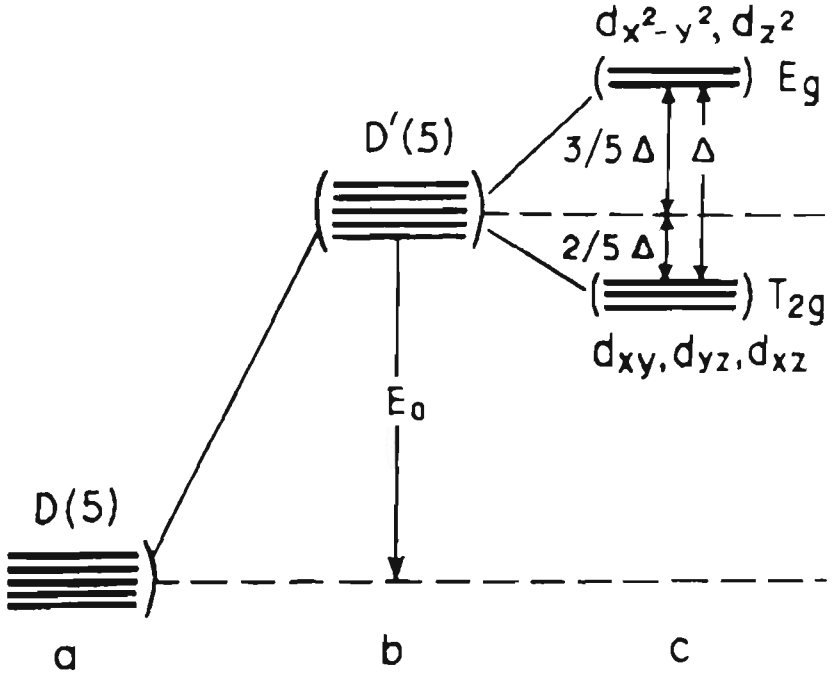

(b)

Fig. 2-8 (a) Ligand numeration in octahedral complex.
(b) The splitting of d states under the octahedral field.

systems always operate under nonequilibrium conditions. The electrochemical reactions that occur in battery systems therefore result in uneven production and distribution of reaction products. At the end of the 4 V plateau in $Li/Li_xMn_2O_4$ or $C/Li_xMn_2O_4$ cells, under nonequilibrium conditions, for example, constant current discharge, it is therefore expected that there will always be some spinel particles that are more extensively lithiated than others. It is also likely, when the cell voltage is between 4 and 3 V, and while most of the spinel particles still have an average composition $Li_{1-x}Mn_2O_4$ (i.e., a slightly lithium deficient spinel), the onset of Jahn-Teller effect may start to occur on the surface of some particles that have already reached the stoichiometric spinel composition, $LiMn_2O_4$. In practice, when the discharge voltage is close to 3V, it is plausible that a few spinel particles may reach an overall composition, $Li_{1-x}Mn_2O_4$, in which the average Mn oxidation state falls below 3.5. A Jahn-Teller distortion might occur at the particle surface, inducing the growth of tetragonal phase. The incompatibility between the oxygen arrays of the cubic and tetragonal phases could then cause a highly crystalline electrode particle to degrade at the crystal surface, which would damage structural integrity and particle-to-particle contacts. Therefore, the electronic conductivity and lithium diffusivity will degrade. Fortunately, this damaging effect can be reduced by suppressing the onset of the Jahn-Teller distortion by modifying the composition of the spinel electrode to keep the average Mn oxidation state slightly above 3.5 at the end of the 4 V discharge plateau.

2.2.2.2 Synthesis of $LiMn_2O_4$ Spinel

Traditionally, the $LiMn_2O_4$ compound is made by heat treatment of the corresponding carbonates (Li_2CO_3 and $MnCO_3$) at high temperatures in the range 700 - 900°C. But in general, it can be prepared by heating lithium carbonate or lithium nitride

or lithium hydroxide with manganese carbonate or manganes oxide or EMD (electrolytic manganese oxide). The solution synthesis routes have been investigated. The Sol-gel synthesis of manganese oxide is discussed in details in previous publications [77-79]. Chemical precipitation methods also have been used to prepare $LiMn_2O_4$ spinel using $Mn(CH_3COO)_2$, LiOH and NH_4OH as precursors. The crystalline $LiMn_2O_4$ can be easily obtained by heating the precipitates at a low temperature in the range of 400°C - 500°C. The Pechini process can produce high quality $LiMn_2O_4$ spinel powders, in which the polybasic acid chelates with Li and Mn cations are formed. When heated, the chelates undergo polyesterification to form a solid polymeric resin throughout which the cations are uniformly distributed. Thus the resin retains homogeneity on the atomic scale and may be calcined at low temperature to yield fine particulate oxides [80, 81].

The electrochemical properties of $LiMn_2O_4$ spinel such as capacity and rechargeability vary greatly with different synthesis routes. The low temperature synthesized $LiMn_2O_4$ spinels have a high capacity, but poor cycle life. Generally, $LiMn_2O_4$ spinel prepared by solid-state reaction has a discharge capacity between 120 – 140 mAh/g and a reasonably good cycle life. The lithium-rich composition $Li_{1+x}Mn_{2-x}O_4$ leads to improved performance in terms of capacity fading. However, fading, particularly at elevated temperature, is still worse than that observed with nickel or cobalt-rich materials.

2.2.2.3 Doped $LiM_xMn_{2-x}O_4$ Spinels and their Electrochemical Performanc

The cycleability of $LiMn_2O_4$ spinel electrode can be improved by suppressing the Jahn-Teller effect at the end of the 4 V discharge, by substituting Mn with other metal elements such as M^+ (e.g. Li^+), M^{2+} (e.g. Zn^{2+}, Mg^{2+}), M^{3+} (e.g. Co^{3+}, Cr^{3+}, Al^{3+}) and

M^{4+}(e.g. Ti^{4+}) etc. But, a trade-off has to be made since the capacity decreases with the increased concentration of the substitution metal. Robertson et al. [82] investigated the dopant effect of M = B, Cr, Fe, Ti, Al and Ga in single-phase $LiM_xMn_{2-x}O_4$ spinel. The best result was found to be the Cr^{3+} dopant effect. Reversible capacities exceeding 110 mAh/g were attained with $LiCr_{0.02}Mn_{1.98}O_4$, with virtually no capacity fade over 100 cycles. This was attributed to a combination of ionic size coordination site and crystal-structure preferences and oxidation state stability. The cobalt doping also has the excellent effect of stabilizing the $LiMn_2O_4$ spinel. The best overall performance in terms of the capacity and cycle life was obtained for $LiCo_{1/6}Mn_{11/6}O_4$ spinel. The energy density of the cathode for the Li/ $LiCo_{1/6}Mn_{11/6}O_4$ cell at the 300th cycle was about 370 wh/kg (cut-off 4.45 to 3.60 V, $i_C = i_D = 0.2$ mA.cm^{-2}) [83].

Substitution of Co in $Li_xMn_2O_4$ can increase the particle size and decrease the total surface area of the spinel by up to 50%, which is beneficial for the good capacity retention properties of the cathode. Increasing the Co content in the spinel from y = 0 to y= 0.05 and 0.06 in $LiCo_yMn_{2-y}O_4$, resulted in an increase in initial capacity and decrease in capacity fade during cycling. The lithium-ion diffusion coefficient (D_{Li^+}) for Co-doped spinel was estimated to be in the range 2.4×10^{-12} to 1.4×10^{-11} m^2/s as a function of SOC and was found to be higher than the value estimated for the pure spinel (9.20×10^{-14} to 2.6×10^{-12} m^2/s). The Li^+ partial conductivity estimated in Co-doped spinel (in the range between 8×10^{-5} and 1.85×10^{-4} S/cm) was higher than those estimated for pure spinel [(1.2-7.2) $\times 10^{-5}$ S/cm]. The larger particle size of Co-doped spinel resulted in less contact between the active material and the electrolyte, contributing to a decrease in the rate of electrolyte and electrode decomposition, and consequently, to a smaller self-discharge rate [84].

The improvement of the cycle performance is not only ascribed to the suppression of Jahn-Teller distortion but also to the enhancement of the stability of the octahedral sites in the spinel skeleton structure. The binding energy of MnO_2, CrO_2 and CoO_2 could be estimated as 946, 1142 and 1067 $kJ.mol^{-1}$, respectively. So, it would be reasonable to say that the M-O bonds for M = Cr and Co are stronger than the Mn-O bond, so that the dopants enhance the stability of the spinel structure.

The overlithiated spinel with a general formulation $Li_{1+x}Mn_{2-x}O_4$ exhibits strongly reduced capacity fading, with some reduction in initial discharge capacity. In spinel notation, these stoichiometric compounds are represented by the formula $(Li)_{8a}[Mn_{2-x}Li_x]_{16d}O_4$. Therefore, as x increases the manganese ions in the octahedral (16d) sites are replaced by lithium ions with a concomitant increase in the manganese-ion oxidation state to maintain charge neutrality. The limiting composition $Li[Mn_{1.66}Li_{0.33}]O_4$ is reached when all the manganese ions are tetravalent. The cycling performance of $Li/Li_{1.22}Mn_{1.77}O_4$ (x=0.22) and $Li/Li_{1.29}Mn_{1.71}O_4$ (x=0.29) cells showed that these cells demonstrated reasonably good reversibility when cycled over both the 3 V and 4 V regions and yield total capacities of 160 mAh/g and 140 mAh/g respectively on the initial discharge cycles [85].

When the $LiMn_2O_4$ spinel electrode is stored at elevated temperature, Mn^{3+} dismutation and dissolution of the Mn^{2+} produced, is a severe problem of the spinel. It contributes greatly to the occurrence of the irreversible capacity loss during storage at elevated temperature. This can be partially improved by using low surface area materials, or surface modification.

A lot of research work is still in progress to improve the electrochemical performance. Due to its low cost, it is expected that $LiMn_2O_4$ spinel will be widely used as cathode materials in large scale lithium batteries.

2.2.2.4 The Reaction Mechanism of $LiMn_2O_4$ Spinel in Lithium Batteries

The lithium insertion and extraction in spinel $LiMn_2O_4$ involves the lithium ions diffusion through a three dimensional tunnel network in spinel skeleton. The reaction proceeds as follow:

$$[Li]_{8a}[Mn_2]_{16d}[O_4]_{32e} \rightleftharpoons Li^+ + [M_2]_{16d}[O_4]_{32e} + e^- \qquad (2.5)$$

two pairs of oxidation and reduction peaks were generally observed in cyclic voltammograms of $LiMn_2O_4$ spinel electrode [86-88]. These two pairs of redox peaks relate to the reversible two-step process for lithium ion intercalation and de-intercalation in $LiMn_2O_4$ spinel. The areas of the two reduction or oxidation peaks are essentially equal, which suggests that in each stage lithium ions occupy half of the total available crystallographic sites. The first and the second reduction peaks thus can be indexed to equilibrium λ-MnO_2-$Li_{0.5}Mn_2O_4$ and $Li_{0.5}Mn_2O_4$-$LiMn_2O_4$. The structural basis for the two-step reduction and oxidation process in $LiMn_2O_4$ spinel is not yet known. One possible interpretation is that during the discharge process, in the first peak region, lithium ions occupy every other available tetrahedral site (8a) in the spinel structure, until half the sites are filled. At this point, the phase transformation from λ-MnO_2 to $Li_{0.5}Mn_2O_4$ is completed, inducing single-phase $Li_{0.5}Mn_2O_4$. In the second peak region, lithium ions may fill the remaining empty 8a sites. This arrangement increases repulsion between the lithium ions, resulting in a small increase in the free-energy in the system as reflected by the observed 100 mV voltage drop. In the fully discharged state, the transformation from $Li_{0.5}Mn_2O_4$ to $LiMn_2O_4$ is complete. Vise versa, it is the same for charging process [80]. In situ synchrotron x-ray diffraction studies on the $LiMn_2O_4$ electrode indicated that three cubic phases with different lattice constants were

observed. The deintercalation of lithium in lithium-rich spinel cathode materials proceeds through a series of phase transitions from a lithium-rich phase to a lithium-poor phase and finally to a λ-MnO_2-like cubic phase; rather than through a continuous lattice constant contraction in a single phase [89].

The $LiMn_2O_4$ spinel structure provides a stable 3-dimensional network for lithium ion insertion and extraction. Although the Jahn-Teller distortion at the end of 4 V discharge plateau induces the damage of the spinel structure and therefore an unsatisfactory cycle life, the modification by a doping effect can considerably improve the cyclability of $LiMn_2O_4$ spinel.

2.2.3 The Monoclinic $LiMnO_2$, orthorhombic $LiMnO_2$ and their Derivatives

The $LiMnO_2$ compounds are of great interest in the lithium battery area recently, since their theoretical specific capacities are almost twice that of the spinel $LiMn_2O_4$ (285 mAh/g). There are two different phase structure for the $LiMnO_2$ compound. One is layered monoclinic $LiMnO_2$ (C2/m in space group; or called m-$LiMnO_2$). The other is the orthorhombic phase (Pmnm in space group; or called o-$LiMnO_2$). The layered m-$LiMnO_2$ is difficult to synthesize under equilibrium conditions. Many attempts have been made to prepare layered $LiMnO_2$, mainly involving the use of aqueous solutions [90-91]. The resulting products have stoichiometries which differ from $LiMnO_2$, contain water or protons, are of poor crystallinity or do not maintain their structure during cycling. The first successful synthesis of layered $LiMnO_2$ was reported by Armstrong and Bruce in 1996 [92]. It was made through an ion exchange process, starting from a layered α-$NaMnO_2$ precursor. The $NaMnO_2$ was synthesized by solid-state reaction between stoichiometric quantities of Na_2CO_3 and manganese (III) oxide at 700 °C – 730 °C for 18 - 72 hours under flowing argon. The layered m-$LiMnO_2$ was obtained by

refluxing $NaMnO_2$ with an excess of LiCl or LiBr in n-hexanol at 145 – 150 °C for 6 - 8 hours. The layered structure of the as synthesized (m-$LiMnO_2$) was confirmed by powder neutron diffraction, which is shown in Fig. 2-9 [92].

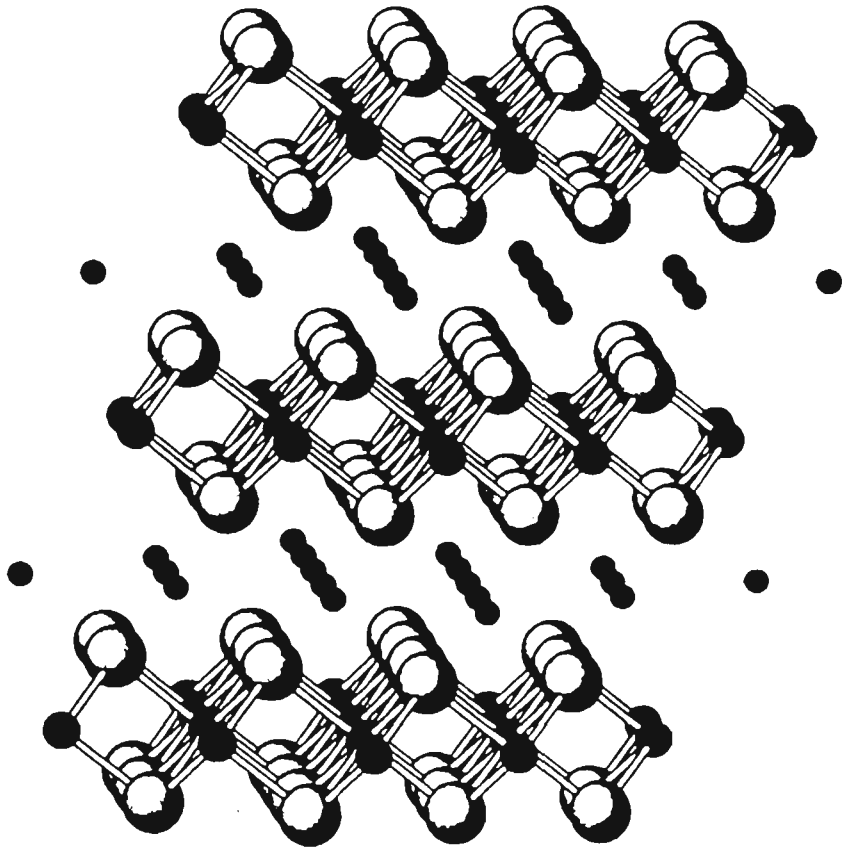

Fig. 2- 9 The schematic of layered $LiMnO_2$.

Although a large capacity of 200 – 270 mAh/g can be obtained on the initial charging and discharging, the capacity decreased very quickly with cycling. X-ray diffraction revealed that for $(1-x) \geq 0.5$ in $Li_{1-x}MnO_2$ the structure is rhombohedral. On removal of lithium from $LiMnO_2$, the Jahn-Teller Mn^{3+} ion is oxidized to Mn^{4+} with the

resulting loss of the monoclinic distortion. The monoclinic phase gradually transforms to a spinel-like phase. The monoclinic phase can be stabilized via Al^{3+} doping. A series of doped m-$LiAl_yMn_{1-y}O_2$ compounds has been prepared [93]. The electrochemical tests showed that these compounds display two-step discharging at ~ 4 V and ~ 2.9 V respectively. The doped m-$LiAl_yMn_{1-y}O_2$ is more stable on cycling than pure m-$LiMnO_2$. However, the phase transformation still proceeds slowly on cycling. Analysis of the cycled m-$Li_xAl_{0.05}Mn_{0.95}O_2$ by XRD and TEM revealed a complex phase assemblage after 100 cycles, which consists of a mixture of the monoclinic phase and the tetragonal spinel phase. For any practical application, two problems have to be overcome. One is the two-step discharging which differs by 1 V. Such a 1 V voltage gap is not suitable for the operation of any electronic devices. The other is phase transformation on cycling, which limits the cycle life of the electrode.

Orthorhombic o-$LiMnO_2$ can be easily obtained by solid-state reaction under a controlled atmosphere. The crystallization, structure and morphology of o-$LiMnO_2$ strongly relies on the synthesis conditions. In return, electrochemical performance of o-$LiMnO_2$ is quite sensitive to its crystallization state. Some investigations have showed that crystalline powders with a $\varphi \approx 450$ Å crystalline size are the best cathode candidates in rechargeable lithium cells, and attributed to the kinetic limitation of the intercalation/deintercalation process. The electrochemical removal of lithium from orthorhombic o-$LiMnO_2$ leads to a phase transition with a first plateau at about 3.7 V. This corresponded to the formation of a spinel-like material, suggesting structural differences between the two materials. An extended x-ray absorption fine structure study at the manganese K edge revealed that there is a marked difference between the manganese second neighbors for original o-$LiMnO_2$ and cycled o-$LiMnO_2$. This can be related to the orthorhombic-to-cubic phase transition itself or to the memory effect of

the stacking faults originally present in o-$LiMnO_2$. The highly divided and disordered phase, associated with stacking faults, favor high cycling capacities that may reach 200 Ah/kg. This capacity is rather well maintained upon cycling over the two 3 and 4 V plateaus [94-98].

An in situ x-ray diffraction study demonstrated that o-$LiMnO_2$ converts to a cubic structure $LiMn_2O_4$ after the initial charge (equal to delithiation) of the cathode. However, this cubic phase is not a simple crystalline spinel structure. It appears that stacking faults or other dislocations are present initially, but disappear after ten cycles or so. The transition between the cubic and tetragonal phase in the flat 3 V plateau was also confirmed [99]. The cyclability of o-$LiMnO_2$ as cathode in lithium cells is much better than that of m-$LiMnO_2$ when cycled in a voltage range of 2.2 V- 4.3 V. However, its electrochemical performance parameters such as the voltage plateau and cyclability still need to be further improved. Doping o-$LiMnO_2$ with Al^{3+}, Cr^{3+} and Ga^{3+} etc. have been attempted. It is surprising to find that the discharge plateau of o-$LiM_xMn_{1-x}O_2$ can be modified to 3.4 V (the average discharge voltage) versus lithium. The cyclability also has been considerably improved by the dopant effect. The lithium cells with such modified $LiMnO_2$ electrodes can be cycled more than 300 times with only 20% capacity degrade [100]. Therefore, the layered $LiMnO_2$ type cathode materials could provide an attractive future for lithium-ion battery applications in large-scale lithium ion batteries such as those used in Electric Vehicles (EVs) and for Stationary Energy Storage.

In addition to m- and o-$LiMnO_2$, some other lithium manganese oxides have also been reported. One of the most interesting materials is manganese oxyiodide e.g. $Li_{1.5}Na_{0.5}MnO_{2.85}I_{0.12}$. This compound was made by reacting $NaMnO_4$, LiI and acetonitrile. The as-prepared sample exhibits an amorphous structure. The

$Li_{1.5}Na_{0.5}MnO_{2.85}I_{0.12}$ electrode demonstrated a high reversible capacity of 260 mAh/g in the range 1.5 – 4.3 V versus lithium with excellent cycling characteristics [101, 102].

2.2.4 Vanadium Oxides and Lithium Vanadium Oxides as Cathode Materials for Lithium-ion Batteries

Lithium vanadium oxides and vanadium oxides are some of the attractive cathode materials for lithium-ion batteries. In lithium metal polymer batteries, lithium metal is used as the anode. Because the lithium anode provides the lithium ion source for the lithium shuttle, it is not necessary that a lithium source must be present in cathode materials. Therefore, vanadium oxides are very suitable for use in lithium polymer batteries, since they provide very high specific capacity and a voltage range between 2 V to 3 V versus lithium.

2.2.4.1 Lithium Vanadium Oxide Cathode Materials

Lithium vanadium oxide, $Li_{1+x}V_3O_8$, has been studied as one of the cathode materials of lithium secondary batteries since Wadsley first reported its crystal structure in 1957 [103]. At the beginning of the studies on the lithium insertion behavior of this compound, this oxide was prepared by high temperature synthesis, in which slow or rapid cooling of a melt of lithium vanadium oxide occurred [104, 105]. The $Li_{1+x}V_3O_8$ prepared this way is termed the HT lithium vanadium oxide. Pistoia et al. [106] presented a new synthesis route to obtain $Li_{1+x}V_3O_8$ in the gel state by precipitation from an aqueous solution containing lithium hydroxide (LiOH) and vanadium pentooxide (V_2O_5), which is usually called the sol-gel process. The $Li_{1+x}V_3O_8$ obtained from aqueous solution is termed the LT lithium vanadium oxide. Nassau and Murphy [107] reported the larger discharge capacity of glassy $Li_{1+x}V_3O_8$ in early cycles and

more rapid deterioration in subsequent cycles than the crystalline oxide. The theoretical discharge capacity of LiV_3O_8 was estimated to be 279 mAh/g, assuming the accommodation of up to three equivalents of Li^+ ions per formula unit, i.e. x = 3.0 in $Li_{1+x}V_3O_8$.

The electrochemical properties of $Li_{1+x}V_3O_8$ compounds strongly depend on its crystallinity. The amorphous $Li_{1+x}V_3O_8$ was inferior to the crystalline samples with respect to the rate capability of the lithium insertion reaction, because the repulsive interaction between pre-existing and inserted Li^+ ions in the amorphous oxide led to slower diffusion of Li^+ ions than in the crystalline one. The amorphous $Li_{1+x}V_3O_8$ exhibits a lower coulombic efficiency during the first discharge and charge cycle [108]. The $Li_{1+x}V_3O_8$, prepared by sol-gel methods resulted in high discharge capacity (372 mAh/g; x = 4.0) and reversible discharge and charge cycles were attained owing to improvement of the insertion and extraction kinetics.

The electrochemical behaviour of LiV_3O_8 can be improved by a ultrasonic treatment. It was found that the ultrasonic treatment of crystalline LiV_3O_8 causes a decrease in crystallinity resulting in a considerable increase in specific surface area and interlayer spacing. The as-treated LiV_3O_8 electrode has the advantages of both higher discharge capacity (62% higher than that of the starting LiV_3O_8) and better cycling performance [109].

2.2.4.2. Lithium Insertion In Vanadium Oxides

Vanadium oxides with octahedral or distorted octahedral coordination are known for all oxidation states between V^{5+} and V^{2+}. The energy differences between these different oxidation states are not very great and numerous examples of mixed valence and

metallic compounds exist. The structure of the vanadium oxides V_2O_5, V_6O_{13} and VO_2 (B) can be viewed as shear structures derived from that of ReO_3 [110].

The capacities of the V_6O_{13} electrode were evaluated in the range of 3.6 – 6 mole Li per formula V_6O_{13}, corresponding to 188 – 314 mAh/g. The voltage range was between 2.0 V - 3.0 V. Electrochemical tests have shown that the VO_2 (B) electrode had lower average voltages, less capacity, and poorer rechargeability than that of the V_6O_{13} electrode [111].

Owens et al.[112] synthesized various vanadium pentooxides such as xerogel (XRG), Aerogel (ARG) and aerogel-like (ARG-like) compounds, which have an amorphous structure. The degree of lithium ion insertion in such porous vanadium oxide solids is much higher than that typically observed in crystalline metal oxide materials. These vanadium oxides exhibited high lithium insertion capacity in the range of 500 – 600 mAh/g. The voltage range (discharge) is generally between 3.5 V – 2.0 V versus lithium. The amorphous vanadium pentoxides could be an attractive cathode candidate for lithium metal polymer batteries.

2.3 Anode Materials for Lithium-ion Batteries

Before the emergence of lithium-ion batteries, lithium metal was used for lithium primary batteries. When lithium is used as anode in secondary lithium batteries, high energy density can be obtained, because pure lithium has the highest specific capacity of the available choices. However, the rechargeable lithium batteries were unsuccessful in early trials. The main reason was the safety problem caused by using a lithium metal anode. During the charge/discharge cycle, lithium is often deposited in a dendritic form. These lithium dendrites are porous and have high surface area, and are very reactive in organic electrolytes. Also, lithium dendrites gradually grow on cycling and penetrate the

separator after a certain number of cycles. The resulting short circuiting could lead to fire or explosion. So, lithium metal anodes were eventually abandoned by the battery manufacturers.

The problems relating to the use of lithium metal anodes can be overcome by using lithium insertion anode materials. The most common materials are lithium-carbon (either graphitized carbon or non-graphitized carbon) and intermetallic lithium alloys. Suitable alloying elements are Sn, Al, Pb, Bi, Sb, and As etc.. Some oxides such as $Li_4Ti_5O_{12}$ and lithium perovskites also can reversibly react with lithium at relatively low potentials (1.0 – 1.5 V versus lithium). These compounds may be used as anode materials in lithium-ion cells but with some sacrifice of the energy density.

There are three basic requirements for anode materials. One is that the potential of lithium insertion and extraction in the anode versus lithium must be as low as possible. Secondly, the amount of lithium which can be accommodated by the anode material should be as high as possible to achieve a high specific capacity. Finally, the anode hosts should endure repeated lithium insertion and extraction without any structural damage to obtain long cycle life. In practice, until now, only carbon materials have met the above strict requirements. Thus, carbon materials are widely used in commercial lithium battery production.

2.3.1 Carbon Materials as Anodes in Lithium-ion Batteries

Carbon has exceptional behavior as the anode materials for lithium-ion cells. In the history of lithium-ion battery development, the successful use of carbon anodes determined the success of commercialization of the lithium-ion battery. The critical property for carbon anodes in organic electrolyte is the formation of a passivation layer on the surface of the lithiated carbon. This passivation layer ensures that the electrode

has sufficient stability and reversibility to ensure a high cycle life of thousands of cycles without irreversible lithium corrosion.

The first attempts to use graphites as the anodic host for lithium ions failed, because of electrode disintegration. The situation changed with the finding that poorly crystalline carbons were less sensitive to that electrolyte decomposition. The feasibility was demonstrated but with modest capacities compared to that expected with graphite [113]. Sony was the first company to produce commercial lithium-ion batteries based on such a non-crystalline carbon anode. After that, crystalline carbon materials then regained interest when LiC_6 stoichiometry was achieved with a careful design of electrolyte composition mainly base on ethylene carbonate (EC) [114].

2.3.1.1 Structure and Texture of Carbon Materials.

There are hundreds of commercially available carbon types, including natural and synthetic graphites, carbon blacks, active carbons, carbon fibres, cokes and various other carbonaceous materials prepared by the pyrolysis of organic precursors in inert gas environment. Therefore, carbon materials have wide ranges of structure, texture and properties. As a consequence of this diversity, carbon materials have many applications.

The pure graphite has a structure shown in Fig. 2-10, which consists of hexagonal net planes of carbon stacked along the c-axis in a staggered array usually denoted as ABAB..., where the lateral shift, on going from layer A to layer B. The space group of graphite is Pb3/mmC, with a=b=2.46 Å and C=6.70 Å. The abnormal graphite stacking, ABCA, ... or ABAC..., etc. are possible sequences and the commonly observed stacking faults in graphite, which are a reflection of these discrete stacking alternatives [115].

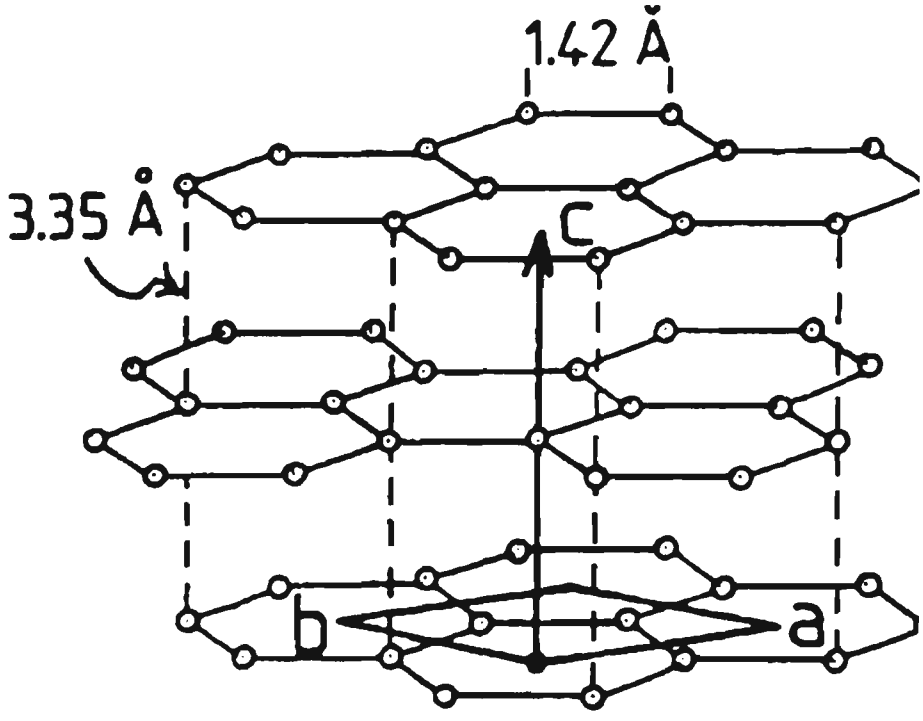

Fig. 2-10 The structure of hexagonal graphite showing the ABAB stacking of honeycomb carbon layers.

Dahn et al. described three classes of lithium-ion battery relevant carbons [116]. One is graphitic carbons, which are normally prepared by heating so-called soft carbon precursors to the temperature above ~ 2400°C, where well graphitized materials result. The second one is hydrogen containing carbons, which are prepared by pyrolyzed organic precursors at temperatures near 700°C. The third class of carbons are hard carbons or non-graphitized carbons. The structure and chemistry of carbons strongly depends on the procedures of heating organic precursors. During the early stages of pyrolysis in inert gas (below 600 °C), organic compounds decompose and emit gases that contain carbon such as CO and CH_4. The remaining C atoms condense into planar aromatic structures (graphene sheet). If the decomposing precursor forms a semifluid state, then these planar sheets can align in a more parallel fashion that leads to easy graphitization when heating to very high temperatures. Such precursors yield "soft" or

graphitizable carbons. However, if the organic precursor is sufficiently cross-linked, then a fluid state is not realized during decomposition and the planar aromatic structure cannot align. These carbon materials are difficult to graphitize at high temperature and thus are called "hard" or nongraphitizable carbons. All carbon materials formed by heating up to about 1300 – 1500 °C (so called soft carbon) have been shown to consist of small domains of graphite-like hexagonal layers of carbon atoms with the diameter of 1-1.5 nm and parallel stacking of two or three layers. These have been called basic structure units (BSUs). Fig. 2-11 shows the nanotextures of BSUs according to the ways of aggregation and degree of preferred orientation [117].

The first scheme is the orientation of the carbon layers along a reference plane. Highly orientated pyrolytic graphite (HOPG) is a typical example of synthetic graphite having a high degree of plane orientation. The second scheme is the axial orientation of layers, which has the cases of coaxial and radial. All of the fibrous carbon materials have this scheme of orientation. The third scheme is the orientation of BSUs around a reference point (point orientation), in which two cases have to be differentiated, radial and concentric. Most of spherical carbon particles have this texture. Fig. 2-12 shows three kinds of arrangements of BSUs in spherical particles. The spherical particles were obtained in pitches, so-called mesophase spheres (or mesocarbon microbeads MCMB), and also by pressure carbonization of a mixture of polyethylene with a small amount of polyvinylchloride called carbon spherules. These particles were found to have a radial arrangement of BSUs.

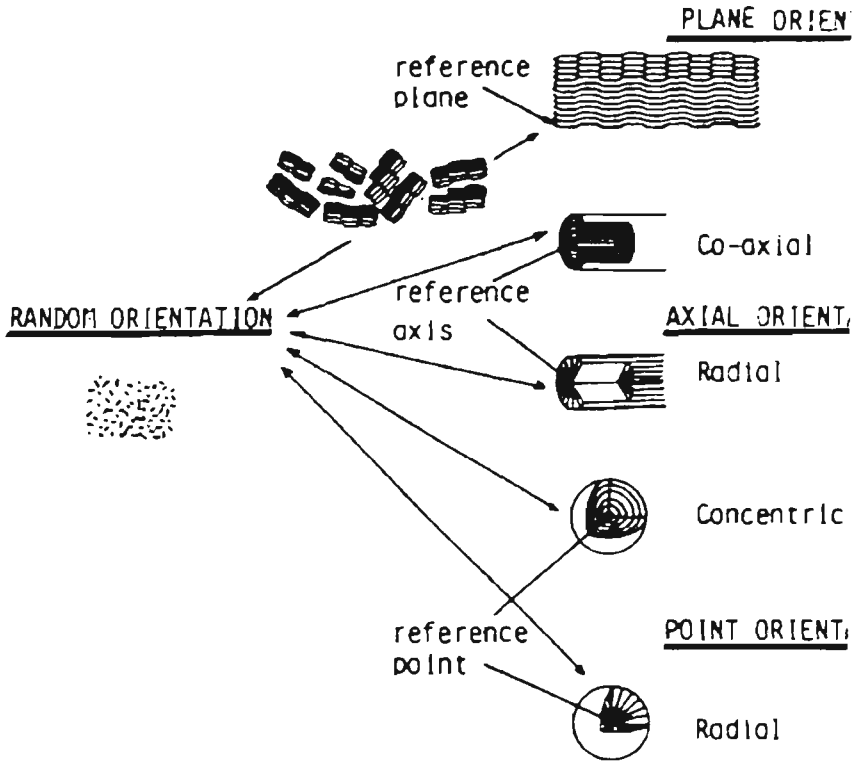

Fig. 2-11 The nano textures in carbon materials.

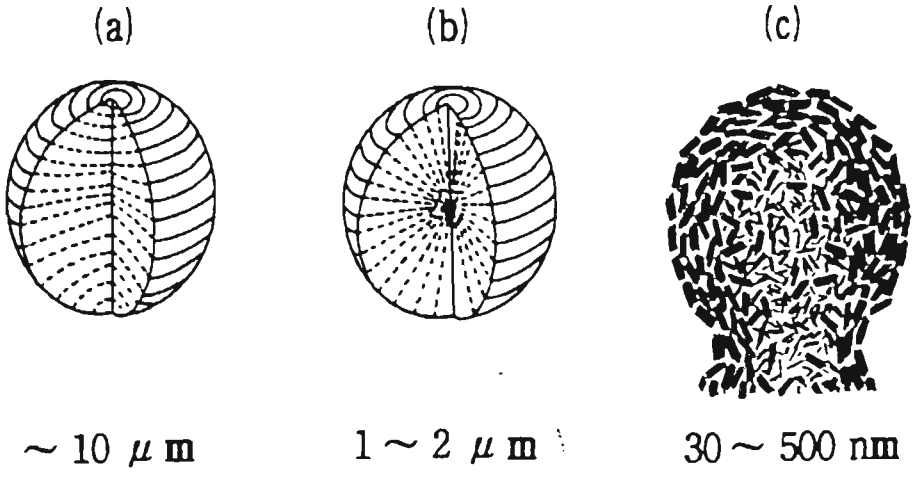

Fig. 2-12 The arrangement of basic structure units in spherical particles.
(a) Mesophase sphere. (b) Carbon spherule.
(c) Carbon black.
A short bar means either hexagonal carbon layer or a stack of layers (BSU).

Another extreme case opposite to perfect orientation is random arrangement of BSUs in carbon materials, for example the glass-like carbons. In the low temperature sugar carbon, BSUs are very small and oriented in random.

The structure of carbon materials strongly depends on precursors and heat treatment conditions (temperature and pressure). The average interlayer spacing between neighbouring hexagonal carbon layers d_{002}, crystallite sizes along c and a axes L_c and L_a, and probability of graphitic AB stacking between adjacent layers P1 are commonly used as fundamental structure parameters. In general, the degree of graphitization P1 and crystallite thickness $L_c(002)$ increase with heat treatment temperature.

2.3.1.2 . Lithium Intercalation Properties of Carbon Materials

The theoretical capacity of graphite is 372 $mAh.g^{-1}$ (850 $mAh.cm^{-3}$) based on the reaction to form the LiC_6 compound.

$$Li^+ + 6C + e^- \longrightarrow LiC_6 \qquad (2.6)$$

The insertion compound LiC_6 has a golden color and belongs to graphite intercalation compounds (GICs) of stage-1, where the stage number corresponds to the number of graphite layers which separate two successive intercalated planes. Fig. 13 illustrates a typical voltage-capacity curve and a derived plot for a graphite electrode, determined by monitoring its voltage versus a lithium counter electrode during the first intercalation-deintercalation cycle [118].

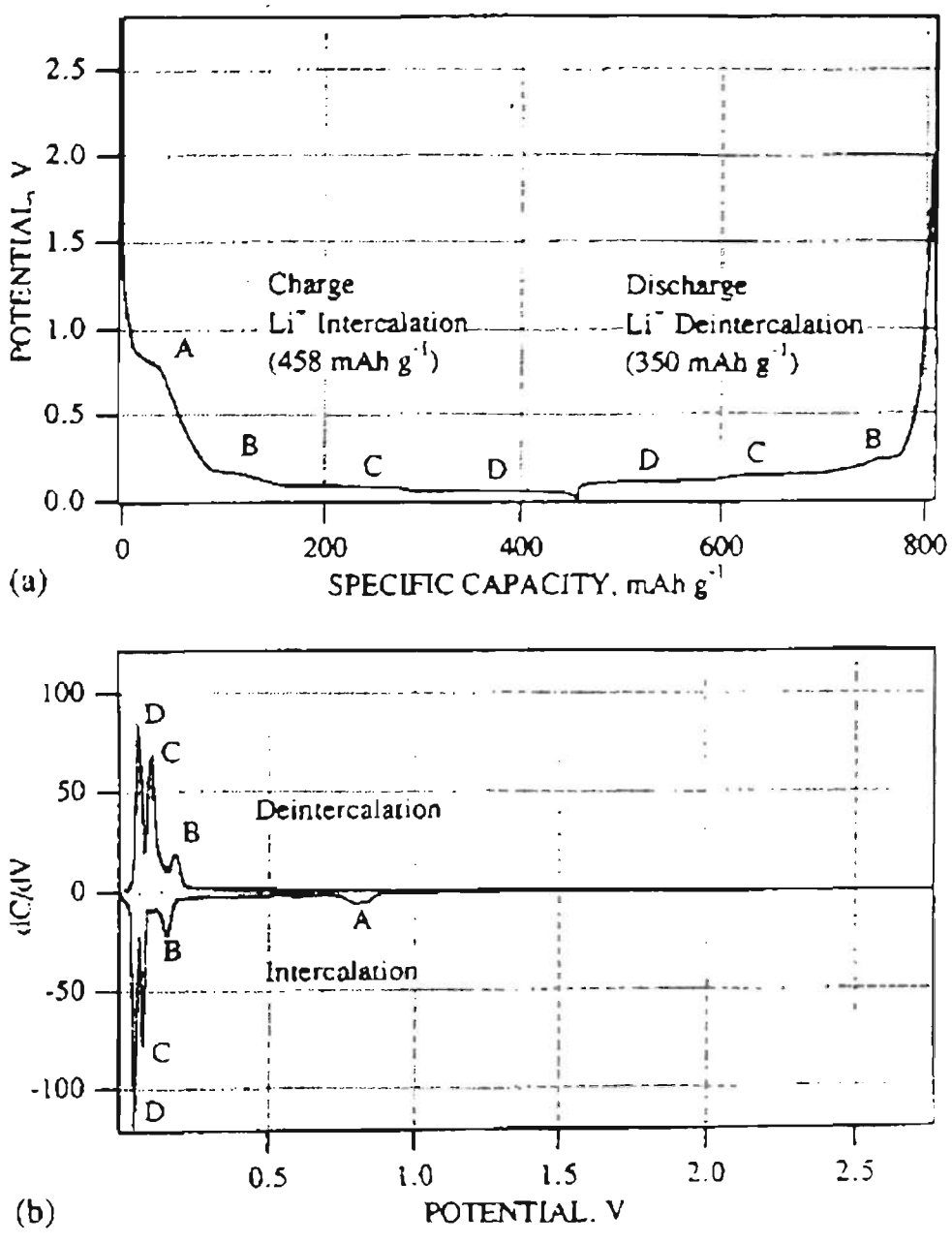

Fig. 13 (a) Voltage-capacity profile (b) derivative plot of of lithium intercalation and de-intercalation in a synthetic graphite electrode [118].

The charge consumed in the first intercalation usually exceeds the theoretical capacity, eg. 372 mAhg-1 for the formation of LiC_6. This is generally regarded as caused by a side reaction involving the decomposition of electrolyte. The decomposition of electrolyte has been attributed to exfoliation of graphite, thus inducing irreversible capacity. Therefore, the electrolyte must be carefully chosen to avoid such catastrophic

effects on the electrode. During the first intercalation, the side process induces the formation of a passivation layer on the electrode surface called the solid electrolyte interface (SEI). This SEI layer is electronically insulating, but ionically conducting, which prevents further electrolyte decomposition while allowing ionic transfer with the solution. The formation of the passivation layer is an essential effect in assuring the stability and cyclability of the carbon electrode, since it provides the conditions for the desired electrochemical reactions even at voltage levels which fall well below the limit of the stability of the most common electrolyte.

The lithium insertion behavior in hard carbon electrodes such as coke is somewhat different from that observed in graphite electrodes. In contrast with graphite, the cycling profile of the hard carbon electrode shows no evidence of staging plateaus but rather continuous charge/discharge curves sloping between 1.2 V and 0.2 V associated with lithium intercalation[119]. It is believed that the insertion of lithium in hard carbon electrodes corresponds to the filling of micro-pores in the carbon by clusters of lithium. This mechanism would be expected to produce weakly bound lithium (relative to that in Li metal) and have a very low plateau consistent with experimental results. Hard carbon materials consisted primarily of small single layers of carbon arranged more or less like a house of cards. Lithium could be absorbed on both surfaces of these single sheets, leading to more lithium per carbon than in intercalated graphite, which would have the theoretical maximum capacity of Li_2C_6 or 740 $mAhg^{-1}$. In the structurally disordered coke electrodes, the intercalation process does not promote formation of the staging phases, and due to its lack of crystallinity, these electrodes are not as sensitive to the nature of the electrolyte as is the case for the graphite electrodes. In fact, coke electrodes are successfully used in commercial lithium-ion batteries, such as Sony Camcorder battery.

Hydrogen-containing carbons can deliver high lithium intercalation capacity up to 800 – 900 $mAhg^{-1}$. The hydrogen could be playing a crucial role in the mechanism of lithium insertion. The reversible capacity increases with the increase of H/C atomic ratio in this material. It was suggested that lithium atoms can bind in the vicinity of H atoms in the hydrogen-containing carbons. The inserted lithium could transfer part of its 2s electrons to a nearby hydrogen, resulting in a corresponding change to the H-C bond, which would cause changes in the relative atomic position of the C and H atoms. The hydrogen-carbon electrodes do not maintain their large capacities for long term cycles [120, 121].

Carbon anode materials are still under intensive investigation to improve their specific capacity and cycle life. Some super carbons prepared by pyrolysizing special precursors have demonstrated a capacity of more than 1000 $mAhg^{-1}$ [122], but with short cycle life. Nano-crystalline carbons prepared via high energy ball-milling had a lithium-insertion capacity of up to 2500 mAh/g in the first charge. Unfortunately, only half of this capacity was reversible during the first discharge. Such large irreversible capacity in the first cycle is unacceptable for any practical application [123, 124]. Nevertheless, it is expected that carbon materials will reach a capacity of 600 – 700 $mAhg^{-1}$ with satisfactory cycle life and reversible capacity.

2.3.2 Tin Oxide and Tin Oxide Composites Anode Materials

The tin-based amorphous composite oxide (TCO) anode materials was first developed by Fujifilm Celltec [125, 126]. The TCO anode yields a specific capacity for reversible lithium adsorption more than 50 percent higher than those of the carbon families. It provides a gravimetric capacity of > 600 $mAhg^{-1}$ for reversible Li adsorption and release, which corresponds in terms of reversible capacity per unit volume to more

than 2200 $mAhcm^{-3}$. The tin-based composite oxide active material has a basic formula represented by SnM_xO_y, where M is a group of glass-forming metallic elements whose total stoichiometric number is equal to or more than that of tin ($x \geq 1$) and is typically comprised of a mixture of B (III), P (V), and Al (III). In the oxide structure, Sn (III) forms the electrochemically active center for Li insertion and potential development, and the other metal group provides an electrochemically inactive network of –(M-O)- bonding that delocalizes the Sn (II) active center. To confer high reversibility in Li storage and release, the Sn-O framework was thus anisotropically expanded by incorporating glass-forming network elements – B, P, and Al in view of the enhancement of Li-ion mobility in the anisotropic glass structure, favorable for ionic diffusion and release. The TCO $SnB_{0.5}P_{0.4}Al_{0.42}O_{3.6}$ was prepared by mixing SnO, B_2O_3, $Sn_2P_2O_7$ and Al_2O_3, sintering at high temperature of 1100 °C for more than 10 hours, and then quenched to room temperature. The TCO anode can be coupled successfully with several cathode materials such as $LiCoO_2$, $LiNiO_2$, $LiMn_2O_4$ and $LiMnO_2$. Such lithium-ion batteries have been tested to have an energy density of more than 420 wh/l, and good cyclability. The major drawback for the TCO anode is the large irreversible capacity in the first cycle (~ 40 percent of the first charge), which requires excess cathode material to compensate.

Various tin oxides have been investigated as anode materials for lithium-ion batteries, including SnO, SnO_2, Li_2SnO_3 and $SnSiO_3$ glass. All of these oxides can react reversibly with lithium with a capacity between 1200 $mAhg^{-1}$ to 1500 $mAhg^{-1}$ in the first charge, but with large irreversible capacity. In situ x-ray diffraction measurement revealed that these tin oxides and tin oxide composites follow a similar mechanism for lithium insertion. When lithium ions are inserted into these oxides, Li_2O and Sn are generated simultaneously. Then the lithium alloys with Sn to form a series of Li_xSn

alloys. The subsequent cycle is a process of alloying/de-alloying of lithium with tin. These process is shown as follows.

$$6.4Li + SnO \longrightarrow Li_2O + Li_{4.4}Sn \rightleftharpoons Li_2O + 4.4Li + Sn \quad (2.7)$$

$$8.4Li + SnO_2 \longrightarrow 2Li_2O + Li_{4.4}Sn \rightleftharpoons 2Li_2O + 4.4Li + Sn \quad (2.8)$$

$$6.4Li + SiSnO_3 \longrightarrow Li_2O + SiO_2 + Li_{4.4}Sn$$

$$\rightleftharpoons Li_2O + SnO_2 + 4.4Li + Sn \quad (2.9)$$

$$8.4Li + Li_2SnO_3 \longrightarrow 3Li_2O + 4.4Li + Sn \quad (2.10)$$

The formation of a Li_2O and SiO_2 matrix may act to retard the aggregation of tin atoms into large coherent regions. When large tin regions form, the large volume differences between coexisting bulk Li-Sn phases may introduce cracking and crumbling of the electrode structure. Therefore, the capacity will lost [127].

The electrochemical performance of the SnO_2 electrode can be improved by Mo doping. It was found that the Mo doping influences the habit growth of the SnO_2 crystallites and facilitates growth along the [hk0] direction. The presence of Mo in the Li-Sn alloy formed may favor Sn atom dispersion, which contributes to the improvement of the reversibility of Li reaction [128].

The reaction mechanism of lithium insertion/extraction in TCO and tin oxide anodes was furtherly studied via x-ray absorption spectroscopy in conjunction with lithium-7 nuclear magnetic resonance, which leads to a more coherent picture of the processes of Li insertion and deinsertion [129]. Lithium insertion into TCO results in the nucleation of Sn nanoparticles within the matrix which retain some oxygen in their immediate coordination environment, accompanied by insertion of Li^+ into the holes vacated by the Sn^{2+}, corresponding to partial reaction with the oxygen-rich region to form Li_2O. Upon further lithium insertion, Li may penetrate into the skin of the Sn particles to form a Li-

Sn nanophase region. The region surrounding this core is a Li-SnO region, which becomes richer in Li-O in the outer regions of the nanocomposites. During lithium extraction, the lithium diffuses out of the nanoparticles, commencing at the outer Li_2O-rich region. This lithium is immediately replaced by progressive diffusion of lithium from the inner Li-Sn-O region, and ultimately in the innermost Li-Sn core, accompanied by oxygen migration into the interior, and regenerating the Sn-O bonds. During deep discharge, the Sn active centers accumulate more Sn cycle by cycle thus leading to the growth of bulk Li-Sn phase. Therefore, in the TCO, participation of the remaining components of the glassy matrix may not only limit the growth of Sn centers, but also act as a reversible reservior for the uptake and release of lithium and oxygen. This can be used to explain why doping SnO_2 with Mo can improve its cyclability.

Much work has been done on TCO and tin oxides. Although TCO glass and some nanocrystalline tin oxides have demonstrated excellent rechargeability, the problem of large irreversible capacity related to oxygen in the first cycle is still not solved, which prevents their commercial application.

2.3.3 Lithium-Alloys and Intermetallic Alloys as Anode Materials for Lithium-ion Batteries

Lithium-alloys and intermetallic alloys as anodes for lithium-ion batteries were thoroughly studied long before carbon materials. There are several advantages for these alloy anode materials over carbon anode materials. Firstly, the lithium insertion in alloy anodes has higher energy density than that of carbon anodes, specially in terms of volumetric capacity, since the alloy density normally is much higher than carbon. Secondly, the operating voltage of alloy anodes is well above the potential of metallic lithium. Thus, the problem of lithium deposition during charging can be minimized,

resulting in improved safety and rapid charging capabilities. Furthermore, alloy anodes seem to have no drawback of solvent co-intercalation, which is a common problem for some carbonaceous materials. However, the theoretical volume changes related with the insertion and extraction of lithium in alloy materials are quite substantial, usually by a factor of two to three. This results in a fast disintegration of the alloy anodes (cracking and crumbling). In contrast, carbon anodes are almost dimensionally stable during lithium intercalation and deintercalation, in which only minor changes of interlayer spacing and stacking order occur. The volume change of alloy anodes has a detrimental effect on the performance of batteries. It usually causes a short cycle life. Fortunately, this disadvantage can be overcome by employing nanocrystalline alloys with properly designed morphology and structure. Such nanomaterials bring hope for alloys used as anodes in the next generation of lithium-ion batteries.

2.3.3.1 Lithium-Alloy Anode Materials

Many metallic elements can alloy with lithium to form Li_xM_y alloys. Fig. 2-14. Compares the gravimetric capacity of some lithium-alloy forming metal elements. Pure lithium has the largest specific capacity of all the metallic elements. Fig. 2-15 gives a comparison of volume change after lithium insertion. It is obvious that there is no volume change for the carbon anode upon lithium intercalation. Almost all other metallic elements have a dramatic volume increase upon lithium insertion.

In order to circumvent the problem of volume change upon lithium insertion, alloy powders with small particle size have been synthesized by chemical reaction method. The powders of Sn, SnSb, and SnAg (typical grain size: 200-400 nm) were prepared.

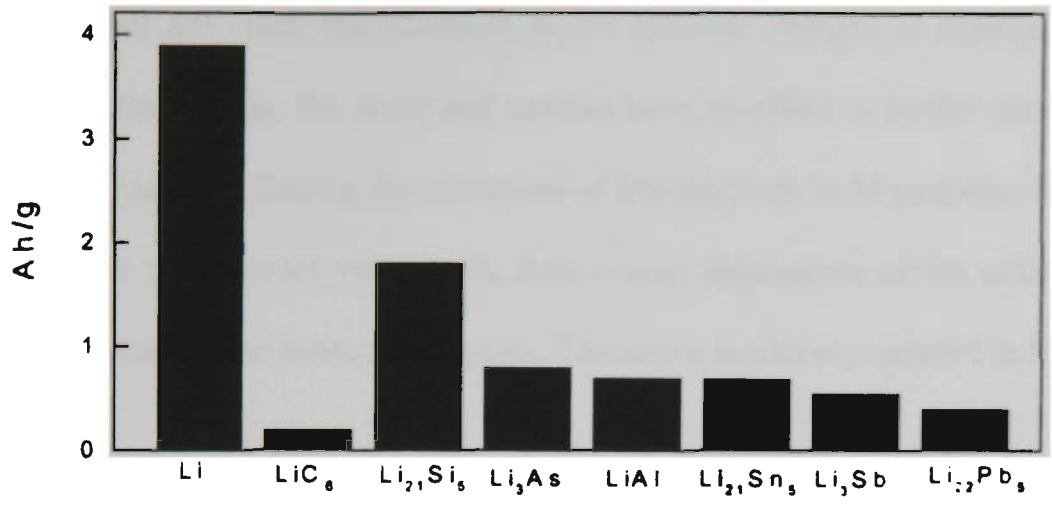

Fig. 2-14. Gravimetric capacity of lithium-alloy forming elements.

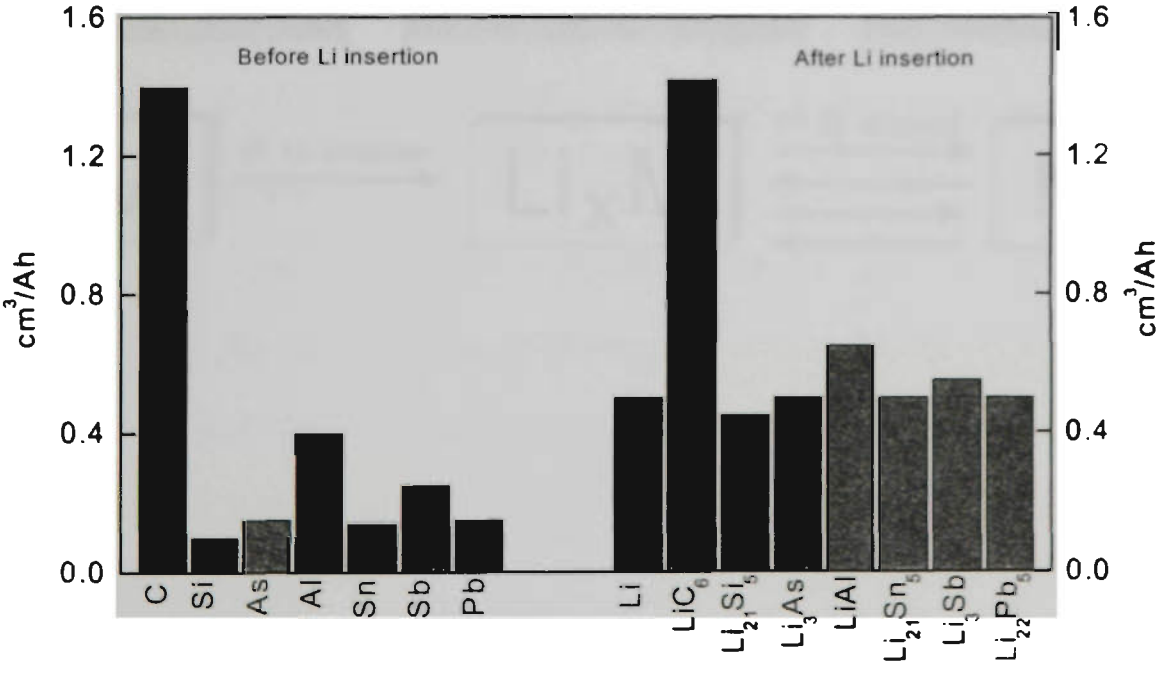

Fig. 2-15 The volume change of lithium-alloy forming element before and after lithium insertion.

These fine grained alloy elements have demonstrated excellent cycling performance[130]. A model for lithium insertion in alloys with small particle size was proposed. There exist many pores and cavities in a loosely packed small particle size

metallic matrix. During lithium insertion, even 100% volume expansion of individual particles will not crack the electrode as the absolute changes in dimensions are still small. In other words, the pores and cavities have an effect to buffer the expansion of individual particles. During the extraction of lithium from Li_xM particles, the expanded particles do not contract very much, thus overall dimensions of the electrode remain almost constant in the subsequent cycles. The above model is presented in Fig. 2-16.

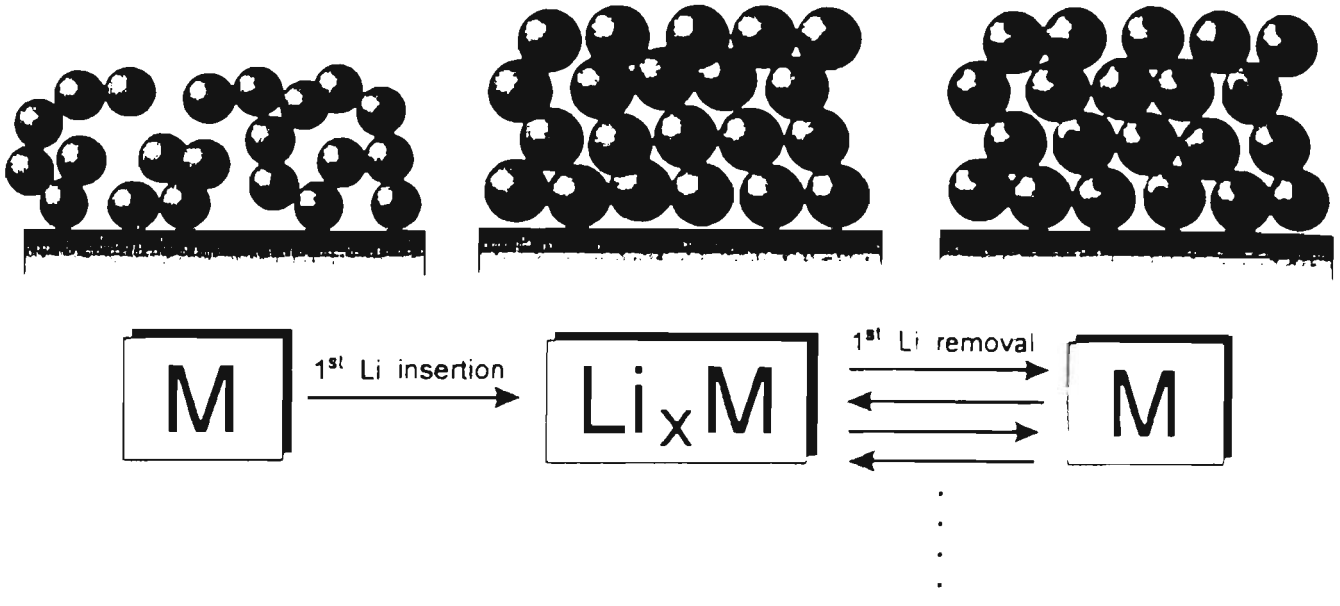

Fig. 2-16 Model of lithium insertion/extraction in lithium-alloys with small particle size.

Whereas, Wolfenstine [131] made a prediction of the critical grain size below which microcracking does not occur based on volume change as a result of Li insertion into brittle Li-alloys. The predicted critical grain size was less than the unit cell size for a single-phase materials, which suggests that decreasing the particle/grain size cannot

fundamentally solve the mechanical instability problem associated with Li-alloys. Some potential solutions to solve the mechanical instability problems were proposed: (i) Incorporating within the Li-alloys a ductile Li-ion conducting metal or polymer matrix. (ii) Surrounding the alloys within a matrix which placed them under a compressive stress [131]. The use of intermetallic alloys is one choice to provide a ductile matrix for lithium alloying.

2.3.3.2 Intermetallic Alloys As Anode Materials for Lithium-ion Batteries

The intermetallic alloys MM' emerged as a new class of anode materials for lithium-ion batteries. The operating voltage of these alloy anode materials is a few hundred millivolts above lithiated graphite, which is generally considered to be safer than carbon anodes. In the intermetallic compound MM', M is an "inactive" element, and M' is an "active" element which can react with lithium to form Li_xM' alloy. The reaction is supposed to proceed as follow:

$$xLi^+ + MM' + e^- \longrightarrow Li_xM' + M \qquad (2.11)$$

At the same time, the inactive M matrix is generated simultaneously. So, the reactions between lithium and MM' intermetallic alloys are generally described as displacement reactions in which domains of lithium alloy Li_xM' are created within the inactive M' matrix.

It is well known that Li_xM' alloy systems undergo several phase change when the active element M' alloys with lithium to form a series of Li_xM' alloys. For example, Sn can alloy with lithium to form variuos Li_xSn alloys: Li_5Sn_2, Li_7Sn_2, $Li_{13}Sn_5$ and eventually, if heavily lithiated, $Li_{22}Sn_5$. The severe volume expansion and contraction is expected during charge/discharge cycle. These dramatic volume changes cause cracking of alloy particles, damage the integrity of the electrode, and limit the cycle life of the

alloy electrode. This problem can be significantly improved by finely dispersing the active lithium-alloying element in an inactive composite matrix. The inactive matrix must be electrochemically conducting and mechanically ductile. It is believed that the inactive matrix provides structural stability to the composite electrode and combats the volume change of the active element. Various intermetallic MM' alloys show improved cycling performance compared to the pure lithium-alloying metal. For example, some intermetallic alloys such as Cu_6Sn_5 [132], $FeSn_2$, FeSn [133] have demonstrated much improved cycling behavior compared to pure Sn. These alloys were prepared by either powder sintering or ball-milling. When lithium ions inserts into these anode materials, the displacement reaction occurs in which the intermetallic structure is broken down to form a series of Li_xSn alloys within the inert Cu or Fe matrix. In situ x-ray diffraction studies combined with Mossbauer spectroscopy have confirmed the formation of metallic Cu and Fe in Cu_6Sn_5 and $FeSn_2$ electrodes after cycling. This displacement reaction is partially reversible. On cycling, the capacity fade has been attributed to the agglomeration of the inactive phase into larger grains.

Nanocrystalline alloys provide an approach to further improve the electrochemical performance of intermetallic MM' alloy anode materials. Since there exist countless pores and cavities within nano-crystalline materials, these cavities provide some free room for the volume expansion of the active element when reacting with lithium to form Li_xM' alloys. The generated inactive matrix is also nanocrystalline in nature, which will be compatible with the original MM' alloys if the starting materials are nanocrystalline.

Theoretically, the intermetallic MM' alloys can be any combination of active element M' and inactive element M depending on their ability to react with lithium to form lithium-alloy. Therefore, there will be many intermetallic alloys which have the potential to be used as anode materials for lithium-ion batteries. Furthermore, the

intermetallic alloys can be ternary, or multi-elements. This means that there can be two, three or more different active elements and vise versa for inactive element. Thus the possibilities for intermetallic alloys are many. It requires intensive research work to explore and classify appropriate intermetallic alloys for lithium-ion batteries.

2.3.4 Other Anode Materials for Lithium-ion Batteries

In addition to carbons, lithium-alloys and intermetallic alloys as anode materials, some metal oxides like WO_2 or Fe_2O_3 [134], and more recently $Li_4Ti_5O_{12}$ were proposed for lithium-ion batteries. In particular, spinel $Li_4Ti_5O_{12}$ which is called zero-strain insertion material, has a very stable structure for lithium insertion/extraction. $Li_4Ti_5O_{12}$ spinel demonstrated excellent cyclability [135]. Some perovskite materials also can accommodate lithium insertion since there exist some ion vacancies in the structure of some defect perovskites. However, all of the above oxide electrode materials exhibit a high average voltage versus metallic lithium for lithium intercalation and de-intercalation. Some of them have limited reversible capacity. This results in low energy density when used as the anode in a complete cell.

Conducting polymers like polyacetylene are stable for lithium insertion at low potential, but their volumetric capacity for lithium insertion is too low for practical application and the cycle life is limited.

Carbonaceous materials are the dominant anode materials, and seem to be well established. After the initial interest in non-crystalline carbons, the general trend is to use crystalline carbons. In this regard, natural or synthetic graphites are preferred. Intermetallic alloys, especially nanocrystalline alloys are emerging as new anode materials for the new generation of lithium-ion batteries with high energy density.

2.4 Electrolyte for Lithium-ion Batteries

The electrolyte is an important aspect of lithium-ion battery technology. The overall electrochemical performance of lithium-ion cells strongly depends on the properties of the electrolyte. Unlike other battery systems, lithium-ion batteries must employ an organic electrolyte system due to the very active nature of lithium. The constitution of the electrolyte is usually dissolved lithium salts of non-coordinating anions into an organic solvent. The water in such an electrolyte must be strictly controlled to less than several ppm. Non-liquid electrolytes are also under development for use in lithium-ion technology. In recent developments, polymer electrolytes, specially gel-type polymer electrolytes have attracted wide attention. Lithium-ion polymer batteries and lithium polymer batteries are already in commercial production. Some lithium-ion conducting glasses or ceramics also have potential to be used as electrolytes to construct all-solid-state lithium-ion batteries. For solid-state lithium-ion batteries employing either polymer electrolyte or Li-ion conducting glass or ceramics, the rate capacity of the cell is usually limited by the lithium ion conductivity of the solid-state electrolyte.

2.4.1 Liquid Electrolyte for Lithium-ion Batteries

The liquid electrolyte system for lithium-ion batteries is very complicated. In the past several decades, numerous electrolyte systems have been developed for the lithium-ion battery. All of these systems are a combination of a lithium salt and organic solvents. The lithium salt must be nontoxic and thermally, chemically, and electrochemically stable. Further requirements for lithium salts are sufficiently high solubility (> 1M) in dipolar aprotic solvents, sufficiently high conductivity of the electrolyte solutions (> 5 mS/cm) and compatibility with all cell materials. The

commonly used lithium salts are $LiClO_4$, $LiAsF_6$, $LiPF_6$, $LiSO_3CF_3$ and $LiN(SO_2CF)_3$ etc.. There are some problems associated with these salts. For example, $LiClO_4$ solutions are thermally unstable and have explosion risks in ethers [136]. $LiPF_6$ itself is thermally unstable in the solid state and decomposes to yield scarcely soluble LiF and Leis acid PF_5 [137]. The search for new lithium salts is continuing.

The solvents used to form electrolytes usually are aprotic organic solvents. In fact, all polar aprotic solvents can form conductive solutions of Li salts. The popularly used solvents include PC (propylene carbonate), DME (1,2-dimethoxyl-ethane), EC (ethylene carbonate), DMC (dimethyle carbonate), DEC (diethyl carbonate), THF (tetrahydrofurane), 2MeTHF (2-methyltetrahydrofuran) etc.. As mentioned before, a passivation film formed on the surface of the carbon anode is critical for successful operation of lithium-ion cells. The solvents relevant to lithium-ion battery systems should undergo thermodynamically favourable reduction to form insoluble, stable lithium salts (organic or inorganic), which will passivate on the surface of the anode [138].

The combinations of different lithium salts and aprotic solvents can be many. To optimize the electrolyte system, the electrolyte has to be incorporated in the lithium cells with certain cathodes and anodes. Only the performance of the cell can tell whether the electrolyte is suitable for use in a particular battery system.

2.4.2 Lithium-ion Conductive Polymer Electrolyte

Many types of conducting polymers have been developed in the past two decades[139-142]. The science of polymer electrolytes is an interdisciplinary field, encompassing the disciplines of electrochemistry, polymer science, organic chemistry and inorganic chemistry. One of the most important applications for polymer

electrolytes is as the solid-state electrolyte in lithium or lithium-ion polymer battery. The Li-ion conducting polymer electrolyte must satisfy certain criteria:

(i) Ionic conductivity. The conductivity of the liquid electrolyte is in the range of 10^{-3}-10^{-2} Scm^{-1}. The polymer electrolyte should have a conductivity of more than 10^{-3} Scm^{-1} at room temperature, in order to ensure that the batteries can be charged and discharged at a current density of several $mAcm^{-2}$.

(ii) Chemical, thermal and electrochemical stability. The polymer electrolytes must be chemically stable in contact with both anode (lithium or carbonaceous materials) and cathode. They should also have an electrochemical stability range of 0-4.5 V vs. Li/Li^+, in which the batteries operate. Furthermore, the polymer electrolyte must have a good thermal stability because batteries sometimes operate at elevated temperature.

(iii) Mechanical strength. The polymer electrolyte must be robust enough to act as a free-standing membrane .

(iv) Transference number. It is desirable that the transference number of Li-ions in polymer electrolyte as high as possible. The conductivity of the electrolyte relies on the movement of ionic charge. Therefore, the transference number for polymer electrolyte should be more than 0.5.

There are two categories of polymer electrolyte systems: pure solid polymer electrolyte (SPE) and gelled polymer electrolyte system. The SPE system usually has poor conductivity but strong mechanical strength. Whereas, the gelled polymer electrolyte system has good conductivity but is not mechanically strong. The polymers like poly(vinylidene fluoride)(PVdF), poly(methyl methacrylate) (PMMA) and poly(acrylonitrile)(PAN) polymers and several different lithium salt LiX (X=PF_6, ClO_4, BF_4, $N(CF_3SO_2)_2$ etc. are usually used to prepare polymer electrolyte. The gel network

can be formed either via chemical cross-linking or physical crossing, through which, the mechanical strength can be improved. The general trend is to use gel-type polymer electrolyte because of its high Li-ion conductivity and good flexibility.

Chapter 3 Experimental

3.1 Materials and Chemicals

The materials and chemicals were supplied by several chemical companies. Most of were from the Aldrich Chemical Company Pty. Limited. The details are given in table 3-1.

Table 3-1 Description of materials and chemicals

Materials or chemicals	Formula	Purity	Supplier
Lithium carbonate	Li_2CO_3	99.99%	Aldrich
Manganese oxide	Mn_2O_3		Aldrich
Lithium hydroxide	$LiOH.H_2O$	99.95%	Aldrich
Nickel nitride	$Ni(NO_3)_2.6H_2O$	Regeant	Aldrich
Ammonium metavanadate	NH_4VO_3	99%	Aldrich
Lanthanam oxide	La_2O_3	99.99%	Aldrich
Manganese carbonate	$MnCO_3$	99%	Aldrich
Lithium nitride	$LiNO_3$	99.98%	Aldrich
Lithium hexafluorphosphate	$LiPF_6$		Aldrich
EC(ethylene carbonate)			Aldrich
DEC (dithyl carbonate)	$(C_2H_5O)_2CO$		Aldrich
Zinc oxide	ZnO	99+%	Aldrich
Manganese oxide	MgO	99+%	Aldrich
Cobalt oxide	Co_2O_3		Aldrich
Nickel oxide	NiO	99.9%	Aldrich
Aluminium powder	Al	99%	Aldrich
Lithium nickel cobalt oxide	$LiNi_{0.8}Co_{0.2}O_2$	99.9%	Merck KaGa, Germany
Lithium cobalt oxide	$LiCoO_2$	99.9%	Union Minera, Belgium
Titanium oxide	TiO2	99.99%	Aldrich
Niobium oxide	Nb_2O_5	99.99%	Aldrich
Strontium oxide	$SrCO_3$	99.9%	Aldrich
Graphite	C	99.99%	Aldrich
Nickel powder (100mesh)	Ni	99.8%	Aldrich
Silicon powder (325 mesh)	Si	99%	Aldrich
Copper powder	Cu	99.5%	Aldrich

Tin powder	Sn	99%	Aldrich
Iron powder	Fe	99.99%	Aldrich
Polyvinylidene fluoride (PVDF)			Aldrich
Dimethyl phalate (DMP)			Aldrich
Carbon black			Cabot Australasia Pty. Ltd.
LP30 electrolyte	EC:DMC 1:1 w/w		Merck
LP 31	EC:DMC 2:1 w/w		Merck
Polypropylene separator			Celgard 2500, Hoechst, USA
Propylene carbonate		99.7%	Aldrich
CR2032 coin cell hardware			Hosen Corp., Japan

3.2 Experimental procedures

Various different cathode materials and anode materials were synthesized and characterized in the present work. The synthesized electrode materials were then used for preparing test electrodes. Teflon test cells or CR2032 coin cells were assembled to examine the electrochemical properties. The overall experimental procedure is schematically illustrated in Fig. 3-1.

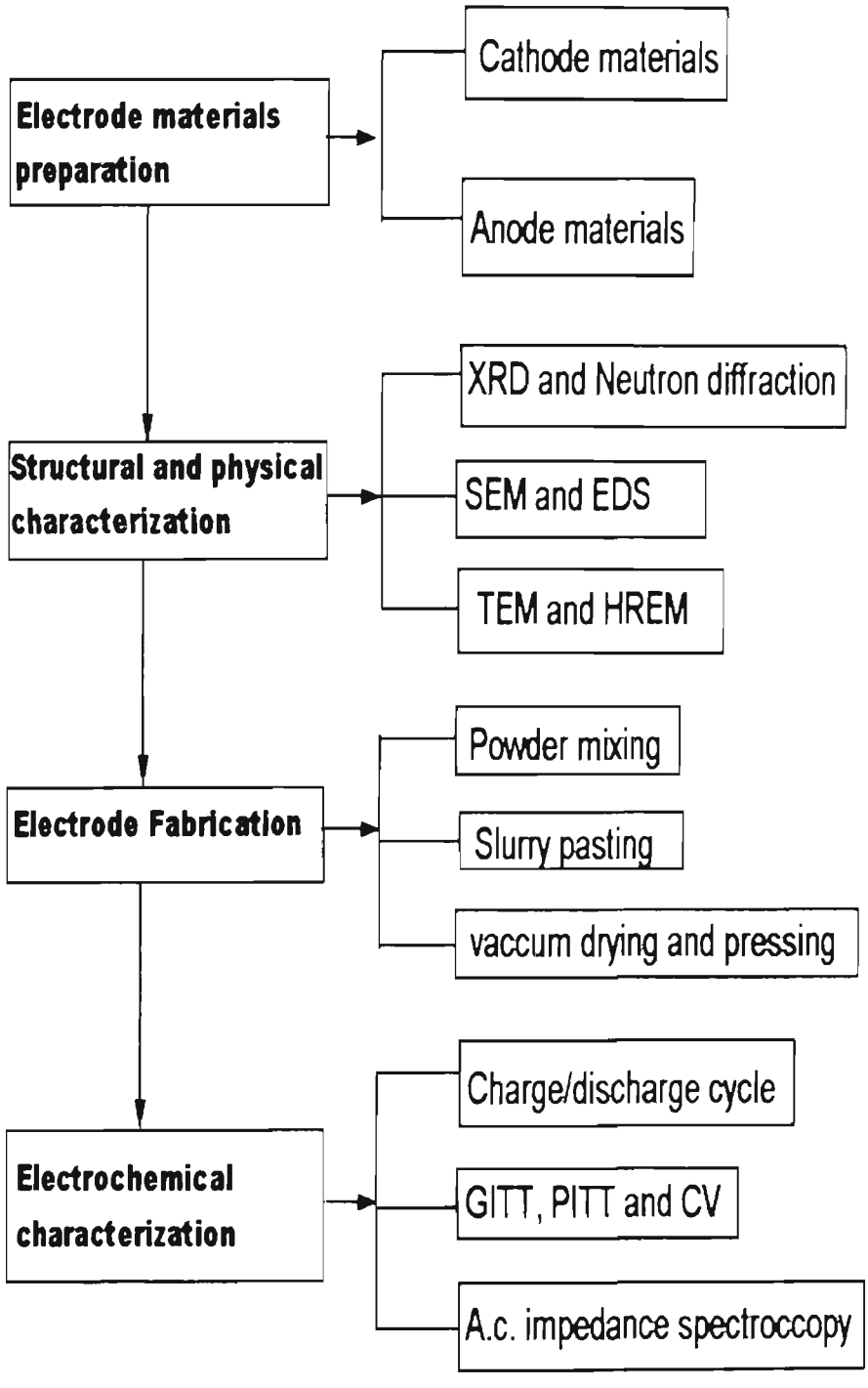

Fig. 3-1 The experimental procedure

3.3 The preparation of electrode materials

3.3.1 Cathode materials

The cathode materials investigated were $LiMn_2O_4$ amd doped $LiM_xMn_{2-x}O_4$ spinels, $LiNiO_2$ and doped $LiM_xNi_{1-x}O_2$, $LiCoO_2$ and $LiNi_xCo_yO_2$ compounds as well as the inverse spinel compound $LiNiVO_4$. Most of these compounds were prepared by solid-state reaction at high temperature. The precursor materials are lithium carbonate or lithium hydroxide and corresponding metal oxide. The precursors were mixed through ball-milling and then heated at high temperature for decomposition. The decomposed mixtures were pressed into pellet form and sintered at high temperature. After that, the pellets were ground to fine powders.

A series of $LiCr_xMn_{2-x}O_4$ spinels were prepared by the solution method - Pechini process [258]. In this case, $LiNO_3$, $Cr(NO_3)_3$ and $Mn(NO_3)_3$ were used as the cationic sources, and citric acid and ethylene glycol as the monomers for forming the polymeric matrix. The metal nitrates of the appropriate composition ratio were dissolved in a mixture of citric acid and ethylene glycol. The resulting solution was then heated at 140 °C to distill out excess ethylene glycol and induce esterification. The viscous solution was then vaccum dried at 180 °C to yield an organic polymer foam. Fine powders can be obtained by calcining their precursors at high temperature.

3.3.2 Anode materials

The anode materials studied in the present investigation include intermetallic alloys, graphite-tin composites, lithium titanium oxide and $La_{0.33}NbO_3$ perovskite. The intermetallic alloys were prepared by sintering and high-energy ball milling. The sintering process involves mixing precursor metal powders, pressing into pellet and then

sintering at high temperature under argon flow. The ball milling was carried out in a Pulverisette-5 ball-milling machine (Labtechnics, Australia) for 80-140 hours.

The lithium titanium oxide and $La_{0.33}NbO_3$ anode materials were synthesized by solid-state reaction.

3.4 Electrode preparation and testing cell construction

3.4.1 Electrode preparation

The electrodes were made by dispersing a mixture of 85 wt % active materials, 10 wt % carbon black and 5 wt % PVDF binder into dimethyl phthalate to obtain a slurry. The slurry was spread on to an aluminum foil (for cathode materials) or a copper foil (for anode materials). The electrodes were then dried and pressed under a pressure of 400 kg/cm^2. The electrodes were then dried in a vacuum furnace for 24 hours and then finally transferred to a Glove-box. The electrode area is approximately 1.2 cm^2 and the typical thickness of the electrode is about 100 μm.

3.4.2 Test cell construction

The test cells were assembled in an argon filled glove-box (Unilab, Mbraun, USA), in which moisture and oxygen were automatically controlled to be less than 5 ppm. In order to examine the electrochemical properties of the prepared electrode materials, lithium metal was used as a standard counter electrode in all test cells. The electrolyte was 1 M $LiPF_6$ in the solution of EC (ethylene carbonate) and DMC (dimethyl carbonate) (1:1 in volume). The separator is celgard 2500 porous plastic film. There were two configurations of test cells, Teflon test cells and standard CR2032 coin cells. The Teflon test cell is shown in Fig. 3-2. A reference electrode can be put in the side of this Teflon test cell to construct three – electrode cell, which were used for CV and a.c. impedance measurements.

Electrodes were initially tested using Teflon test cells. For long term cycle life testing, the CR2032 coin cells were assembled. The CV and a.c. impedance experiments were conducted on Teflon test cells with lithium metal as both counter electrode and reference electrode.

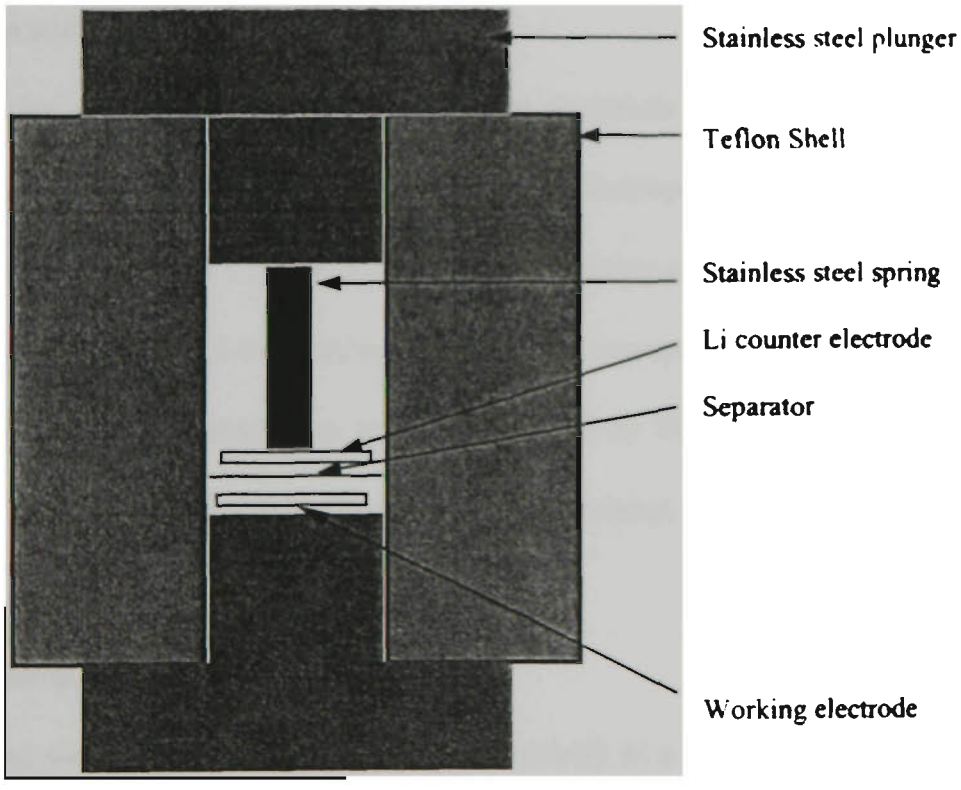

Fig. 3-2 The schematic of the configuration of Teflon test cell

3.5 Structural and physical characterization of electrode materials

The synthesized cathode materials and anode materials were throughly characterized by a variety of approaches. The structural characteristics were determined by x-ray diffraction using a MO3xHF[22] diffractometer (MacScience Co. Ltd, Japan) with a diffracted beam monochromator curved crystal (graphite 002) and Cu-Kα radiation. Some cathode materials have been examined using Neutron diffraction to determine the cation position in the crystal structure. The neutron diffraction was performed on the medium resolution powder diffractometer (MRPD) at the High-Flux Australia Reactor (HIFAR) at Lucas Heights Research Laboratory, Australia Nuclear Science & Technology Organisation (ANSTO).

The morphology and surface images of electrode materials were observed by SEM (Leica/Cambridge Steroscan 440 scanning electron microscope equipped with energy dispersive spectroscope), TEM (JEOL 2000 FX transmission electron microscope) and HREM (EM 2010 JEOL high-resolution electron microscope). The stability of the electrode materials at high temperature was investigated by DTA/TG analysis using a SETARAM (92 model, France) simultaneous DTA-TG thermal analyser.

3.6 Electrochemical testing

The assembled test cells were cycled galvanostatically at a constant current density with a certain cut-off voltage. The cycling tests were performed at different current density for different electrode materials.

The cyclic voltammetry (CV) was performed to determine the characteristics of lithium insertion/extraction reactions for investigated electrodes. The CV measurements were carried out on a potentiostat (M362, EG&G Princeton Applied Research, USA) with a slow scanning rate of 0.1 mV/S. The PITT (Potentiostatic intermittent titration

technique) and GITT (Galvanostatic intermittent titration technique) were used to measure the kinetic parameters of lithium insertion and extraction in the crystal structure of the electrode materials. The a.c. impedance measurements were used to further characterise the kinetic properties of the electrode materials using an EG&G Princeton Applied Electrochemical Impedance Analyser (model 6310). The a.c. amplitude was 5 mV. The frequency range was 100 kHz – 1 mHz.

Chapter 4 Spinel $LiMn_2O_4$ and Its Doped Derivatives As Cathode Materials for Li-ion Batteries

4.1 Introduction

The spinel $LiMn_2O_4$ is the most attractive and promising cathode candidate for 4 V lithium-ion batteries. It is low in cost, easy to prepare, has no toxicity, and is benign to the environment. However, the specific capacity of $LiMn_2O_4$ cathode was found to fade gradually on cycling. Several mechanisms of degradation of the capacity of the $LiMn_2O_4$ spinel cathode on charge/discharge cycling have been proposed as [85]:

(a) structural damage of cubic spinels due to the Jahn-Teller distortion effect at the end of the 4 V discharge plateau.

(b) dissolution of the spinel $LiMn_2O_4$ into the electrolyte.

(c) oxidation of the electrolyte on the surface of the cathode in the highly charged state.

Considerable research work has been done on these aspects in order to combat these effects. One effective approach is to prepare low valence alien ion doped spinels. This is ascribed to an increase in the average manganese valence slightly above 3.5, which dilutes the concentration of Jahn-Teller Mn^{3+} ions. The initial capacity of the doped spinel electrodes decreases with the dopant effect. This is because the lithium insertion and extraction in doped $LiM_xMn_{2-x}O_4$ proceeds as follows:

$$LiM_xMn_{2-x}O_4 \rightleftharpoons (1-x)Li^+ + Li_xM_xMn_{2-x}O_2 + e^- \qquad (4.1)$$

The lithium insertion/extraction in $LiM_xMn_{2-x}O_4$ spinel relies on the reduction/oxidation of Mn ions. The dopant M ions are supposed to have no valence change during lithium insertion and extraction. Therefore, the capacity of the doped $LiM_xMn_{2-x}O_4$ spinel is determined by the amount of Mn in the spinel structure.

A series of doped $LiM_xMn_{2-x}O_4$ spinels (M = Li, Mg, Zn, Al, Cr, and Co) with different dopant level have been synthesized either by conventional solid-state reaction or chemical methods. Their electrochemical performances in lithium cells were investigated by assembling lithium test cells. The kinetic parameters of these spinel electrodes were determined by a.c. impedance spectroscopy combined with other electrochemical techniques such GITT and PITT etc..

The oxygen stoichiometry in $LiMn_2O_4$, which is influenced by the synthesis condition and heat treatment also plays a critical role in the electrochemical properties of the spinel electrode. Yamada et al. [143] have systematically studied the structural aspects of $LiMn_2O_{4-\delta}$ compounds that were prepared by different procedures. However, less attention was paid to the electrochemical properties of this class of compounds. The influence of oxygen stoichiometry on the electrochemical performance of the $LiMn_2O_{4-\delta}$ electrode was also investigated.

4.2 Structural and Electrochemical Characterics of $Li_{1+x}Mn_{2-x}O_4$ and $LiMn_2O_{4-\delta}$ compounds

$Li_{1+x}Mn_{2-x}O_4$ spinel samples (x=0, 0.04, 0.08, 0.12, 0.14, 0.18) were synthesised by reacting stoichiometric amounts of Li_2CO_3 and Mn_2O_3. The starting powders were ball milled in ethanol for 12 h. The ethanol was evaporated and the samples were ground and

prefired at 450°C for 48 h. The precursor was then reground , fired at 750 °in air for 24 h and cooled to room temperature at a rate of 2 °C/min. For $LiMn_2O_{4-\delta}$, the $LiMn_2O_4$ powders were pressed into pellets and then fired at various temperature in the range of 820°C~1100°C for 20 h. After firing, the samples were quickly taken out of the furnace and quenched into liquid nitrogen.

X-ray diffraction was performed on the synthesized spinels. The lattice constants were refined against an internal silicon standard. Thermal analysis was carried out to investigate phase changes and oxygen extraction from $LiMn_2O_4$ at high temperature .

The electrochemical performance of $Li_{1+x}Mn_{2-x}O_4$ and $LiMnO_{4-\delta}$ compounds as cathodes was measured using a Teflon test cell containing a lithium foil anode. The testing cells were cycled galvanostatically at a constant current of $0.4mA/cm^2$ between 3.5V~4.5V.

Spinel $LiMn_2O_4$ belongs to the cubic system $Fd\bar{3}m$, in which Li^+, Mn^{n+}, and O^{2-} occupy tetragonal 8a, octahedral 16d and 32e positions respectively. This structure with a cubic-closed-packed (ccp) oxygen array provides a 3 dimensional tunnel for lithium intercalation and deintercalation, during which the unit cell expands and contracts isotropically. Fig.4-1 shows the powder X-ray diffraction patterns of the $Li_{1+x}Mn_{2-x}O_4$ compounds. All diffraction peaks were indexed to the cubic system. No impurity phases were detected by X-ray analysis. A single cubic phase was found to exist in the range of $0<x<0.18$, which is consistent with the study by Gummow et al. [85]. It was reported that new phases Mn_2O_3 and Li_2MnO_3 will appear for $Li_{1+x}Mn_2O_4$ when $x>1.15$ [144, 145]. It is reasonable that $Li_{1+x}Mn_2O_4$ represents nonstoichiometric compounds in which the excess lithium will occupy 16c sites and form the rock salt structure Li_2MnO_3 outside a certain range. However, the $Li_{1+x}Mn_{2-x}O_4$ compounds prepared in this investigation are stoichiometric.

excess lithium ions replace manganese ions in 16d sites. This results in that the lattice constant and unit cell volume of lithium doped spinel phase decrease with the increase of x. The calculated lattice constant a_o versus composition x is shown in Fig. 4-2.

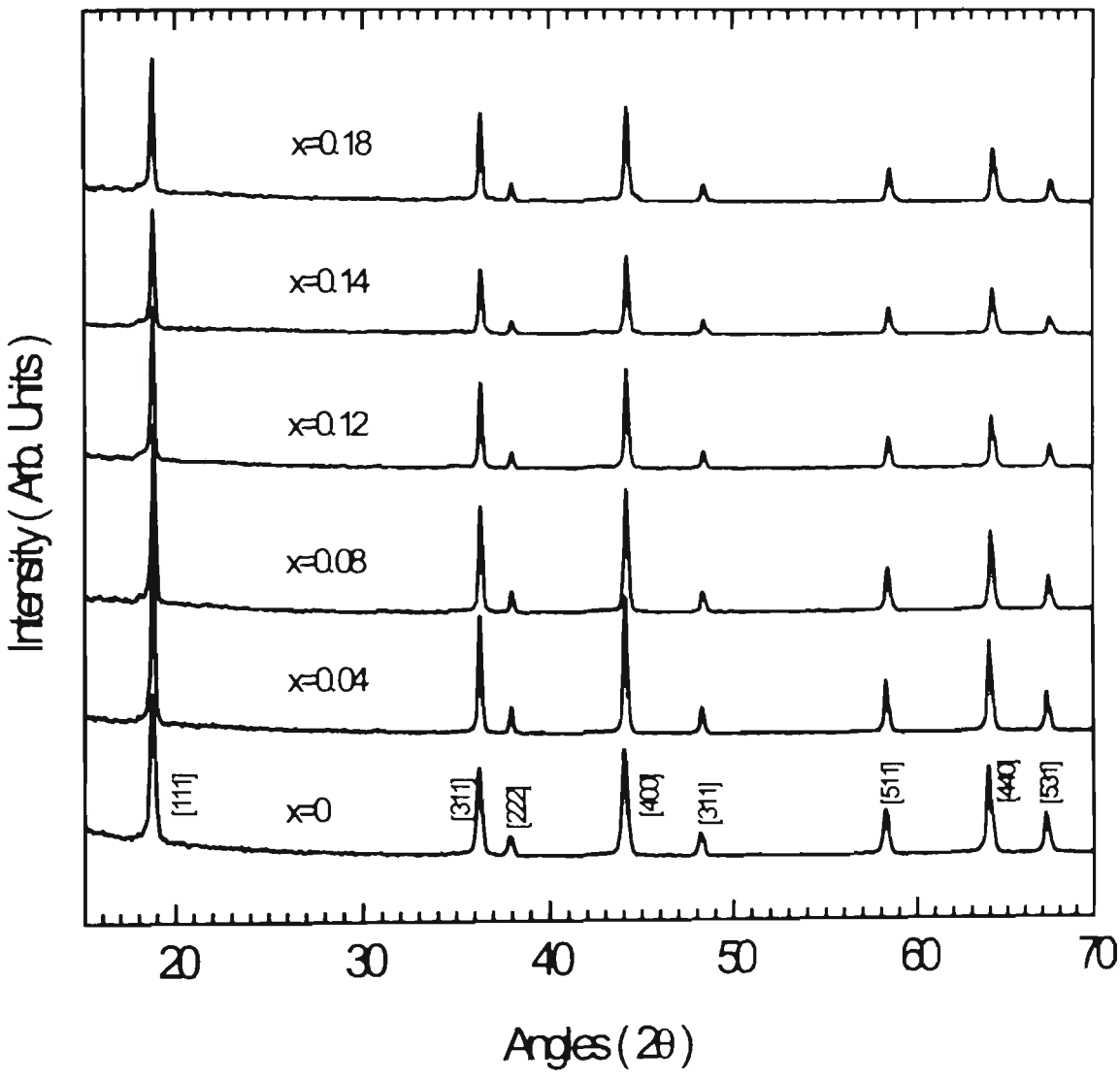

Fig. 4-1 Powder x-ray diffraction patterns of $Li_{1+x}Mn_{2-x}O_4$ compounds.

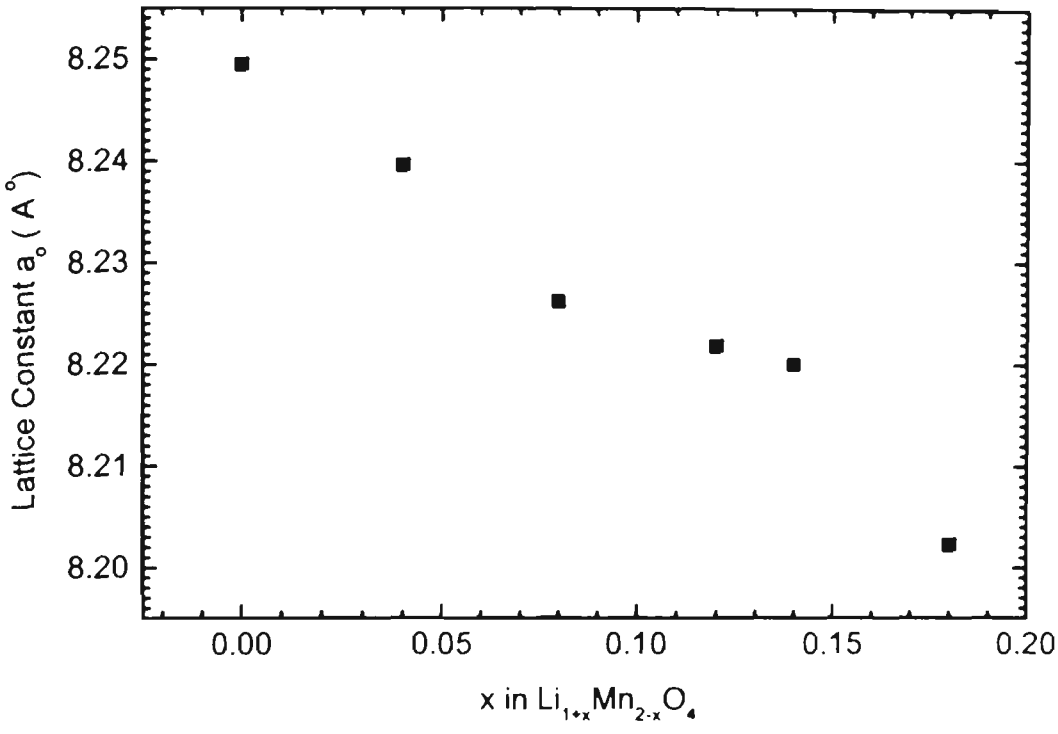

Fig. 4-2 The lattice constant a_o versus x in $Li_{1+x}Mn_{2-x}O_4$ compounds.

It is considered that structural damage of the spinel $LiMn_2O_4$ electrode possibly is the main reason which contributes to the gradual capacity loss of the $Li/LiMn_2O_4$ cell on cycling [72] . So, it is important to maintain the structural integrity of the $LiMn_2O_4$ electrode during each charge/discharge cycle in order to improve capacity retention of the cell. In the spinel $LiMn_2O_4$ system, Jahn-Teller distortion starts at $Mn^{n+}=3.5$(c/a=1) and reaches a maximum at the valence of $Mn^{n+}=3$ (c/a=1.16). For the $LiMn_2O_4$ cathode, the Mn oxidation state reaches 3.5 at the end of the 4v discharge plateau. Jahn-Teller distortion begins, which reduces the symmetry of the cubic spinel phase to the tetragonal phase($Li_2Mn_2O_4$) and increases c/a to 1.16 concomitantly. Such distortion accompanying the

volume change of the unit cell would cause the crystal structure of the electrode to degrade and the electrochemical properties thus to deteriorate. Since Mn^{3+} is stabilised by the Jahn-Teller effect, when Li ions intercalate into $LiMn_2O_4$ structure, Mn^{3+} ions form immediately and induce the tetragonal $Li_2Mn_2O_4$ phase to separate from cubic $LiMn_2O_4$. Therefore, the phase transformation from cubic to tetragonal is discontinuous. Theoretically, if we strictly control the charge/discharge voltage, the cubic spinel $LiMn_2O_4$ phase could be retained. But, actual, battery systems are operated under nonequilibrium conditions. Therefore, there should be some spinel particles which are more lithiated than others, such as particles on the surface of the cathode in contact with the electrolyte. So, the Jahn-Teller distortion starts to occur on these particles while most particles are still of the composition $Li_{1-x}Mn_2O_4$. Due to the discontinuous nature of this phase transformation, the integrity of the electrode is degraded .

Table 4-1 The Structural and Electrochemical Parameters of $Li_{1+x}Mn_{2-x}O_4$

Stoichiometry of $Li_{1+x}Mn_{2-x}O_4$	x	Lattice constant (A)	Volume of unit cell (A^3)	Theoretical Mn oxidation state	Fully oxidised composition ($n^*_{Mn}=4$)	Theoretical(1) capacity (mAh/g)	n_{Li} (2)
$LiMnO_4$	0	8.2495	561.4085	3.50	Mn_2O_4	148	0
$Li_{1.04}Mn_{1.96}O_4$	0.04	8.2396	559.3983	3.55	$Li_{0.16}Mn_{1.84}O_4$	132	0.10
$Li_{1.08}Mn_{1.92}O_4$	0.08	8.2262	556.6609	3.60	$Li_{0.32}Mn_{1.68}O_4$	115	0.20
$Li_{1.12}Mn_{1.88}O_4$	0.12	8.2218	555.7708	3.66	$Li_{0.48}Mn_{1.52}O_4$	98	0.30
$Li_{1.14}Mn_{1.86}O_4$	0.14	8.2200	555.4080	3.69	$Li_{0.56}Mn_{1.44}O_4$	89	0.35
$Li_{1.18}Mn_{1.82}O_4$	0.18	8.2023	551.8396	3.75	$Li_{0.72}Mn_{1.28}O_4$	72	0.45

(1) Theoretical capacity: Based on the mass of $Li_{1+x}Mn_{2-x}O_4$, in which fully charged compounds were discharged to stoichiometric $Li_{1+x}Mn_{2-x}O_4$.

(2) n_{Li}: the number of lithium ions per formula $Li_{1+x}Mn_{2-x}O_4$ that can be inserted into the cathode before the onset of the Jahn-Teller effect at $n^*_{Mn}=3.5$.

The cycle life is the most important property for rechargeable batteries. To improve the capacity retention of the spinel $LiMn_2O_4$ electrode, excess lithium doped $Li_{1-x}Mn_{2-x}O_4$ compounds were synthesised. Table 4-1 shows the structural and electrochemical parameters of the $Li_{1+x}Mn_{2-x}O_4$ compounds. The average Mn oxidation state in lithium doped $Li_{1+x}Mn_{2-x}O_4$ kept marginally above 3.5 at the end of 4v discharge plateau. This effect may be expected to possibly suppress the onset of the Jahn-Teller distortion, thus reducing structural damage of the electrode to improve the cycle life of the cell.

Fig. 4-3 shows the galvanostatic cycling data for the first, fifth, tenth, and twentieth discharge cycles of Li/ $Li_{1+x}Mn_{2-x}O_4$ cells between 3.5 V–4.5 V. As expected from the theoretical analysis, the standard $LiMn_2O_4$ electrode delivered the highest initial discharge capacity of 114 mAh/g, but the capacity faded slowly on cycling. On the other hand, lithium doped $Li_{1+x}Mn_{2-x}O_4$ electrodes demonstrated superior capacity retention on cycling over the standard $LiMn_2O_4$ electrode. This may be seen from the data of Fig. 4-4 which further compares the data of discharge capacity of $Li_{1+x}Mn_{2-x}O_4$ electrodes versus cycle number. The discharge capacity of $Li_{1.08}Mn_{1.92}O_4$ and $Li_{1.12}Mn_{1.88}O_4$ electrodes actually increased a little on cycling. After twenty cycles, the discharge capacity of the $Li_{1.04}Mn_{1.96}O_4$ electrode is almost the same as the $LiMn_2O_4$ electrode. Fig. 4-5 shows the discharge profile of the standard $LiMn_2O_4$ electrode between 2 V–3.5 V. The capacity is lost at a higher rate at 3 V than 4 V . This demonstrated that the cubic phase is more forgiving than the tetragonal phase on cycling and also that structural damage of the $LiMn_2O_4$ electrode is responsible for capacity fade. The initial discharge capacity delivered by doped $Li_{1+x}Mn_{2-x}O_4$ electrodes was less than the undoped one.

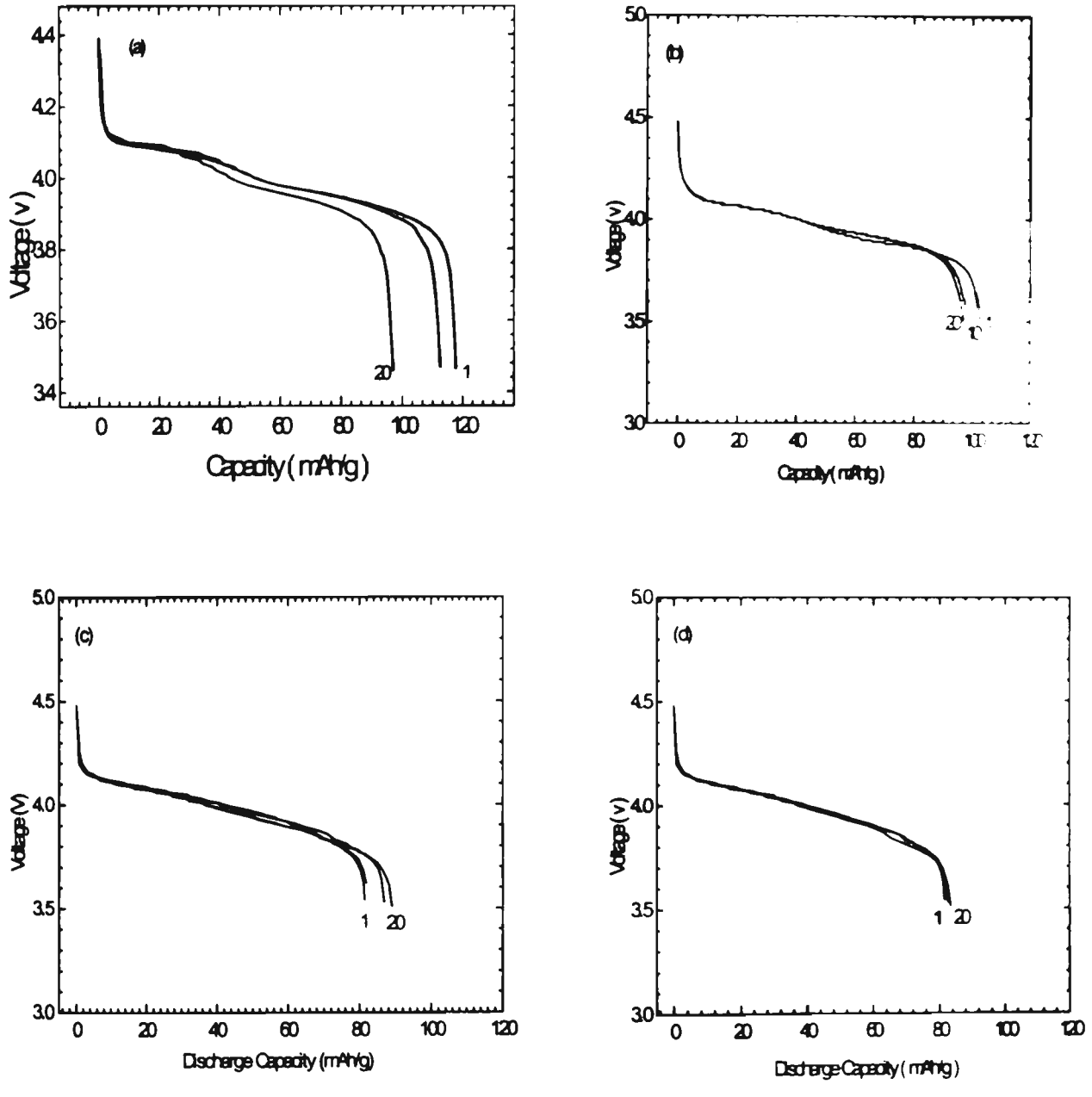

Fig. 4-3 Discharge profiles of $Li/Li_{1+x}Mn_{2-x}O_4$ cells under a current density of 0.4 mA/cm^2. (a) x=0 (b) x=0.04 (c) x=0.08 (d) x=0.12

From table 4-1, we noted that not all of the lithium can be electrochemically removed from the $Li_{1+x}Mn_{2-x}O_4$ spinel structure, because that would induce an average oxidation

state of $Mn^{n+}>4$. Thereofore, the residual lithium in the compound will help to restrict the lattice contraction at the end of the 4 V discharge. The changes in the volume of the unit cell of $Li_{1+x}Mn_{2-x}O_4$ during lithium insertion/extraction should be less than undoped $LiMn_2O_4$. This mechanism should also contribute to improve the cycle stability of Li / $Li_{1+x}Mn_{2-x}O_4$ cells.

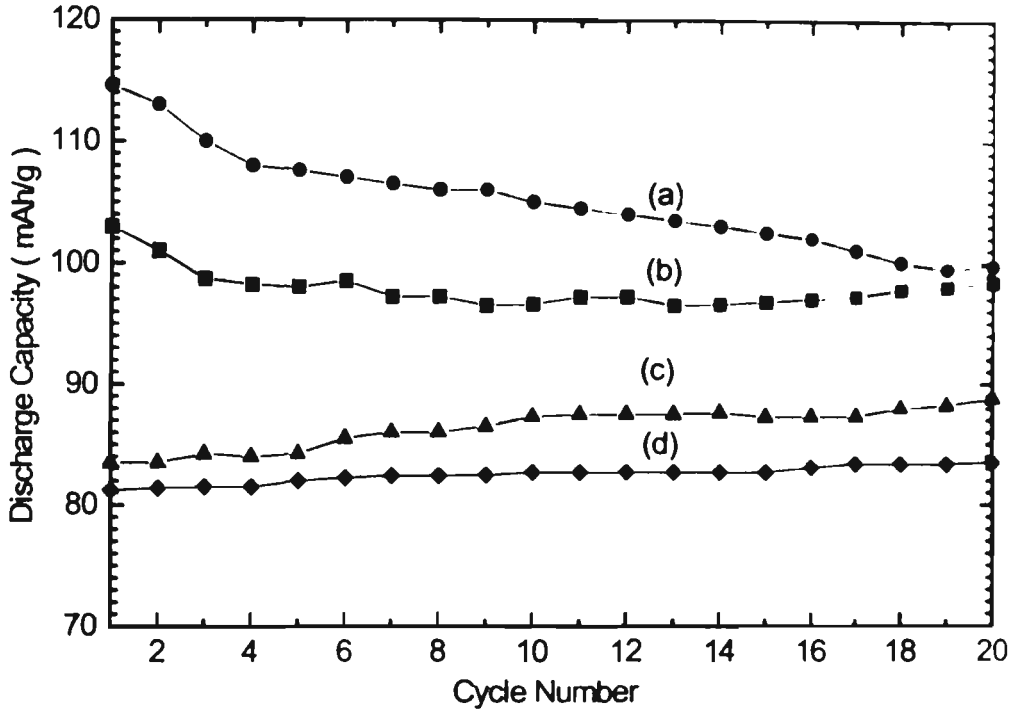

Fig. 4-4 Discharge capacity of Li / $Li_{1+x}Mn_{2-x}O_4$ cells versus cycle number.
(a) x=0 (b) x=0.04 (c) x=0.08 (d) x=0.12

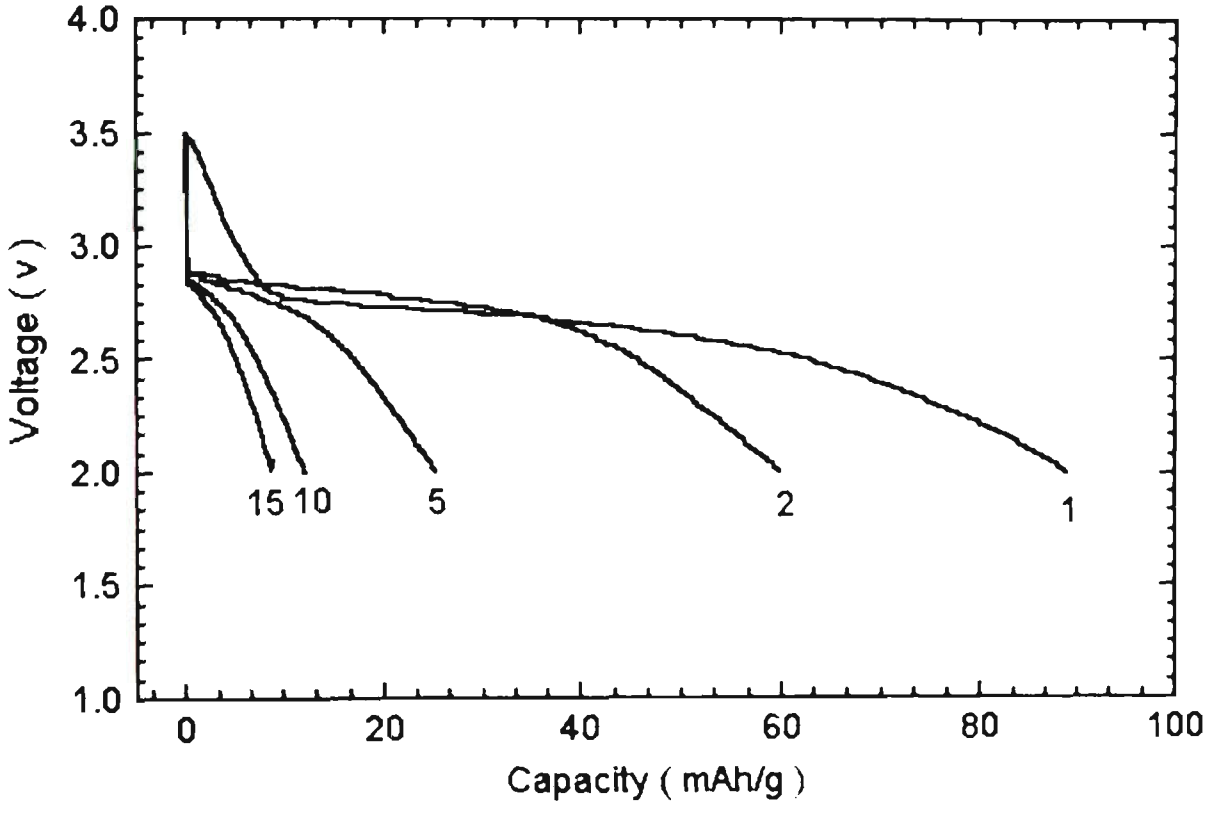

Fig. 4-5 The discharge voltage profile of Li / $LiMn_2O_4$ cell between 2.0 V – 3.5 V. Current density: 0.4 mA/cm^2.

Thermo gravimetric and differential thermal analysis were performed on $LiMn_2O_4$ in dry air. The sample was heated at 5°C/min up to 1200°C and cooled also at 5°C/min. Fig. 4-6 shows the DTA and TG curves. Oxygen extraction occurs above 820°C. The extent of oxygen deficiency could be calculated from the TG data. Generally, the DTA curve demonstrates the feature of an endothermic peak. Yamada et al. have calculated that the heat of oxygen extraction for $LiMnO_4$ is about 63.8 kcal/mol [143] . The following reaction corresponds to the oxygen extraction:

$$LiMnO_4 \text{ (cubic)} \leftrightarrow LiMnO_{4-\delta} \text{(tetragonal)} \quad (4.2)$$

$$LiMnO_{4-\delta} \text{(tetragonal)} \leftrightarrow LiMnO_2 \text{ (orthorhombic)} \quad (4.3)$$

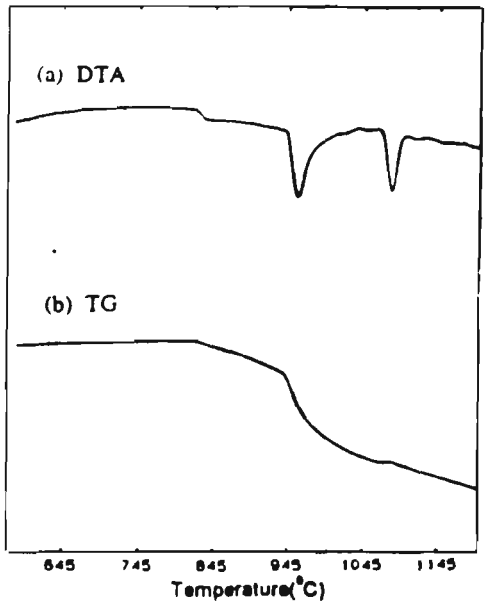

Fig. 4-6 (a) Differential thermal analysis for $LiMn_2O_4$.
(b) Thermo gravimetric curve for $LiMn_2O_4$.

Powder X-ray diffraction patterns of $LiMnO_{4-\delta}$ obtained by quenching samples from high temperature directly into liquid nitrogen are shown in Fig. 4-7. The sample quenched from 820°C is single cubic phase. Above 820°C, the tetragonal phase starts to form and corresponds to a two phase region. As the firing temperature increased, the cubic [hkl] peaks split into two continuously, which could be explained in terms of the phase transformation from cubic $LiMn_2O_4$ to tetragonal $LiMn_2O_{4-\delta}$ being a kind of continuous change.

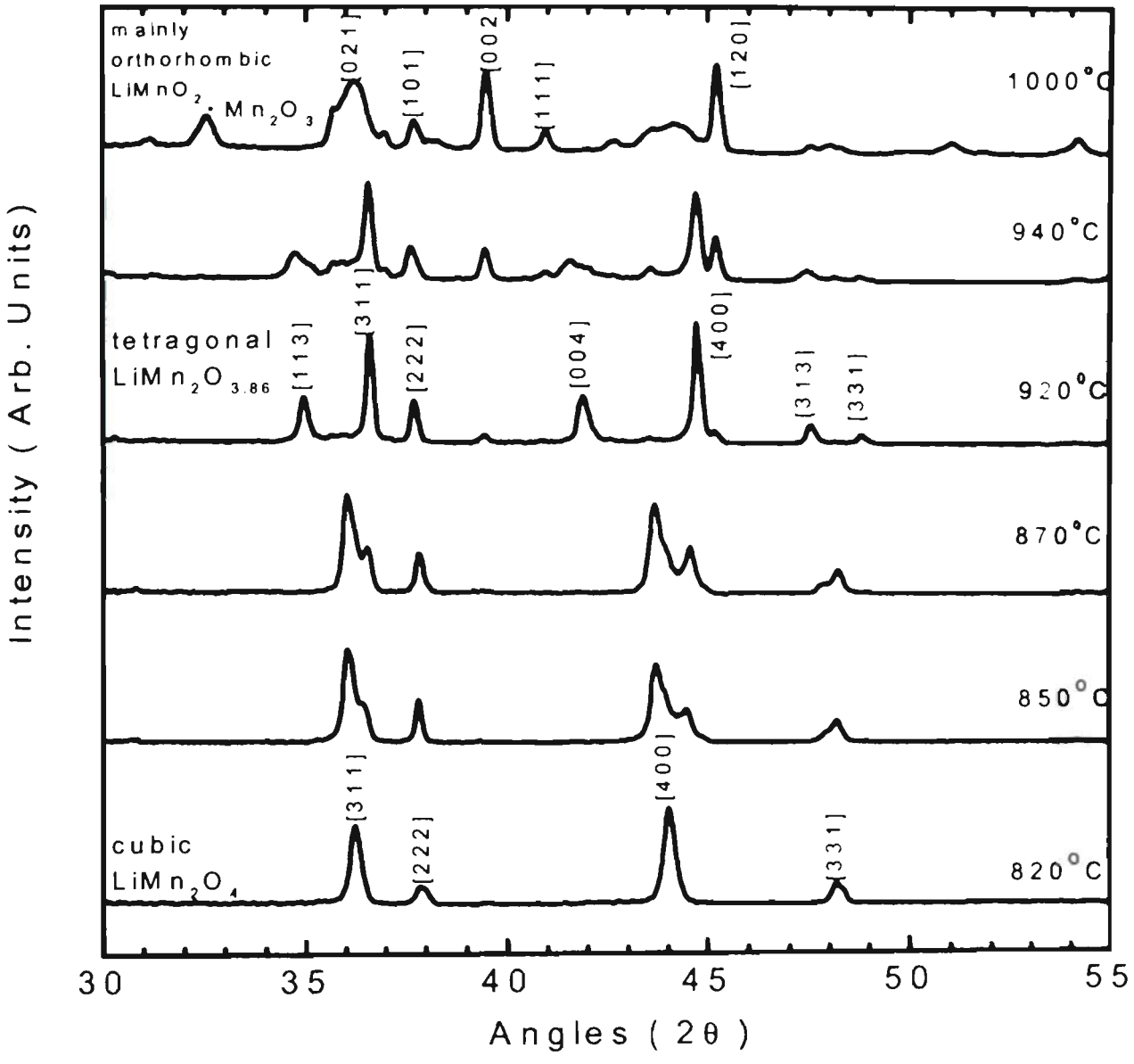

Fig. 4-7 X-ray diffraction patterns for samples quenched from various high temperatures.

Fig. 4-8 shows the X-ray pattern of tetragonal $LiMn_2O_{3.86}$ (quenched from 920°C). Using Rietveld refinement program, the peaks of tetragonal phase were indexed and lattice constants were calculated as: a = 8.1061 Å, c=8.6244 Å, v=566.6942 Å, c/a=1.064. The oxygen extraction from $LiMn_2O_4$ induces increased Mn^{3+} concentration according to the principle of electric neutrality. So, a cooperative Jahn-Teller distortion of Mn^{3+} ions in octahedral sites was incurred, which reduced cubic symmetry to tetragonal phases.

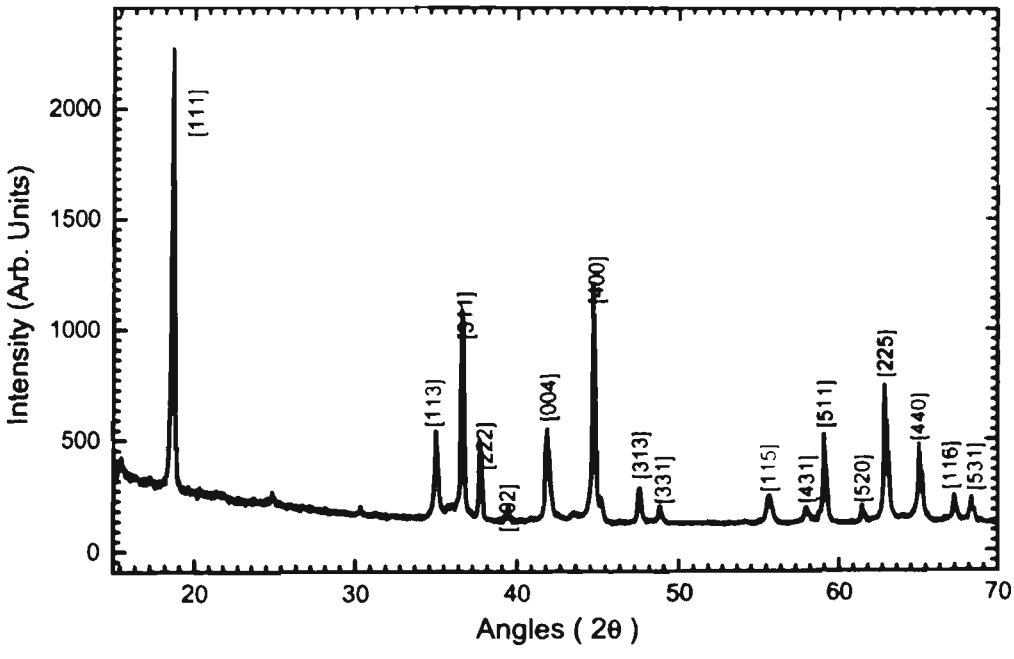

Fig. 4-8 Powder x-ray diffraction pattern of tetragonal $LiMn_2O_{3.86}$.

The capacity of the tetragonal $LiMn_2O_{3.86}$ electrode faded more quickly and also deliver less initial capacity than the $LiMn_2O_4$ electrode (Fig. 4-9). During charge and discharge, there are two phases (cubic and tetragonal) in the $LiMn_2O_{3.86}$ electrode, which are not compatible in structure. So, the structure integrity is damaged gradually with cycling and the capacity fades.

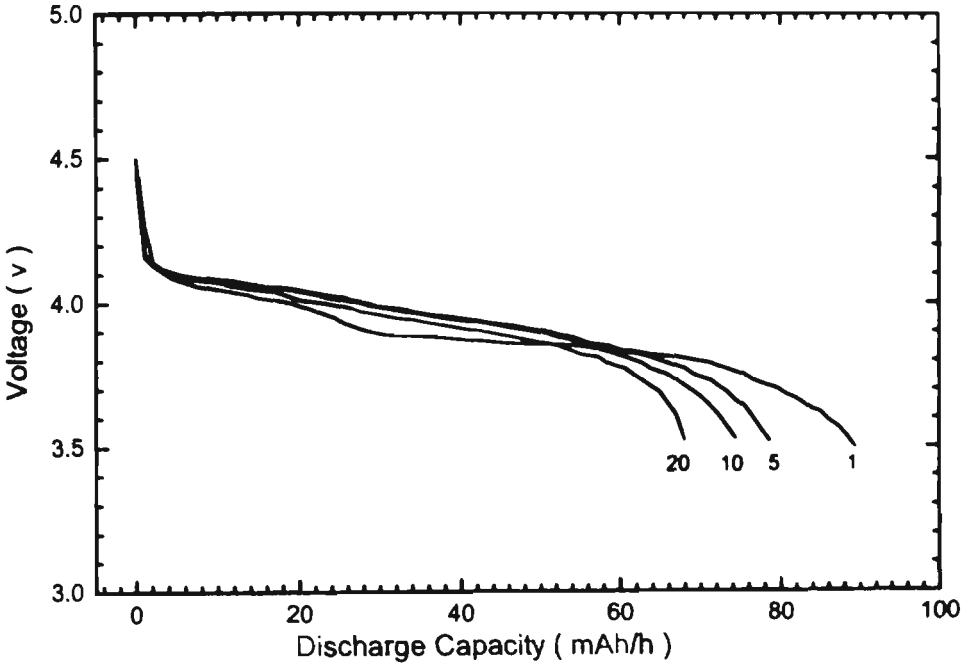

Fig. 4-9 Discharge profile of Li / $LiMn_2O_{3.86}$ cell, current density: 0.4 mA/cm^2.

Excess lithium doped spinel $Li_{1+x}Mn_{2-x}O_4$ electrodes demonstrated improved capacity retention but delivered low discharge capacity compared to the undoped $LiMn_2O_4$ electrode. The damage to the structural integrity of the electrode resulting from Jahn-Teller distortion appears to be responsible for capacity fade on cycling. The oxygen can be extracted from

$LiMn_2O_4$ compound at high temperature. Oxygen deficient tetragonal $LiMn_2O_{3.86}$ electrode delivered low capacity and lost capacity at a higher rate on cycling than $LiMn_2O_4$ electrode. Thus, oxygen extraction must be strictly prevented in the synthesis of the $LiMn_2O_4$ compound. It is expected that adjusting the composition of spinel $LiMn_2O_4$ could optimise its electrochemical performance to satisfy the commercial applications.

4.3 Improvement of electrochemical performance of the spinel $LiMn_2O_4$ by cation dopant effect

To combat the Jahn-Teller distortion effect, doping the $LiMn_2O_4$ spinel structure with low valence ions is an effective approach. Since the average valence of Mn in $LiMn_2O_4$ is + 3.5, when partially replacing Mn with other low valence ions, the average valence of Mn will be increased above + 3.5. Correspondingly, at the end of the 4 V discharge (lithium insertion into the spinel structure), the average valence of Mn will be kept slightly above +3.5. Because the Jahn-Teller distortion starts at Mn^{n+} = 3.5, low valence ion doping can suppress the Jahn-Teller effect in $LiMn_2O_4$ spinel. However, the theoretical capacity of $LiMn_2O_4$ spinel decreases with increasing amounts of dopant ions. It is supposed that the redox reaction accompanying lithium insertion and extraction relies on the valence change of Mn in $LiMn_2O_4$ spinel. Doping Mn with other ions inevitably reduces the amount of lithium which can be reversibly extracted from the spinel structure. So, a trade-off has to be made to achieve the optimum balance between suppressing the Jahn-Teller effect and keeping an appropriate capacity.

A series of doped spinel compounds with the general formula of $LiM_\delta Mn_{2-2\delta}O_4$ (M = Co, Zn and Mg; δ = 0.02, 0.03 and 0.05) were synthesized. In this type of doped $LiM_\delta Mn_{2-2\delta}O_4$

spinel, one fraction of M ion substitutes for 2 fractions of Mn ions. Therefore, the average valence of Mn can be maximally increased to suppress the Jahn-Teller distortion effect. The resulting compound $LiM_\delta Mn_{2-2\delta}O_4$ is cation deficient. The triple or double valence of the M cations partially substitute for Mn^{n+} ions at 16d sites. Thus, there are unoccupied 16d sites in $LiM_\delta Mn_{2-2\delta}O_4$ spinels. It is expected that more Li ions can be accommodated by such partial substitution.

4.3.1 Structural Aspect of Doped $LiM_\delta Mn_{2-2\delta}O_4$ Spinels

The X-ray patterns of the $LiMn_2O_4$ and doped $LiCo_\delta Mn_{2-2\delta}O_4$ (δ = 0.02, 0.03, 0.05) compounds are shown in Fig.4-10. The XRD data of the other doped spinels are not shown since they were similar. All diffraction peaks are indexed to the cubic phase. No impurity phases were detected by x-ray diffraction. In doped $LiM_\delta Mn_{2-2\delta}O_4$ spinels, the valence of Zn and Mg ions should be assigned to +2 because it is the only common valences for these ions. The valence of Co ions is +3 since the spinels were synthesized at high temperature and Co^{2+} ions were oxidised to Co^{3+} ions. Therefore, the doped spinel $LiM_\delta Mn_{2-2\delta}O_4$ can be successfully synthesized without any impurity phase. The lattice constants (a_o) of $LiM_\delta Mn_{2-2\delta}O_4$ spinels are shown in Fig. 4-11. The lattice constants a_o decrease with the increase of δ for doped $LiM_\delta Mn_{2-2\delta}O_4$ spinels.

The Li / $LiPF_6$ (EC+DMC) / $LiM_\delta Mn_{2-2\delta}O_4$ cells were constructed to examine the electrochemical performances of the spinel electrodes. The voltage of freshly assembled cells was 3.25-3.42 V. The slight difference of initial voltage of the cells perhaps was due to minor differences in the composition of the cathodes.

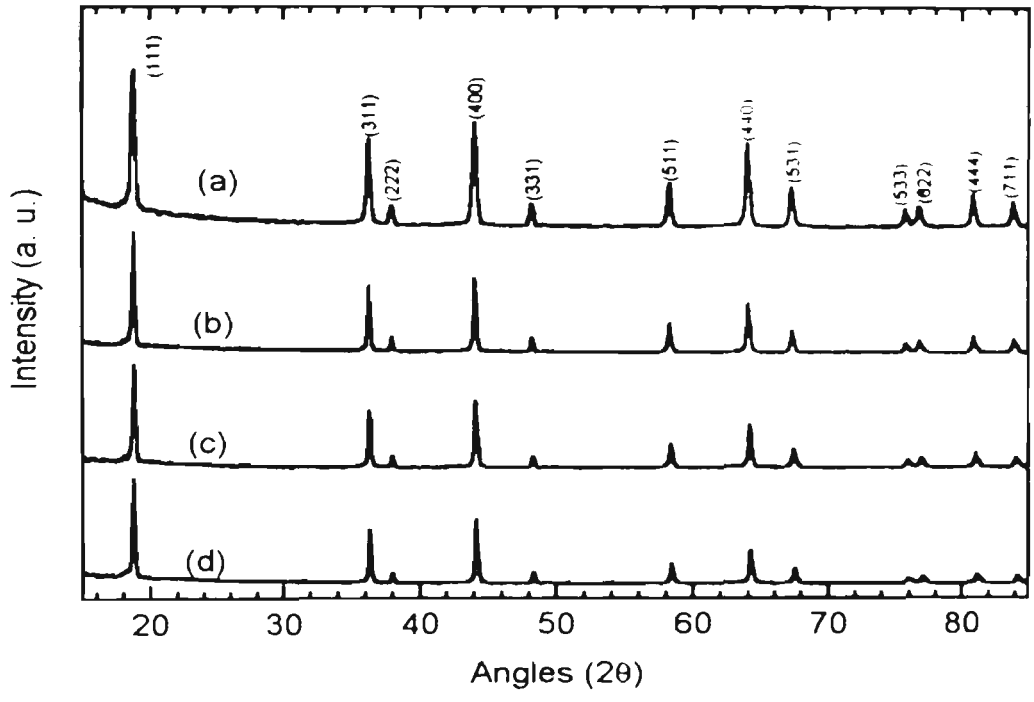

Fig. 4-10 X-ray diffraction patterns of $LiCo_\delta Mn_{2-2\delta}O_4$ compounds. (a) $\delta = 0$ (b) $\delta = 0.02$ (c) $\delta = 0.03$ (d) $\delta = 0.05$

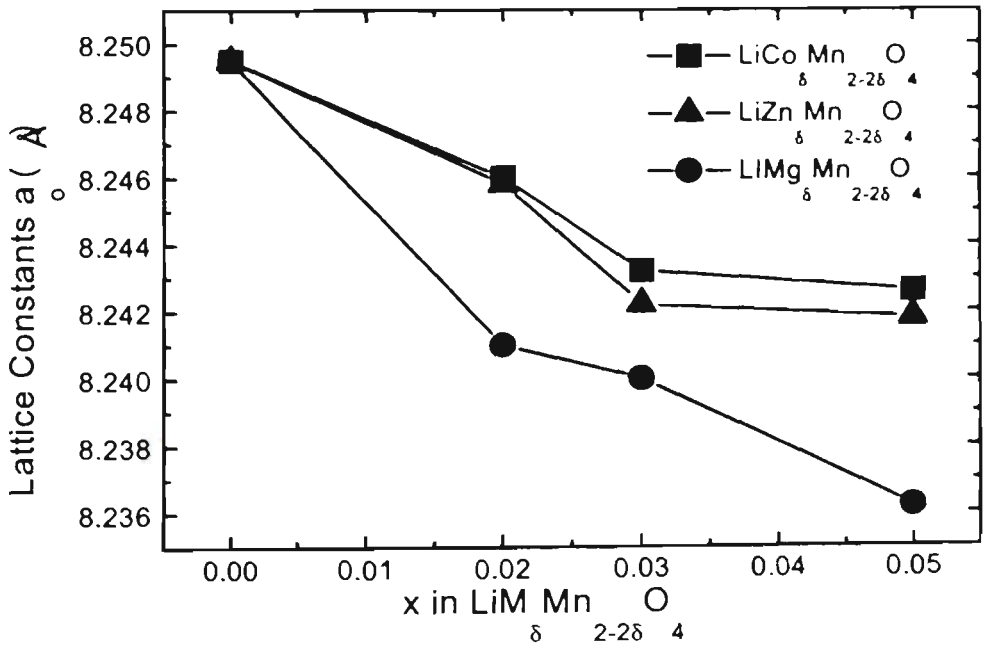

Fig 4-11 The variation of lattice constants (a_o) with x in doped $LiM_\delta Mn_{2-2\delta}O_4$ compounds.

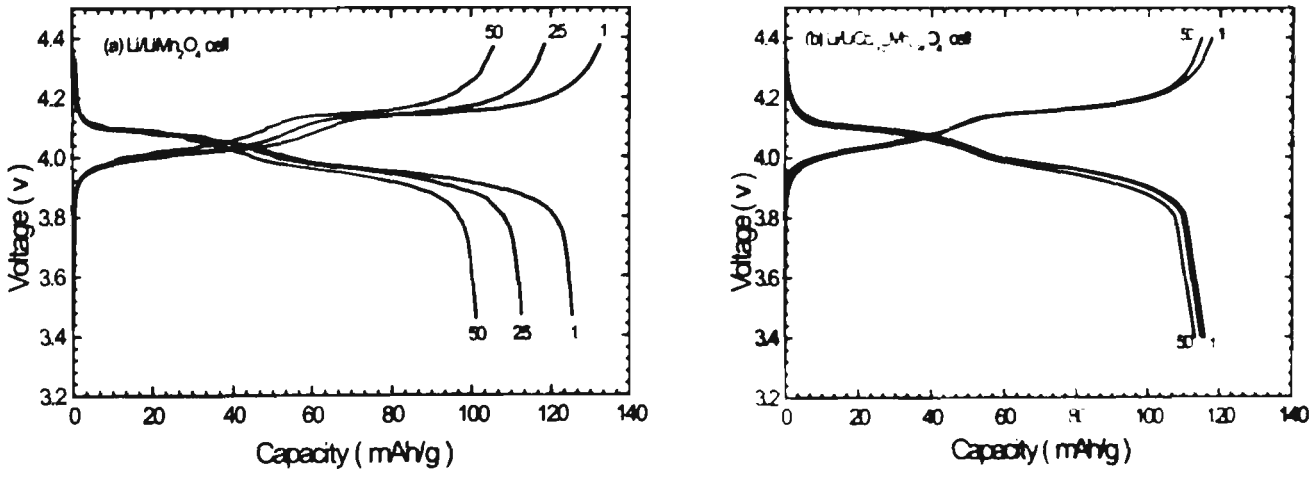

Fig. 4-12 The comparison of cycling data of (a) Li/$LiMn_2O_4$ cell (b) Li/$LiCo_{0.03}Mn_{1.94}O_4$ cell, current density: 0.25 mA cm^{-2}.

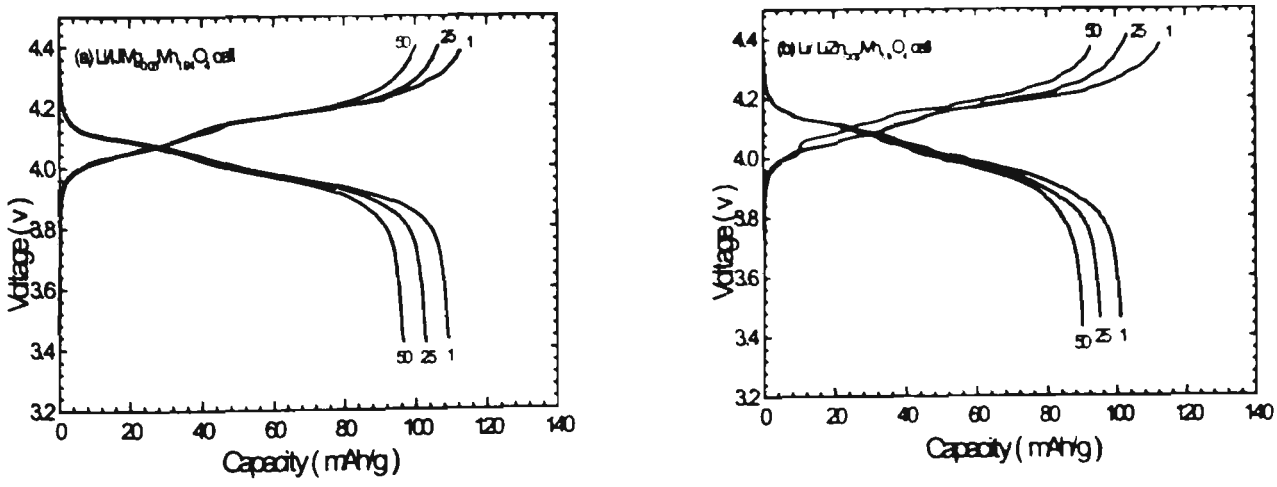

Fig. 4-13 The charge/discharge profiles (a) Li/$LiMg_{0.03}Mn_{1.94}O_4$ cell (b) Li/$LiZn_{0.05}Mn_{1.9}O_4$ cell, current density: 0.25 mA cm^{-2}.

Fig. 4-12 shows a comparison of the cycling data of $LiMn_2O_4$ and $LiCo_{0.03}Mn_{1.94}O_4$ electrodes. The $LiMn_2O_4$ electrode delivered an initial discharge capacity of 125 mAh g but

its capacity then faded at an average rate of 0.5 mAh/g per cycle during the first fifty cycles. In contrast, the $LiCo_{0.03}Mn_{1.94}O_4$ electrode delivered a relatively smaller initial discharge capacity of 118 mAh/g. But the rate of capacity decrease for the $LiCo_{0.03}Mn_{1.94}O_4$ electrode was only 0.15 mAh/g which was much lower than for the $LiMn_2O_4$ spinel electrode. Fig. 4-13. shows the charge/discharge profiles of $LiMg_{0.03}Mn_{1.94}O_4$ and $LiZn_{0.05}Mn_{1.9}O_4$ electrodes. Mg, Zn doped spinels also delivered smaller initial discharge capacity and demonstrated improved cyclability. Comparing with the charge/discharge curves of the $LiMn_2O_4$ electrode and the doped spinel electrodes, it may be seen that the dopant effect does not change the shape of the charge and discharge curves. The two charge and discharge plateaus are similar for the all electrodes tested. One is around 4.1 V and the other is about 3.9V. Table 4-2 further compares the cycle life of undoped and doped spinels. The Co doped spinel electrode demonstrated better rechargeability than either Zn or Mg doped spinels. However, the capacity for all spinel electrodes faded gradually. The rates were different for individual electrodes.

The reasons for the degradation of spinel electrodes on cycling have been identified as: (i) The structural damage to the electrode due to the volume change of unit cell caused by Jahn-Teller distortion in the 3V discharge regime. (ii) The disproportionation reaction of Mn^{3+} from the cathode to the electrolyte: $Mn^{3+} \rightarrow Mn^{2+} + Mn^{4+}$. (iii) the organic electrolyte is becoming unstable at high voltage.

The dopant effect can combat (i) to suppress Jahn-Teller distortion and preserve the structural integrity of the spinel electrode during cycling. Since we use the electrolyte of $LiPF_6$ in EC+DMC, which can resist oxidation even at 5 V, cause (iii) could be excluded. The Co doped spinel electrodes demonstrated excellent cyclability. It is possible that the Co

dopant effect prevents the Mn^{3+} disproportionation reaction in the electrolyte [146]. Wakihara et al. proposed that the improvement in cycling behavior of the Co doped $LiMn_2O_4$ compound was attributed to the enhancement in the stability of the spinel skeleton structure. Because the binding energy of CoO is larger than that of MnO [147]. However, the exact mechanism is still not completely clear. Some structural and electrochemical parameters are summarized in table 4-2. As shown, not all the lithium can be electrochemically extracted from the doped $LiM_xMn_{2-2x}O_4$ spinel structure, because complete removal of lithium would result in an average oxidation state of Mn^{n+} >4. That is chemically impossible. Residual lithium could also contribute to suppress chemical decomposition of the electrode at a high level of the charge.

Table 4-2. The Structural and Electrochemical Parameters of $LiM_xMn_{2-2x}O_4$ Compounds

Compounds	Lattice Constants (A)	Theoretic Mn oxidation state in $LiM_\delta Mn_{2-2\delta}O_4$	Fully Oxidised Composition (n^+_{Mn}=4)	Theoretical Capacity (mAh g)	Initial discharge capacity (mAh/g)	The av. rate of capacity fade (mAh/g per cycle)
$LiMn_2O_4$	8.2495	3.5	Mn_2O_4	154	125	0.5
$LiCo_{0.02}Mn_{1.96}O_4$	8.2458	3.54	$Li_{0.1}Co_{0.02}Mn_{1.96}O_4$	139	120	0.15
$LiCo_{0.03}Mn_{1.94}O_4$	8.2422	3.56	$Li_{0.15}Co_{0.03}Mn_{1.94}O_4$	131	116	0.06
$LiCo_{0.05}Mn_{1.9}O_4$	8.2418	3.61	$Li_{0.25}Co_{0.05}Mn_{1.9}O_4$	116	109	0.08
$LiZn_{0.02}Mn_{1.96}O_4$	8.2460	3.55	$Li_{0.12}Zn_{0.02}Mn_{1.96}O_4$	134	118	0.32
$LiZn_{0.03}Mn_{1.94}O_4$	8.2432	3.58	$Li_{0.18}Zn_{0.03}Mn_{1.94}O_4$	126	111	0.24
$LiZn_{0.05}Mn_{1.9}O_4$	8.2426	3.63	$Li_{0.3}Zn_{0.05}Mn_{1.9}O_4$	108	101	0.24
$LiMg_{0.02}Mn_{1.96}O_4$	8.2410	3.55	$Li_{0.12}Mg_{0.02}Mn_{1.96}O_4$	136	114	0.28
$LiMg_{0.03}Mn_{1.94}O_4$	8.2400	3.58	$Li_{0.18}Mg_{0.03}Mn_{1.94}O_4$	127	108	0.25

$LiMg_{0.05}Mn_{1.9}O_4$	8.2362	3.63	$Li_{0.5}Mg_{0.05}Mn_{1.9}O_4$	109	98	0.22

* Theoretical capacity, based on the mass of the fully oxidised composition, when discharged to the composition $LiM_\delta Mn_{2-2\delta}O_4$.

4.3.3. AC. Impedance characterisation

The electrochemical insertion and extraction of lithium ions into and from $LiM_\delta Mn_{2-2\delta}O_4$ electrodes may be shown as:

$$Li_yM_\delta Mn_{2-2\delta}O_4 + (1-y)Li^+ + (1-y)e^- \rightleftharpoons LiM_\delta Mn_{2-2\delta}O_4 \qquad (4.4)$$

The kinetic parameters of the reaction (4.4) can be determined by a.c. impedance spectroscopy. The a.c. impedance measurements were carried out on the OCV state. The OCVs for $LiM_\delta Mn_{2-2\delta}O_4$ electrodes are around 3.2 V – 3.4 V. The results of the impedance spectroscopy of the Li/$LiPF_6$ (EC+DMC) / $LiM_\delta Mn_{2-2\delta}O_4$ system were presented as Nyquist plots (complex plane, Z_{Re} vs. $-Z_{Im}$). The typical Nyquist plot consists of (i) A semicircle centered on the real axis at high frequencies, from which the ohmic resistance (R_Ω), charge transfer resistance (R_{CT}) and double layer capacitance (C_{dl}) can be deduced. The exchange current density i_o ($i_o=RT/nFR_{CT}$) also could be obtained. (ii) A straight line with an angle of 45° to real axis at low frequency, this corresponds to the Warburg diffusion impedance: $Zw = A\omega^{-1/2} - JA\omega^{-1/2}$. Fig. 4-14 shows the impedance diagrams of $LiMn_2O_4$ and doped $LiM_\delta Mn_{2-2\delta}O_4$ electrodes (M=Co, Mg, Zn; δ=0.03 for Co and Mg, δ=0.05 for Zn). The semicircles are obtained in the frequency range of 65 KHz to several tenth Hz. The end of the semicircles are distorted due to the overlap of the charge-transfer process and diffusion process. At low frequency, a straight line with a slope of 45° to the real axis was observed, which corresponds to the Warburg diffusion. The kinetic

parameters of standard $LiMn_2O_4$ and doped $LiM_\delta Mn_{2-2\delta}O_4$ electrodes in lithium cells are summarised in Table 4-3. There was no significant variation of the kinetic parameters for undoped and doped electrodes.

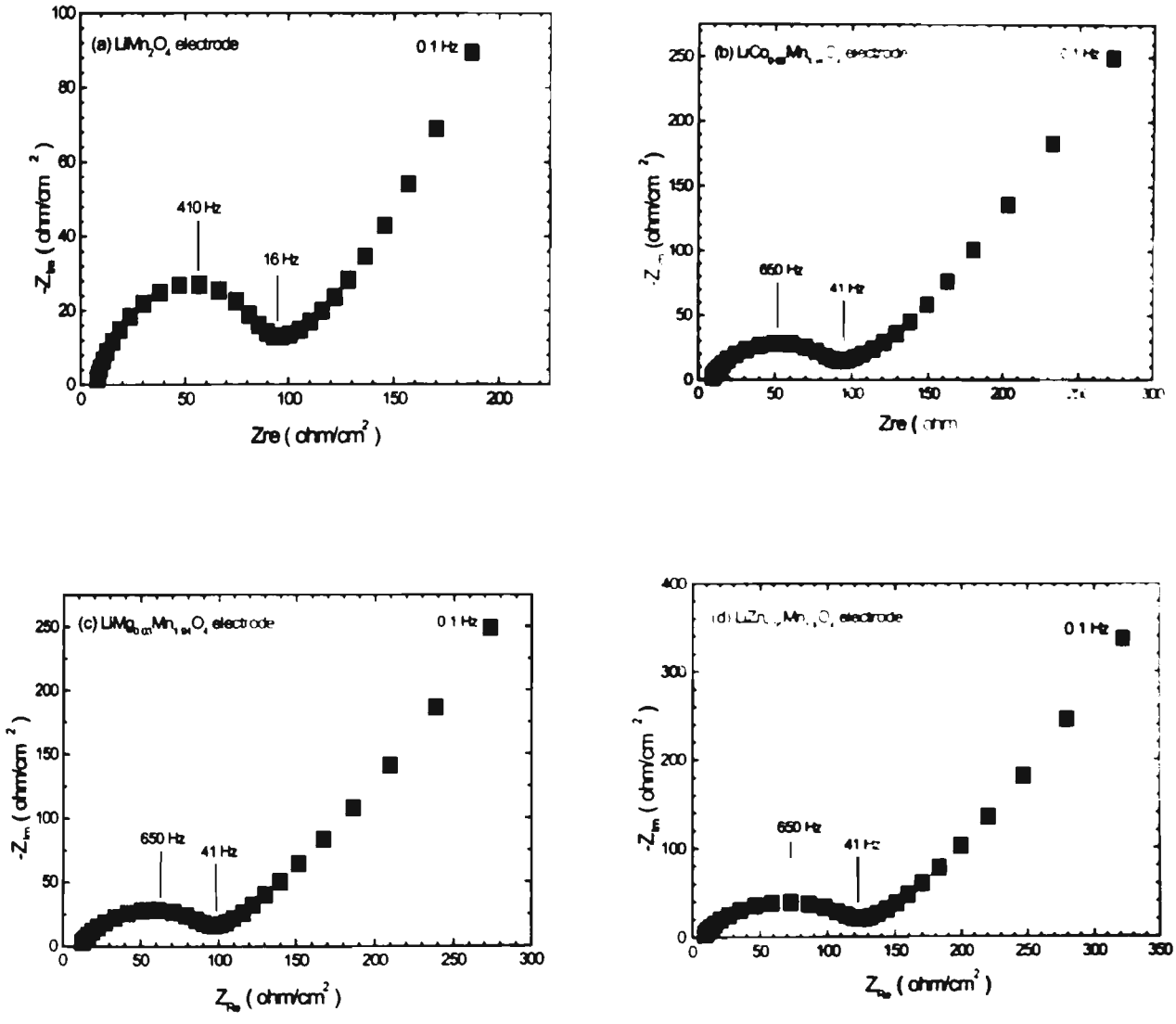

Fig. 4-14 The a.c. impedance spectra of $LiM_\delta Mn_{2-2\delta}O_4$ electrodes.

The exchange current densities i_o for all electrodes tested were very close to each other. The double layer capacitances are several μF (1.8~4.0 μF). So, it may be could concluded that the influence of the dopant effect on the kinetic process of lithium ions intercalation into and deintercalation from the electrode is relatively small.

However, we noted there exists an obvious difference in a.c. impedance spectra between the stoichiometric $LiMn_2O_4$ and the doped $LiM_\delta Mn_{2-2\delta}O_4$ electrodes in the low frequency range (1 Hz – 0.1 Hz), which corresponds to the finite length diffusion process. The value of $|-Z_{im}|$ for the stoichiometric $LiMn_2O_4$ electrode is lower than that for the doped electrodes, but for doped electrodes, the values are almost the same regardless of the species of doped cations in the low frequency range. The possible explanation for this phenomenon is that doped ions (Co, Mg, Mn) could change the properties of the double layer of the electrode. The double layer capacitance (C_{dl}) of the $LiMn_2O_4$ electrode is approximately twice that of the doped electrodes (see table 4-3). However, the electrode process is very complicated and needs further investigation.

Table 4-3 The Kinetic Parameters of $LiM_xMn_{2-2x}O_4$ electrodes in Lithium Cells

Electrodes	Double Layer Capacitance (μF)	Ohmic Resistance R_Ω ($\Omega\,cm^2$)	Charge transfer resistance R_{CT} ($\Omega\,cm^2$)	Exchange current density (i_o) ($10^{-4}\,A/cm^2$)
$LiMn_2O_4$	3.98	6.40	97.4	2.64
$LiCo_{0.03}Mn_{1.94}O_4$	1.58	8.18	97.82	2.62
$LiMg_{0.03}Mn_{1.94}O_4$	2.43	11.31	100.9	2. 54
$LiZn_{0.05}Mn_{1.9}O_4$	1.85	7.15	132.4	1.93

Doped $LiM_xMn_{2-2x}O_4$ (M=Co, Mg, Zn) spinels as the cathode in lithium cells demonstrated improved rechargeability and lower initial discharge capacity. The Co doped spinels were the most stable on cycling, possibly because the Co dopant effect not only

suppresses the Jahn-Teller distortion at the end of 4V discharge plateau but also prevents the disproportionation of Mn^{3+} in the electrolyte. The kinetic parameters for stoichiometric $LiMn_2O_4$ and doped spinel electrodes are almost the same. However, some variation of AC impedance spectra between doped and stoichiometric $LiMn_2O_4$ electrodes at low frequency was observed.

4.4 Electrochemical properties of $LiCr_xMn_{2-x}O_4$ spinels synthesized by Pechini method

It was reported that Co and Cr doped $LiMn_2O_4$ spinels synthesized by solid-state reaction have shown the greatest improvement in the cycle life without dramatically sacrificing the initial capacities [82, 83]. However, traditional solid-state reaction produces heterogeneous spinels with uneven distribution of the dopant cations.

In this investigation, a series of $LiCr_xMn_{2-x}O_4$ spinels were synthesised by the Pechini method, in which the cations can be mixed on an atomic scale. With more homogeneous distribution of the dopant Cr ions in the spinel structure, the electrochemical properties of $LiMn_2O_4$ spinel possibly could be optimised. Neutron diffraction was performed on $LiCr_xMn_{2-x}O_4$ spinels to determine their structural characteristics.

4.4.1 Synthesis and physical characterization of $LiCr_xMn_{2-x}O_4$ spinels

The $LiCr_xMn_{2-x}O_4$ spinels (x=0, 0.02, 0.04, 0.06 and 0.1) were synthesised by the Pechini method. The synthesis procedure is described in Chapter 3.3.1. Powder x-ray diffraction was first performed on the synthesised spinels to detect phase purity. The lattice constants were calculated against an internal silicon standard. Neutron diffraction was then carried out on three $LiCr_xMn_{2-x}O_4$ samples (x=0, 0.02 and 0.04) to confirm the spinel

structure and to determine whether Cr ions occupy 16d Mn sites in the $LiMn_2O_4$ spinel structure.

In the $LiMn_2O_4$ spinel structure (cubic, $Fd\bar{3}m$), Li^+, $Mn^{3+,4+}$ and O^{2-} ions occupy the tetragonal 8a, octahedral 16d and 32e sites respectively in the cubic-close-packed (ccp) oxygen array [148]. This structure provides a 3-dimensional tunnel for lithium insertion and extraction. The results of the powder x-ray diffraction of the synthesised spinels confirmed that pure $LiCr_xMn_{2-x}O_4$ (x=0 - 0.1) solid-solution was obtained. No impurity phase was detected by XRD for any of the samples.

Using XRD analysis alone, it is not possible to provide sufficient evidence to judge definitely whether there is a mixture of Li^+ and $Mn^{3+,4+}$ at 8a and 16d sites and whether the dopant Cr ions are present instead of Mn ions at 16d sites. Consequently, we performed neutron diffraction on three samples: pure $LiMn_2O_4$, $LiCr_{0.02}Mn_{1.98}O_4$ and $LiCr_{0.04}Mn_{1.98}O_4$. Because of the distinctive properties of thermal neutrons, light elements such as Li can be easily located [149].

Fig. 4-15 shows the neutron diffraction patterns obtained for pure $LiMn_2O_4$ and $LiCr_{0.04}Mn_{1.96}O_4$ spinels. A Reitveld method and LHPM program were employed to refine the neutron diffraction patterns [150]. The determination of the crystal structure of a compound depends very much on calculating the diffraction pattern assuming a model of the crystal structure, and comparing the calculated diffraction pattern with the observed one [151]. For pure $LiMn_2O_4$, when we assumed that there are some mixing of Li^+ and $Mn^{3+,4+}$ at 8a and 16d sites, there is a substantial difference between the experimental data and the calculated pattern. As shown in Fig. 4-15(a), when it was assumed that all of the Li ions were in 8a and the Mn ions were in 16d sites, the best fit was obtained. During the

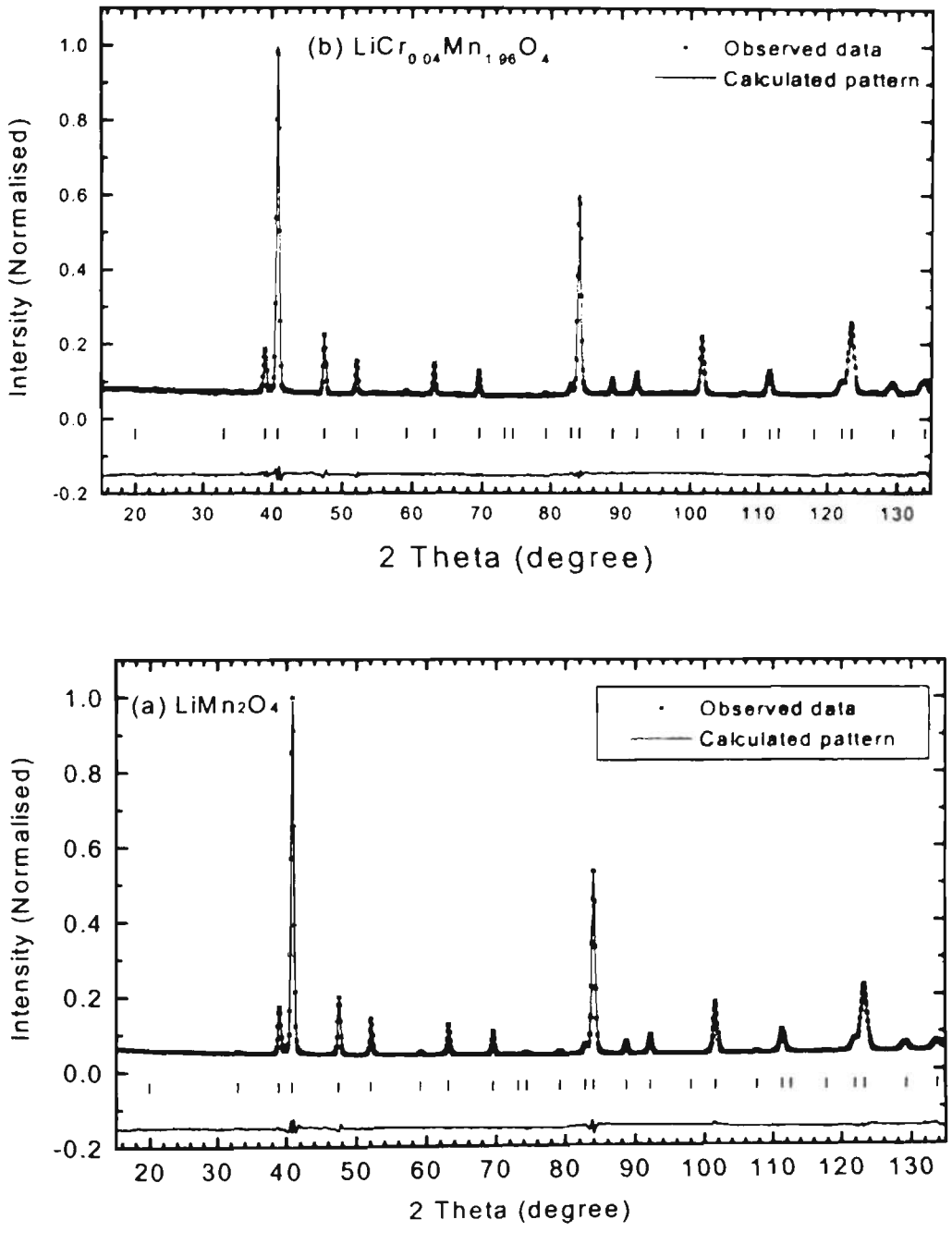

Fig. 4-15 Neutron diffraction patterns of (a) $LiMn_2O_4$ (b) $LiCr_{0.04}Mn_{1.96}O_4$

refinement of the $LiCr_xMn_{2-x}O_4$ structure (x=0.02 and 0.04), assuming that there were some Cr ions in 8a Li sites, the differences between the experimental data and the calculated pattern were obvious. Only when it was assumed that all Cr ions were in 16d Mn sites, did

the calculated intensities best fit the observed ones, and the differences were almost negligible (see Fig. 4-15(b)). It was clearly elucidated that there was no mixing of Li and Mn ions in the $LiMn_2O_4$ spinel structure and that the dopant Cr ions occupy 16d Mn sites in doped $LiCr_xMn_{2-x}O_4$ spinels.

Table 4-4 Lattice constants of $LiCr_xMn_{2-x}O_4$ spinels

Compounds	$LiMn_2O_4$	$LiCr_{0.02}Mn_{1.98}O_4$	$LiCr_{0.04}Mn_{1.96}O_4$	$LiCr_{0.06}Mn_{1.94}O_4$	$LiCr_{0.1}Mn_{1.9}O_4$
a (Å) calculated from XRD	8.2434	8.2369	8.2294	8.2243	8.2210
a (Å) calculated from neutron diffraction data	8.2443	8.2386	8.2365	-	-

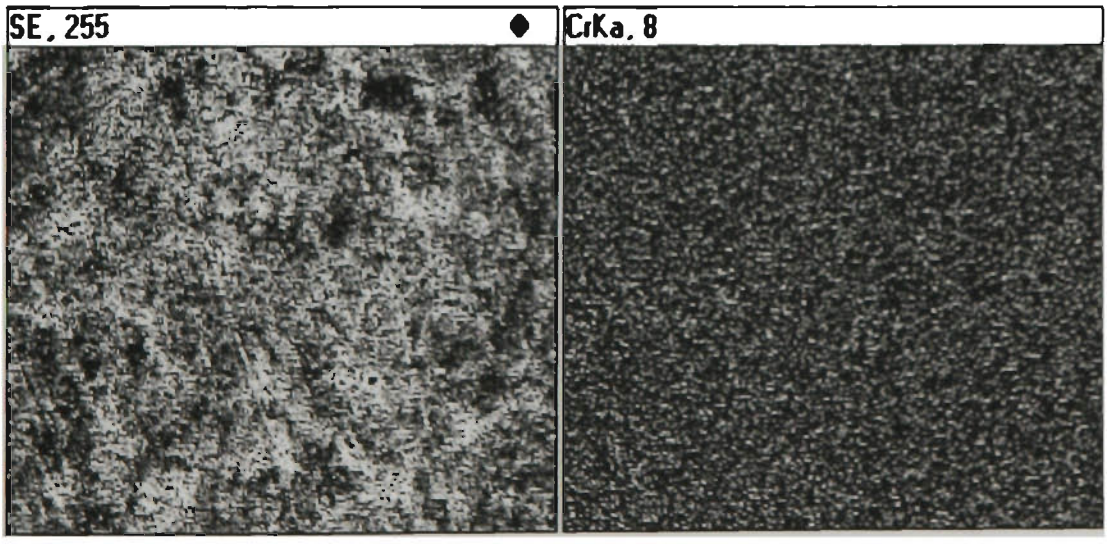

Fig. 4-16 Secondary electron image (left) and EDS map of Cr distribution (right) in doped $LiCr_{0.06}Mn_{1.94}O_4$ spinel. The bright dots represent the distribution of Cr ions.

Table 4-4 gives the lattice constants of $LiCr_xMn_{2-x}O_4$ calculated both fron XRD and neutron diffraction data. The lattice constants decreased with increasing the dopant Cr content. EDS analysis was employed to determine whether Cr ions are distributed

homogeneously in spinel compounds. Fig. 4-16 shows the secondary electron image (left) and EDS map of Cr distribution (right) in $LiCr_{0.06}Mn_{1.94}O_4$. No Cr-rich areas were detected. Statistically, Cr ions are distributed in the spinel compound evenly. With the homogeneous distribution of Cr ions in $LiMn_2O_4$ spinel structure, the dopant effect is expected to be maximised to decrease the capacity fade on cycling.

4.4.2 Electrochemical performance of $LiCr_xMn_{2-x}O_4$ spinels

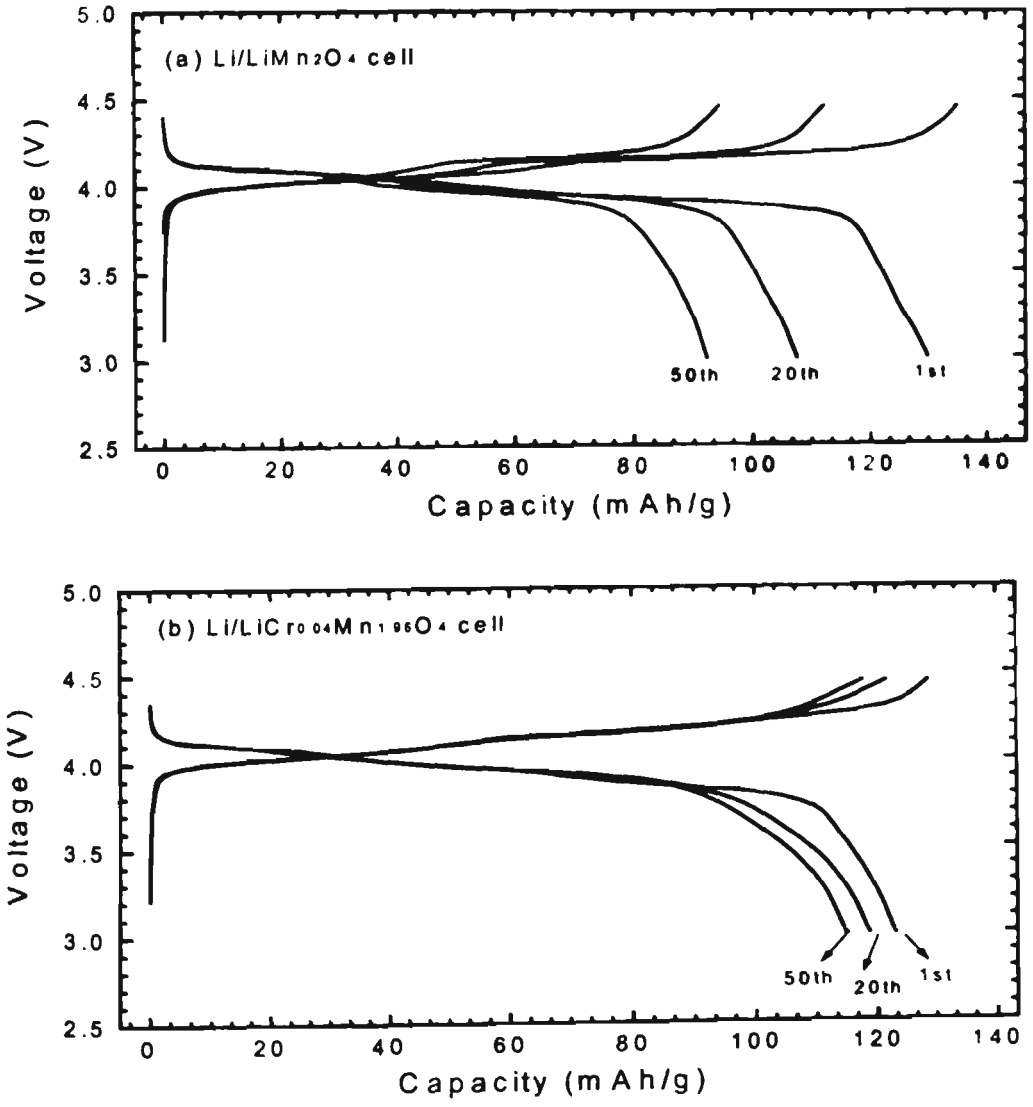

Fig. 4-17 Charge/Discharge profiles, current density: 0.1 mA/g.

Lithium coin cells were cycled galvanostatically in the voltage range of 3.0V to 4.45V. Fig. 4-17 shows the typical charge/discharge profiles of Li/$LiMn_2O_4$ and Li/$LiCr_{0.04}Mn_{1.96}O_4$ cells. Two steps of charge and discharge were observed, corresponding to the re-ordering of Li in the spinel structure when half of the Li ions were extracted or inserted. Cyclic voltammograms give a further elucidation of this process (see Fig. 4-18). From the CV graphs, the two oxidation peaks and two reduction peaks can be easily identified. Compared to $LiMn_2O_4$, the reaction peaks were not observed to shift to low potential for the $LiCr_{0.06}Mn_{1.94}O_4$ electrode. This is opposite to the CV behavior reported for Co doped spinel electrodes [84]. This might be explained if the Cr dopant effect does not significantly disturb the $LiMn_2O_4$ spinel structure.

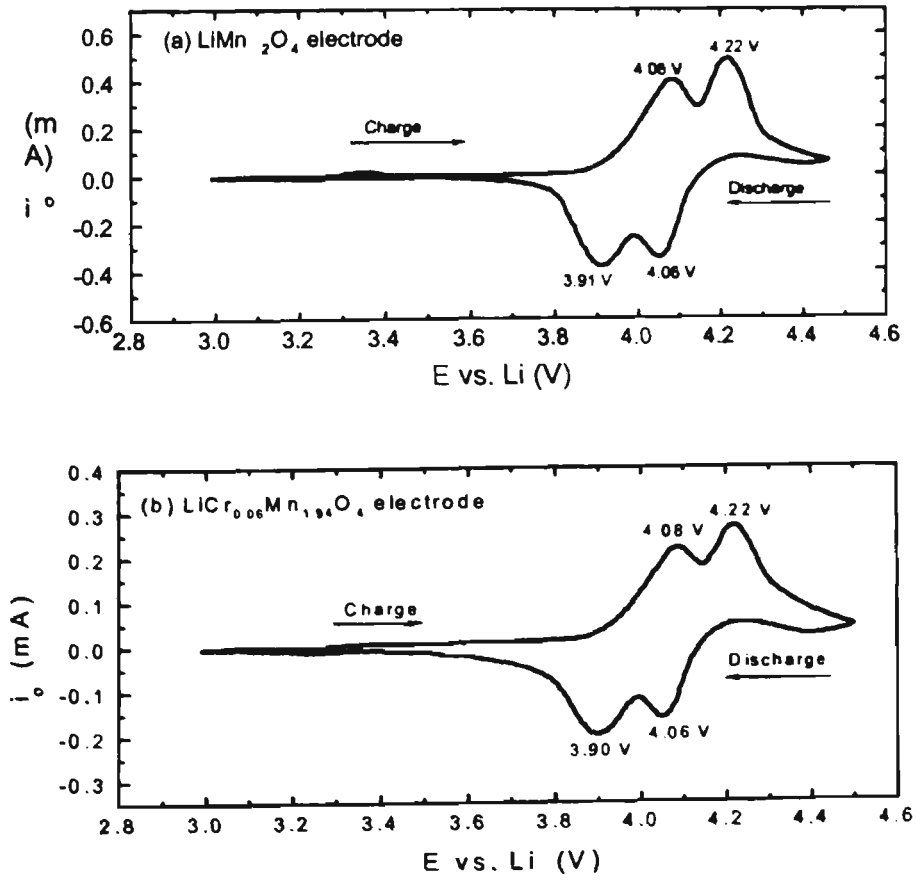

Fig. 4-18 Cyclic Voltammograms, scan rate: 0.1 mV/s.

Fig. 4-19 compares the fading of the discharge capacity of $LiCr_xMn_{2-x}O_4$ (x=0, 0.04, 0.06 and 0.1) electrodes with increasing cycle number. The initial discharge capacity decreased with increasing amount of dopant Cr ions. However, the cyclability was improved substantially. After fifty cycles, the discharge capacities were still above 110 mAh/g for the doped $LiCr_xMn_{2-x}O_4$ electrodes.

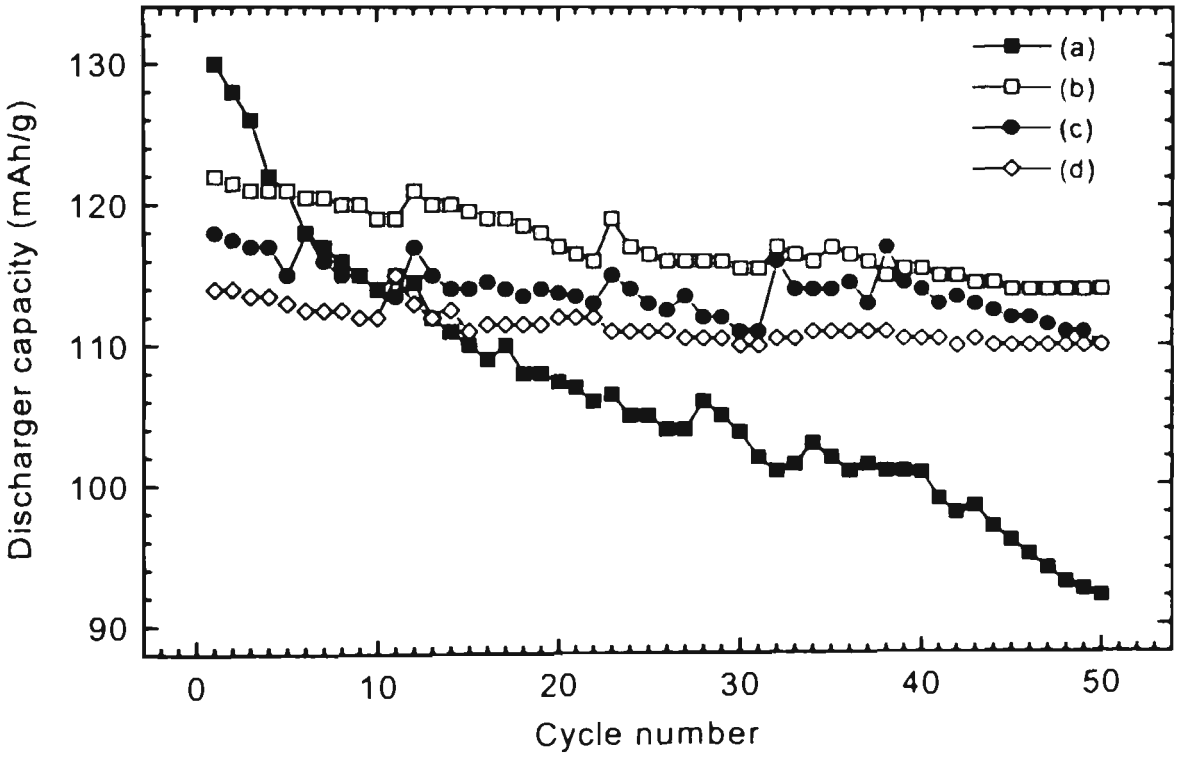

Fig. 4-19 Capacity fade vs. cycle number for $LiCr_xMn_{2-x}O_4$ as cathodes in lithium cells. (a) x=0 (b) x=0.04 (c) x=0.06 (d) x=0.1

Self-discharge commonly occurs for oxidised $LiCoO_2$, $LiNiO_2$ and $LiMn_2O_4$ electrodes in lithium cells [152, 153]. The mechanism for self-discharge is quite complicated. The capacity loss depends on many factors such as the intrinsic properties of the active

materials, the purity of the electrolyte, the electrode and cell preparation techniques. In the fully charged state, transition oxides (CoO_2, NiO_2 and Mn_2O_4) are at an ionisation state of M^{4+}, which is very active and unstable in the organic electrolyte. They tend to react with the electrolyte, causing the voltage of the cell to decline.

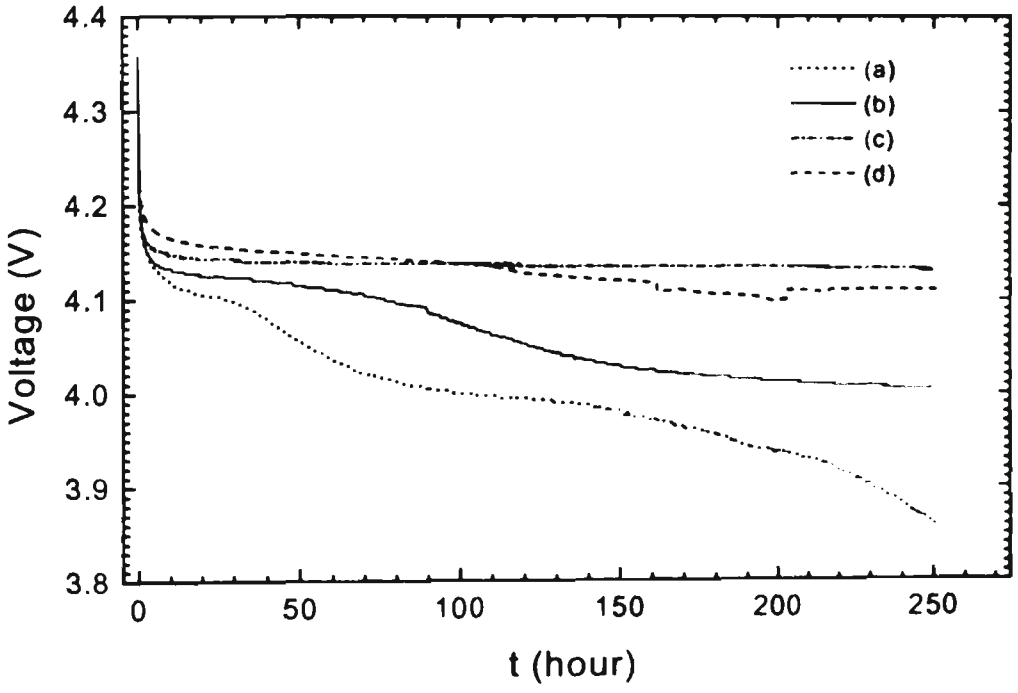

Fig. 4-20 Self-discharge of $LiCr_xMn_{2-x}O_4$ as cathodes in lithium cells (a) x=0 (b) x=0.02 (c) x=0.04 (d) x=0.1

The self-discharge tests were carried out on lithium coin cells. The cells were first charged to 4.4 V and then the charging current was switched off. The variation of the cell voltage was recorded. Fig. 4-20 shows the voltage decay for cells with the $LiMn_2O_4$ and the Cr doped spinel electrodes. The self-discharge rate for the $LiMn_2O_4$ cell was 48 mV/day. Generally, the self-discharge rates for the cells with $LiCr_xMn_{2-x}O_4$ electrodes were much lower than for the cell with the pure spinel electrode. For example, for the cell

with the $LiCr_{0.04}Mn_{1.96}O_4$ electrode, a decay rate of only 22 mV/day was observed. In our investigation, the self-discharge rate of the $LiMn_2O_4$ cell was much higher than that reported by Arora et al.. [84]. This is because the $LiMn_2O_4$ synthesised by the Pechini method has a higher surface area than that synthesised by solid-state methods. Clearly, the influence of the Cr dopant effect on the self-discharge of spinel electrodes is great. The following two factors could contribute to the lower self-discharge rate of the Cr doped spinels. Firstly, Cr stablises the $LiMn_2O_4$ spinel structure, because the binding energy of Cr-O is larger than that for Mn-O [82]. Secondly, the Cr^{3+} ion is in stable $3d^3[(t_{2g})^3(e_g)^0]$ O_h symmetry configuration, which possibly modifies the surface energy state of fully charged Mn_2O_4. Therefore, the reactivity of Mn_2O_4 is reduced, decreasing the reaction between the electrolyte and the surface of the fully charged electrode.

4.4.3 Kinetic characterization of $LiCr_xMn_{2-x}O_4$ electrode by a.c. impedance measurement

AC impedance spectroscopy is widely used to determine the kinetic parameters of the electrode process. The Nyquist plots obtained at different conditioned DC potentials for pure and Cr doped $LiCr_{0.1}Mn_{1.9}O_4$ spinels are shown in Fig. 4-21 (a) and (b) respectively. Initially, EIS experiments were performed on working electrodes at the OCV state, then potentiostatically charged to 4.4V. After 8 hours equilibration, ac excitation was applied. Two semicircles were observed for both $LiMn_2O_4$ and $LiCr_{0.1}Mn_{1.9}O_4$ electrodes. At the low frequency region, a straight line was obtained with an angle to the real axis of 45°C, which represents a diffusion-controlled process in the solid electrode by Warburg

impedance (Z_w). The first semicircle corresponds the charge-transfer resistance (R_{CT}) and the double-layer capacitance (C_{DL}).

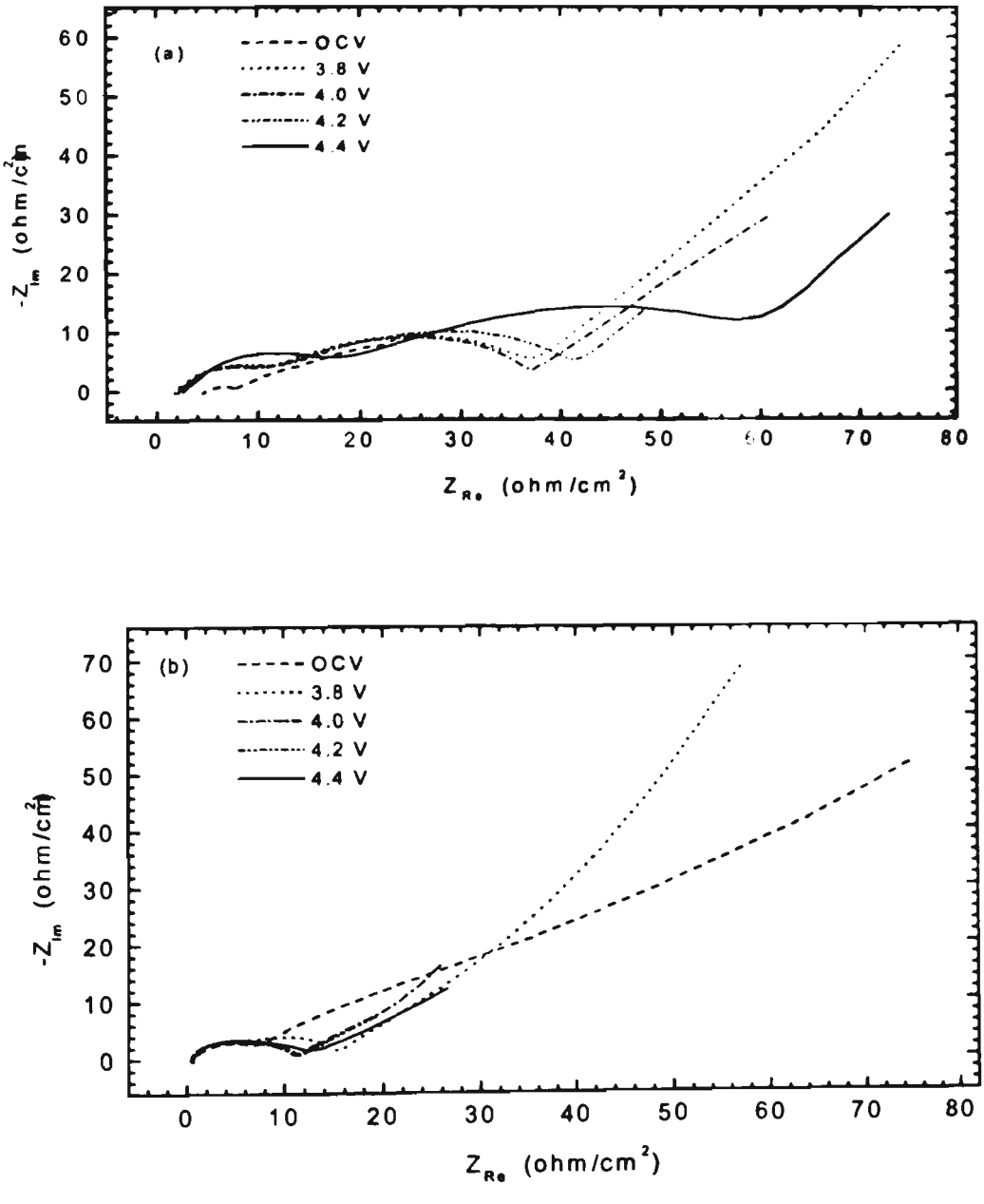

Fig. 4-21 (a) AC impedance spectra of pure $LiMn_2O_4$ obtained at different conditioned potential.
(b) AC impedance spectra of doped $LiCr_{0.1}Mn_{1.9}O_4$ obtained at different conditioned potential.
(OCV=3.4 V, refer to the state of the freshly assembled cell)

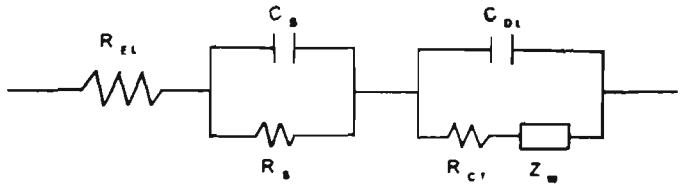

Fig. 4-22 Equivalent circuit for Li/$LiPF_6$ (EC+DMC)/$LiCr_xMn_{2-x}O_4$ system.

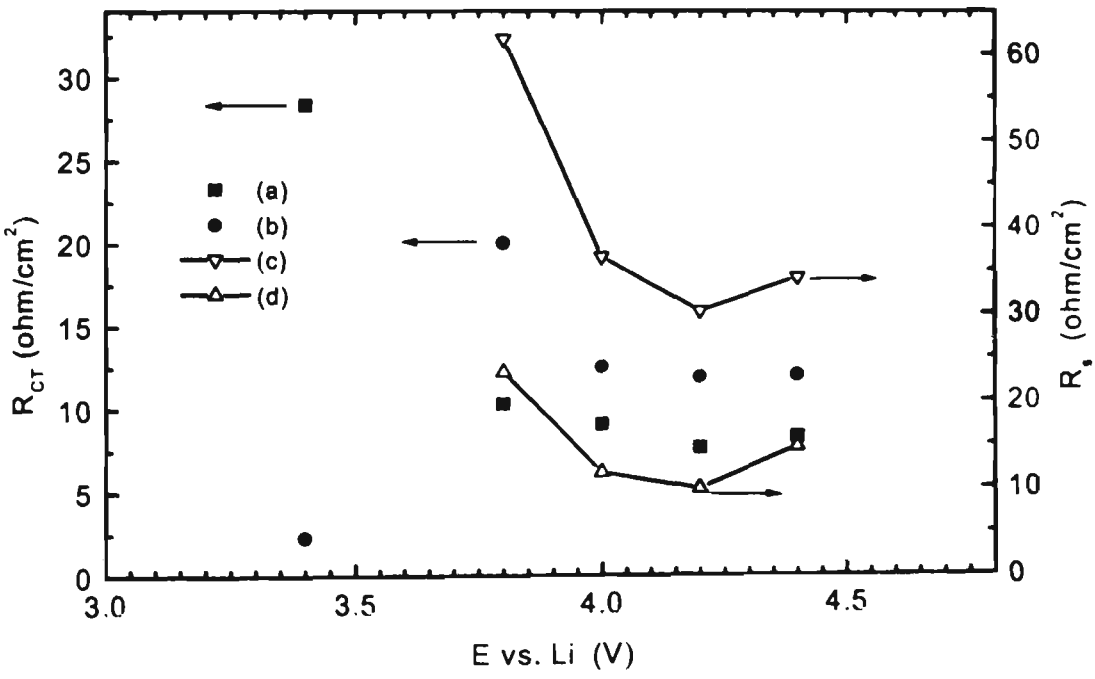

Fig. 4-23 Charge-transfer resistance (R_{CT}) and surface-layer resistance (R_s) of spinel electrodes vs. different conditioned potential.

(a) R_{CT} of pure $LiMn_2O_4$ electrode. (b) R_{CT} of $LiCr_{0.1}Mn_{1.9}O_4$ electrode.

(c) R_S of pure $LiMn_2O_4$ electrode. (d) R_S of doped $LiCr_{0.1}Mn_{1.9}O_4$ electrode.

A surface-layer is formed in the highly charged state due to the passivation reaction between the electrolyte and the surface of the electrode [154]. The surface layer contributes to the second semicircle. In Fig. 4-21, the second semicircles are not observed when the working electrodes are at the OCV state (freshly assembled cells). Therefore, the surface layer is only formed in the highly charged state. The equivalent circuit for the Li/$LiPF_6$ (EC+DMC) /$LiCr_xMn_{2-x}O_4$ system is shown in Fig. 4-22; where R_{EL} is the resistance of the electrolyte; C_S and R_S are the capacitance and the resistance of the surface layer respectively. C_{DL} is the double layer capacitance. The charge transfer resistances (R_{CT}) and the surface layer resistance (R_S) are calculated from AC impedance data and shown in Fig. 4-23. The average values of R_{CT} for $LiMn_2O_4$ and $LiCr_{0.1}Mn_{1.9}O_4$ electrodes are almost at the same amplitude. However, there are quite big variations for R_S. The average R_S is 40.72 Ω/cm^2 for $LiMn_2O_4$ electrode and 14.95 Ω/cm^2 for $LiCr_{0.1}Mn_{1.9}O_4$ electrode. This probably means that a thicker surface layer was formed on the pure $LiMn_2O_4$ than that on the doped $LiCr_{0.1}Mn_{1.9}O_4$ electrode, which supports the proposal that the high self-discharge rate of the pure $LiMn_2O_4$ electrode is due to the decomposition of the electrolyte on the surface of the highly charged electrode. At this stage, it is not clear whether this surface layer is robust or not. If it is not firm enough, it will become debris and enter into the electrolyte during subsequent charge/discharge cycle. In that way, the electrolyte will undergo continuous decomposition, causing a loss in capacity of the cell. This will be detrimental to the operation of the battery.

By comparison with the $LiCr_xMn_{2-x}O_4$ spinels demonstrated substantially improved capacity retention on cycling than pure $LiMn_2O_4$ spinel. Neutron diffraction confirmed that dopant Cr ions substitute for Mn at the octahedral 16d sites in the spinel structure. The Cr

dopant effect could modify the surface state of the highly charged spinel electrode, reducing the self-discharge rate. Through EIS experiments, it was observed that there was a higher surface-layer resistance (R_s) for the pure $LiMn_2O_4$ electrode than for the $LiCr_{0.1}Mn_{1.9}O_4$ electrodes. Correspondingly, a thicker surface layer was probably formed on the pure $LiMn_2O_4$ electrode. The decomposition of the electrolyte on the surface of the spinel electrode could also contribute to the capacity fade of the cell on cycling.

4.5 Secondary Aqueous Lithium Ion Batteries with Spinel Anode and Cathode

All of the present lithium battery technologies use nonaqueous electrolytes in which a lithium salt is dissolved in an organic solvent. The conductivity of an organic electrolyte is typically two orders of magnitude less than that of an aqueous system, which limits the rate capacity and power density. Usually, the nonaqueous cells must be assembled in an argon filled chamber in which the oxygen and moisture have to be strictly excluded. Thus, extra cost for manufacturing is incurred.

The "rocking-chair" concept takes advantage of the difference of chemical potential of the lithium ion in an anode and cathode host. It is now understood that intercalation hosts in which the binding energy of lithium ion differs by several eV can be coupled to construct a lithium ion cell. A variety of such systems have been developed with $LiCoO_2$, $LiNiO_2$, $LiMn_2O_4$ as the cathode and carbonaceous materials or other intercalation compounds as the anode [155 - 158].

Spinel lithiated oxide is an ideal host for lithium insertion/extraction due to its structural stability. It is the most promising electrode materials for lithium ion batteries. Recently, it has been demonstrated that lithium ions can intercalate into and deintercalate from spinel

$LiMn_2O_4$ in aqueous electrolyte [159, 160]. However, the following reaction can occur in aqueous solution for spinels:

$$Li_xA_2B_4 + xH_2O \Leftrightarrow A_2B_4(s) + xLiOH(aq) + x/2\ H_2(g) \qquad (4.5)$$

Concentrated Li^+ can drive the equation (1) to the left and make the lithium intercalation compound become stable in aqueous solution. Consequently, it is theoretically possible for an aqueous secondary lithium battery to be made with appropriate intercalation compounds.

An aqueous lithium cell using $VO_2[B]$ as anode and $LiMn_2O_4$ as cathode with average voltage 1.5 v has been reported [161,162], but the preparation of $VO_2[B]$ is tedious. In this chapter, an aqueous lithium ion system is described with spinel $Li_2Mn_4O_9$ or $Li_4Mn_5O_{12}$ as anode and $LiMn_2O_4$ as cathode which are structurally stable compounds for lithium ion insertion and extraction.

4.5.1 Structural analysis of spinel compounds

The electrode materials were synthesised by solid state reaction at high temperature. The starting powders were mixed by ball-milling in ethanol for 12h. The ethanol was evaporated. The samples were ground and pressed into pellets, then fired at high temperature. The pellets were then pulverised and reground. The coarse powders thus obtained were ball-milled in ethanol for 24h to produce fine powders. The synthesis conditions for anode and cathode materials were summarised in table 4-5.

Table 4-5 Conditions for the synthesis of spinel anode and cathode materials

	Reactants	Firing temperature(°C)	sintering Time (hour)
Cathode materials			
$LiMn_2O_4$	Li_2CO_3, Mn_2O_3	750	20
Anode materials			
$Li_2Mn_4O_9$	$LiOH.H_2O$, $MnCO_3$	380	24
$Li_4Mn_5O_{12}$	$LiOH.H_2O$, $MnCO_3$	380	24

The spinels $Li_2Mn_4O_9$ and $Li_4Mn_5O_{12}$ have a defect spinel-framework structure, which can be expressed as: $[Li_{0.89}]_{8a}[Mn_{1.78}]_{16d}[O_4]_{32e}$ and $[Li]_{8a}[Li_{0.33}Mn_{1.67}]_{16d}[O]_4$ respectively [135]. This structure provides three dimensional tunnels for Li^+ insertion and extraction with minimal change in unit-cell volume [163]. The X-ray diffraction patterns of synthesised spinels are shown in Fig. 4-24. Using a Rietveld refine program, all peaks were indexed to cubic spinel phase. The peaks of $Li_2Mn_4O_9$ and $Li_4Mn_5O_{12}$ spinels are much more broader than those $LiMn_2O_4$, which reflect a disordered characteristic and a low degree of crystallinity. The unit cell parameters a_o were calculated as 8.2495 Å, 8.1092 Å, and 8.1267 Å for $LiMn_2O_4$, $Li_2Mn_4O_9$ and $Li_4Mn_5O_{12}$ respectively.

Spinel $Li_2Mn_4O_9$, $Li_4Mn_5O_{12}$ were synthesised at low temperature(380°C). The oxygen will evolve to form $LiMn_2O_4$ when heated above 400°C. Per formula $Li_2Mn_4O_9$ and $LiMn_2O_4$ can accommodate 3 Li ions. The topotactic reactions for lithium intercalation are as follow:

$$\underset{8a\ \ 16d\ \ 32e}{3Li_{0.89}Mn_{1.78}O_4} + 3Li^+ + 3e \rightarrow \underset{16c\ 16d\ 32e}{Li_4Mn_5O_9} \qquad (4.6)$$

$$\underset{8a\ \ 16d\ \ 32e}{3Li[Li_{0.33}Mn_{1.67}]O_4} + 3Li^+ + 3e \rightarrow \underset{16c\ 16d\ 32e}{Li_7Mn_5O_{12}} \qquad (4.7)$$

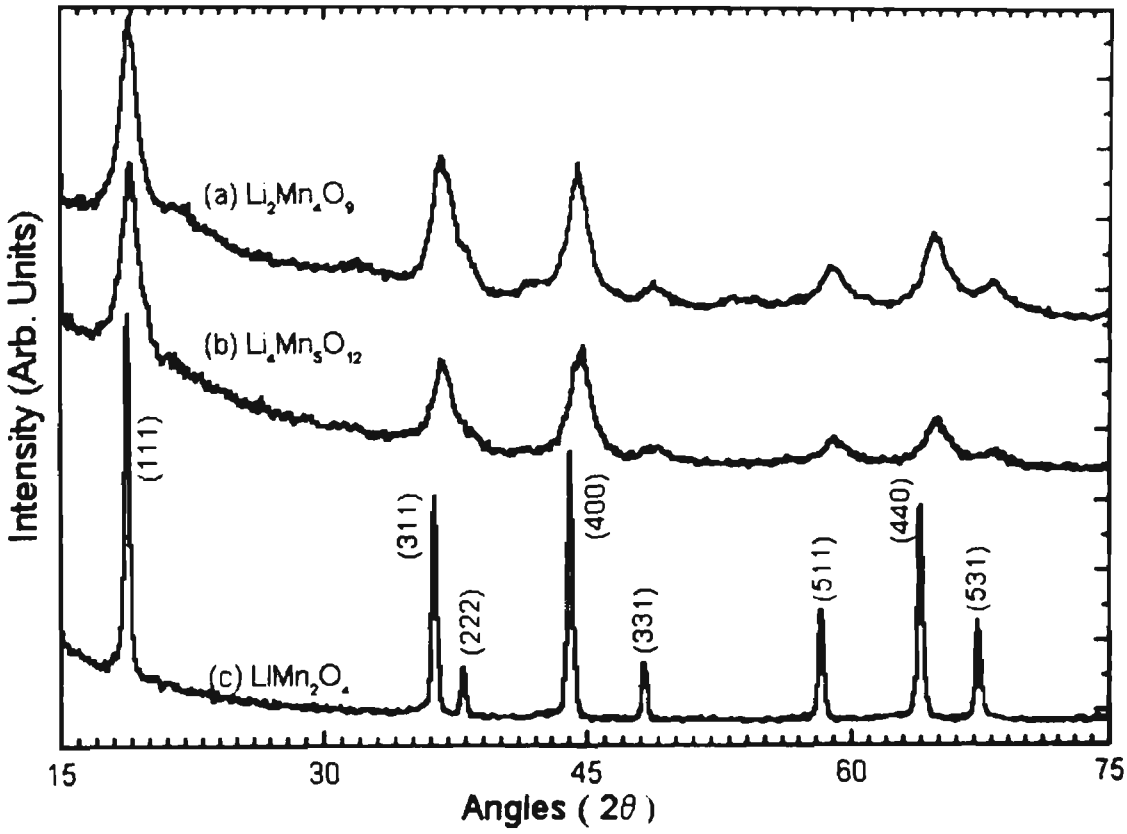

Fig. 4-24 X-ray diffraction patterns of synthesised spinels:
(a) $Li_2Mn_4O_9$, (b) $Li_4Mn_5O_{12}$ (c) $LiMn_2O_4$.

The spinels $Li_2Mn_4O_9$ and $LiMn_2O_4$ have theoretical capacities of 156mAh/g and 202mAh/g respectively.

4.5.2 Electrochemical behaviour of $Li_2Mn_4O_9$ and $Li_4Mn_5O_{12}$ electrodes in aqueous Li-ion cells

The potential of $Li_2Mn_4O_9$ and $LiMn_2O_4$ vs. lithium is about 2.8v, and the potential of $LiMn_2O_4$ vs. lithium is 3.8~4.1v. Thus, coupled $Li_2Mn_4O_9$ and $Li_4Mn_5O_{12}$ with $LiMn_2O_4$, the cell should deliver an average voltage of 1.0~1.3v. In basic aqueous electrolyte with 1M OH^- and 1M Li^+, the potential of spinel $Li_{1-x}Mn_2O_4$, $Li_{2+x}Mn_4O_9$ and $Li_{4+x}Mn_5O_{12}$ as well

as the potentials for oxygen and hydrogen evolution with respect to SHE are shown in Fig. 4-25.

The H_2 and O_2 evolution can be controlled by shifting the potential of reactions (4.8) and (4.9) by adjusting the PH of the solution.

$$2H_2O + 2e^- \rightarrow H_2 + 2OH^- \quad (4.8)$$

$$4OH^- \rightarrow 2H_2O + O_2 + 4e^- \quad (4.9)$$

An aqueous electrolyte was used with 6M Li^+ and 0.0015M OH^-. Compared with the 1M OH^-, the potential of H_2 and O_2 evolution were shifted by 0.16v according to the Nernst equation. So the reactions (4.8) and (4.9) were suppressed and Li ion intercalation and deintercalation became the predominant reaction.

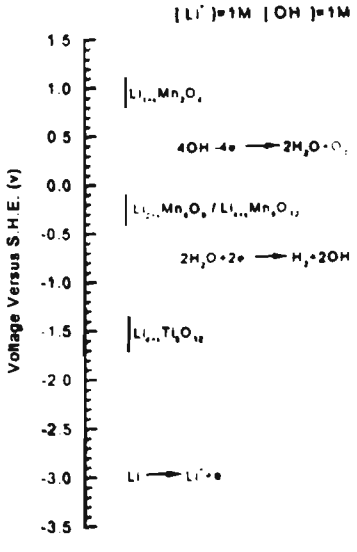

Fig. 4-25 The potentials of the electrode materials, H_2 and O_2 evolution reactions vs. SHE. in 1M OH^- and 1M Li^+ aqueous electrolyte.

The $Li_2Mn_4O_9$ / $LiMn_2O_4$ and $Li_4Mn_5O_{12}$ / $LiMn_2O_4$ cells were made with 6M $LiNO_3$, 0.0015M OH^-. The cells were cycled under a current of 1mA/cm^2 between lower voltage limit of 0.5v and upper voltage limit of 1.6v. The ideal reaction in $Li_2Mn_4O_9$ / $LiMn_2O_4$ and $Li_4Mn_5O_{12}$ / $LiMn_2O_4$ cells are:

$$Li_5Mn_4O_9 + Mn_2O_4 \leftrightarrow Li_2Mn_4O_9 + 3LiMn_2O_4 \quad (4.10)$$

$$Li_7Mn_5O_{12} + Mn_2O_4 \leftrightarrow Li_4Mn_5O_{12} + 3LiMn_2O_4 \quad (4.11)$$

During charging, the Li ions are extracted from the $LiMn_2O_4$ cathode host and inserted into the $Li_2Mn_4O_9$ or $Li_4Mn_5O_{12}$ anode. During discharge, Li ions deintercalate from the anode and intercalate into the cathode. The voltage profile of charge/discharge are shown in Fig.4-26. The cells delivered an average voltage of 1.1v and a maximum capacity of approximately 100mAh/g(with respect to cathode active materials). It was noted that the charge and discharge capacity was not in balance in Fig. 4-26. The charge capacity is almost 8~10% more than the discharge capacity. This can be explained if a part of the current was used for the oxygen evolution reaction on the cathode during charging, which is similar to nickel-cadmium batteries. About 10% of the first charging capacity is irreversible. This might be an intrinsic property of the low temperature synthesised defect spinel $Li_2Mn_4O_9$ and $Li_4Mn_5O_{12}$, rather than the aqueous electrolyte. Following the second cycle, the reversibility is good. Both cells delivered approximate 50% capacity under 1v. The H_2 evolution reaction is easy at low voltage, which induces instability of the discharge performance(see Fig.4-26). So, the electrochemical reaction of the lithium ion system in aqueous electrolyte is more complicated than in nonaqueous electrolyte.

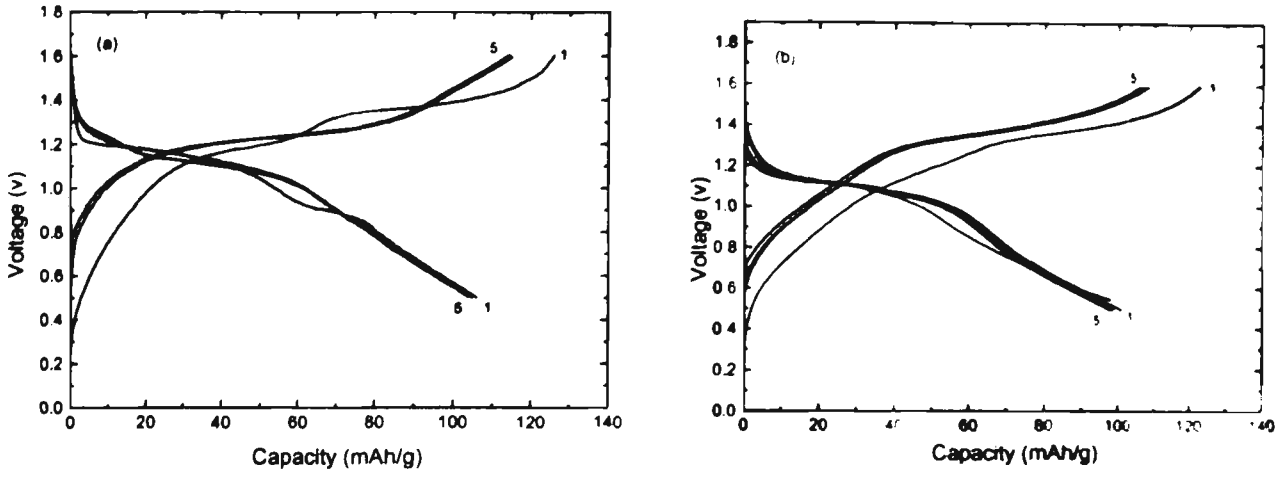

Fig. 4-26 The voltage profile of charge/discharge for aqueous lithium ion cells, electrolyte is 6M $LiNO_3$ and 0.0015M OH^-, Current density is 1mA cm^{-2}.

(a) $Li_2Mn_4O_9$ / $LiMn_2O_4$ cell.
(b $Li_4Mn_5O_{12}$ / $LiMn_2O_4$.cell.

In order to determine whether the Li ion intercalation reaction is a predominant reaction in aqueous electrolyte cells, $Li_2Mn_4O_9$ / $LiMn_2O_4$ and $Li_4Mn_5O_{12}$ / $LiMn_2O_4$ cells with an organic electrolyte(1M $LiPF_6$ in EC/DMC) were constructed and cycled between 0.5~1.6v at a constant current of 0.25mA/cm^2. Fig.4-27 shows the comparison of the second charge voltage profile of aqueous and nonaqueous cells. The dotted line is for the nonaqueous cell. The electrochemical behaviour for aqueous and nonaqueous cells agree well except that the aqueous cells consume more charge capacity due to O_2 evolution. This demonstrated that Li ions do shuttle in aqueous electrolyte in a similar manner to that in nonaqueous cells.

A $Li_4Ti_5O_{12}$/$LiMn_2O_4$ aqueous cell was also constructed. This cell should deliver 2.4~2.5v voltage according to the data of Fig.2. But, unfortunately, it only could be charged to 2.0v in the first charging before failure. The H_2 evolution on the $Li_4Ti_5O_{12}$ anode could be responsible for the cell failure due to the potential gap between the H_2 evolution reaction and the $Li_4Ti_5O_{12}$ electrode.

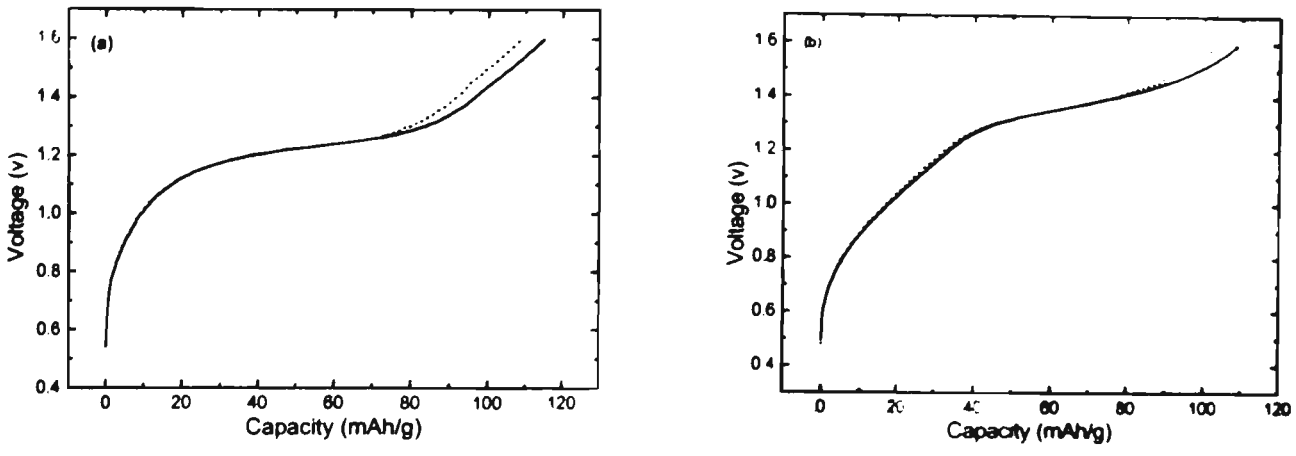

Fig. 4-27 The comparison of electrochemical behaviours of aqueous and nonaqueous lithium ion cells, Current density is 0.25mA/cm^2. The dash lines are nonaqueous lithium-ion cells.
(a) $Li_2Mn_4O_9$ / $LiMn_2O_4$ cell. (b) $Li_4Mn_5O_{12}$ / $LiMn_2O_4$ cell.

At present, $Li_2Mn_4O_9$ / $LiMn_2O_4$ and $Li_4Mn_5O_{12}$ / $LiMn_2O_4$ aqueous cells cannot compete with Ni-Cd cell in terms of their energy density and electrochemical behaviour. But optimisation of the synthesis of Li-Mn-O oxides might be expected to improve their electrochemical performance in aqueous electrolytes. Addition of organic and inorganic additives to aqueous electrolyte can inhibit the hydrogen evolution reaction. Also, low potential anode materials such as TiS_2, $Li_4Ti_5O_{12}$ etc. could be expected to be used as anodes in aqueous lithium ion cells.

In summary, aqueous lithium-ion systems would provide a very cost-effective technology for manufacturing. Accordingly, lithium-ion cells were fabricated with spinel $Li_2Mn_4O_9$, or $Li_4Mn_5O_{12}$ as anode and $LiMn_2O_4$ as cathode in an aqueous electrolyte. In the preliminary testing, the cells could deliver approximately 100 mAh/g capacity at an average voltage of 1~1.1V.

4.6 A high potential cathode material – $LiNiVO_4$ inverse spinel

The inverse spinel $LiNiVO_4$ was found to be a new type of high voltage (4.8V) cathode material for secondary lithium ion batteries. However, the electrochemical performance of $LiNiVO_4$ is rather poor. A discharge capacity of only 40 mAh/g can be delivered, compared to its theoretical capacity of 148 mAh/g. The reason seems to be that there are no obvious tunnels along which the Li ions can move because of the structure of the inverse spinel, in which Li^+ and Ni^{2+} occupy 16d octahedral sites and V^{5+} is in 8a tetrahedral sites [164]. Dopant ions have been widely used to improve the physical and electrochemical properties of these materials. It has been reported that doping the inverse spinel $LiNiVO_4$ with the rare earth elements (La, Gd and Yb) could improve its electrical conductivity [165]. But there has been no report about its electrochemical performance in lithium cells.

A series of trace La doped La_δ-$LiNiVO_4$ (where δ=0, 0.1, 0.01, 0.0001) were prepared by reacting $LiOH.H_2O$, $Ni(NO_3)_2.6H_2O$, NH_4VO_3 and La_2O_3 according to the molar ratio of $Li:Ni:V:La=1:1:1:\delta$. LiOH, $Ni(NO_3)_2$ and NH_4VO_3 were dissolved in distilled water to obtain a green solution into which a nitric acid solution of La_2O_3 was added. After stirring, a yellow-brown precipitate was formed. The precipitate was vacuum filtered and dried at 120°C. The dried powders were heated at 700°C for 4 hours and then ground by pestle and mortar.

Fig. 4-28 shows the XRD patterns of La_δ-$LiNiVO_4$ (δ=0, 0.1, 0.01, 0.001 and 0.0001). The miller indices were determined assuming the cubic S.G: Fd3m system. The $La_{0.1}$-$LiNiVO_4$ contained a lot of impurity phase and its XRD pattern is not shown. At the dopant level of δ=0.1 and 0.01, NiO and $LaVO_4$ impurity phases were formed, which indicates that $LiNiVO_4$ had reacted with La_2O_3. Therefore, these two samples were

eliminated from further electrochemical tests. At the lower dopant levels of δ=0.001 and 0.0001, no impurity phase was detected by XRD, indicating that the La had entered into the $LiNiVO_4$ structure to form a solid solution. However, at these low concentrations, the sites which the trace lanthanum ions occupied in the inverse spinel structure could not be determined by XRD analysis. The lattice constants were calculated and are shown in Table 4-6. The lattice constant of pure $LiNiVO_4$ was 8.2201 Å, which is in good agreement with JCPDS data, 8.21984 Å [166]. The lattice constants increase slightly with increasing La content. The ionic radii of La^{3+}, Ni^{3+} and V^{5+} are approximately 0.127, 0.056 and 0.046 nm respectively. La^{3+} has larger radius than either Ni^{2+} or V^{5+}. When trace La^{3+} dissolves in the $LiNiVO_4$ structure, the unit cell expands marginally. This factor is favourable for Li^+ ion diffusion in the inverse spinel structure.

Table 4-6 Lattice constants of La_δ-$LiNiVO_4$ vs. the content of dopant La (δ)

Samples	$LiNiVO_4$	$La_{0.0001}$-$LiNiVO_4$	$La_{0.001}$-$LiNiVO_4$	$La_{0.01}$-$LiNiVO_4$
Lattice constants c (Å)	8.2201	8.2242	8.2278	8.2369
Volume of the unit cell ($Å^3$)	555.4325	556.2640	556.9948	558.8450

Teflon test cells Li/ La_δ-$LiNiVO_4$ (δ=0, 0.001 and 0.0001) were constructed to examine the electrochemical properties of the La-doped compounds as cathodes in lithium cells. The voltages of the freshly assembled cells were in the range of 3.22 V-3.45 V. The cells were cycled between 3 V-5 V at a constant current density of 0.1 mA/cm^2. Fig.4-29 shows the charge/discharge profiles of the cells. During charging, the voltage of the cell increased to 4.5 V rapidly and then followed a plateau around 4.8 V-4.9 V. In the discharge process, the voltage dropped to 4.75V quickly, following a discharge plateau from 4.75 V to 4.5 V.

Another small descending discharge plateau between 4.25 V-3.9 V was observed for all of the Li/ La_δ-$LiNiVO_4$ cells. Fig. 4-30. shows the differential chronopotentiometric curves of dQ/dV vs. E as a further illustration of this second discharge plateau. One oxidation peak around 4.8V-4.9V corresponds the charging plateau. However, as expected, there were two reduction peaks during the discharge process. One was around 4.75 V-4.5 V. The second small broad peak was observed between 4.25V to 3.9V and this peak did not appear on the charging process, indicating that this second reduction reaction is irreversible. Lithium ions diffusing to 8a tetrahedral sites probably are responsible for this second discharge plateau. Because 8a tetrahedral sites are predominantly occupied by V^{5+} ions, Li ions cannot be extracted due to the blockage of the V^{5+} ions rendering this second reduction reaction irreversible.

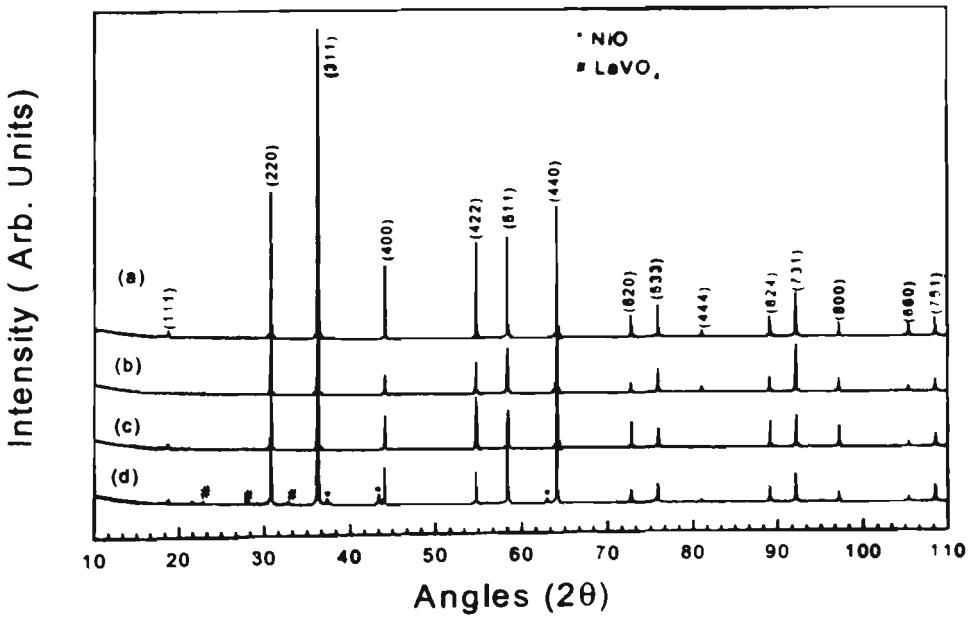

Fig. 4-27 The X-ray diffraction patterns of La_δ-$LiNiVO_4$.
(a) δ=0 (b) δ=0.0001 (c) δ= 0.001 (d) δ=0.01.

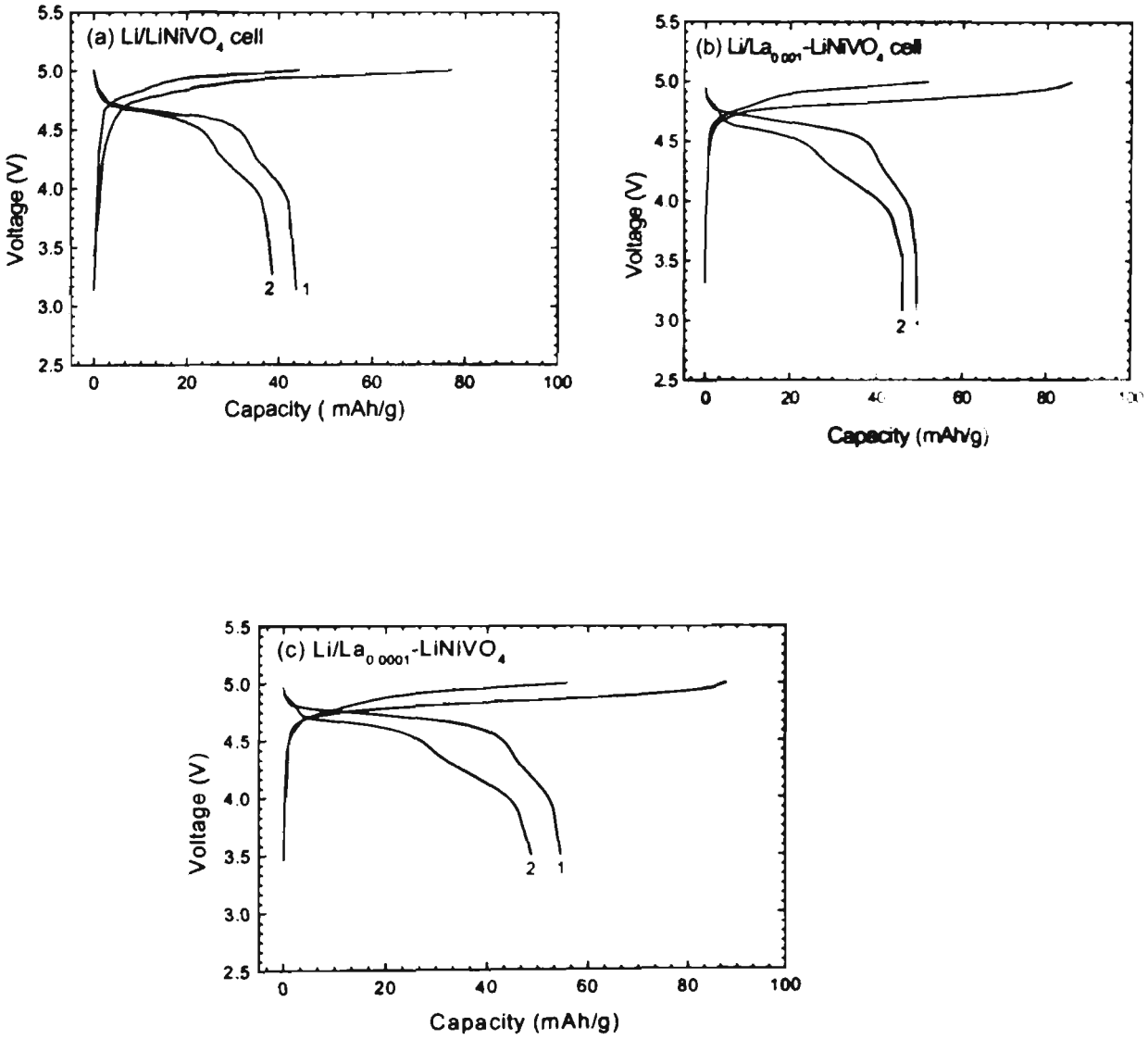

Fig. 4-29 The Charge/discharge profiles of Li/La$_\delta$-$LiNiVO_4$ cells.

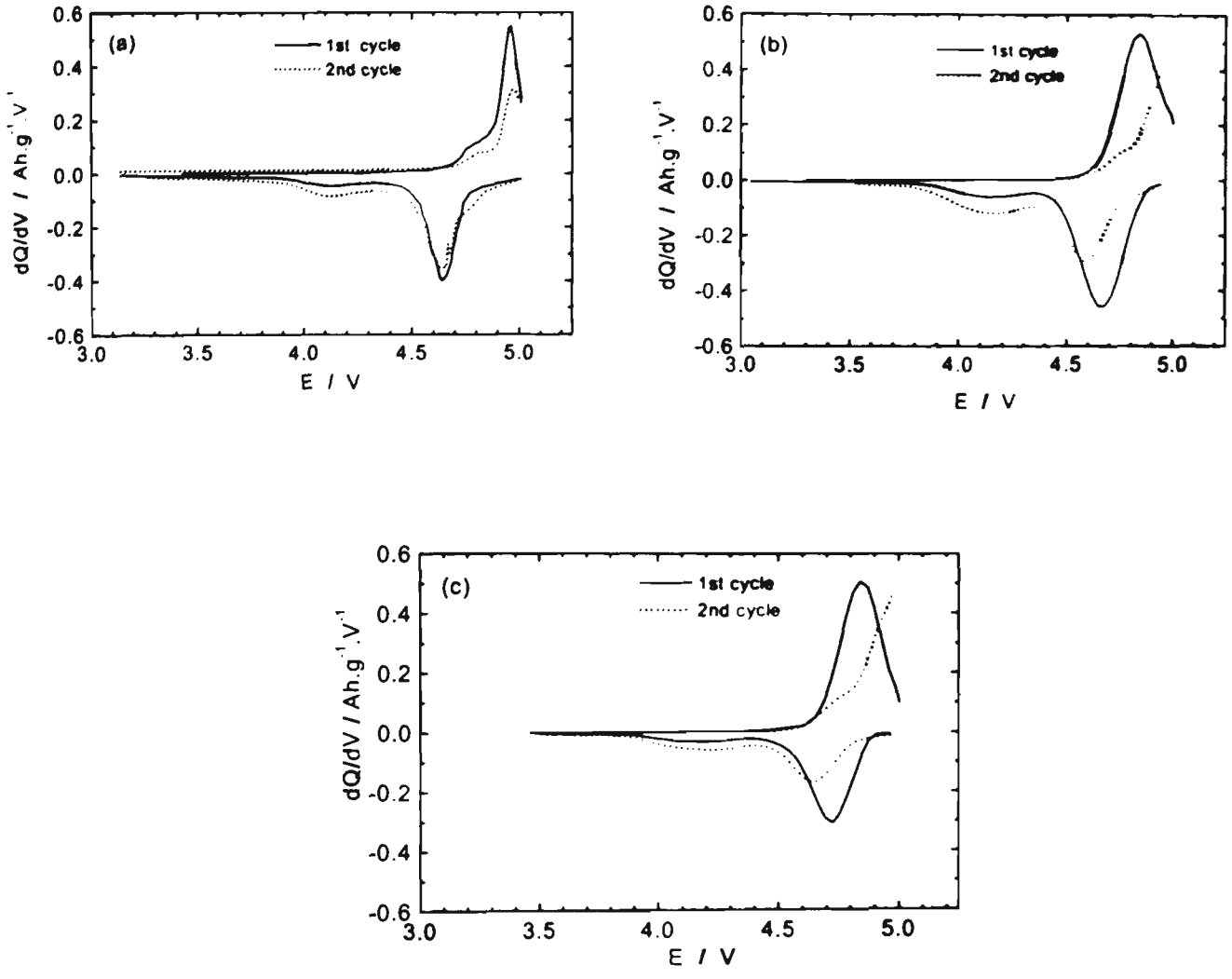

Fig. 4-30 Differential chronopotentiometric curves for the oxidation and reduction reactions
(a) $LiNiVO_4$/Li cell. (b) $La_{0.001}$-$LiNiVO_4$ cell. (c) $La_{0.0001}$-$LiNiVO_4$/Li cell.

The first charge capacities for $LiNiVO_4$, $La_{0.001}$-$LiNiVO_4$ and $La_{0.0001}$-$LiNiVO_4$ were 77 mAh/g, 85 mAh/g and 88 mAh/g respectively. The doped $LiNiVO_4$ electrodes delivered a slightly higher capacity. The reason for that is unknown. However, approximately 35-40 mAh/g of the total capacity was irreversible for all of the electrodes in the first cycle. The

theoretical capacity for $LiNiVO_4$ is 148 mAh/g. Therefore only half of the theoretical capacity was achieved.

There are two possibilities for the low practical capacity of $LiNiVO_4$: (1) The extraction of some Li ions takes place above 5V. Electrolyte oxidation then limits the further extraction of Li ions. (2) A certain fraction of the Li ions perhaps cannot be extracted from the inverse structure at all, which is intrinsically related to the characteristics of the inverse spinel. Both Li^+ and Ni^{2+} occupy 16d sites. Ni^{2+} ions could block Li^+ extraction. After twenty cycles, the capacities of all electrodes tested was reduced by almost 50%.

The rechargeabilities for all of the doped and undoped $LiNiVO_4$ electrodes were poor. Although it has been reported that the dopant effect at a La dopant level of 0.0001 improved the electrical conductivity of $LiNiVO_4$ by two orders of magnitude from 8.12×10^{-8} S/cm to 2.21×10^{-6} S/cm [165], in this work it was not found that La doping could improve the capacity and rechargeability of $LiNiVO_4$ greatly.

Lithium intercalation into and de-intercalation from $LiNiVO_4$ has been proved to be reversible via insitu x-ray diffraction[9]. The topotactic reaction for $LiNiVO_4$ in the lithium cell is suggested to proceed as:

$$LiNiVO_4 \rightleftharpoons Li_{1-x}NiVO_4 + xLi^+ + xe^- \qquad (4.12)$$

The kinetic parameters of above reaction can be determined by a.c. impedance spectroscopy. The impedance spectra are reported as Nyquist plots through which charge-transfer resistance(R_{CT}) and exchange current density($i_o=RT/nFR_{CT}$) can be deduced. The Nyquist plots of $Li/LiNiVO_4$ and $Li/La_{0.0001}$-$LiNiVO_4$ cells at different voltages are shown in Fig. 4-31. The cells were potentiostatically charged from OCV to 4.7 V, 4.8V, 4.9V and 5V respectively and then kept at that voltage during the a.c. impedance measurement.

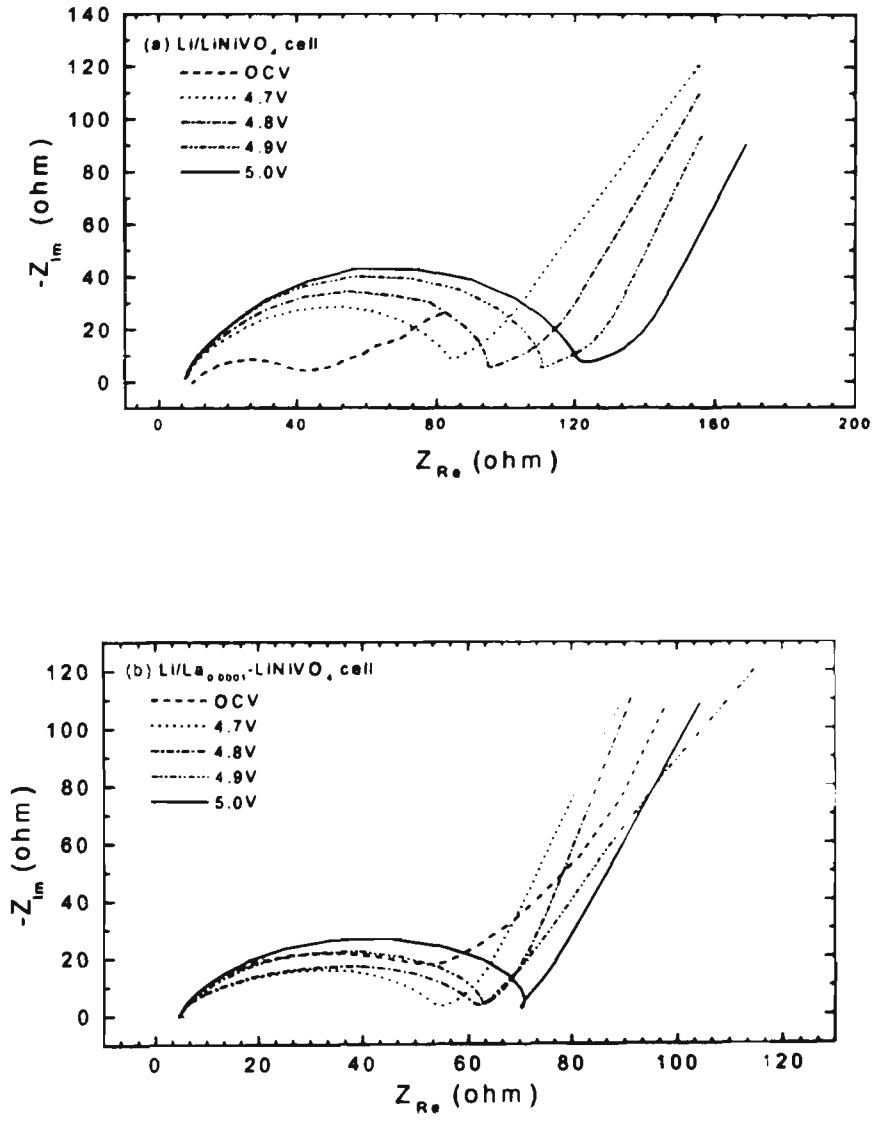

Fig. 4-31 A. C. impedance spectra of at different voltages of
(a) Li/$LiNiVO_4$ cell. (b) Li/$La_{0.0001}$-$LiNiVO_4$ cell.

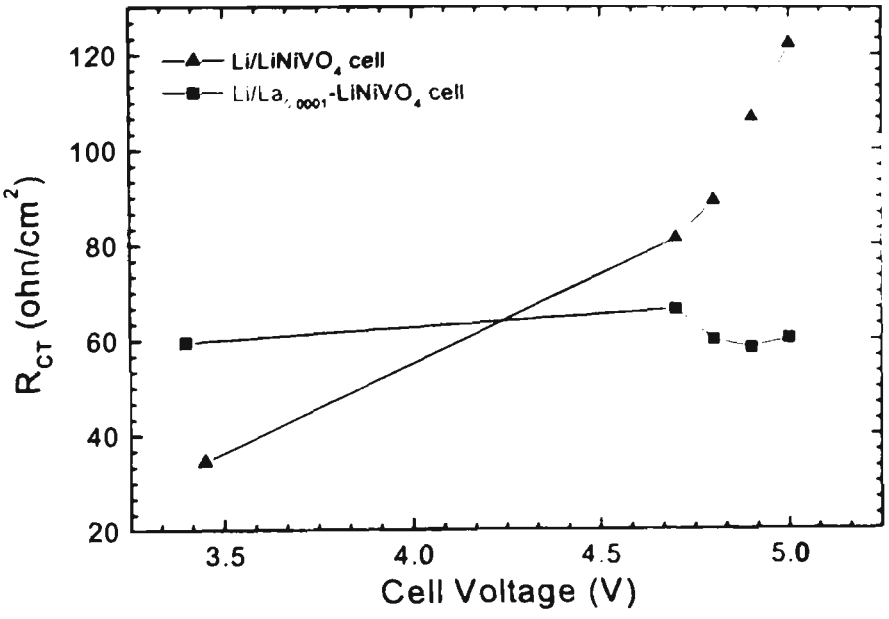

Fig. 4-32 The Charge transfer resistances (R_{CT}) as a function of cell voltage.

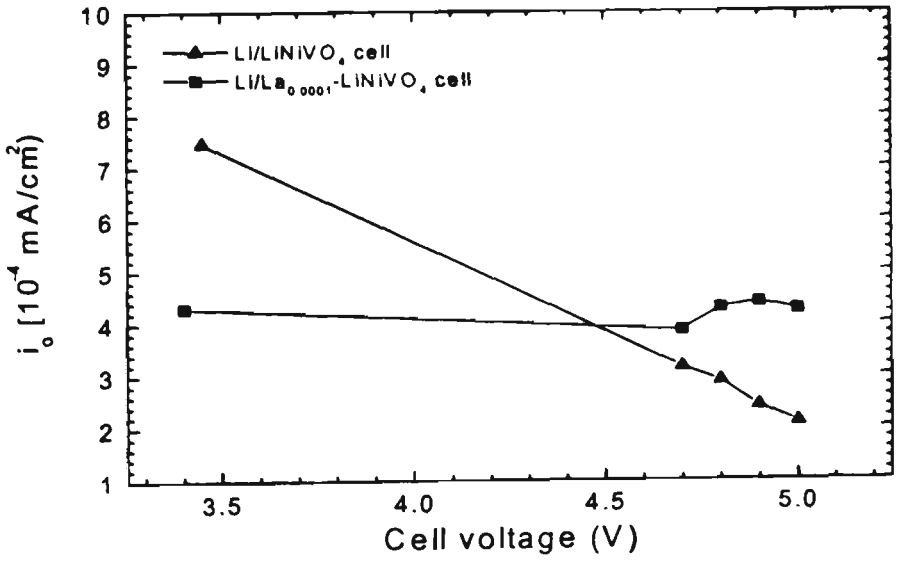

Fig. 4-33 The exchange current density (i_o) as a function of cell voltage.

Semicircles were observed for both pure $LiNiVO_4$ and $La_{0.0001}$-$LiNiVO_4$ electrodes. In the low frequency range (a few Hz to 0.1Hz), a straight line inclined to the real axis at 45° corresponding to the Warburg impedance indicates the diffusion-controlled process in the solid electrodes. Fig. 4-32 shows the charge-transfer resistance(R_{CT}) for $LiNiVO_4$ and the $La_{0.0001}$-$LiNiVO_4$ electrode at different voltages. The values of R_{CT} for pure $LiNiVO_4$ increased with the charge state greatly, which means that the electron transfer process becomes more difficult at the high voltage. However, R_{CT} for doped $La_{0.0001}$-$LiNiVO_4$ did not change obviously. Correspondingly, the exchange current densities for pure $LiNiVO_4$ decreased with the increase of the voltage, but there was almost no variation for doped $La_{0.0001}$-$LiNiVO_4$ (see Fig. 4-33). At present, the mechanism accounting for these observations is not understood.

When used as a cathode in a lithium cell, the inverse spinel $LiNiVO_4$ delivered a high voltage of 4.8V. There are two discharge plateaus at 4.75V-4.5V and 4.25V-3.9V respectively. Lanthanum doping can improve the capacity of the $LiNiVO_4$ electrode slightly. The rechargeabilities of doped and pure $LiNiVO_4$ electrodes are poor. Further work needs to be done to improve the practical capacity and cyclability of $LiNiVO_4$. The high voltage material $LiNiVO_4$ provides a challenge for chemists to identify a new electrolyte with oxidation resistance above 5V.

4.7 Summary

The physical, structural and electrochemical properties of $LiMn_2O_4$, some doped $LiM_xMn_{2-x}O_4$ and doped $LiM_xMn_{2-2x}O_4$ spinels have been investigated. In general, $LiMn_2O_4$ or its doped derivatives can deliver an average discharge capacity of approximate

120 mAh/g. There are two main mechanisms which are considered to be responsible for the capacity fading of the spinel electrode. One is the Jahn-Teller distortion effect, which damages the structure of the active material particles. Another is the dissolution of Mn into the electrolyte solution. Low valence cation doping can effectively combat the above two factors by suppressing the Jahn-Teller effect. Some cations such as Cr^{3+} and Co^{3+} have higher binding energy for the M-O bond than that of the Mn-O bond. Therefore, Cr^{3+} and Co^{3+} doping can enhance the stability of the spinel structure by preventing the dissolution of Mn. Doped spinel electrodes demonstrated satisfied cycle life for Li-ion cells. Some lithium manganese oxides such as $Li_2Mn_4O_9$ and $Li_4Mn_5O_{12}$ have a low potential versus lithium. Therefore, they can be coupled with high potential $LiMn_2O_4$ spinel to construct a lithium-ion cell with a voltage of around 1.2 V. Such lithium-ion cell can use aqueous electrolyte. Rechargeable lithium-ion cells with lithium manganese oxide as cathode and anode has been successfully demonstrated. The high potential cathode material-$LiNiVO_4$ inverse spinel also has been investigated.

Chapter 5 A Study of Layered $LiMO_2$ (M=Ni, Co and Al) Compounds and Orthorhombic $LiMnO_2$ As Cathode Materials

5.1 Introduction

Layered $LiCoO_2$ compounds are currently used as cathode materials in commercial lithium-ion batteries. The $LiCoO_2$ cathodes provide excellent electrochemical performance for Li-ion batteries due to their long cycle life and moderate capacity of about 140 mAh/g. But $LiCoO_2$ compounds suffer several disadvantages because of their high cost, toxicity and associated impact on the environment. This prevents $LiCoO_2$ cathode materials from being used in any application in large scale lithium-ion batteries. The search for alternatives for $LiCoO_2$ is being pursued worldwide. The $LiNiO_2$, doped compounds $LiM_xNi_{1-x}O_2$ and $LiNi_xCo_yO_2$ are alternative cathode materials for lithium-ion batteries. Furthermore, the orthorhombic $LiMnO_2$ has also shown some promise as a cathode material. The electrochemical performance of these cathode materials is strongly dependent on their physical and chemical properties such as stoichiometry, microstructure and morphology etc.. The structural and electrochemical properties of these compounds will be presented and discussed in this chapter.

5.2. Synthesis of $LiNiO_2$ Compounds as Cathodes for Lithium-ion Batteries

$LiNiO_2$ is an attractive cathode candidate because of the relatively abundant natural resources of nickel and the compound is environmentally benign. However, it is difficult to synthesise the stoichiometric $LiNiO_2$ with satisfactory electrochemical performance [167]. The electrochemical properties of $LiNiO_2$ are strongly dependent on the stoichiometry, crystal structure and cation disorder [34, 38, 40]].

In view of the potential importance of $LiNiO_2$ as a cathode material for lithium ion batteries, it is valuable to optimise the synthesis conditions. The $LiNiO_2$ compounds

were synthesized under various conditions and their electrochemical properties were examined. The thermal behaviour of $LiNiO_2$ compound was identified via DTA/TG analysis. The kinetic parameters of lithium nickelate electrodes were characterised by a.c. impedance spectroscopy .

5.2.1 Synthesis, XRD data and DTA/TG of $LiNiO_2$ compounds

The $LiNiO_2$ compounds were synthesised via a solid state reaction of precursors of $LiOH.H_2O$ and NiO with the molar ratio of Li:Ni from 1:1 - 1:1.14. The reactants were thoroughly mixed by ballmilling and then pressed into pellets. The pellets were fired at different temperatures from 650°C to 750°C in air or oxygen for 20~48 hours.

The stoichiometric $LiNiO_2$ compound belongs to the rhombohedral system(SG:$R\bar{3}m$) in which Li^+ and Ni^+ ions occupy the octahedral 3a and 3b sites respectively of fcc packing. This structure provides a two-dimensional channel for lithium ions intercalation and de-intercalation. The hexagonal parameters are a=2.8806 Å and c=14.2050 Å [34]. Table 5-1 shows the synthesis conditions and structural parameters of samples A to H of the $LiNiO_2$ compounds prepared. The $LiNiO_2$ compounds synthesised at 650°C or 700°C in air (sample A and B) contained impurity phases of Li_2O and NiO. The mechanism of the reaction is via solid-state diffusion. The reactants were not thoroughly reacted at these lower temperatures. The impurity phase of Li_2O was also detected in sample H. The Li_2O impurity contained in the $LiNiO_2$ compound could be leached by dissolved it in water, but this process affects the electrochemical performance of $LiNiO_2$ compounds adversely due to chemical delithiation through the cation exchange reaction [167]:

$$LiNiO_2 + xH_2O \rightarrow Li_{1-x}H_xNiO_2 + xLiOH \qquad (5.1)$$

Consequently, the samples A, B, and H were eliminated from further electrochemical tests.

Table 5-1 Synthesis conditions and structural parameters of $LiNiO_2$ Compounds

$LiNiO_2$ samples	The molar ratio of Li:Ni in precursors	Calcination temperature (°C)	Atmos-phere	Lattice constants (Hexagonal)		Impurity phase	Bragg ratio $R_{(003)}=I_{(003)}/I_{(104)}$
A	1:1	650	air			Li_2O, NiO	
B	1:1	700	air			Li_2O, NiO	
C	1:1	750	air	2.8816	14.211		0.86
D	1:1	750	oxygen	2.8825	14.217		1.05
E	1.05:1	750	oxygen	2.8820	14.185		1.45
F	1.08:1	750	oxygen	2.8780	14.182		1.32
G	1.1:1	750	oxygen	2.8800	14.200		1.14
H	1.14:1	750	oxygen			Li_2O	

Fig. 5-1 shows the typical X-ray diffraction patterns of $LiNiO_2$ compounds synthesised under the different conditions shown in table 5-1. The intensity of peaks (003) and (104) differs for different samples. It has been reported that the Bragg intensity ratio $R_{(003)}=I_{(003)}/I_{(104)}$ can be used as a reliable quantitative criterion for the stoichiometry of $Li_xNi_{1-x}O_2$ compounds [168]. However, it is possible that the texture of the powder could also influence the intensity of the diffraction peak. The XRD samples for the same $LiNiO_2$ compound were prepared in different ways which were chosen to change the texture of the powder particles. The intensities of (003) and (104) peaks were observed to change slightly with the preparation methods of the XRD sample. On the other hand, the exact chemical composition of the $LiNiO_2$ compound is not the main factor determining the electrochemical performance when the Li:Ni ratio is close to the unity. Therefore, for optimum preparation conditions, examination of the electrochemical properties is needed rather than relying on the XRD data.

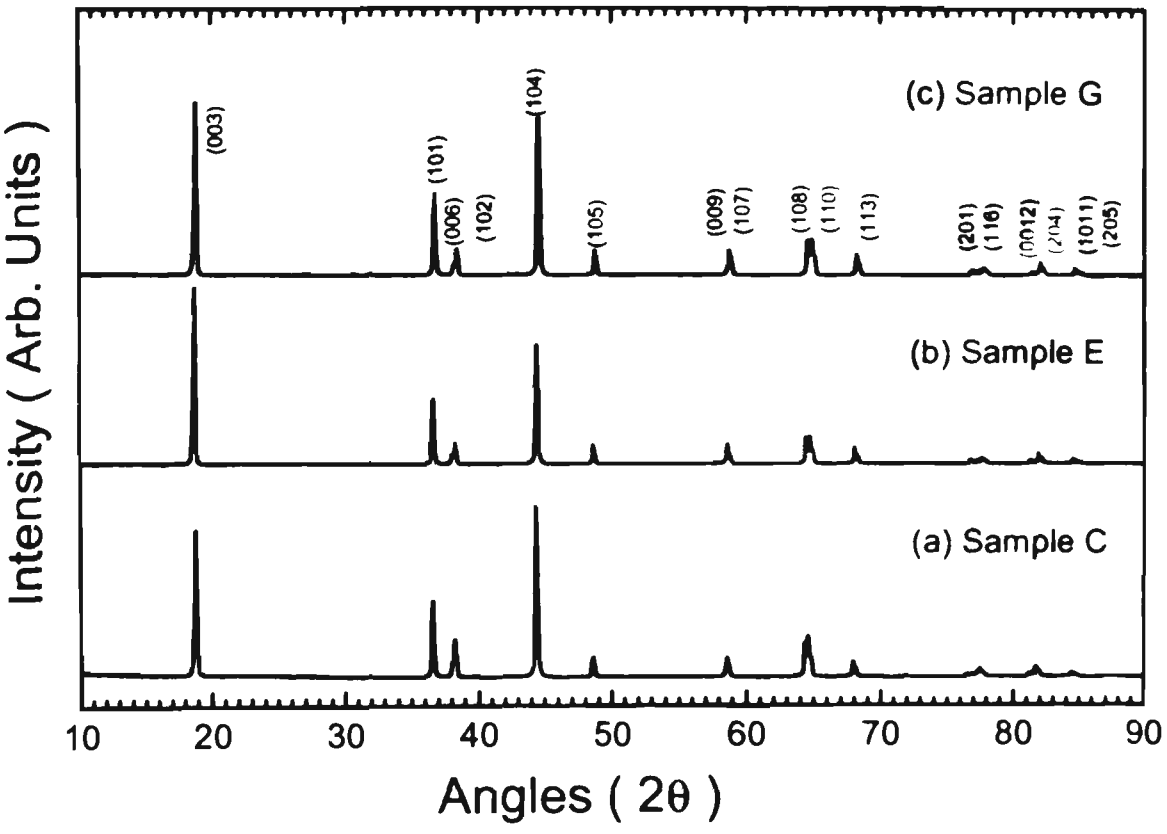

Fig. 5-1 X-ray diffraction patterns of $LiNiO_2$ compounds.
(a) Sample C (b) Sample E (c) Sample G.

The thermal behavior of the $LiNiO_2$ compound was determined by DTA-TG analysis which is shown in Fig. 5-2. There is an endothermic peak on the DTA curve. The onset temperature is at 860°C and the peak ends at 960°C. Within this temperature range, the sample lost weight continuously, which can be assigned to the decomposition of $LiNiO_2$ to $Li_{1-x}Ni_{1+x}O_2$ and oxygen evolution. It is proposed that the decomposition of $LiNiO_2$ could be expressed as:

$$(1+x)\ LiNiO_2 \rightarrow Li_{1-x}Ni_{1+x}O_2 + xLi_2O + x/2O_2 \qquad (5.2)$$

Based on eq (5.2), the decomposition of $LiNiO_2$ at high temperature could be suppressed in an oxygen atmosphere. The excess Li in the precursors could compensate for the loss of the volatile LiOH at high temperature. The decomposition product $Li_{1-x}Ni_{1+x}O_2$ has a disordered cation distribution with Ni ions partially occupying the

lithium sites in the layered structure. The Ni ions in the lithium layers impede the lithium ions diffusion. Thus, the electrochemical properties of a disordered $LiNiO_2$ is very poor. Consequently, the synthesis temperature for $LiNiO_2$ compound should be controlled below 860 °C to avoid any decomposition and oxygen evolution.

The $LiNiO_2$ compound(sample D) was fired at 900°C for 24 hours and then quenched into liquid nitrogen. In this way, the state of $LiNiO_2$ at high temperature was preserved at room temperature. Fig. 5-3 shows the XRD pattern of the quenched $LiNiO_2$ compound which was identified to be the hexagonal $Li_2Ni_8O_{10}$ (JCPDS-23-362). This confirms the equation (2) and that the structure of $LiNiO_2$ was changed during the heat treatment at high temperature.

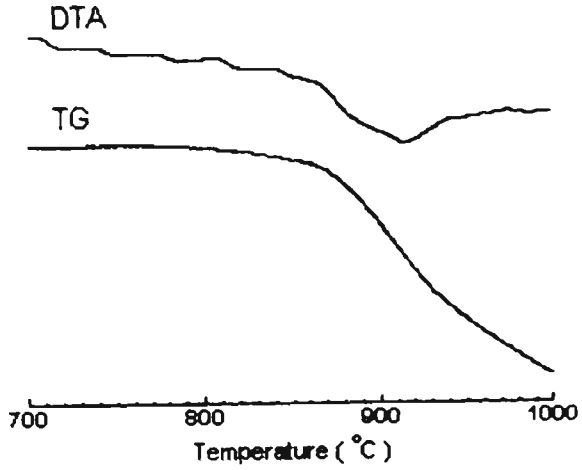

Fig.5-2 DTA/TG curves of $LiNiO_2$ compound.
The scan rate is 10 °C/min.

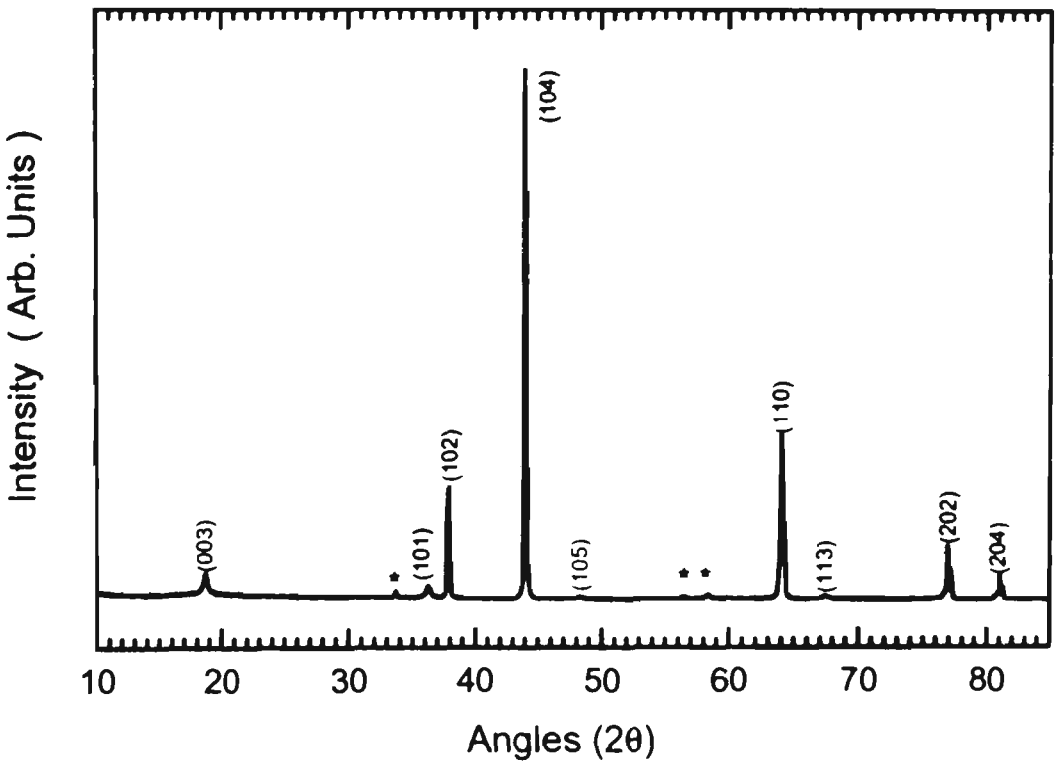

Fig. 5-3 X-ray diffraction pattern of the quenched $LiNiO_2$($Li_2Ni_8O_{10}$).
* Li_2O

5.2.2 Electrochemical characterisation

The charge/discharge tests of Li/$LiNiO_2$ cells were carried out in the voltage range of 3 V to 4.25 V at a constant current density of 0.25 mA/cm^2. Fig. 5-4 shows the cycling profiles of different $LiNiO_2$ samples. Sample E demonstrated the best electrochemical activity. It delivered 214 mAh/g initial charge capacity and 181 mAh/g discharge capacity.

During the first cycle, approximate 32 mAh/g specific capacity is irreversible. After the second cycle, the reversibility of the electrode is quite excellent. After fifty cycles, the electrode still maintained 170 mAh/g specific discharge capacity with a rate of capacity loss of 0.122% per cycle. Sample C which was synthesised in air only delivered the first discharge capacity of 90 mAh/g, which reflected its poor

electrochemical reactivity. Samples F and G also demonstrated satisfactory discharge capacities in the range of 140-160 mAh/g. The average discharge voltage of $LiNiO_2$ electrode for all of the $LiNiO_2$ samples tested was about 3.7~3.8V . The slightly lower operating voltage than that of $LiCoO_2$ and $LiMn_2O_4$ is beneficial for the stability of the organic electrolyte.

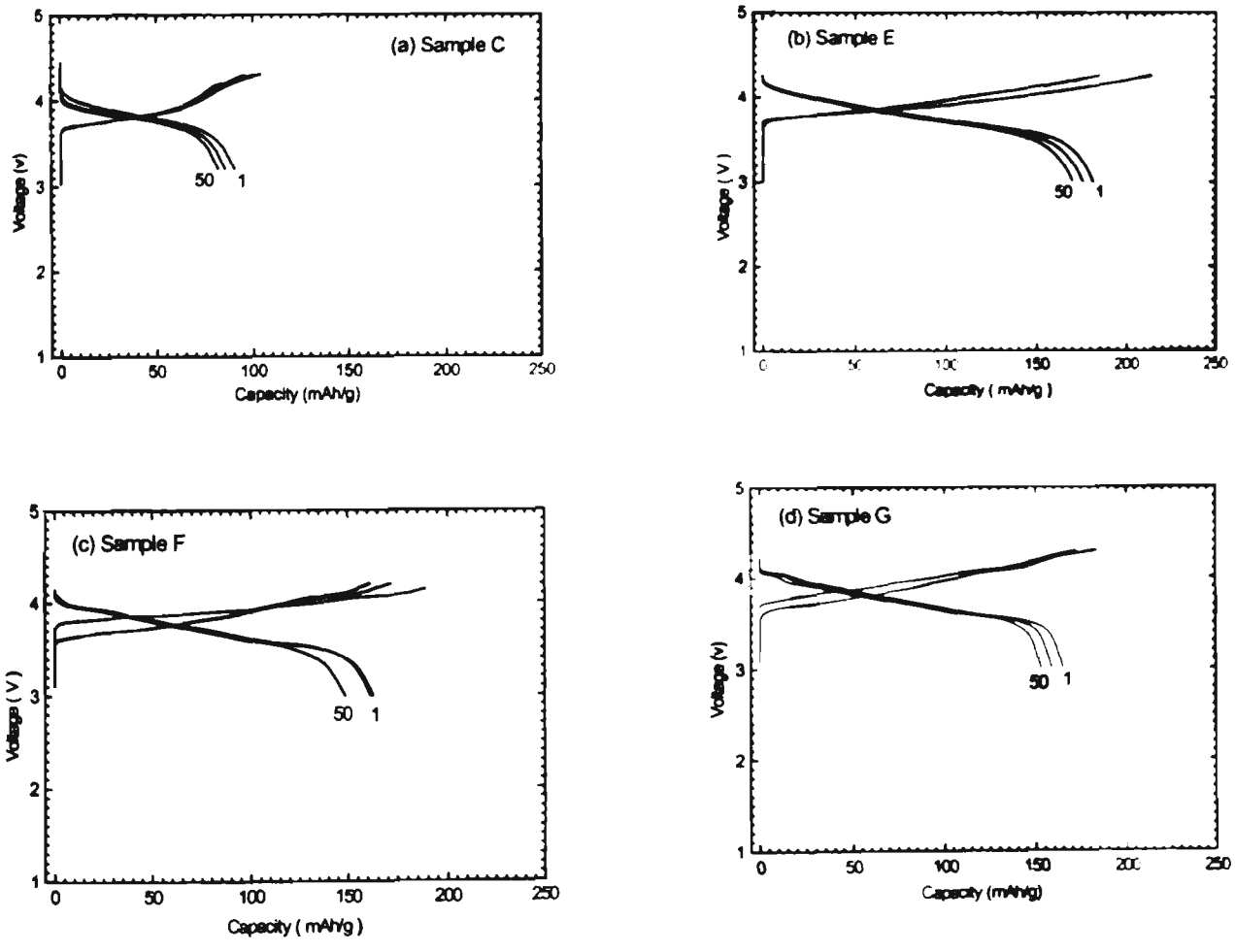

Fig. 5-4 Charge/discharge profiles of the different $LiNiO_2$ electrodes.
(a) Sample C (b) Sample E (c) Sample F (d) Sample G

The electrochemical properties of the quenched $LiNiO_2(Li_2Ni_8O_{10})$ as cathode in the lithium cells were tested. The quenched $LiNiO_2(Li_2Ni_8O_{10})$electrode was found to have no electrochemical reactivity at first. The $Li_2Ni_8O_{10}$/Li cell could be quickly charged to 4.25 V and discharged to 3V in a few minutes. No charge discharge capacity was delivered by this test cell. The $Li_2Ni_8O_{10}$ structure can be written as: $(Li_{2/5}Ni_{3/5})_{3a}(Ni)_{3b}(O_2)_{6c}$ in which Ni ions partially occupy 3a Li ions' sites in the hexagonal array. The Li ions cannot move in such a disordered structure although it is iso-structural with the layered $LiNiO_2$. Further investigation needs to be done to understand this phenomenon.

The results of the cycling test revealed that the $LiNiO_2$ compounds prepared in an oxygen atmosphere can achieve better electrochemical properties than those synthesised in air. This is related to the fact that the $LiNiO_2$ tends to decompose at high temperature due to Ni^{3+} being reduced to Ni^{2+} at lower partial oxygen pressure. Oxygen can suppress the decomposition of $LiNiO_2$ and prevent structural disorder.

The lithium insertion into and extraction from $LiNiO_2$ compound is already known to be a reversible topotatic reaction:

$$LiNiO_2 \leftrightarrow Li_{1-x}NiO_2 + xLi + xe^- \qquad (5.3)$$

The kinetic parameters of the $LiNiO_2$ electrodes in lithium cells have been determined by a.c. impedance spectroscopy. Fig. 5-5 shows the typical complex impedance diagrams(Nyquist plots) for $LiNiO_2$ compounds synthesised under different conditions. The semicircles were obtained, from which the ohmic resistance(R_0), double-layer capacitance and charge transfer resistance(R_{CT}) were calculated. The end of the semicircle is distorted because of the overlap of the charge-transfer and diffusion processes.

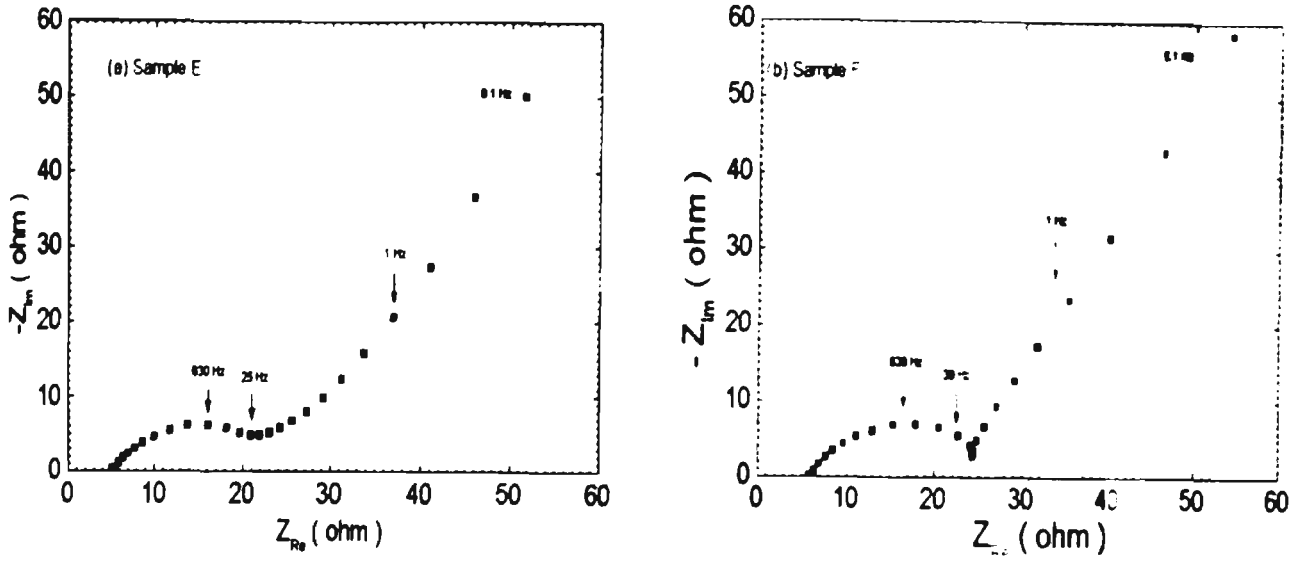

Fig. 5-5 A.c. impedance spectroscopy of $LiNiO_2$ electrodes.

Table 5-2 The Kinetic Parameters of $LiNiO_2$ electrodes in lithium cells

$LiNiO_2$ samples	Ohmic resistance(Ω)	Charge-transfer resistance(Ω)	Double layer capacitance(μF)	Exchange current density(I_0) (A/cm^2)
C	5.04	45.41	5.5	0.72×10^{-3}
D	5.56	24.5	10.3	1.34×10^{-3}
E	5.28	21.65	11.6	1.52×10^{-3}
F	6.55	19.03	13.2	1.73×10^{-3}
G	10.65	21.48	11.7	1.53×10^{-3}

Table 5-2 shows the kinetic parameters of the different $LiNiO_2$ electrodes. The $LiNiO_2$ compound synthesised in the air had a high charge-transfer resistance (R_{CT}) which is not favourable for cell operation. The exchange current densities (I_0) deduced from the charge-transfer resistances(R_{CT}) were around $0.7\sim1.7\times10^{-3}$ A/cm^2 for the $LiNiO_2$ compounds prepared under the different conditions. These values are consistent with those for the lithium insertion compounds previously reported [169, 171].

In summary, the $LiNiO_2$ compound synthesised at 750°C in oxygen with excess Li (Li:Ni=1.05) was found to be an optimum preparation condition in this research. A cathode prepared from this compound could deliver approximately 180 mAh/g discharge capacity with good reversibility. However, this by no means represents the most appropriate synthesis condition for $LiNiO_2$ compounds. The thermogravimetric analysis revealed that the $LiNiO_2$ compound could decompose to $Li_{1-x}Ni_{1-x}O_2$ with poor electrochemical reactivity. The kinetic parameters of the $LiNiO_2$ electrode were characterised by a.c. impedance. The $LiNiO_2$ compound synthesised in the air had a high charge-transfer resistance(R_{CT}) and low exchange current density.

5.3 $LiAl_\delta Ni_{1-\delta}O_2$ Solid Solutions As Cathode Materials for Rechargeable Lithium Batteries

$LiNiO_2$ is one of the most promising cathodic materials for rechargeable lithium batteries [171. The lithium ion intercalation into and de-intercalation from $LiNiO_2$ are already known to consist of three single-phase reactions for $0<x<0.75$ and a two-phase reaction for $0.75<x<1$ in the compound $Li_{1-x}NiO_2$. The rechargeability in the two-phase region for $LiNiO_2$ is not good due to the shrinkage of the unit cell associated with the formation of nickel dioxide [49, 173]. It is necessary therefore to set the charge-end voltage below 4.2V to prevent overcharge. By partially substituting Al^{3+} for Ni^{3+} in $LiNiO_2$, the number of lithium ions which may be extracted from $LiNiO_2$ is expected to be limited, because Al only has one valence of +3. Thus, the structural integrity of the electrode could be maintained to extend the cycle life of the electrode. On the other hand, the fully charged $LiNiO_2$ (nickel dioxide) is unstable in organic electrolyte. This could lead to thermal run-away due to the exothermic oxidation reaction of the

electrolyte. The Al^{3+} dopant effect could also prevent the overcharge of the electrode and help to eliminate the safety concern regarding the cell operation. Ohzuku et al [55] have investigated the structural changes of $LiAl_{1/4}Ni_{3/4}O_2$ during charge and discharge processes via ex-situ x-ray diffraction. A single hexagonal phase was preserved over the entire range for $Li_xAl_{1/4}Ni_{3/4}O_2$, which is beneficial for long cycle life of the electrode.

The synthesis and electrochemical characteristics of $LiAl_\delta Ni_{1-\delta}O_2$ solutions are reported in the following sections, which concentrate on the electrochemical properties of $LiAl_\delta Ni_{1-\delta}O_2$ in lithium cells. The kinetic parameters of $LiAl_\delta Ni_{1-\delta}O_2$ as cathodes in lithium cells were determined by a.c. impedance spectroscopy and the galvanostatic intermittent titration (GITT) technique.

5.3.1 Synthesis and Structural Analysis of $LiAl_\delta Ni_{1-\delta}O_2$ Solid Solutions

$LiAl_\delta Ni_{1-\delta}O_2$ (σ=0, 0.1, 0.2, 0.25) solid solutions were synthesised by heating $LiOH.H_2O$, NiO, and Al powder at 750°C under an oxygen stream for 24-40 hours.

$LiAlO_2$ is isostructural with $LiNiO_2$. It should be possible to substitute Al^{3+} for Ni^{3+} in the $LiNiO_2$ structure and retain solid solutions [54]. $LiOH.H_2O$, NiO and Al powders were heated at 750°C under an oxygen stream. Single phase $LiAl_\delta Ni_{1-\delta}O_2$ solid solutions were obtained. Fig. 5-6 shows the X-ray diffraction patterns of the $LiAl_\delta Ni_{1-\delta}O_2$ compounds. No impurity phase was detected by X-ray diffraction. As the aluminium content increases, (006)(102) and (108)(110) peaks were observed in Fig. 5-6 to split clearly. All of the diffraction peaks become broadened with the increase of doped Al^{3+} ions, which suggests a microscopic strain in the unit cell structure due to mismatch of Al^{3+} and Ni^{3+} ions. Fig. 5-7 gives the structural parameters of $LiAl_\delta Ni_{1-\delta}O_2$. The lattice constants change slightly with increasing fraction of Al^{3+} ions. The a-axis shrinks and c-

axis enlarges. From the XRD characterisation, we know that the layered hexagonal structure was retained for all $LiAl_\delta Ni_{1-\delta}O_2$ solid solutions in the range of $\delta \leq 0.25$. Therefore, lithium intercalation and de-intercalation in $LiAl_\delta Ni_{1-\delta}O_2$ should take place in the same way as it does in undoped $LiNiO_2$.

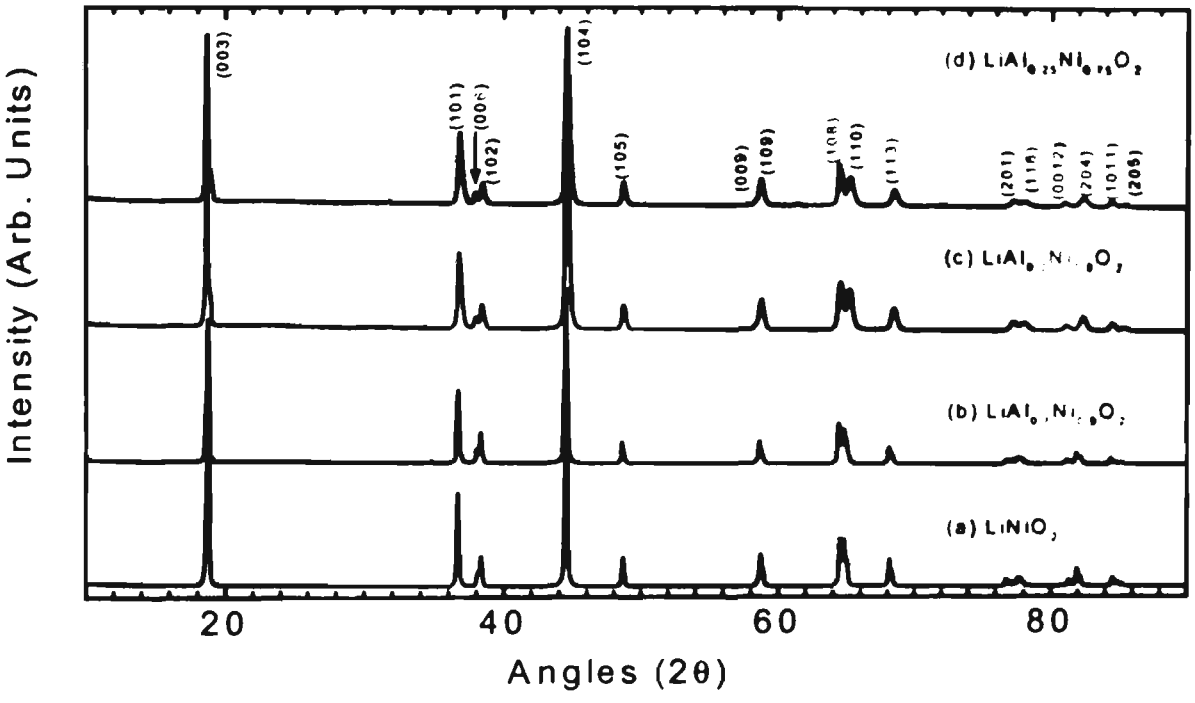

Fig. 5-6 X-ray diffraction patterns of $LiAl_\delta Ni_{1-\delta}O_2$ solid solutions.

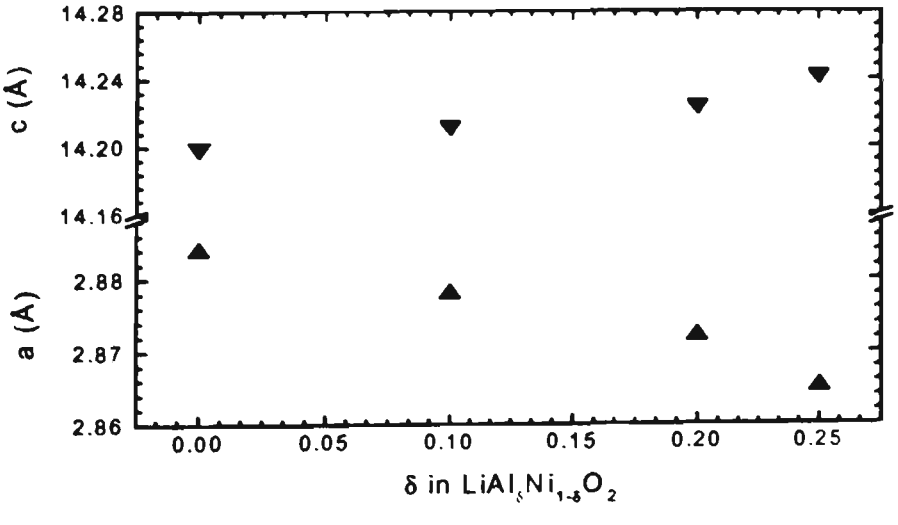

Fig. 5-7 Structural parameters of $LiAl_\delta Ni_{1-\delta}O_2$ solid solutions. Lattice constants a and c were calculated via a Rietvelt program

5.3.2 Electrochemical Characterization

Fig. 5-8 shows the variation of the OCVs vs. lithium compositions x of the Li/$Li_xAl_\delta Ni_{1-\delta}O_2$ cells (δ=0, 0.1, 0.2, 0.25). The OCV curve of the Li/$LiNiO_2$ cell is also shown for comparison. The Al doped $LiAl_\delta Ni_{1-\delta}O_2$ electrode demonstrated lower voltage than the $LiNiO_2$ electrode at the same composition x. In the cut-off range of 3.4V to 4.6V, the maximum amount of lithium which could be extracted from $LiAl_\delta Ni_{1-\delta}O_2$ electrodes is about Δx=0.8. At higher voltages than 4.5 V, the electrolyte could be oxidised and consume part of the charge current. In that case, the value of x cannot be calculated correctly. No big differences of OCV curves were observed for any of the doped $LiAl_\delta Ni_{1-\delta}O_2$ electrodes.

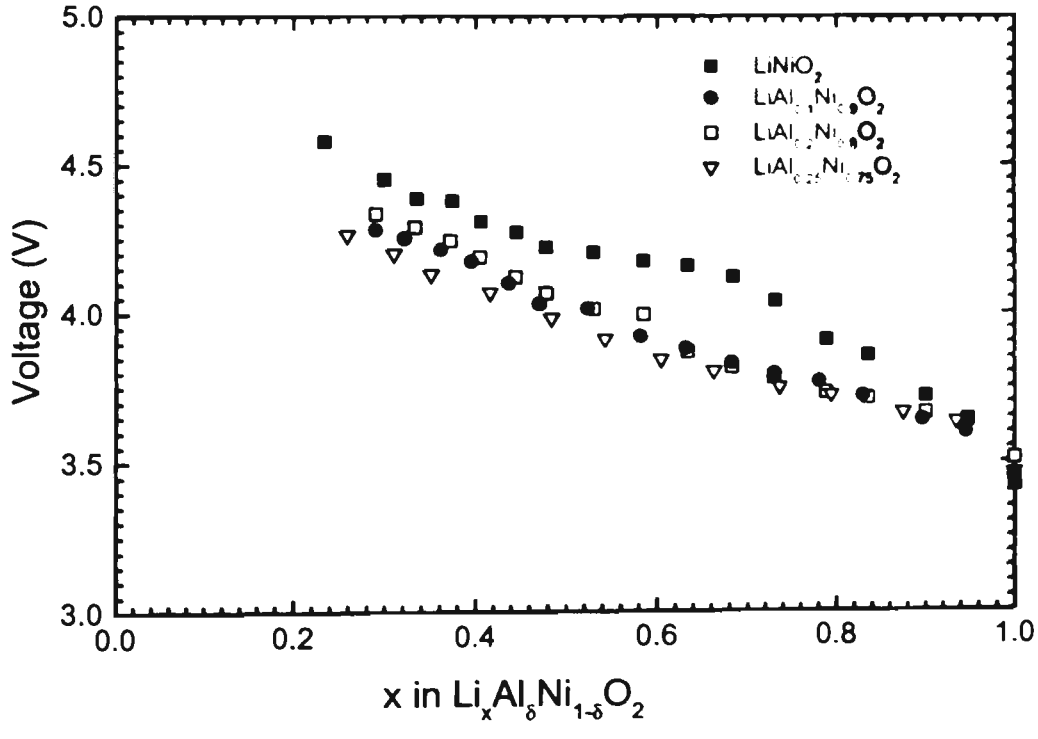

Fig. 5-8 Open-circuit potentials versus lithium compositions x of Li / $Li_xAl_\delta Ni_{1-\delta}O_2$ cells (δ = 0, 0.1, 0.2 and 0.25).

The cycling behavior of the Li/ $LiAl_\delta Ni_{1-\delta}O_2$ cells were tested at a constant current density of 0.25 mA/cm^2 between 3V to 4.3V. The charge discharge profiles are shown in Fig. 5.9. The open-circuit voltages of freshly assembled cells were in the range of 3.3 to 3.45 V. The Al doped $LiAl_\delta Ni_{1-\delta}O_2$ electrodes demonstrated almost the same cycling behaviour as the $LiNiO_2$ electrode. During charge, the voltage increased to 3.75 V rapidly and then rose steadily to 4.3 V; In the discharge process, the voltage decreased to 4.1 V quickly and then declined to 3.5 V gradually. The Al dopant effect influences the capacities of the electrodes between 3 V to 4.3 V. Both the initial charge and discharge capacities decreased with the increase of dopant Al^{3+} ions. However, the rechargeability was improved for doped $LiAl_\delta Ni_{1-\delta}O_2$ electrodes in the voltage range of 3 V to 4.3 V. This could be because the Al dopant effect prevents Li^+ ion extraction in the voltage range of 4.1V to 4.3V to avoid the two-phase region for $0.75<x<1$ in $Li_{1-x}Al_\delta Ni_{1-\delta}O_2$. During the first charge/discharge, approximate 40-50 mAh/g capacity is irreversible for all of the electrodes. It is suggested that the topotactic reaction for $LiAl_\delta Ni_{1-\delta}O_2$ in lithium cell proceeds as:

$$[Li]_{3a}[Al_\delta Ni_{1-\delta}]_{3b}[O_2]_{6c} \rightleftharpoons [Li_{1-x}]_{3a}[Al_\delta Ni_{1-\delta}]_{3b}[O_2]_{6c} + xLi^+ + xe^- \qquad (5.4)$$

The fully charged state of $LiAl_\delta Ni_{1-\delta}O_2$ is $Li_xAl_\delta Ni_{1-\delta}O_2$, in which Al^{3+} and Ni^{4+} are $3S^0$ and it is an electronic insulator. Li ions cannot be further electrochemically extracted from the structure because no electrons can be removed from either Al^{3+} or Ni^{4+}. Residual Li^+ and Al^{3+} are helpful to suppress the dimensional change of the interlayer distance due to the extraction of Li ions. This effect also contributes to keep the structural integrity of the electrode on cycling.

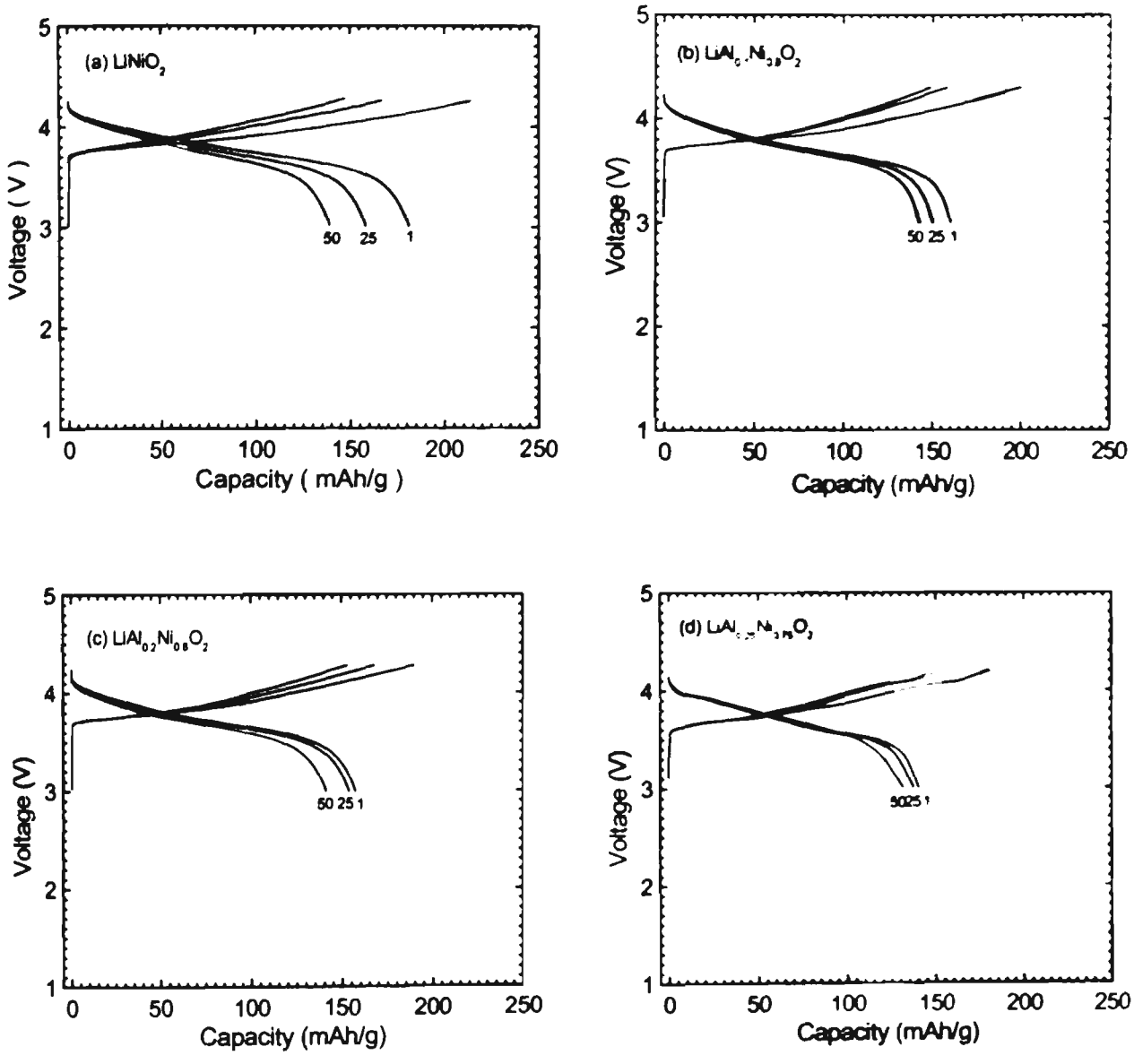

Fig. 5-9 The cycling profiles of Li/ $LiAl_{\delta}Ni_{1-\delta}O_2$ cells.
Current density: 0.25 mA/cm^2; voltage range: 3 V-4.3 V.

The kinetic parameters of reaction (1) can be determined by a.c. impedance spectroscopy(EIS). One question which arises is whether the Al^{3+} dopant effect influences the kinetic process of lithium intercalation and de-intercalation. The impedance spectra were reported as Nyquist plots through which charge-transfer

resistance (R_{CT}), and exchange current density (i_0=RT/nFR_{CT}). the lithium diffusion coefficient D_{Li} in the solid electrode may be obtained via the analysis of Warburg's impedance.

$$D_{Li} = \frac{1}{2}\left[\frac{Vm}{FSA} \times \frac{dE}{dx}\right]^2 \qquad (5.5)$$

where V_m is the molar volume; dE/dx is the slope of OCV vs. lithium ion concentration x at each x value; A is the Warburg coefficient; S is the apparent geometric area.

The Nyquist plots of pure Li/$LiNiO_2$ and L/$LiAl_{0.25}Ni_{0.75}O_2$ cells are shown in Fig.5-10. Semicircles were observed for both pure $LiNiO_2$ and $LiAl_{0.25}Ni_{0.75}O_2$ electrodes. In the low frequency range (a few Hz to 0.1 Hz), a straight line inclined to the real axis at 45°, which corresponds to the Warburg impedance indicates the diffusion-controlled processes in the solid. Fig. 5-11 compares the charge-transfer resistance (R_{CT}) for pure $LiNiO_2$ and doped $LiAl_{0.25}Ni_{0.75}O_2$ electrodes at different states of charge. The average charge-transfer resistance for pure $LiNiO_2$ is higher than that for doped $LiAl_\delta Ni_{1-\delta}O_2$. The Al^{3+} dopant effect decreases the charge-transfer resistance and accelerates the charge-transfer reaction in the active materials. Such an effect is desirable for battery operation. The charge-transfer resistance was also observed to decrease with the increase of the state of charge (SoCs) for both pure $LiNiO_2$ and doped $LiAl_\delta Ni_{1-\delta}O_2$. This is different from spinel $LiCo_\delta Mn_{2-\delta}O_4$ reported by Arora et al [84], where the charge-transfer resistance was independent of SoCs. The mechanisms for these phenomena are unknown yet. The exchange current densities at different SoCs were calaculated and are shown in Fig. 5-12. Obviously, the exchange current densities of $LiAl_{0.25}Ni_{0.75}O_2$ are higher than that of $LiNiO_2$ at each SoC. The values of i_0 are in the range of 4×10^{-4} to 2.6×10^{-3} A/cm^2, which is similar to that reported by B. Garcia [174] for $LiCoO_2$ electrode.

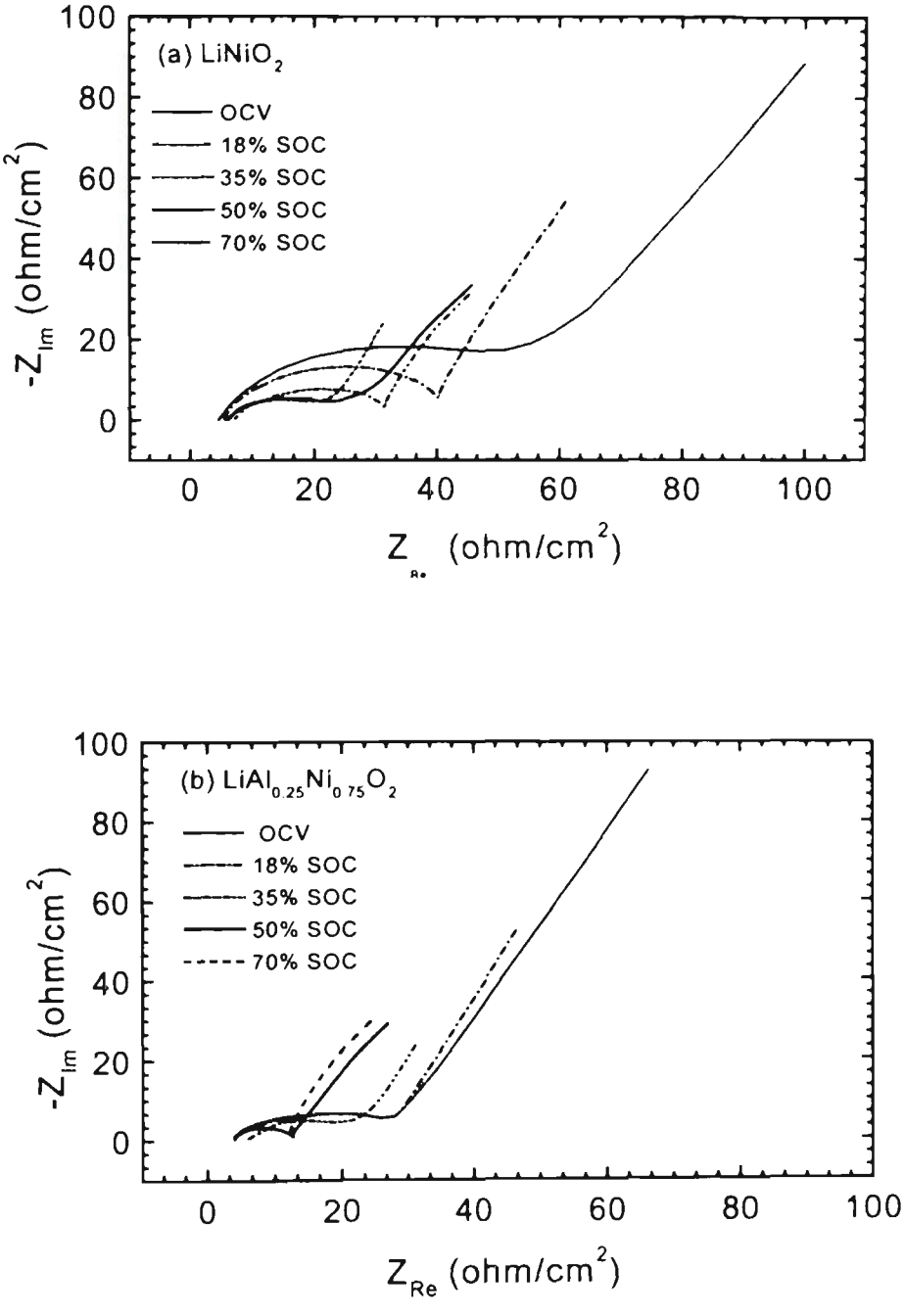

Fig. 5-10 A.c. impedance spectra obtained at different SoCs
(a) $LiNiO_2$ (b) $LiAl_{0.25}Ni_{0.75}O_2$

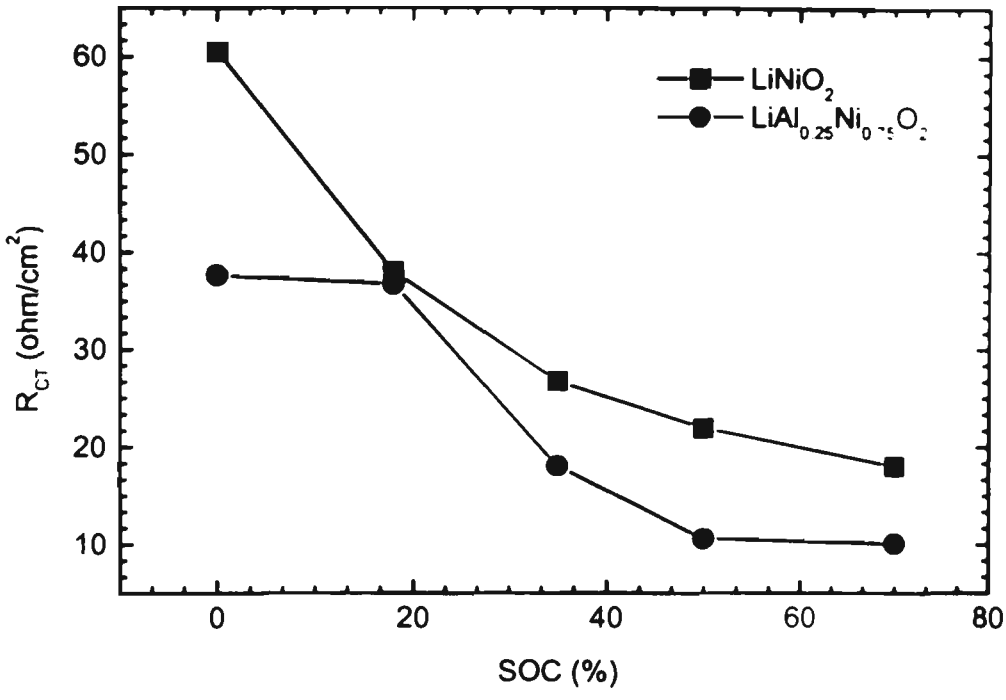

Fig. 5-11 The variation of the charge-transfer resistance (R_{CT}) versus SoC for Li $LiAlNi_{1-x}O_2$ cells

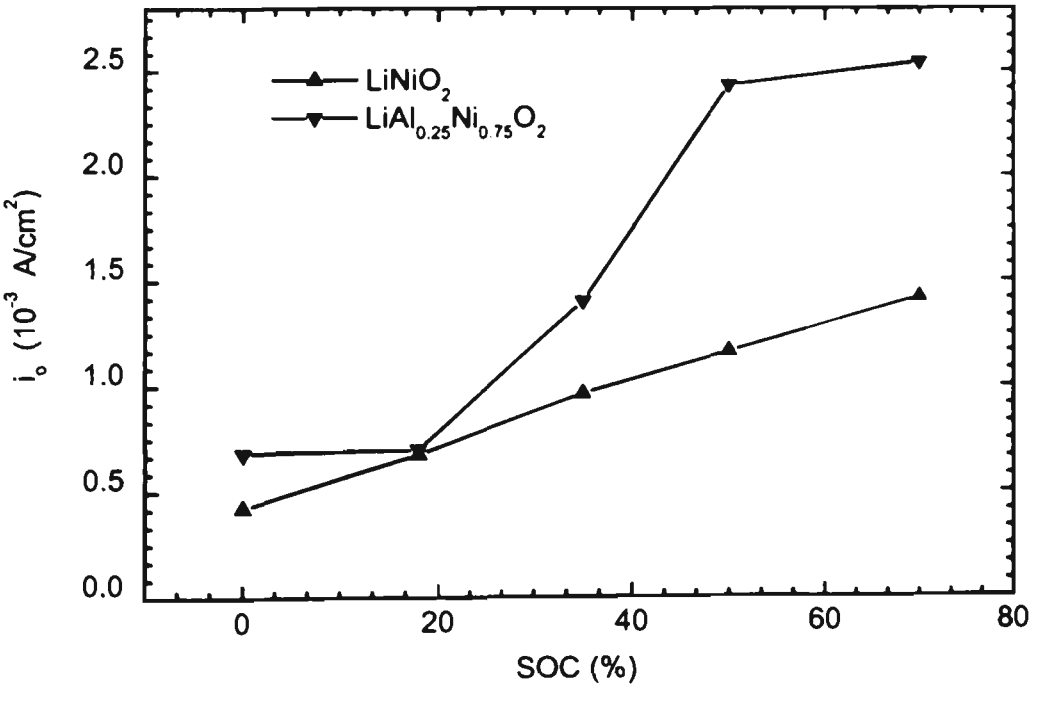

Fig. 5-12 Exchange current densities (i_o) as a function of SoC

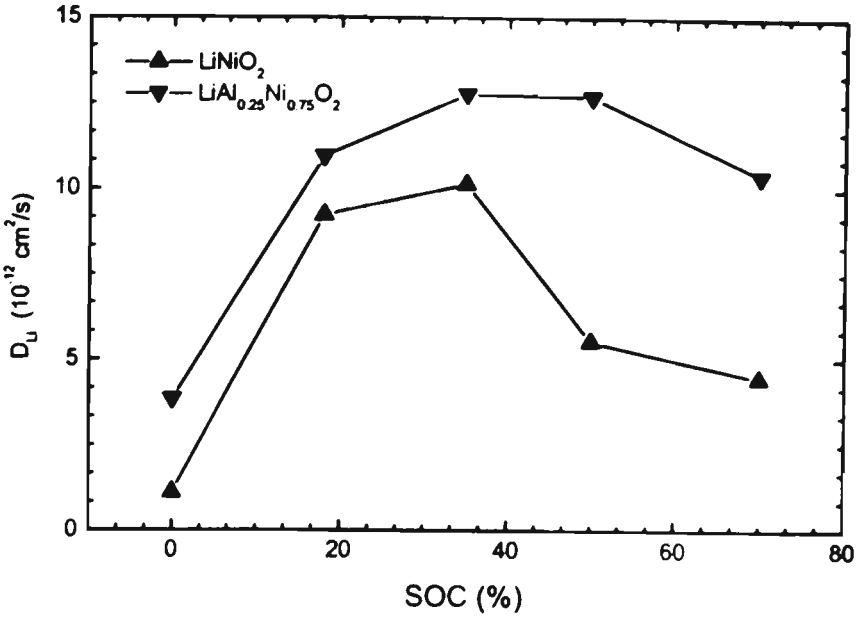

Fig. 5-13 Li-ion diffusion (D_{Li}) as a function of SoC in $LiAl_xNi_{1-x}O2$ electrodes

Li-ion diffusion coefficients were estimated using under semi-infinite boundary diffusion conditions. The Warburg coefficient A could be obtained from the slope of Z_{RE} vs $\omega^{-1/2}$ or Z_{Im} vs $\omega^{-1/2}$. D_{Li} at different SoCs for $LiNiO_2$ and $LiAl_{0.25}Ni_{0.75}O_2$ are shown in Fig. 5-13. The values of D_{Li} for $LiNiO_2$ are lower than those for $LiAl_{0.25}Ni_{0.75}O_2$ at different SoCs indicating that the Al^{3+} dopant effect increases the Li-ion diffusion coefficient in these solid electrodes. During charging, D_{Li} first increased up to about 35% SoC and then decreased at 70% SoC. According to a previous report [175], a second order hexagonal and third order hexagonal phase could form, which could in turn influence D_{Li}. It is possible that the initial increase is due to Li^+ extraction, increasing the interlayer distance to facilitate Li^+ diffusion. After that, second order and third order phase transformations influence D_{Li} inducing a decrease in D_{Li} with the increase of SoC. Being different from layered $LiCoO_2$ and spinel $LiMn_2O_4$, it is difficult to synthesise stoichiometric, ordered $LiNiO_2$ and $LiAl_\delta Ni_{1-\delta}O_2$ compounds in whose

structures there are no Li^+ and Ni^{3+} (Al^{3+}) mixing. Therefore, the transportation process for Li-ion in $LiNiO_2$ or $LiAl_\delta Ni_{1-\delta}O_2$ is more complicated than that in $LiCoO_2$ and $LiMn_2O_4$.

Through systematical electrochemical tests, doped $LiAl_\delta Ni_{1-\delta}O_2$ electrodes demonstrated lower capacity but better rechargeability than the $LiNiO_2$ electrode. The kinetic parameters were determined by a.c. impedance spectroscopy. Al^{3+} dopant effects decreased the charge-transfer resistance and increased the exchange current density as well as the Li-ion diffusion coefficient (D_{Li}), which are favourable changes for battery operation.

5.4 Structural, physical and electrochemical characterization of $LiNi_xCo_{1-x}O_2$ solid solutions

$LiNiO_2$ with the isostructure of $LiCoO_2$ has shown some promise as a cathodic material for lithium ion batteries. $LiNiO_2$ can deliver a higher capacity (170-190mAh/g) than that of $LiCoO_2$ (~140 mAh/g). However, the thermal and electrochemical stability for $LiNiO_2$ is not as good as $LiCoO_2$, resulting in inferior cyclability. Aluminum was chosen to stabilise $LiNiO_2$ and the electrochemical performance of $LiNiO_2$ can be improved by an Al dopant effect. In practical applications, lithium ion batteries have to last for more than one thousand cycles. In this regard, it is still doubtful whether $LiNiO_2$ or $LiAl_xNi_{1-x}O_2$ will replace $LiCoO_2$ as cathode materials.

It might be possible to partially substitute Co with Ni in the $LiCoO_2$ structure and keep the excellent electrochemical performance of $LiCoO_2$. A series of $LiNi_xCo_{1-x}O_2$ solid solution were prepared and their electrochemical properties as cathodes in lithium ion cells were compared.

5.4.1 The preparation, structure and physical characterization of $LiNi_xCo_{1-x}O_2$ solid solution

$LiNi_xCo_{1-x}O_2$ solid solutions (x=0, 0.25, 0.5, 0.75, 1) were prepared by heat-treating the precursors of the reagents $LiOH.H_2O$, NiO, and CoO at 750°C for 24 hours under oxygen flow. Before the heat treatment, the precursors were ball milled to mix for 8 hours and then pressed into pellets. $LiNi_xCo_{1-x}O_2$ powders were characterised by x-ray diffraction.

The x-ray diffraction patterns of the $LiNi_xCo_{1-x}O_2$ solid solutions are presented in Fig. 5-14. No impurity phase was detected by XRD analysis, indicating that Co^{3+} and Ni^{3+} ions are compatible in the layered R3m hexagonal structure and single phase solid solutions were obtained. With the combination of Co^{3+} and Ni^{3+} in the structure, all the diffraction peaks were broader than those of pure $LiCoO_2$ and $LiNiO_2$. This suggests that there is a microscopic stress in the basal plane, probably caused by the mismatch of Co^{3+} and Ni^{3+} ions due to their different ionic radii. For $LiCoO_2$, the (006)(102) and (108)(110) lines split clearly. However, with the addition of Ni^{3+}, these two pairs of lines gradually converge. All the diffraction lines except (003) shift to lower angles with the increasing amount of Ni^{3+} amount. The lattice constants were calculated using a least squares method with 16 diffraction lines. As shown in Fig. 5-15, the lattice constants a_o and c_o increase with increasing Ni^{3+} content.

Thermogravimetric analysis was performed on the $LiNi_xCo_{1-x}O_2$ compounds in dry air. The samples were heated at 4°C/min up to 1000°C. Fig 5-16. Shows the weight losses of the five $LiNi_xCo_{1-x}O_2$ samples. The $LiCoO_2$ is the most stable at high temperature among all of the samples. The thermal stability decreases with increasing Ni content and $LiNiO_2$ demonstrated greater weight loss than the other $LiNi_xCo_{1-x}O_2$ solid solutions.

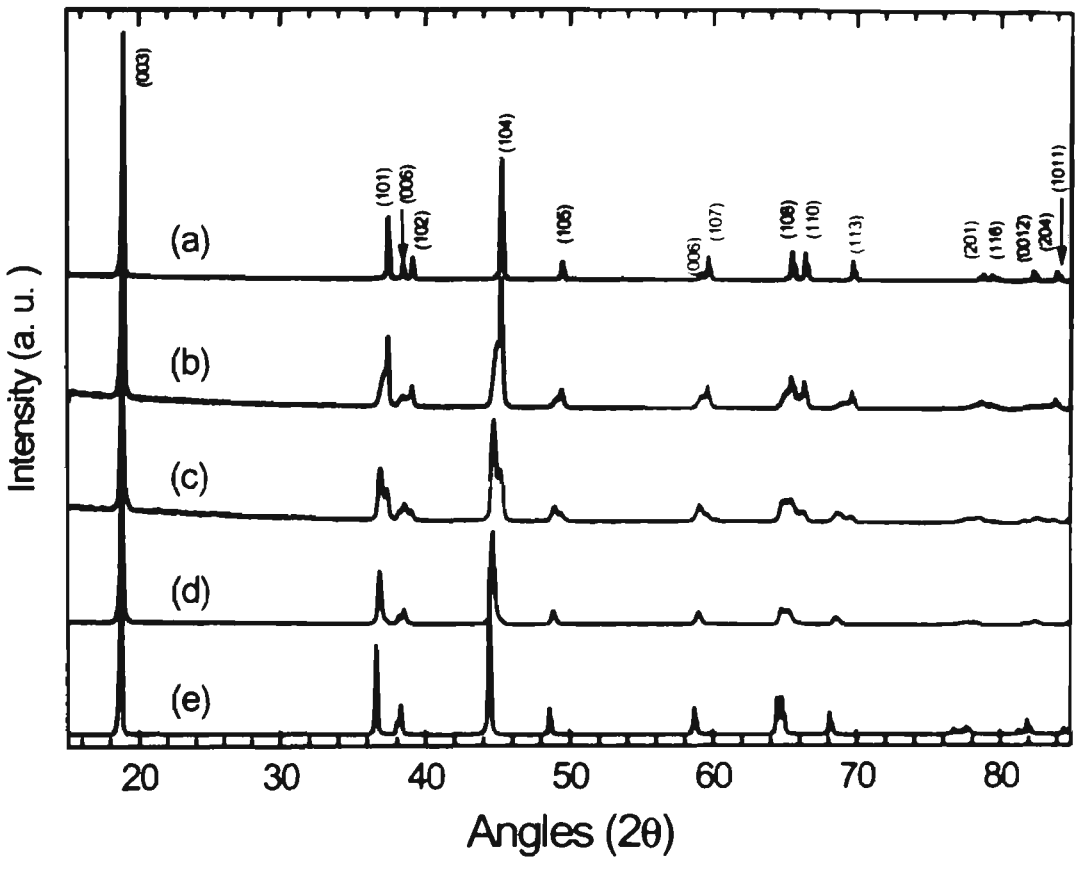

Fig. 5-14. X-ray diffraction patterns of $LiNi_xCo_{1-x}O_2$ solid solutions.
(a) $LiCoO_2$ (b) $LiNi_{0.25}Co_{0.75}O_2$ (c) $LiNi_{0.5}Co_{0.5}O_2$
(d) $LiNi_{0.75}Co_{0.25}O_2$ (e) $LiNiO_2$.

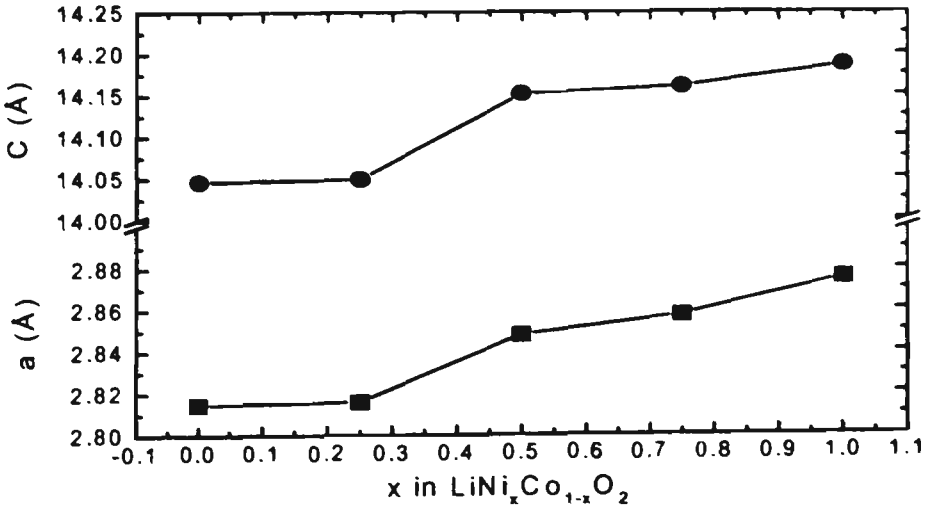

Fig. 5-15 The variation of the lattice constants of a and c in $LiNi_xCo_{1-x}O_2$.

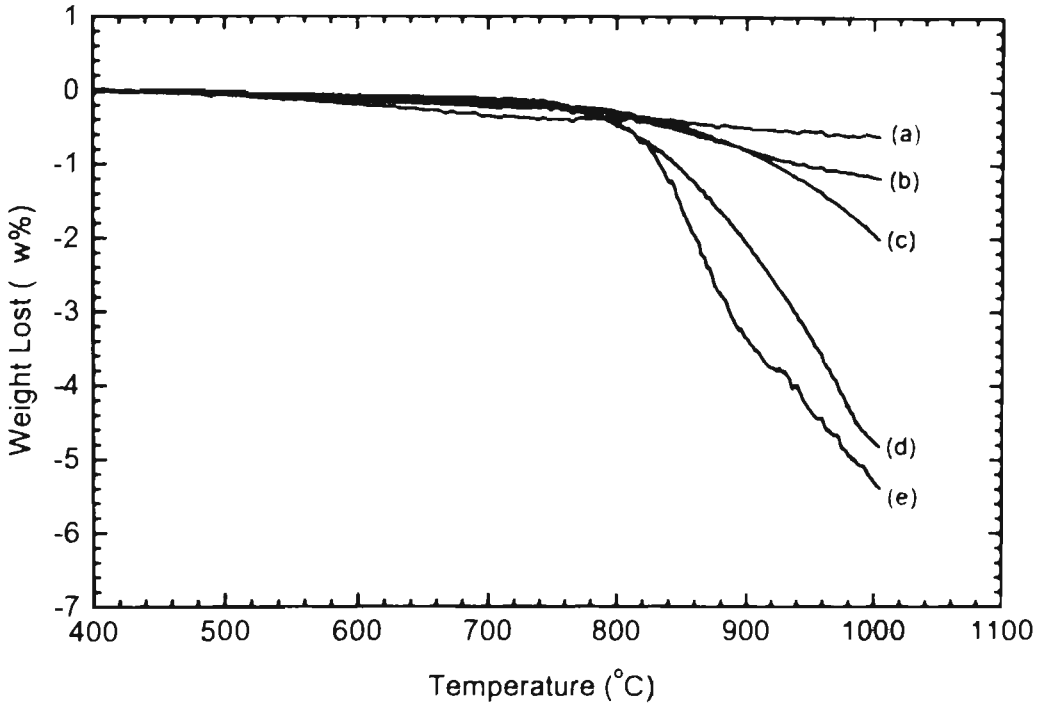

Fig. 5-16. The weight loss vs. temperature for the $LiNi_xCo_{1-x}O_2$ solid solutions. TG was conducted under the dry air at a rate of 10 °C/min from 45°C to 1000°C.
(a) $LiCoO_2$ (b) $LiNi_{0.25}Co_{0.75}O_2$ (c) $LiNi_{0.5}Co_{0.5}O_2$
(d) $LiNi_{0.75}Co_{0.25}O_2$ (e) $LiNiO_2$.

The weight loss of $LiNi_xCo_{1-x}O_2$ compounds at high temperature can be attributed to the extraction of oxygen from the structure as the following reaction:

$$(1+\delta)\ LiNi_xCo_{1-x}O_2 \rightarrow Li_{1-\delta}(Ni_xCo_{1-x})_{1+\delta}O_2 + \delta\ Li_2O + 0.5\delta\ O_2 \qquad (5.6)$$

The deterioration of the thermal stability of $LiNi_xCo_{1-x}O_2$ with the addition of Ni could be associated with the change in binding-energy (E_{BE}) of the M-O bond. The binding-energy data for M-O bond in $LiNi_xCo_{1-x}O_2$ crystal is not available. However, the binding energy can be estimated from relating the thermodynamic functions of MO_2 using the Born-Haber's cyclic process. The binding-energies of CoO_2 and NiO_2 is 1067 and 1029 kJ/mol respectively [83]. Therefore the Co-O bond is stronger than the Ni-O bond. Correspondingly, it is reasonable that the thermal stability of $LiNi_xCo_{1-x}O_2$

deteriorates with the addition of Ni to the structure. Also this is supported by the fact that stoichiometric $LiNiO_2$ is difficult to synthesise.

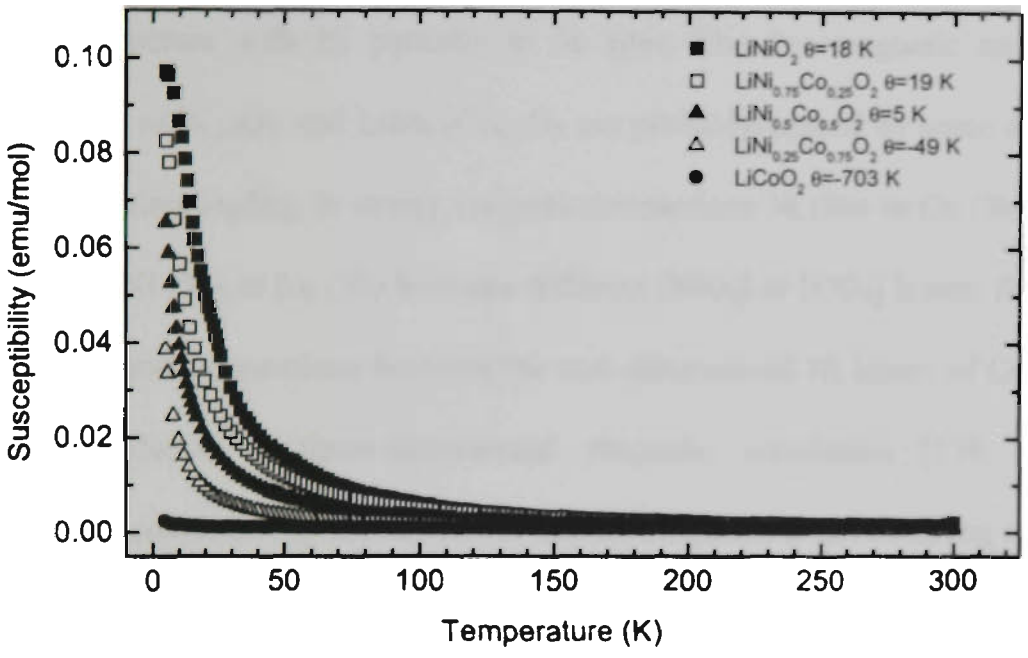

Fig. 5-17 The magnetic susceptibility χ vs. T for $LiNi_xCo_{1-x}O_2$ compounds.

Magnetic susceptibility measurements were performed on $LiNi_xCo_{1-x}O_2$ powders in a DC field of 1000 G using a Quantum Design Magnetometer (PPMS, USA). The temperature-dependence of the magnetic susceptibility of the $LiNi_xCo_{1-x}O_2$ solid solutions is shown in Fig. 5-17. All $LiNi_xCo_{1-x}O_2$ compounds obey the Curie-Weiss law: $\chi=C/(T-\theta)$ at high temperature. $LiCoO_2$ and $LiNi_{0.25}Co_{0.75}O_2$ have a negative paramagnetic Curie constant θ, indicating antiferromagnetic behavior below T_c. However, the compounds $LiNi_{0.5}Co_{0.5}O_2$, $LiNi_{0.75}Co_{0.25}O_2$ and $LiNiO_2$ all have a positive θ, indicating ferromagnetic interactions of the magnetic centers [176, 177]. Both Ni^{3+} ($3d^7$, low spin) and Co^{3+} ($3d^6$, low spin) are magnetic ions. $LiNi_xCo_{1-x}O_2$ solid solutions have a rhombohedral structure R3m in which Li^+, Ni^{3+} or Co^{3+}, and O^{2-} occupy 3a, 3b, and 6c sites respectively. Nonmagnetic Li layers alternate with magnetic

Ni, Co or Ni-Co layers. Therefore, magnetic correlation between Ni ions in $LiNiO_2$, Co ions in $LiCoO_2$ and Ni-Co ions in $LiNi_xCo_{1-x}O_2$ solid solutions are generally considered to be two dimensional. $LiCoO_2$ normally has an ordered structure, whereas $LiNiO_2$ has a disordered structure with Ni partially in 3a sites. The ferromagnetic anomalies for $LiNiO_2$, $LiNi_{0.75}Co_{0.25}O_2$ and $LiNi_{0.5}Co_{0.5}O_2$ are probably caused by some of the Ni or Co ions at 3a sites leading to strong magnetic interactions Ni (3b) or Co (3b)-O-Ni (3a) or Co (3a)-O-Ni (3b) or Co (3b) between different $[NiO_2]$ or $[CO_2]$ layers. Accordingly, three-dimensional connections between the two dimensional Ni layers of Co layers are created, introducing a three-dimensional magnetic correlation [178, 179]. The ferromagnetic susceptibility for $LiNiO_2$ in this investigation is not as strong as described in reference [176], suggesting the sample has a relatively more ordered structure.

5.4.2 Electrochemical Performance of $LiNi_xCo_{1-x}O_2$ as Cathodes in Li-ion Cells.

The $Li/LiNi_xCo_{1-x}O_2$ coin cells were fabricated to examine the electrochemical performance of $LiNi_xCo_{1-x}O_2$ solid solutions as cathodes in the lithium cells. Fig. 5-18 shows the first charge/discharge profiles of five different $Li/LiNi_xCo_{1-x}O_2$ cells. The $LiCoO_2$ electrode delivered an initial discharge capacity of 141 mAh/g. On the other hand, the $LiNiO_2$ electrode reached 181 mAh/g capacity in the first discharge. The first discharge capacities for $LiNi_xCo_{1-x}O_2$ solid solutions were between those of $LiCoO_2$ and $LiNiO_2$. In the first charge, the $LiCoO_2$ was quickly charged to 3.9-4.0 V and then followed a slope up to the cut-off voltage of 4.4 V. During the discharge, The $LiCoO_2$ electrode delivered the discharge capacity mainly in the range of 4.2 - 3.8 V. However, the operating potentials for $LiNi_xCo_{1-x}O_2$ (x=0.25, 0.5, 0.75, 1.0) were between 4.2 to

3.6 V vs. Li/Li^+. It has been observed that all of the $LiNi_xCo_{1-x}O_2$ electrodes were quickly charged to 3.6-3.7 V and then followed a slope up to the cut-off voltage during

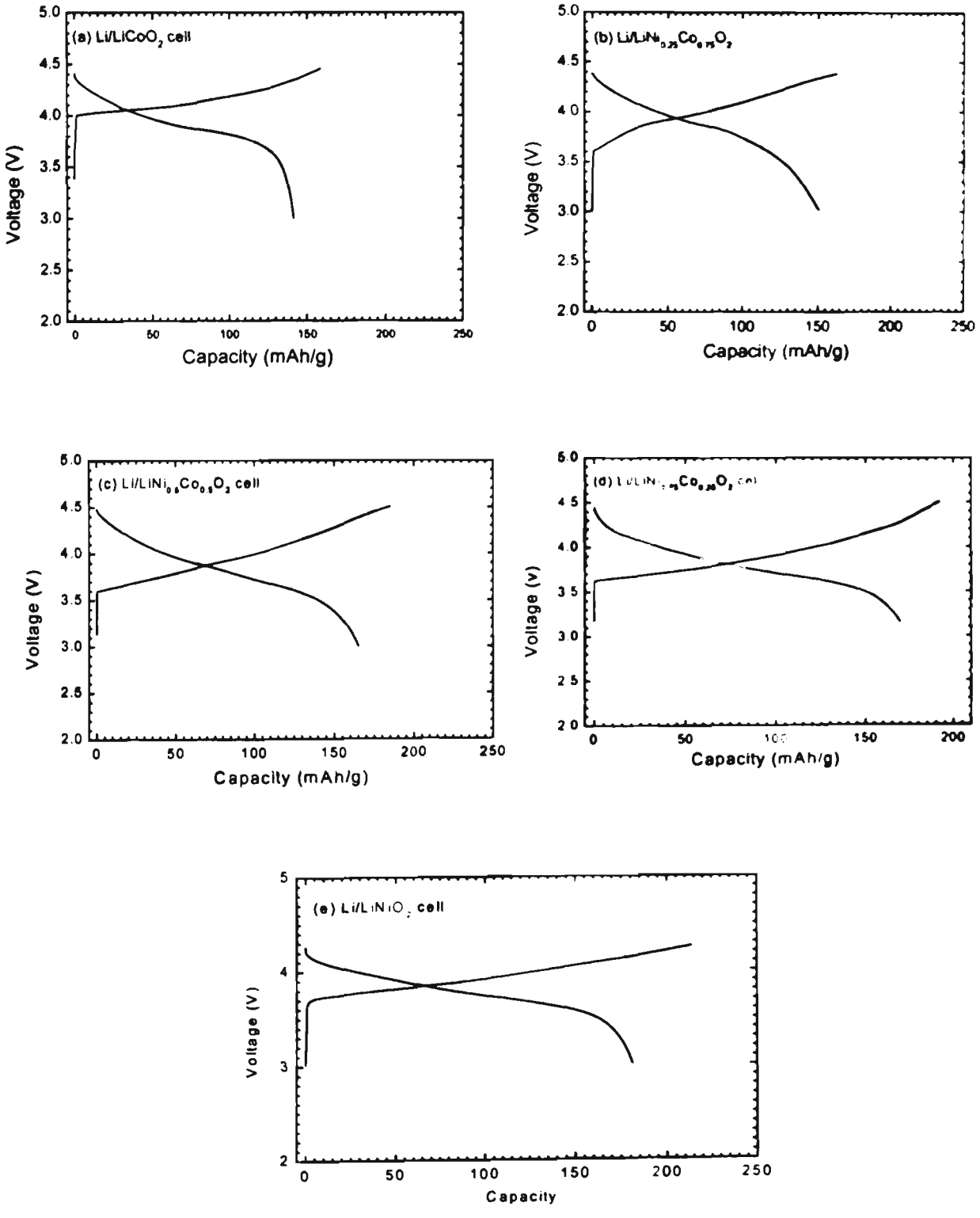

Fig. 5-18 The first charge/discharge profiles of the $Li/LiNi_xCo_{1-x}O_2$ cells.

the first charging process. The same patterns were also observed during the subsequent charge/discharge cycles. Three samples for each composition of $LiNi_xCo_{1-x}O_2$ were tested and the same behavior was found in Fig. 5-18. Therefore, it was concluded that the average charge/discharge potentials of $LiNi_xCo_{1-x}O_2$ electrodes declined as Ni was added into $LiCoO_2$ structure. The operating voltage which is related to the Fermi energy of the electrons in the 3d orbital varies approximately as: MnO_2 ($3d^3/3d^4$) ≥ CoO_2 ($3d^5/3d^6$) > NiO_2 ($3d^6/3d^7$ [51]. The decline of the operating potential for the $LiNi_xCo_{1-x}O_2$ solid solutions means that both Ni and Co participate in the redox reaction during the charge/discharge process. In the first charge/discharge cycle, approximate 15-35 mAh/g capacity is irreversible for the $LiNi_xCi_{1-x}O_2$ electrodes. The highest irreversible capacity of 34 mAh/g was observed for the $LiNiO_2$ electrode. However, for $LiNi_xCi_{1-x}O_2$ containing Co in the structure, the irreversible capacity declined to 15-20 mAh/g. These irreversible capacities in the first cycle can be utilised to compensate for the lithium consumption on the surface of the carbon anode due to the formation of the passivation film during the first charge in commercial lithium ion batteries.

In order to determine the cyclability of the $LiNi_xCi_{1-x}O_2$ electrodes, the $Li/LiNi_xCo_{1-x}O_2$ coin cells were cycled in the voltage range of 3.0-4.4 V at a constant current density of 0.15 mA/cm^2 for 100 cycles. Fig. 5-19 shows the results of the cycling test. The $LiCoO_2$ electrode demonstrated an excellent cyclability compared to the $LiNiO_2$ electrode. The rechargeability for the $LiNi_{0.5}Co_{0.5}O_2$ and $LiNi_{0.25}Co_{0.75}O_2$ electrodes is still good with a capacity fading rate of 0.3 mAh/g and 0.18 mAh/g per cycle respectively. In this investigation, lithium foil was used as anode. After 100 cycles, the cells were dismantled in the glove-box. A layer of lithium powders were found to deposit on the surface of the lithium anode, which influences the cycle life of the cells.

If the commercial carbon is used as anode, the result of the cycle life test would be better.

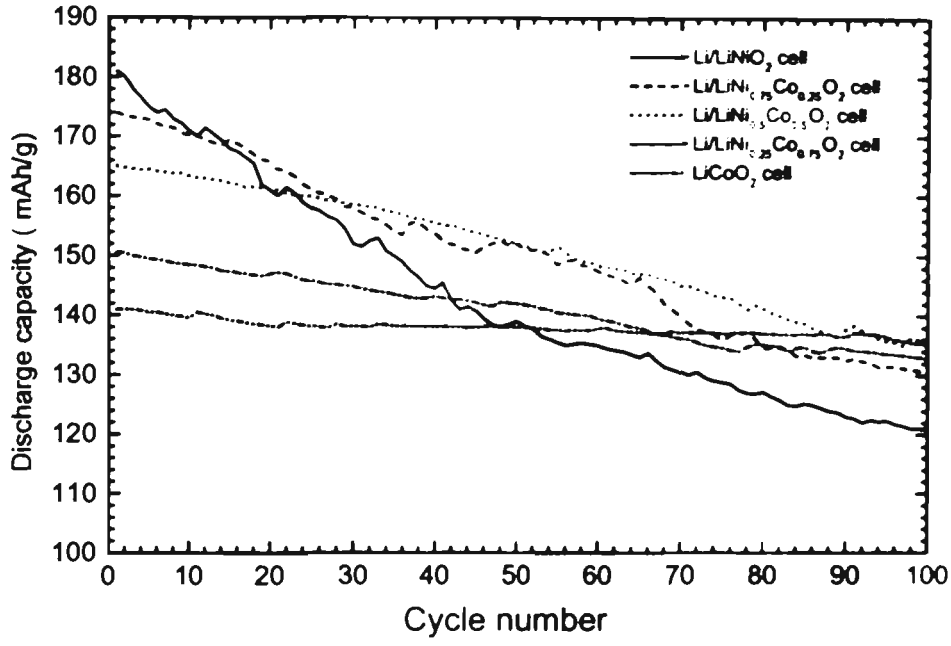

Fig. 5-19 The discharge capacity vs. cycle number for Li/ $LiNi_xCo_{1-x}O_2$ cells.

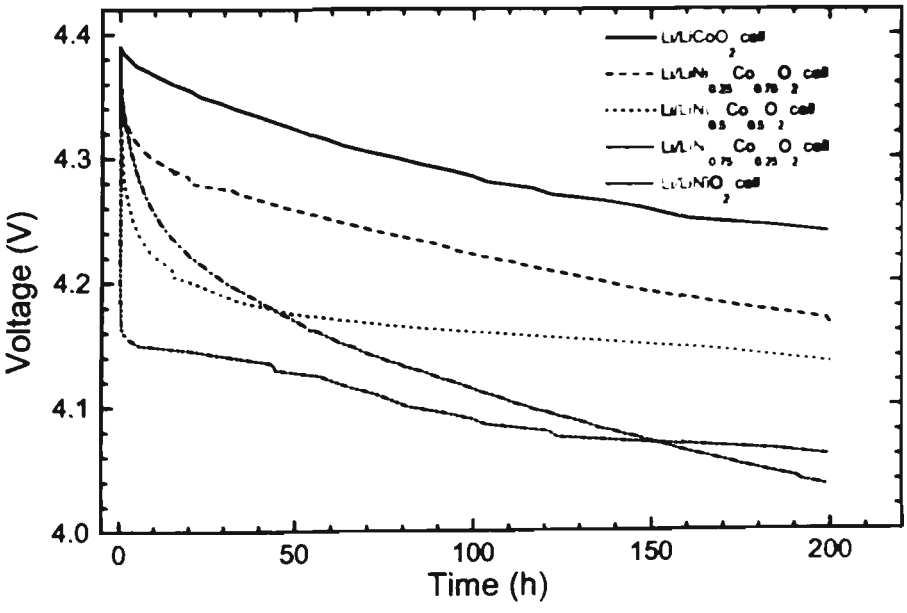

Fig. 5-20 The self discharge of Li/ $LiNi_xCo_{1-x}O_2$ cells at highly charged state.

A mechanism for the capacity fade of $LiNi_xCo_{1-x}O_2$ electrodes on cycling could include the following factors: (i) A structural change due to lithium insertion extraction causes contraction and expansion of the unit cell, which may lead to the formation of fractures in the particles of the active materials. (ii) In the charged state, MO_2 reacts with the organic electrolyte inducing dissolution of M ions into the solution. $LiNiO_2$ has been found to experience several topatactic phase transformations during lithium insertion and extraction. However, $LiCoO_2$ does not behave in this way. Therefore, in the $LiNi_xCi_{1-x}O_2$ solid solutions, Co can stabilize the layered structure for lithium ions insertion and extraction. On the other hand, the binding energy of the Co-O bond is higher than that of the Ni-O bond. The strong Co-O skeleton could contribute to the stability of $LiCoO_2$ in the charged state. In order to confirm this point of view, self-discharge tests have been performed on the $Li/LiNi_xCo_{1-x}O_2$ cells. The $Li/LiNi_xCo_{1-x}O_2$ cells were charged to 4.4 V and then the charging current was cut off. The cells were left to relax for 200 hours and the decade of the cell voltage was recorded. As shown in Fig. 5-20, the stability of the $LiNi_xCo_{1-x}O_2$ electrodes in the charged state increases with increasing amount of Co in the structure. The decline of the cell voltage in the charged state probably was caused by the reaction of $LiNi_xCo_{1-x}O_2$ with the organic electrolyte because in the fully charged state, Ni and Co have a charge of at 4^+ and are very reactive. Therefore, limiting the charging voltage (eg. 4.2 V vs Li/Li^+) could extend the cycle life of the $LiNi_xCo_{1-x}O_2$ electrodes.

In conclusion, the thermogravimetric analysis and self discharge tests show that the thermal stability and electrochemical stability of $LiNi_xCo_{1-x}O_2$ increase with increasing amounts of Co in the structure. This is thought to be associated with the binding energy of the M-O bond. The measurements of the magnetic susceptibility of the $LiNi_xCo_{1-x}O_2$ powders demonstrated that an ordered layered structure can be obtained by an

appropriate synthesis process. The partial substitution of Ni for Co in the layered $LiCoO_2$ structure can improve its initial specific capacity but the cyclability is deteriorated. Correspondingly, the cost and toxicity can be reduced. Trading off all of these factors, $LiNi_{0.5}Co_{0.5}O_2$ could be a reasonable choice as a cathodic material for lithium-ion batteries.

5.5 Physical and Electrochemical Characterization of $LiNi_{0.8}Co_{0.2}O_2$ Thin Film Electrodes Deposited by Laser Ablation

Thin-film lithium ion microbatteries have been developed for several years. These microbatteries can be used as an integral part of micro-electronic circuits (on-chip CMOS memory backup) or miniature electronics such as micromechanics, miniature hearing aids and implanted medical devices [180 - 183]. Thin films of oxides can be made by many techniques. Of these, laser ablation is a new and powerful technology to produce films. It can directly deposit film on the metal substrate without the requirement of a buffer layer and post heat treatment.

The $LiNi_{0.8}Co_{0.2}O_2$ thin film electrodes were deposited using a pulsed laser ablation technique. The $LiNi_{0.8}Co_{0.2}O_2$ compound has the potential to be used as a cathode material instead of $LiCoO_2$, because it is cheaper, less toxic and has a higher capacity than $LiCoO_2$. Thin film electrodes provide an ideal geometry for fundamental research on electrode materials, and overcome the uncertainties of porous powder electrodes. The electrochemical properties of $LiNi_{0.8}Co_{0.2}O_2$ thin-film electrodes were characterized using lithium test cells.

5.5.1 The preparation and characterization of $LiNi_{0.8}Co_{0.2}O_2$ thin-films

$LiNi_{0.8}Co_{0.2}O_2$ thin-films were deposited on a nickel substrate by pulsed laser ablation. $LiNi_{0.8}Co_{0.2}O_2$ powders (Merck, Germany) were pressed into pellets and sintered at 900 °C for 24 hours for use as the target. The laser ablation system is an Excimer Laser LAMBDA PHYSIK, Compex 301 with λ=248 nm, 1~10Hz, 1.2 J/pulse maximum energy output. The incidence angle between direction and target is 45 °C. During deposition, the target was rotated at 10 rpm and the substrate was mounted on a holder which was resistively heated to 600 °C. Films were deposited for 30 minutes under an oxygen pressure of 100 mtorr, using a 5 Hz, 450 mJ/pulse KF laser.

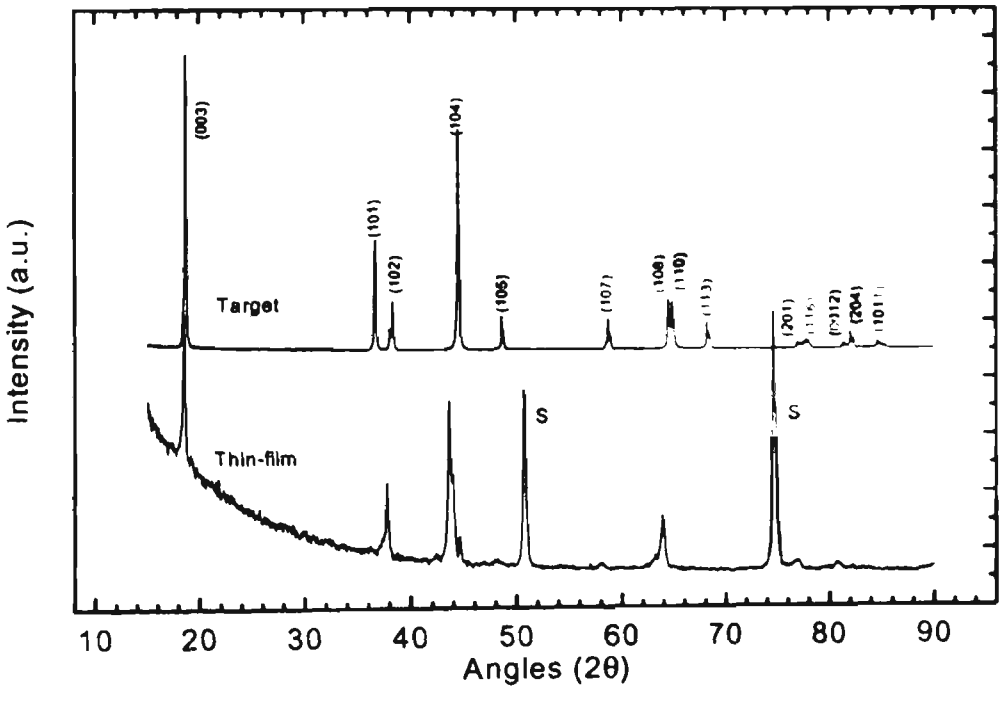

Fig. 5-21 X-ray diffraction patterns of a $LiNi_{0.8}Co_{0.2}O_2$ thin film and target.

Fig. 5-21 shows the x-ray diffraction patterns of a $LiNi_{0.8}Co_{0.2}O_2$ thin film and target. The diffraction lines from the substrate are marked with S. Compared to the XRD pattern of the target, some diffraction peaks of the thin film disappeared or became indistinguishable. This is ascribed to the formation of texture in the thin film. Nevertheless, the hexagonal structure can be identified for the $LiNi_{0.8}Co_{0.2}O_2$ thin films.

The morphology of as deposited thin-films was observed by AFM microscopy. As shown in Fig. 5-22, the roughness of the thin films varies in micro-domain. The thickness of the thin films was measured by AFM to be about 620 nm . In macro-domain, the thin films seem to be deposited homogeneously.

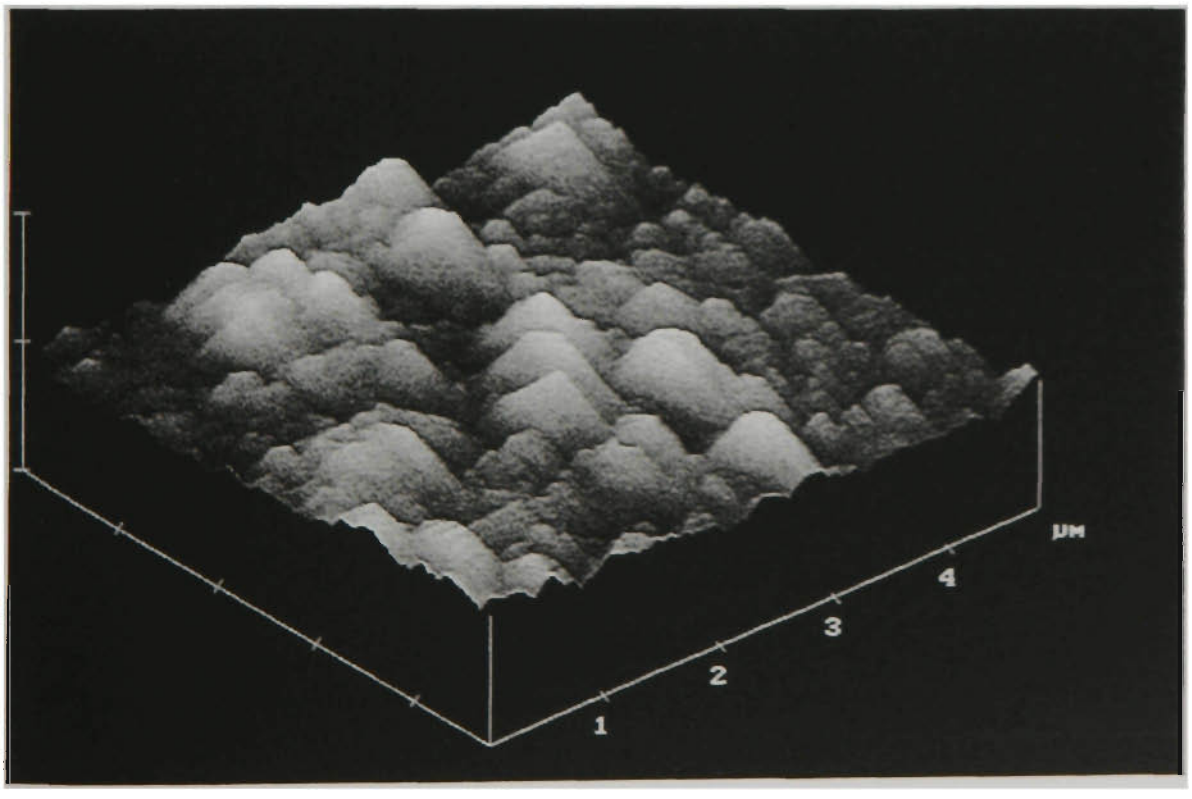

Fig. 5-22 AFM image of $LiNi_{0.8}Co_{0.2}O_2$ thin film.

5.5.2 Electrochemical properties of $LiNi_{0.8}Co_{0.2}O_2$ thin-films

The capacities of the $LiNi_{0.8}Co_{0.2}O_2$ thin-film electrodes were examined by constant current charge/discharge. Four test cells were assembled and cycled in the voltage range of 3.0 V-4.3 V at a constant current density of 10 $\mu A\ cm^{-2}$. Fig. 5-23 shows the voltage vs. capacity profile of the first charge/discharge. A capacity of 60.3 - 62.5 $\mu Ah/cm^2.\mu m$ was delivered in the first discharge. This corresponds to a specific capacity of approximately 125 mAh/g (assuming that the $LiNi_{0.8}Co_{0.2}O_2$ thin film had no porosity and a theoretical density of 4.8 g/cm^3). In the first cycle, the efficiency (ratio of discharge capacity to charge capacity) was about 86.2%. Some charging current might have been consumed by the side reaction. Because Ni in the Ni^{4+} state is very reactive, this could cause the decomposition of the organic electrolyte. A passivation product could be formed on the surface of the thin film electrode, but the nature of this process is unclear so far.

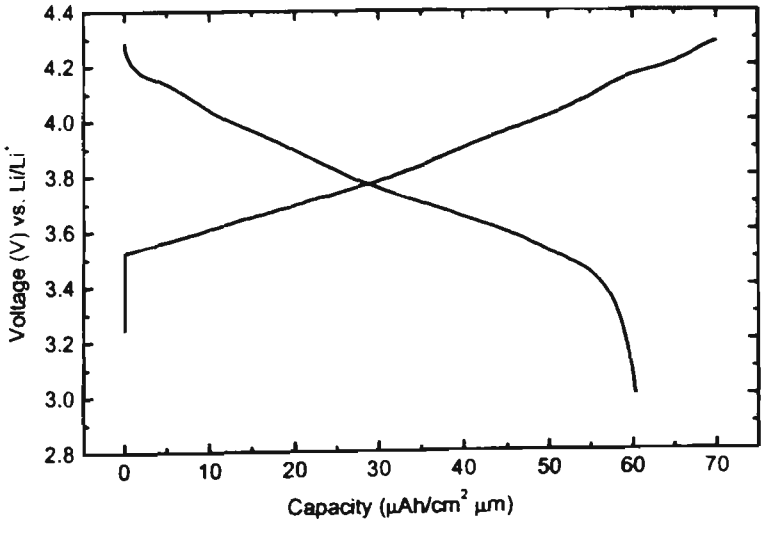

Fig. 5-23 Charge/discharge curves of $LiNi_{0.8}Co_{0.2}O_2$ thin film electrode.

After the second cycle, the capacity of the thin film electrode gradually declined. However, the efficiency of cycling was improved and maintained at 94% for each cycle. After 100 cycles, the capacity of the thin film electrode still retained 85% of its first cycle value. This shows that the $LiNi_{0.8}Co_{0.2}O_2$ thin film deposited by laser ablation technique demonstrated a reasonable capacity and good capacity retention. Further optimization of the thickness of thin films and deposition conditions will probably improve the cyclability of these thin film electrodes.

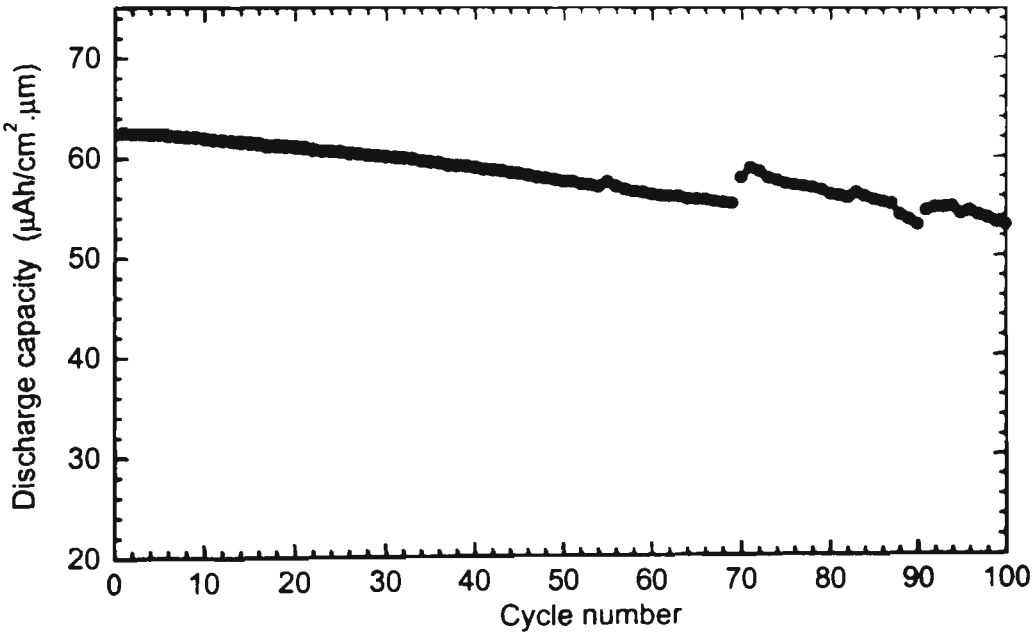

Fig. 5-24 Discharge capacity of $LiNi_{0.8}Co_{0.2}O_2$ thin film electrode vs. cycle number.

Cyclic voltammetry measurements were performed on a $LiNi_{0.8}Co_{0.2}O_2$ thin-film electrode at a sweeping rate of 0.1 mv/s over a voltage range of 2.8 V-4.4 V. The cyclic voltammogram is shown in Fig. 5-25. Four anodic peaks were observed during the charging process (Li-ion extraction from the $LiNi_{0.8}Co_{0.2}O_2$ thin film electrode). These four peaks are at 3.71 V, 3.91 V, 4.0 V and 4.19 V respectively. Correspondingly, in the process of discharging (Li-ion insertion into the $LiNi_{0.8}Co_{0.2}O_2$ thin film electrode), four cathodic peaks were also observed at 3.66 V, 3.90 v, 3.98 v and 4.16 v. On the average, cathodic peaks are 10 mV-50 mV lower than the anodic peaks. These four paired peaks are attributed to the insertion/extraction reactions of Li ions in $LiNi_{0.8}Co_{0.2}O_2$ occuring in four different phase regions. Ohzuku et al. [34] found that there were four regions for the reaction of $LiNiO_2$ and $LiNi_{0.5}Co_{0.5}O_2$ electrodes in lithium cells with an electrolyte of 1 M $LiClO_4$ in propylene carbonate (PC). In region (I) for $0<x<0.25$, the reaction takes place in the rhombohedral phase; In region (II) for $0.25\leq x\leq 0.55$ the reaction occurs in a monoclinic phase; In region (III) for $0.55<x\leq 0.75$, the reaction proceeds in a rhombohedral phase; In region (IV) for $0.75<x<1.0$, the reaction consists of a rhombohedral two-phase reaction [34, 51]. The results of the observation for the $LiNi_{0.8}Co_{0.2}O_2$ thin film using cyclic voltammetry measurement are similar to Ohzuku's investigation via XRD and differential chronopotentiograms. Since no binder or conducting additives were used in the thin film electrodes, the identification of the electrochemical characteristics using thin film electrodes should be more accurate than that using porous, powder pressed electrodes. Cyclic voltamograms obtained from thin film electrodes clearly demonstrated four oxidation and reduction peaks, which are a unique characteristic of $LiNi_{1-x}Co_xO_2$ compounds.

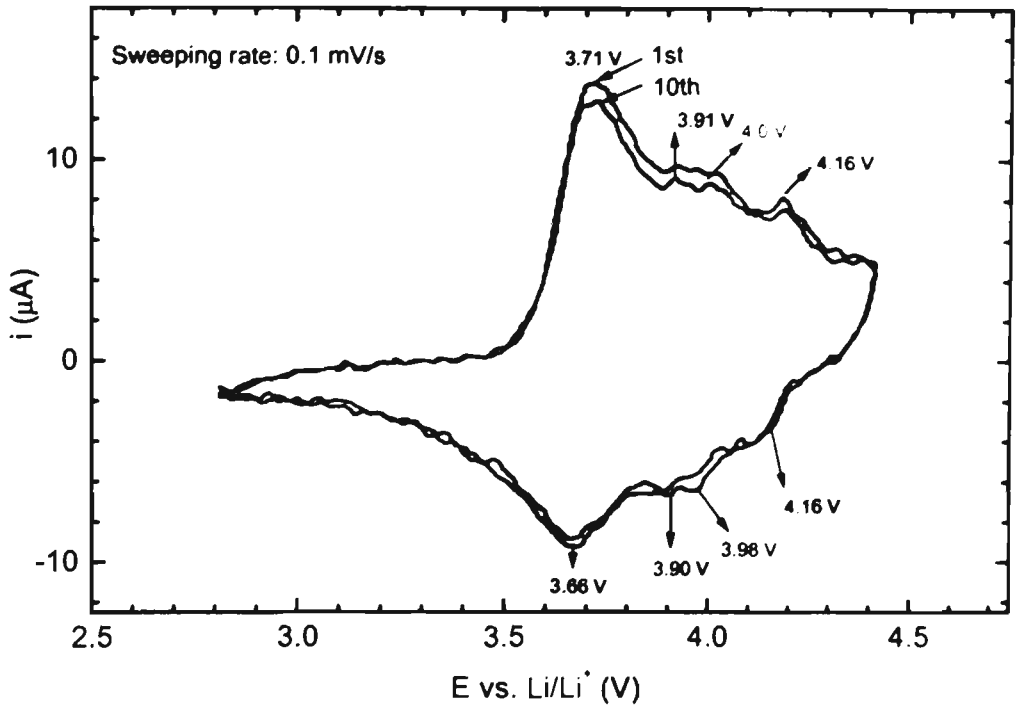

Fig. 5-25 Cyclic voltamograms of $LiNi_{0.8}Co_{0.2}O_2$ thin film electrode.

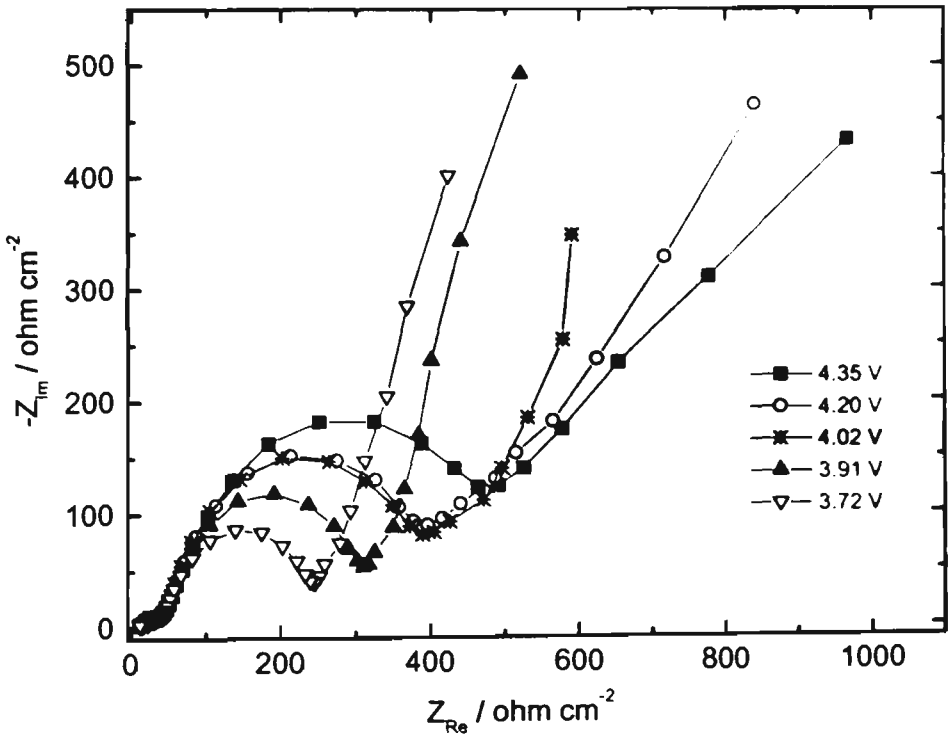

Fig. 5-26 A. c. impedance spectra of $LiNi_{0.8}Co_{0.2}O_2$ thin film electrode.

To investigate the kinetics of lithium intercalation in $LiNi_{0.8}Co_{0.2}O_2$ thin films and the characteristics of the thin film/electrolyte interface, a. c. impedance measurements were carried out on a $LiNi_{0.8}Co_{0.2}O_2$ thin film electrode in different states. The thin film electrode was potentiostatically conditioned at different potentials vs. Li/Li^+ reference electrode. After a certain time for equilibrium to be established, an a. c. perturbation (5 mV) was applied to the thin film electrode. The frequency was in the range of 100 kHz – 1 mHz. Typical a. c. impedance spectra are shown in Fig. 5-26.

In general, two semicircles were observed in the a.c impedance spectra, which explicitly reflect well separated, different time constants for the Li ion insertion processes in the $LiNi_{0.8}Co_{0.2}O_2$ thin film. The high frequency semicircle is independent of the potential of the electrode. This semicircle is attributed to the formation of a surface layer on the electrode, caused either by the electrolyte decomposition product or the adsorption species. When Li^+ ions are electrochemically extracted from $LiNi_{0.8}Co_{0.2}O_2$, Ni^{3+} or Co^{3+} ions are oxidized to Ni^{4+} or Co^{4+}. Ni^{4+} or Co^{4+} ions are very reactive in nature and tend to react with the organic electrolyte, causing the decomposition product deposited on the surface of the electrode to form a passivation film. The medium frequency semicircle is assigned to charge-transfer resistance and non-Faradaic process occuring at the thin film-electrolyte interface related to slow Li^+ interfacial transfer. The low frequency range consists mainly of diffusion-controlled process characterized by Warburg impedance (Z_w). The variation of D_{Li^+} is in the range of $3.19 * 10^{-13}$ - $2.48 * 10^{-10}$ m^2s^{-1}, in agreement with the diffusion coefficient reported in the literature for lithium insertion materials [84, 184].

In summary, the thin-film electrode provides an ideal geometry for electrochemical characterization of electrode materials because it can eliminate any structurally-related side effects caused by a porous powder electrode. In the cyclic voltammetry

measurement, four oxidation and reduction peaks were distinguished, which represent four different phase regions during insertion and extraction of Li^+ ion in $LiNi_{0.8}Co_{0.2}O_2$. Through a. c. impedance characterization, the lithium diffusion coefficient D_{Li} was measured to be in the range of 3.19×10^{-13} - 2.48×10^{-10} m^2s^{-1} at different potentials.

5.6 Electrochemical performance of Orthorhombic $LiMnO_2$ as Cathode in Lithium-ion Batteries

The Li-Mn-O system is one of the most intensively investigated cathodic materials for rechargeable lithium batteries. Recently, the synthesis and electrochemical properties of layered $LiMnO_2$ (monoclinic c2/m, or m-$LiMnO_2$) by an ion-exchange method has been reported [92]. The m-$LiMnO_2$ was found to be intolerant to lithium ion extraction/insertion, although its first charge capacity can reach 270 $mAhg^{-1}$. Another class of $LiMnO_2$ compounds (orthorhombic, Pmnm) or o-$LiMnO_2$ can be synthesised by solid-state reaction both at high temperature and low temperature. A capacity in the range of 50 $mAhg^{-1}$ to 200 $mAhg^{-1}$ has been demonstrated with good cyclability [185 - 190]. O-$LiMnO_2$ was observed to transform to spinel-like $LiMn_2O_4$ when cycled in the voltage range of 2.2 V-4.4 V in the first cycle. This has been confirmed by ex-situ and in-situ x-ray diffraction. The rechargeability of the electrochemically formed spinel-like materials in the voltage range of 2.2 V-4.4 V is much better than that of directly synthesised spinel $LiMn_2O_4$. Nevertheless, the kinetic process of Li ion insertion/extraction in the o-$LiMnO_2$ electrode has not been reported so far.

5.6.1 The synthesis and characterization of o-$LiMnO_2$ powders

Two types of o-$LiMnO_2$ samples were synthesised with the precursors of $LiOH.H_2O$ and Mn_2O_3. Firstly, the mixtures were fired at 450°C for 5 h, thoroughly ground after

cooling and then heated at 600°C for 12 h. The heat treatment of the samples was carried out in a tube furnace with argon flow. The type-I sample was nominally non-stoichiometric with Li:Mn=1.1:1 in the precursors, and the type-II sample was nominally stoichiometric with Li:Mn=1:1 in the precursors

The x-ray diffraction patterns of the two types of o-$LiMnO_2$ compounds are shown in Fig. 5-27. All peaks were indexed by assuming an orthorhombic phase with a space group Pmnm. The lattice constants were refined against an internal silicon standard using a least squares method with 20 diffraction peaks. The parameters of the unit cell were calculated as: a=2.8066 Å, b=5.7506 Å and c=4.5748 Å, which is in good agreement with JCPDS 35-749. According to previous work [191, 192], the non-stoichiometric type-I o-$LiMnO_2$ compound contains more stacking faults than that of the stoichiometric one. From the XRD data in Fig. 5-27, more impurity phase $LiMn_2O_4$ is present in the non-stoichiometric o-$LiMnO_2$. Also, the peaks observed for type-I o-$LiMnO_2$ were brodened, which could be caused by the presence of stacking faults in the crystal structure.

SEM observation was performed on the o-$LiMnO_2$ powders. The two types of $LiMnO_2$ compounds were found to have similar morphology and a crystal size of around 0.5-1 μm. A typical SEM photograph is shown in Fig. 5-28.

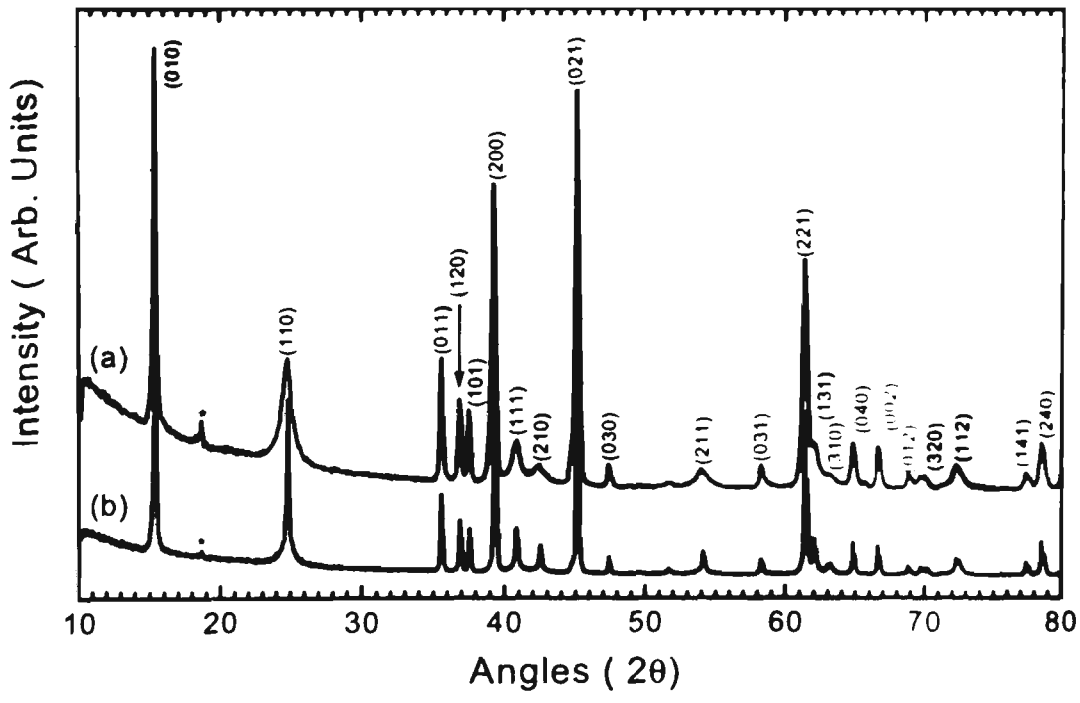

Fig. 5-27 X-ray diffraction patterns of the two types of o-$LiMnO_2$ samples.
(a) Type-I non-stoichiometric o-$LiMnO_2$.
(b) Type-II stoichiometric o-$LiMnO_2$.
* $LiMn_2O_4$ impurity phase.

Fig. 5-28 Scanning electron micrograph of the type-I o-$LIMnO_2$ powder.

5.6.2 Cycling test of o-$LiMnO_2$ electrode

The $Li/LiMnO_2$ cells were cycled in a voltage range of 2.2 -4.3 V at a constant current density of 0.2 mA/cm^2. The first charge curves are shown in Fig. 5-29. The two types of o-$LiMnO_2$ demonstrated different charging behavior in the first charge. As shown in Fig. 5-29, the type-I o-$LiMnO_2$ electrode was quickly charged from OCV to 3.6 V and then followed an ascending plateau between 3.6 V to 3.9 V. A second region of lower slope appeared from 4.0 V to 4.3 V. For the type-II o-$LiMnO_2$ electrode, a fairly flat charging plateau was observed around 3.6 V, which consists approximately of the half charge capacity of the electrode. Following this charging plateau, the voltage increased gradually between 3.8 V and 4.2 V. The initial charging behavior of the type-I o-$LiMnO_2$ is in some ways similar to that of spinel $LiMn_2O_4$. It is considered that o-$LiMnO_2$ gradually transforms to spinel-like $LiMn_2O_4$ during charge/discharge cycles [191. From the analysis of the XRD patterns, it is known that there are relatively more spinel $LiMn_2O_4$ impurity phases and stacking faults in the non-stoichiometric type-I o-$LiMnO_2$ compounds. It is proposed that these $LiMn_2O_4$ phases could initiate the nucleation of spinel-like $LiMn_2O_4$. These stacking faults could accelerate this process. Therefore, the type-I o-$LiMnO_2$ would be expected to be easier to electrochemically transform to the spinel-like $LiMn_2O_4$ than the type-II o-$LiMnO_2$. This view was supported by the results of charge-discharge cycling tests. It was found that a few cycles were necessary to activate the electrochemical reactivity of both types of o-$LiMnO_2$ electrodes. However, type-I o-$LiMnO_2$ only needed four to ten cycles to achieve the maximum capacity of 170-190 mAh/g whereas fifteen to twenty cycles were required to reach the optimum capacity of 110-125 mAh/g for type-II o-$LiMnO_2$. It was considered that the o-$LiMnO_2$ was completely transformed to the spinel-like phase when it delivered the maximum capacity.

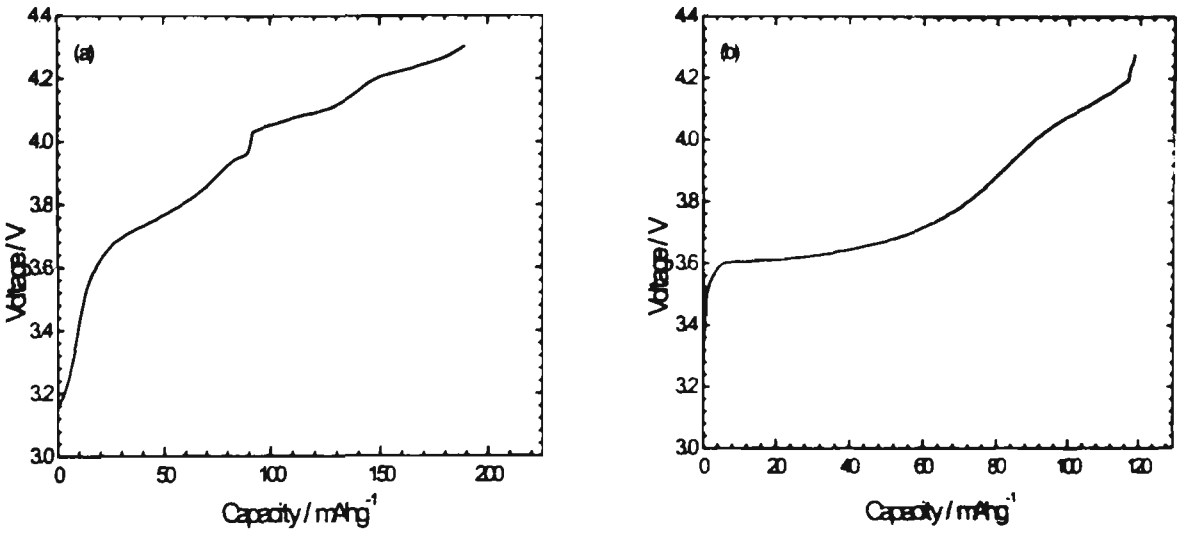

Fig. 5-29 The first charge curves of the o-$LiMnO_2$ electrodes.
(a) Type-I o-$LiMnO_2$. (b) Type-II o-$LiMnO_2$

Fig. 5-30 shows the discharge profiles of type-I o-$LiMnO_2$ at the fourth cycle and type-II o-$LiMnO_2$ at the eighteenth cycle respectively, at which they delivered the maximum capacity. The discharge capacity of type-II o-$LiMnO_2$ is much smaller than that of type-I o-$LiMnO_2$. A two-step discharge profile with constant voltage regions near to 4 V and 3 V respectively is observed. This two-step discharge is the characteristic of the spinel $LiMn_2O_4$ electrode. The ~4 V discharge plateau corresponds to Li intercalation into tetrahedral sites, whereas the ~3 V discharge plateau is associated with Li insertion into the interstitial and octahedral sites. Therefore, we could conclude that o-$LiMnO_2$ transfers to the spinel-like phase after a certain number of charge/discharge cycles.

The differential chronopotentiometric curves as shown in Fig. 5-31 provide further evidence to support the above point. Three reduction peaks are observed at 4.12-4.14 V, 4.02-3.99 V and 2.91 V respectively, exactly the same as those for the spinel $LiMn_2O_4$ electrode.

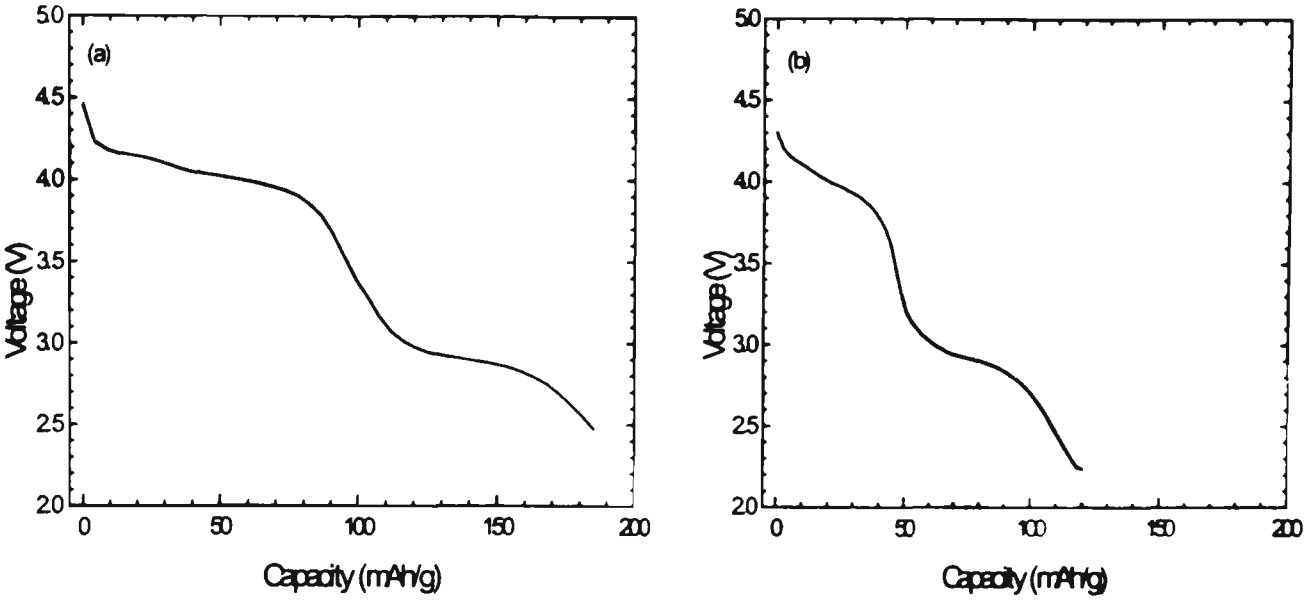

Fig. 5-30 (a) The fourth discharge profile of a Li o-$LiMnO_2$ cell, in which the cathode was made from type-I o-$LiMnO_2$. (b) The eighteenth discharge profile of a Li/$LiMnO_2$ cell, in which the cathode was made from type-II o-$LiMnO_2$.

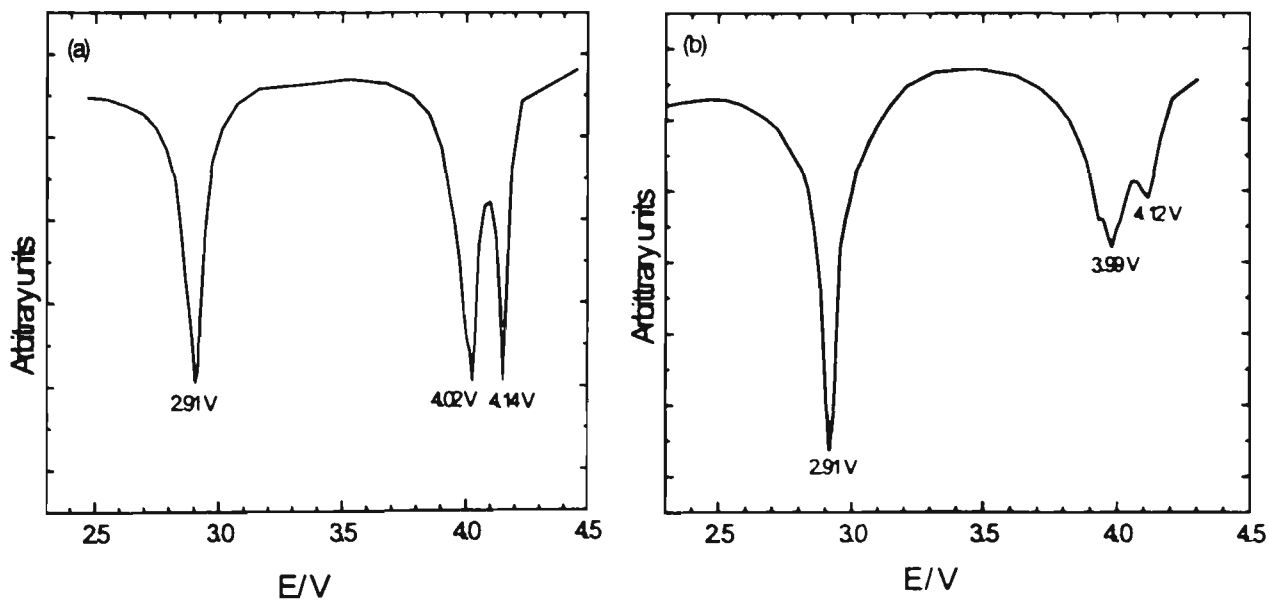

Fig. 5-31 The differential chronopotentiometric curve corresponding to Fig. 5-30
(a) Type-I non-stoichiometric o-$LiMnO_2$ electrode.
(b) Type-II stoichiometric o-$LiMnO_2$ electrode.

In order to identify the cycle life of the o-$LiMnO_2$ electrodes, long term cycle tests were performed. Fig. 5-32 shows the discharge capacities vs. the cycle number. Both types of o-$LiMnO_2$ electrode demonstrated good cyclability, which is different from that of the spinel $LiMn_2O_4$. It is well known that the spinel $LiMn_2O_4$ electrode suffers from short cycle life due to the Jahn-Teller distortion[16]. This means that the electrochemically formed spinel-like phase originating from o-$LiMnO_2$ is more tolerant to cycling. The definitive mechanism is still unknown. However, TEM observation can provide some useful information. Fig. 5-33 shows two TEM micrographs of o-LiMnO2 before cycling (as prepared powders) and after 80 cycles. The morphology of crystal particles was not found to be significantly changed, which is beneficial in long term cycling of the electrode.

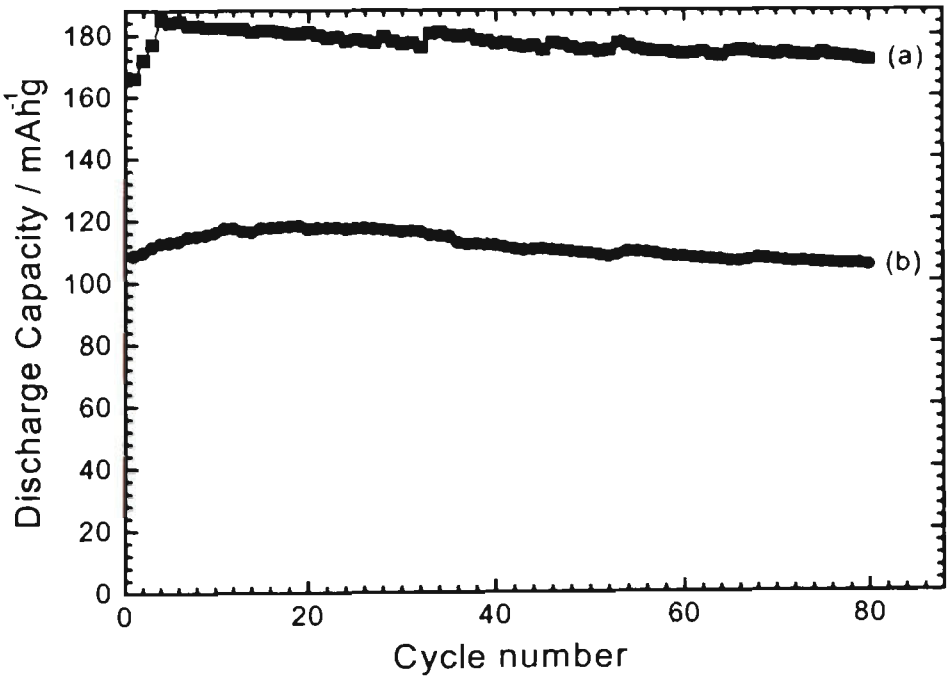

Fig. 5-32 The discharge capacity vs. cycle number of Li / o-$LiMnO_2$ cells.
(a) Type-I non-stoichiometric o-$LiMnO_2$ electrode.
(b) Type-II stoichiometric o-$LiMnO_2$ electrode.

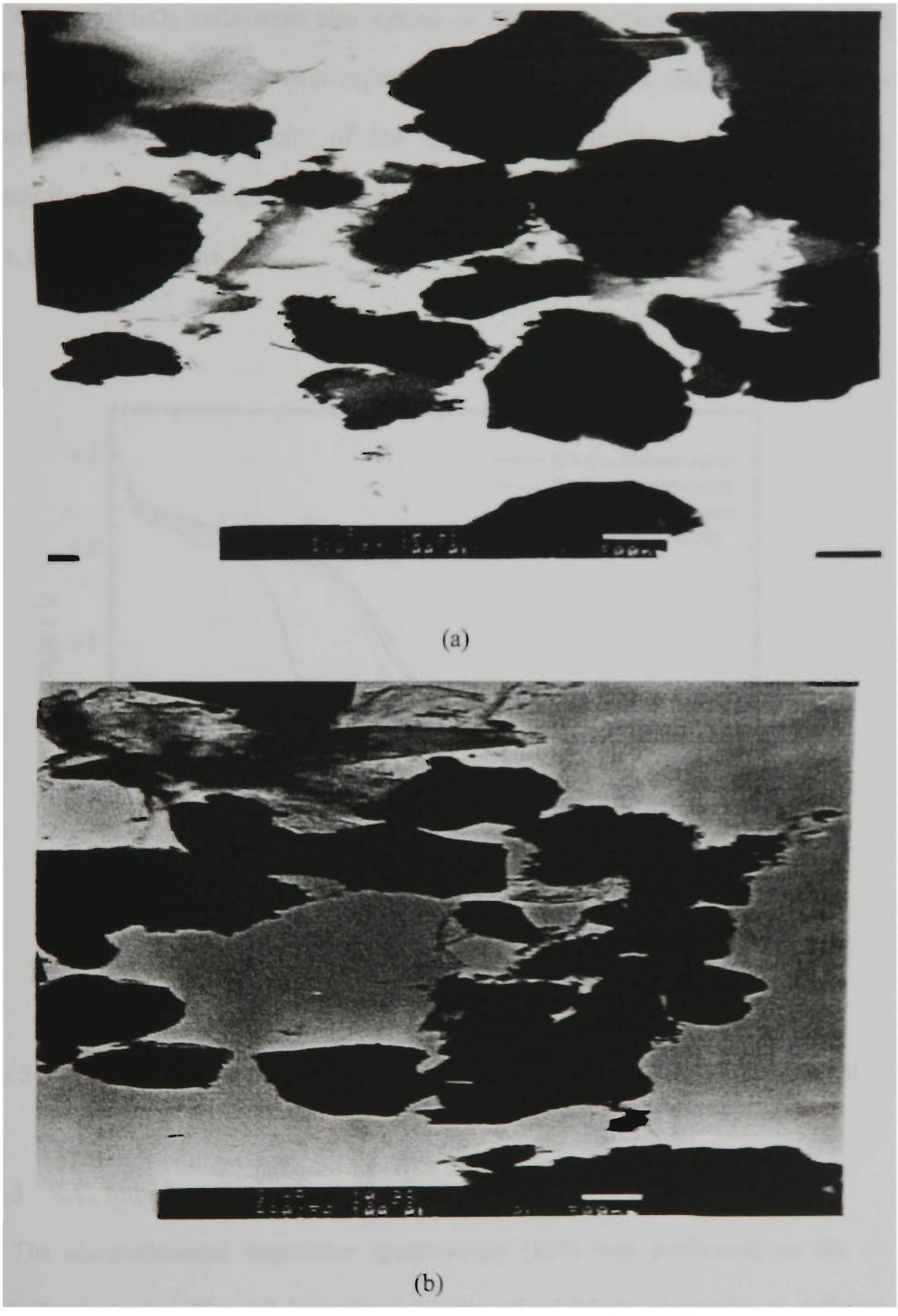

Fig. 5-33 TEM micrographs of o-$LiMnO_2$
(a) The as-prepared powders (before cycling).
(b) After 80 cycles.

The $Li/LiMnO_2$ cells were also cycled at different current densities. Fig. 5-34 compares the maximum discharge capacities of type-I o-$LiMnO_2$ electrodes at different discharge rates. The capacity of the o-$LiMn_2O_4$ electrode is sensitive to the charge/discharge rate, in agreement with the kinetic limitation. The slower the discharge rate, the higher the capacity.

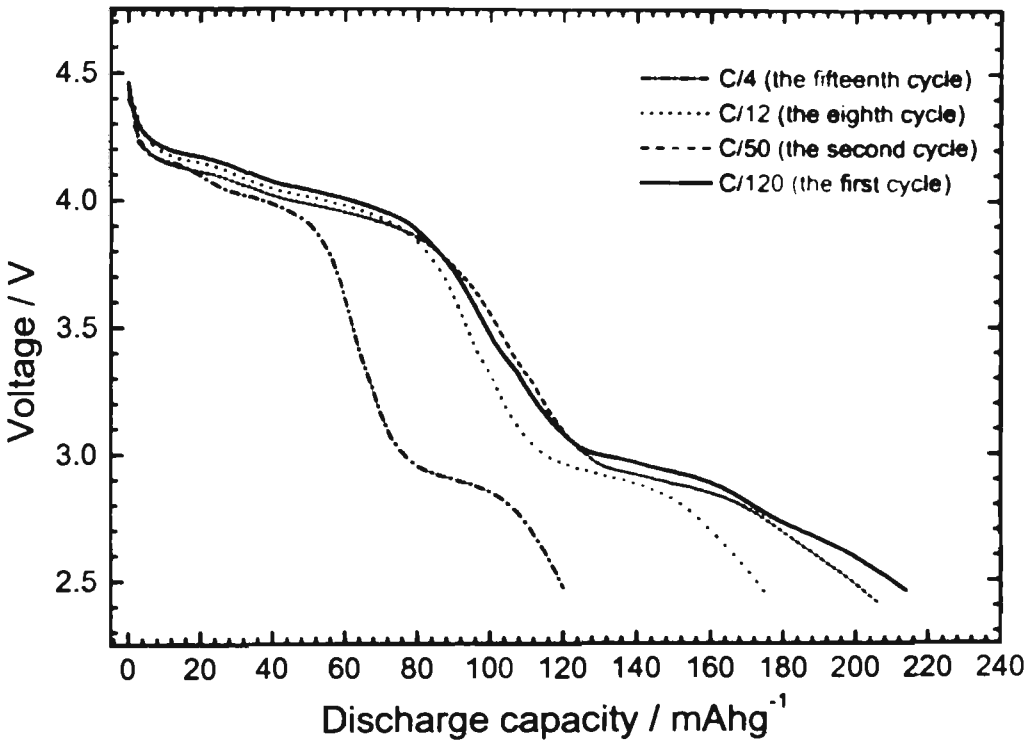

Fig. 5-34 The maximum discharge capacity of type-I o-$LiMnO_2$ electrode at different discharge rates

5.6.3 A.C. impedance measurement

The electrochemical impedance spectroscopy (EIS) was performed on the o-$LiMnO_2$ electrodes. The AC impedance spectra of o-$LiMnO_2$ electrodes at different states of charge (SoC) were obtained and typical Nyquist plots are presented in Fig. 5-35. A semicircle was observed to center on the real axis at high frequencies from which

the charge transfer resistance R_{CT} can be deduced. Consequently, the exchange current density i_o can be calculated from the formula: $i_o=RT/nFR_{CT}$. In the low frequency range, a straight line at 45° to the real axis corresponds to the Warburg impedance. The kinetic parameters of the o-$LiMnO_2$ electrodes are summarised in Table 5-2.

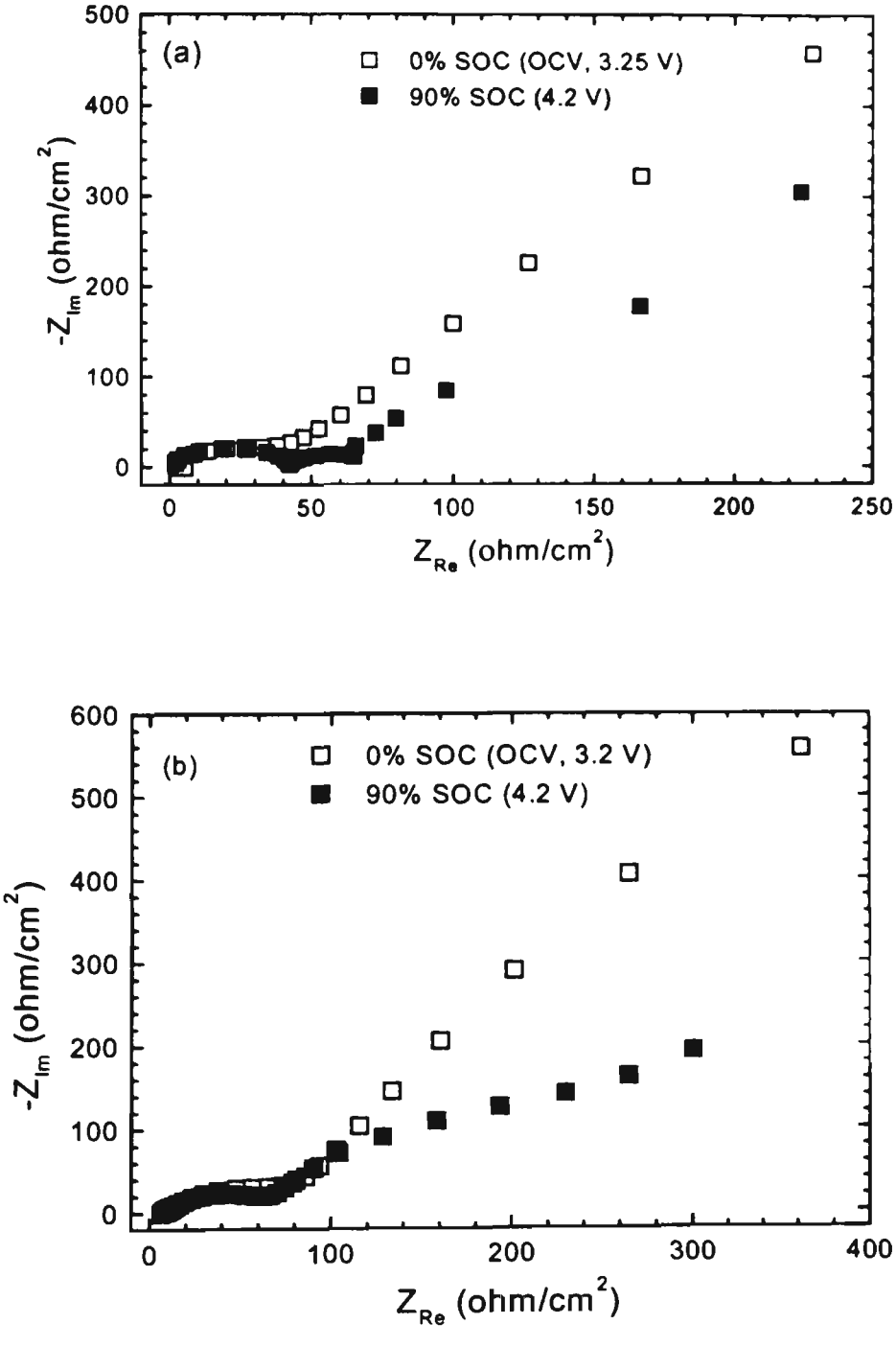

Fig. 5-35 Ac impedance spectra of o-$LiMnO_2$ electrodes at 0% SoC state (3.2-3.4 V) and 90% SoC charged state (4.2 V).
(a) Type-I non-stoichiometric o-$LiMnO_2$ electrode.
(b) Type-II stoichiometric o-$LiMnO_2$ electrode.

Table 5-2 The kinetic Parameters of o-$LiMnO_2$ electrodes

	R_{CT} at 0% SOC (Ω/cm^2)	R_{CT} at 90% SoC (Ω/cm^2)	i_o at 0% SoC ($A\ cm^{-2}$)	i_o at 90% SoC ($A\ cm^{-2}$)
Type-I nonstoichiometric o-$LiMnO_2$	76.5	37.8	3.3×10^{-4}	6.8×10^{-4}
Type-II stoichiometric o-$LiMnO_2$	124.9	80.2	2.1×10^{-4}	3.2×10^{-4}

The values of R_{CT} for the type-I o-$LiMnO_2$ are much smaller than those for the type-II o-$LiMnO_2$. This means that the non-stoichiometric type-I o-$LiMnO_2$ is more electrochemically reactive than the stoichiometric type-II o-$LiMnO_2$, which is in qualitative agreement with the results of the charge/discharge tests. The R_{CT} values at 0% SoC (OCV, 3.2-3.4 V) state are much higher than those at the 90% SoC charged state (4.2 V) for both types of $LiMnO_2$ electrodes. Apparently, o-$LiMnO_2$ phase transfers to the spinel-like phase during the charging process and this electrochemically formed spinel-like phase is more reactive than that of the original o-$LiMnO_2$ phase. For the non-stoichiometric o-$LiMnO_2$ electrode, two semicircles were observed in the charged state (4.2 V). Due to the reaction between the electrolyte and the surface of the electrode, a surface layer formed on the electrode could be responsible for this second semicircle. Nevertheless, no second semicircle was observed at the charged state for type-II o-$LiMnO_2$ electrode. This observation supports the view that non-stoichiometric o-$LiMnO_2$ is more electrochemically reactive than the stoichiometric o-$LiMnO_2$.

To summarize this study of the electrochemical properties of two types of orthorhombic $LiMnO_2$ cathodes in lithium cells. (i) A maximum capacity in the range of 180-190 mAh/g for non-stoichiometric o-$LiMnO_2$ electrode may be reached with fairly good cyclability. (ii) The kinetic characterisation of the electrode process by AC

impedance spectroscopy showed that the spinel-like phase transformed from o-$LiMnO_2$ was more electrochemically active than the original o-$LiMnO_2$. (iii) The non-stoichiometric o-$LiMnO_2$ was more reactive than the stoichiometric o-$LiMnO_2$. (iv) The non-stoichiometric o-$LiMnO_2$ is a promising cathodic materials for rechargeable lithium batteries.

Chapter 6 Intermetallic Alloys As Anode Materials for Lithium-ion Batteries

Metal elements such as Al, Sn, Pb, Sb, and Bi can alloy with lithium to form lithium alloys. But this alloying process is normally accompanied by a volume increase of several times, which could cause cracking or crumbling of the electrodes. Consequently, a short cycle life is induced, preventing any practical application. However, the use of Li-alloys as anode materials in lithium-ion batteries could lead to improvements in specific energy and safety compared with carbonaceous materials. The striking features of Li-alloys are their high gravimetric and volumetric lithium storage capacities and their safe thermodynamic potentials of 1.0 – 0.3 V versus Li/Li^+ instead of 0.2 – 0.1 V versus Li/Li^+ for lithiated graphite [130, 193, 194]. These factors drive the continuing pursuit of Li-alloy materials.

The volume expansion related to the lithium-alloying process can be greatly alleviated by using intermetallic alloys and nano-crystalline alloy materials. In the intermetallic MM' alloys, M is the inactive element and M' is the active element which can react with lithium to form lithium alloys. When lithium inserted into MM' alloys, the ductile inactive M matrix is generated simultaneously, which can buffer the volume increase of the alloy. If MM' alloys are nanocrystalline or amorphous, there exist many pores and cavities in the resulting nano- or amorphous powders. The expanded volume of alloys can occupy this free space in the electrodes. Thus the overall volume of the electrode will not display any increase with lithium insertion and the formation of lithium-alloys [195, 196]. Therefore, nanocrystalline or amorphous intermetallic MM' alloys offers a brilliant prospect for alloy materials to be used as anodes in lithium-ion batteries.

6.1 Nanocrystalline eta-Cu_6Sn_5 Alloy as an Anode Lithium Storage Materials

The tin based glass and intermetallic alloys recently have attracted worldwide attention as lithium storage materials because of their high volumetric capacity. The tin based amorphous composite oxide (TCO) demonstrated a high reversible capacity of 650 mAh/g. However, a 37% irreversible capacity in the initial cycle due to the formation of Li_2O, prevented it from further commercial application [125, 126, 197]]. Theoretically, the intermetallic alloys seem not to have this problem because there is no oxygen in the alloy structure. The mechanism for reversible lithium insertion and extraction in MSn alloys relies on lithium alloying with Sn to form Li_xSn alloy. The nanosize inactive M matrix is generated simultaneously, which buffers the volume expansion of the active phase Sn due to its alloying with Li. Nanosize or amorphous alloy powders are usually required to realize the above process. Several alloys such as SnSb, Sn_2Fe and $SnFe_3C$ have been investigated and the process of lithium alloying with Sn has been confirmed by in-situ x-ray diffraction [198 - 200]. However, a different mechanism for lithium insertion into the crystalline eta-Cu_6Sn_5 alloy has been demonstrated to be a two phase reaction to yield $Li_xCu_6Sn_5$ (x=13), corresponding to a theoretical capacity of 358mAh/g [195].

It is expected that lithium alloying with Sn in eta-Cu_6Sn_5 could be achieved by preparing nanosize eta-Cu_6Sn_5 powders, in which one mole of Cu_6Sn_5 could combine with 22 moles of Li to form $Li_{22}Sn_5$ and generate 6 moles of Cu. The theoretical capacity for this process is 608 mAh/g, which is almost twice that of the mechanism to form $Li_{13}Cu_6Sn_5$ alloy.

6.1.1. The Preparation of eta-Cu_6Sn_5 alloys

Nanocrystalline eta-Cu_6Sn_5 alloy powders were prepared by high energy ball-milling. The elemental powders of Cu and Sn as well as hardened steel balls were put into the steel vial. The vial was initially evacuated and then filled with argon. The ball-milling was carried out in a Pulverisette-5 ball-milling machine. For comparison, crystalline eta-Cu_6Sn_5 alloy was also synthesized by sintering a pellet of a stoichiometric mixture of Cu and Sn powders in argon at 400°C for 15 hours. The sintered pellet was ground and sieved through a 325-mesh stainless steel sieve.

After cycling, the cells were dismantled in an argon filled glove-box and the Cu_6Sn_5 electrodes were taken out. The Cu_6Sn_5 electrodes were covered by a plastic film for ex-situ x-ray diffraction.

The eta-Cu_6Sn_5 alloy has a hexagonal structure with a space group of $P6_3mmc$. It can be synthesized by either sintering the mixture of Cu and Sn powders or ball milling Cu and Sn powders. Fig. 6-1 shows x-ray diffraction patterns of the Cu_6Sn_5 alloys. The sintering process produced a typical crystal Cu_6Sn_5 alloy with a small amount of impurity phase of the un-reacted Sn, while the ball-milling generated fine Cu_6Sn_5 alloy powders. As the ball-milling time was increased, the diffraction peaks became broadened, indicating a decrease of the particle size. When ball-milled for 110 hours, very broad diffraction peaks were observed, from which the grain size was calculated to be 5-10 nm, using the Scherrer formula: $d = \frac{K\lambda}{\beta Cos\theta}$. However, a small amount of tin or copper oxides were formed during the long term ball-milling, probably due to the very active nature of the nanocrystalline Cu_6Sn_5 alloy and traces of oxygen present in the ball-milling vial.

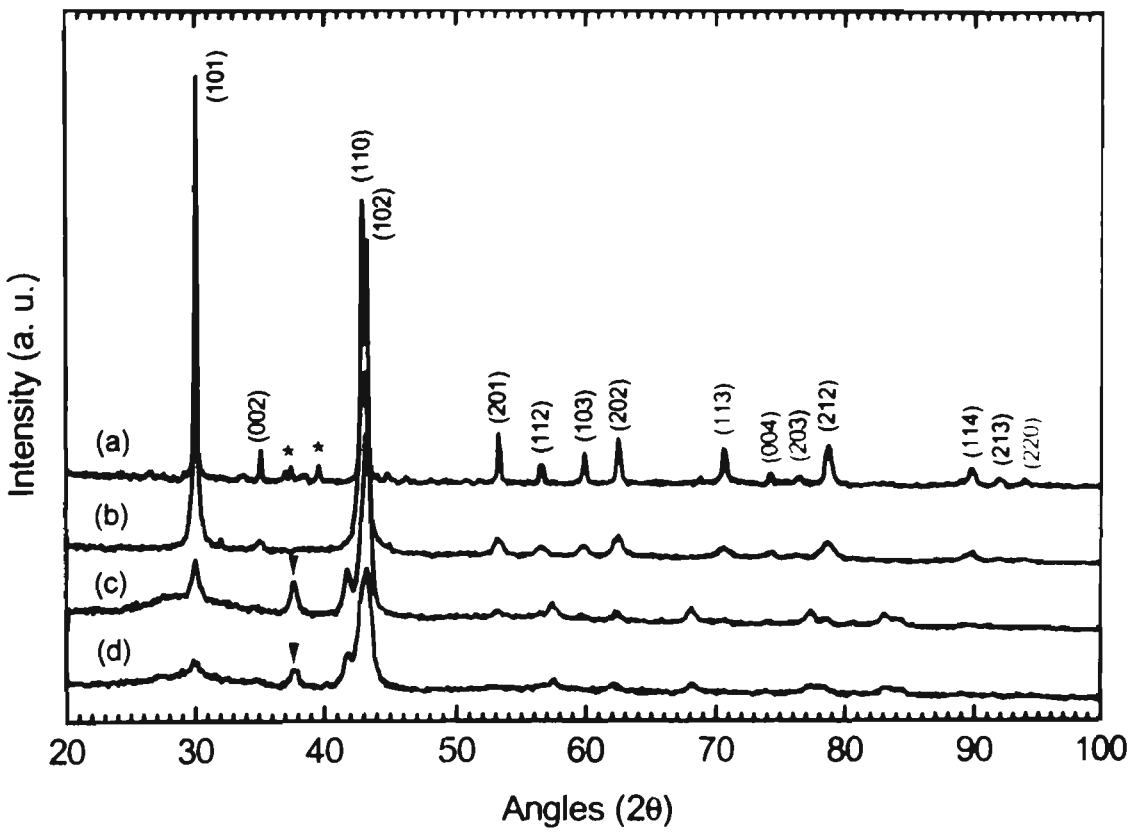

Fig. 6-1 X-ray diffraction patterns of eta-Cu_6Sn_5 alloys.

(a) Cu_6Sn_5 alloy prepared by sintered process.
(b) Cu_6Sn_5 alloy prepared by ball-milling for 18 hours.
(c) Cu_6Sn_5 alloy prepared by ball-milling for 46 hours.
(d) Cu_6Sn_5 alloy prepared by ball-milling for 110 hours.
* α-Sn, ▼ Cu_2O or SnO_2.

6.1.2. The Electrochemical Performance of eta-Cu_6Sn_5 alloy anodes.

Li/Cu_6Sn_5 cells were assembled to test the lithium storage capacity and cyclability of Cu_6Sn_5 anodes. The cells were cycled between 0-1.5 V at a constant current density of 0.25 mA/cm^2 (25mA/g). The lithium insertion into and extraction from Cu_6Sn_5 alloy are defined as discharge and charge respectively. The first discharge and charge profiles of Cu_6Sn_5 alloy electrodes are shown in Fig. 6-2. The ball-milled nanocrystalline Cu_6Sn_5 electrode demonstrated markedly different behaviour for lithium insertion compared to that of the sintered crystalline Cu_6Sn_5 alloy. In the first discharge,

nanocrystalline Cu_6Sn_5 alloy electrode delivered a capacity of 688 mAh/g, corresponding to approximately 25 moles of lithium insertion per mole of Cu_6Sn_5 alloy. Provided lithium alloys with Sn, the maximum lithium insertion achievable theoretically is equivalent to one mole of Cu_6Sn_5 alloy combining with 22 moles of Li to form $Li_{4.4}Sn$ alloy, with a capacity of 608 mAh/g. As shown in Fig. 6-1, a small amount of Sn and Cu oxides are generated during the long term ball-milling. The extra lithium insertion capacity of 80 mAh/g observed might be caused by lithium reacting with Sn or Cu oxides to form Li_2O. This part of the lithium cannot be extracted again, which is similar to the behaviour of tin based glass. A reversible capacity of 412 mAh/g was achieved in the first charging which is 60% of the initial discharge capacity. However, the first discharge capacity for sintered Cu_6Sn_5 alloy was only 284 mAh/g. The theoretical capacity for lithium insertion into Cu_6Sn_5 to form $Li_{13}Cu_6Sn_5$ (isostructural with Li_2CuSn) is 358 mAh/g. Here, the theoretical capacity has not been achieved, possibly due to the relatively large particle size.

With the scrutiny of the differential capacity vs. voltage profiles (the insets in Fig. 6-2), it might be seen that the ball-milled nanocrystalline Cu_6Sn_5 electrode shows several reduction peaks, corresponding to the formation of Li_2O and various Li_xSn alloys, which is similar to the behaviours of Sn, SnO, SnO_2 and $SiSnO_3$ electrodes [127]. By contrast, the crystalline Cu_6Sn_5 alloy electrode only shows one sharp reduction peak, which corresponds to the topotactic insertion of lithium into Cu_6Sn_5 alloy structure to form $Li_xCu_6Sn_5$. Consequently, the two different mechanisms for lithium reaction with ball-milled nanosize and sintered crystalline Cu_6Sn_5 alloys are proposed, as follows:

$$22Li + Cu_6Sn_5 \text{ (nanosize)} \Leftrightarrow 5Li_{4.4}Sn + Cu \quad \text{(Alloying process)} \tag{5.1}$$

$$13Li + Cu_6Sn_5 \text{ (coarse crystalline)} \Leftrightarrow Li_{13}Cu_6Sn_5 \quad \text{(Topotactic insertion process)} \tag{5.2}$$

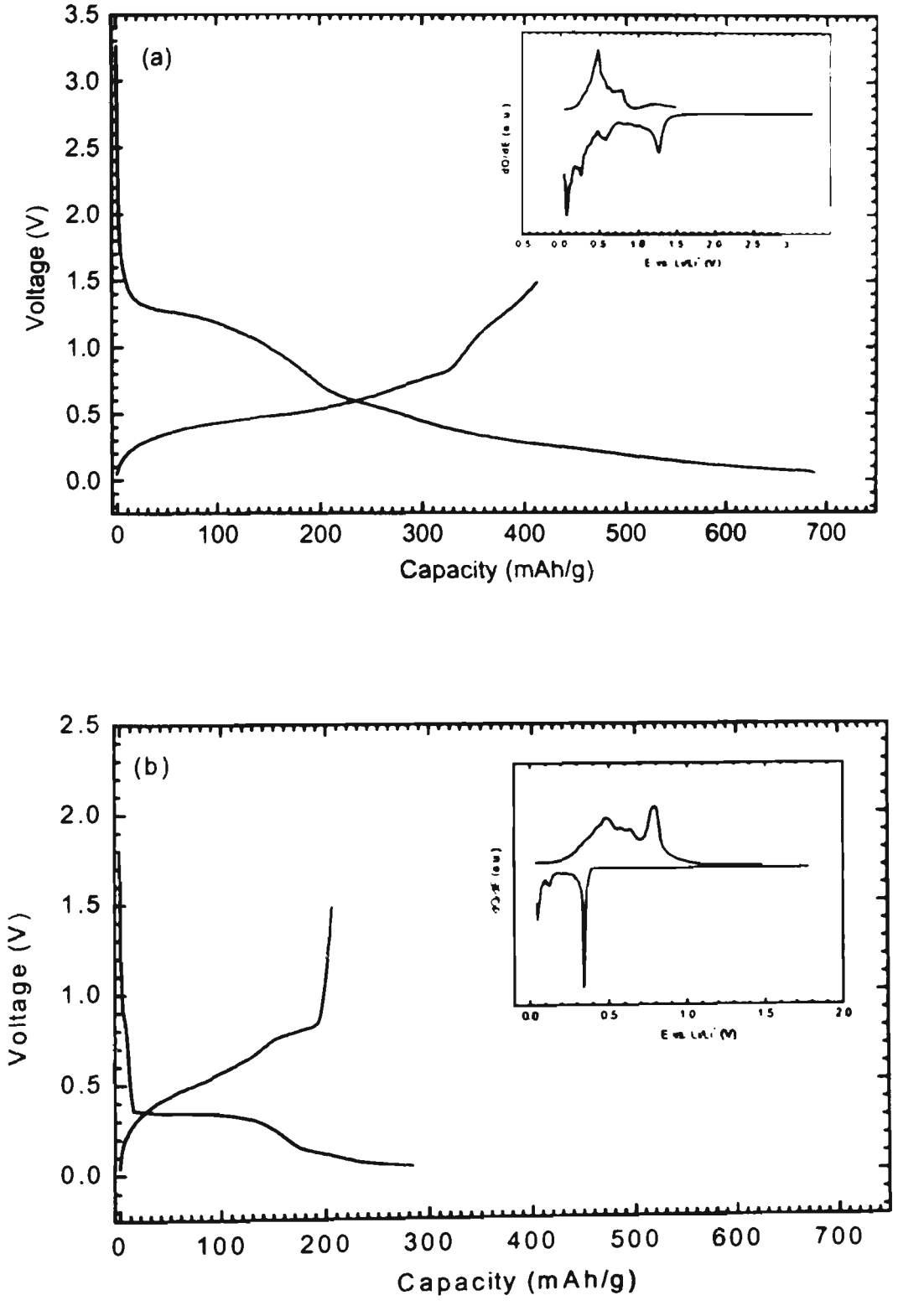

Fig. 6-2 The first discharge/charge profiles of Li/ Cu_6Sn_5 cells. The insets are the corresponding differential capacity vs. voltage.

(a) Ball-milled Cu_6Sn_5 alloy electrode (ball-milling for 110 hours).

(b) Sintered crystalline Cu_6Sn_5 alloy electrode.

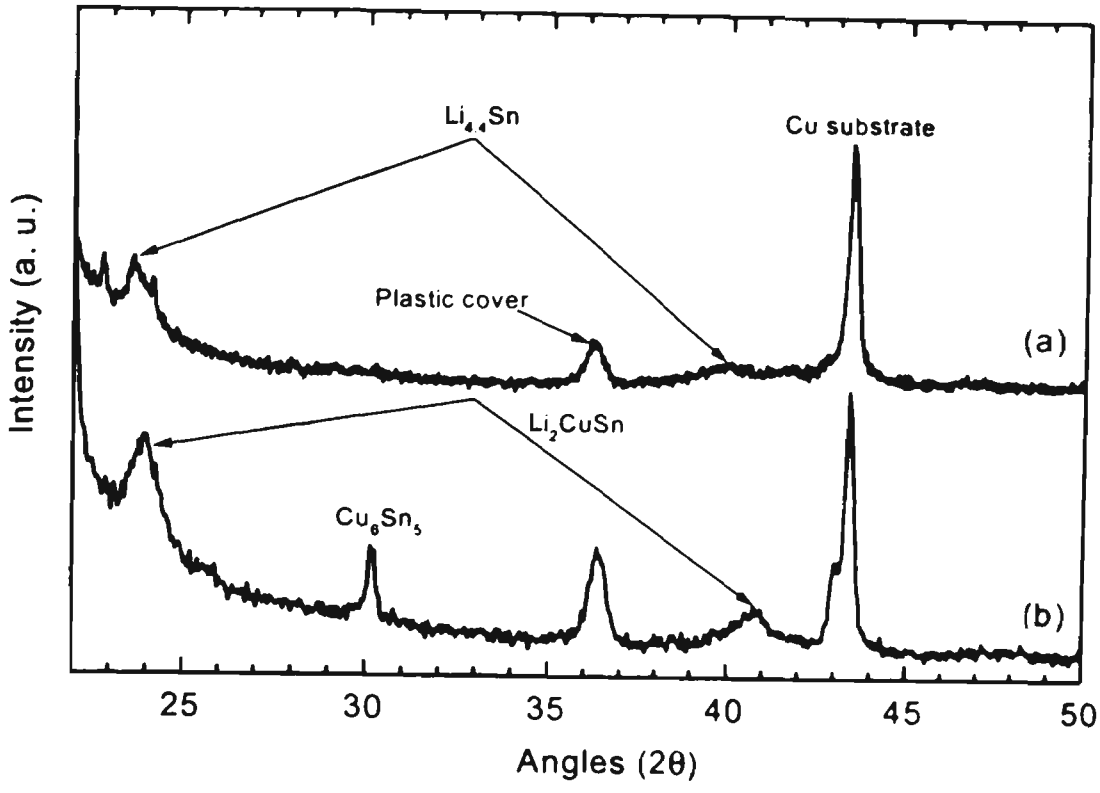

Fig. 6-3 The ex-situ x-ray diffraction patterns of Cu_6Sn_5 alloy electrodes in the fully discharged state.
(a) Ball-milled nanosize Cu_6Sn_5 alloy (ball-milling for 110 hours).
(b) Sintered crystalline Cu_6Sn_5 alloy.

In order to confirm these mechanisms, ex-situ x-ray diffraction was performed on the Cu_6Sn_5 electrode in the fully discharged state. The ex-situ XRD patterns are shown in Fig. 6-3. For the ball-milled nanocrystalline Cu_6Sn_5 electrode in the heavily lithiated state, $Li_{4.4}Sn$ is identified by the two diffraction peaks at $2\theta=23.5°$ and 39.9°. The broad $2\theta=39.9°$ peak suggests a very fine particle size of $Li_{4.4}Sn$. Also, the Li_2CuSn phase was detected for sintered crystalline Cu_6Sn_5 in the fully discharged state, characterized by the diffraction peaks at $2\theta=24.2°$ and 40.7° respectively. The unreacted Cu_6Sn_5 phase was also presented in the XRD pattern. These unreacted Cu_6Sn_5 alloys could be responsible for the low discharge capacity of crystalline Cu_6Sn_5 alloy electrode due to

the large particle size and limited kinetics for lithium insertion. No Li-Sn alloy phase was found, which confirmed the process of lithium insertion into crystalline Cu_6Sn_5 to form the compound $Li_xCu_6Sn_5$.

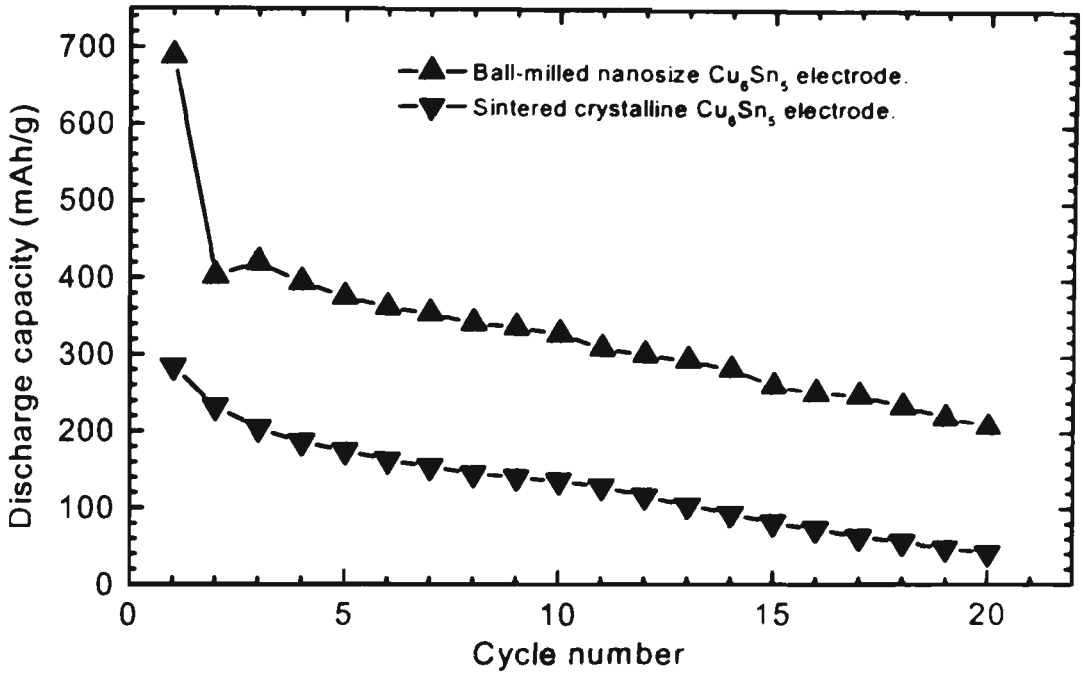

Fig. 6-4 Discharge capacity vs. cycle number for Li/Cu_6Sn_5 cells.

Fig. 6 - 4 shows the discharge capacity vs. cycle number for the two different kinds of Cu_6Sn_5 alloys. The capacity for both nanosize and normal crystal size Cu_6Sn_5 alloys declines on cycling quite quickly. Further work needs to be done to identify the mechanism for this phenomenon and to improve the cyclability of the Cu_6Sn_5 alloy electrodes.

In conclusion, it was found that there were two different mechanisms for lithium reacting with ball-milled nanocrystalline and sintered crystalline eta-Cu_6Sn_5 alloys. The reaction of lithium with nanocrystalline Cu_6Sn_5 is an alloying process, in which lithium alloys with Sn to form Li_xSn and generates Cu simultaneously. By contrast, an insertion

process takes place in the normal crystalline Cu_6Sn_5 alloy, in which Li ions are inserted into the Cu_6Sn_5 structure to form $Li_xCu_6Sn_5$. Nanocrystalline Cu_6Sn_5 alloy demonstrated a much higher initial lithium storage capacity than that of the crystalline Cu_6Sn_5.

6.2 Lithium Storage Alloys with Si as Active Center

So far, in most cases, the lithium storage alloys have utilized Sn as the active element. Actually, another active element Si can also alloy with Li to form Li_xSi to a maximum uptake of $Li_{21}Si_5$ with a theoretical capacity of 4000 mAh g. It has been reported that a nano-Si composite electrode can deliver a large Li insertion capacity of 1700mAh/g, but with the sacrifice of volumetric capacity due to the use of 40% carbon black to enhance the conductivity and provide a ductile matrix [201].

Two types of nanosize intermetallic alloy powders NiSi and FeSi were prepared by high energy ball-milling. These two types of alloys were used as electrode materials in lithium test cells. During lithium insertion into these alloy electrodes, Si atoms act as active centers, which react with Li to form Li_xSi alloys.

6.2.1 Experimental

NiSi and FeSi alloy powders were prepared by high energy ball-milling. The elemental powders of Si, Ni or Fe as well as hardened steel balls were put into the steel vial. The vial was initially evacuated and then filled with argon. The alloy powders were characterised by x-ray diffraction and scanning electron microscopy.

The NiSi and FeSi electrodes were prepared by dispersing 80 wt% active materials, 18 wt% carbon black and 2 wt% polyvinylidene fluoride (PVdF) binder in dimethyl phthalate to form a slurry, which was then spread on to the copper foil. The CR2032 coin cells of Li/NiSi and Li/FeSi were assembled in an argon filled glove-box. The cells were galvanostatically charged and discharged at a current density of 80 $\mu A/cm^2$ in the voltage range of 0 - 2.5 V.

6.2.2 Physical characterization of NiSi and FeSi alloys

X-ray diffraction patterns of NiSi and FeSi alloy powders are shown in Fig. 6-5. The pure NiSi alloy powders were obtained by ball-milling as shown in Fig. 6-5 (a). The diffraction peaks are broadened, indicating small particle size and internal stress. However, only a mixture of FeSi and Si was obtained instead of pure FeSi alloys. This was probably because it is more difficult to synthesise FeSi alloy through ball-milling than by conventional methods. Assuming that the peak broading was entirely due to particle size, the average grain size was calculated according to the Scherrer equation: crystallite size $=k\lambda/\beta Cos\theta$. The estimated average crystallite size for NiSi and FeSi powders was about 4-6 nm. Fig. 6-6 shows the SEM micrographs of NiSi and FeSi-Si alloys. In Fig. 6-6 (a), quite homogeneous NiSi alloy powders were produced by ball-milling. Due to the ultrafine nature of these grains, they tend to form large agglomerates, which are presented in SEM micrograph. For the FeSi-Si powders, well dispersed FeSi-Si particles were observed together with large unalloyed Si particles. EDS analysis confirmed that these large particles were elemental Si.

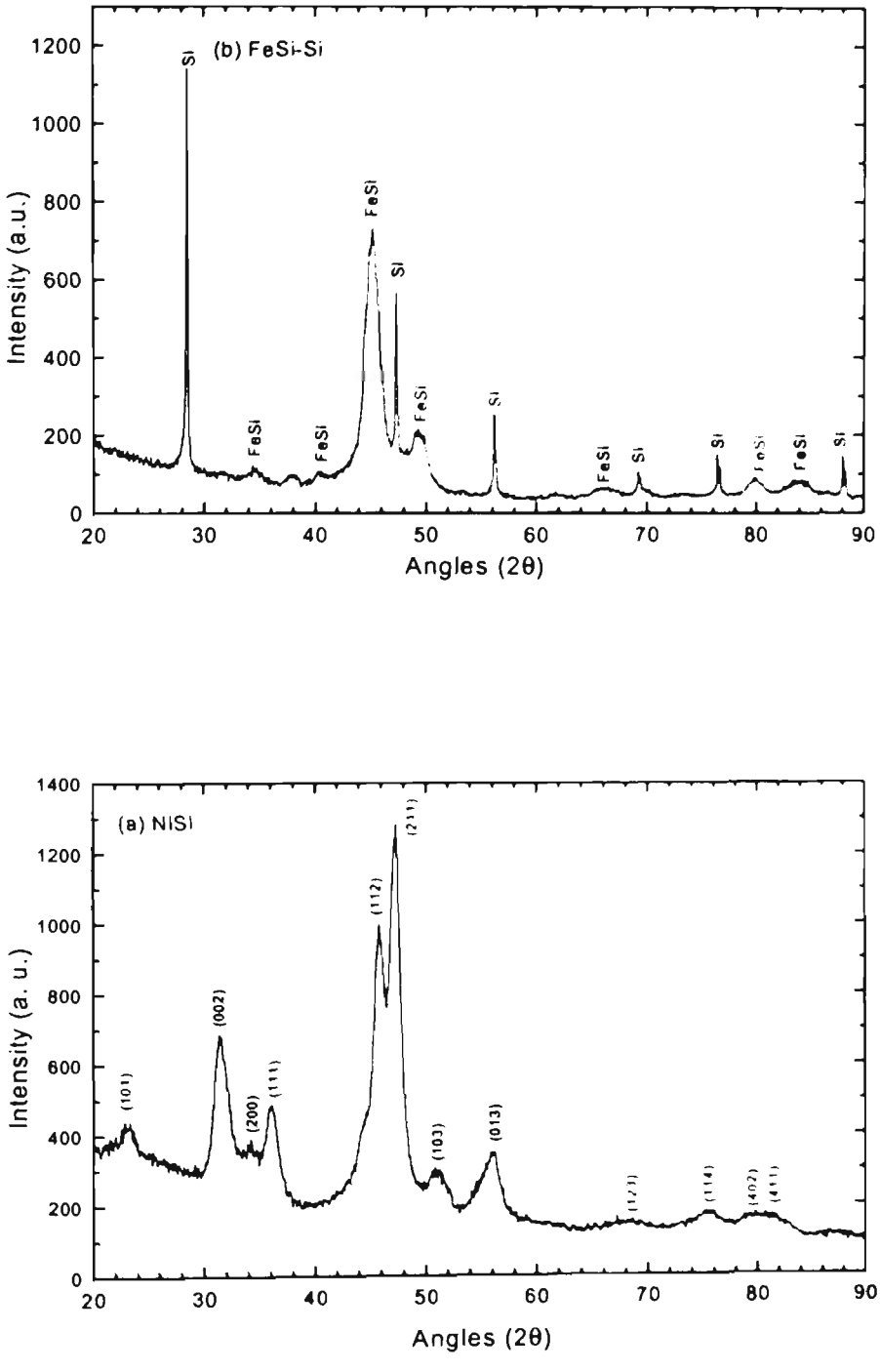

Fig. 6-5 X-ray diffraction patterns of (a) NiSi powders. (b) FeSi-Si powders.

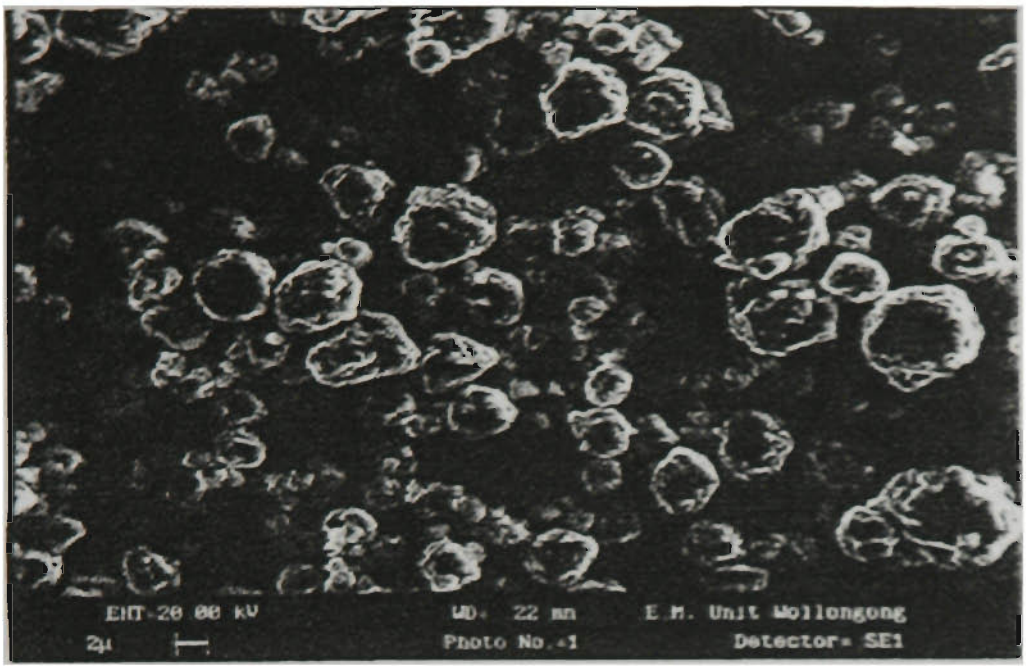

(a)

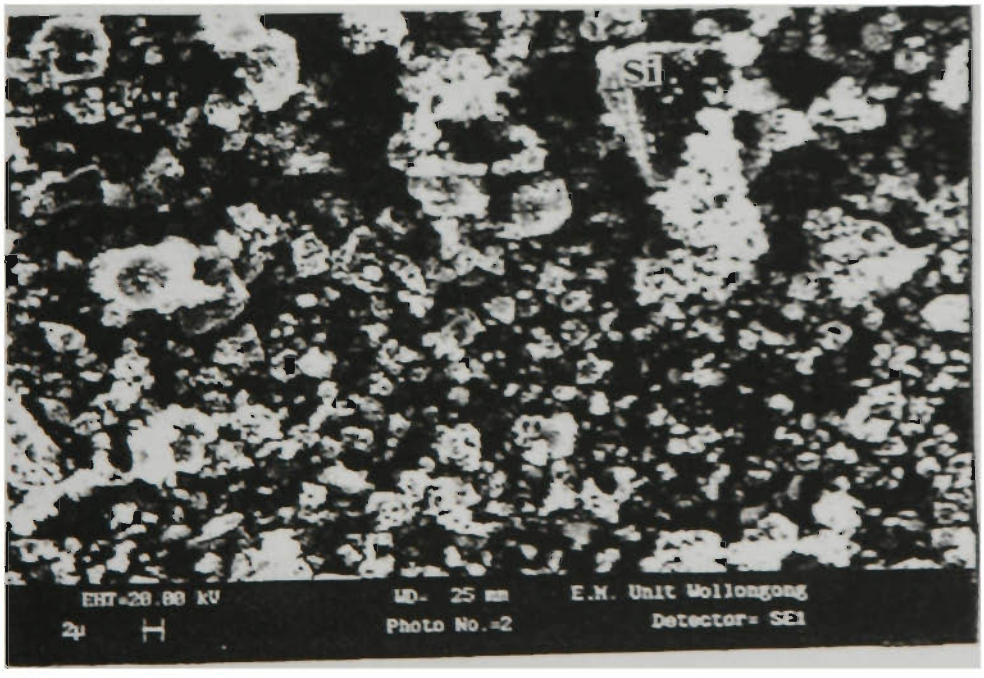

(b)

Fig. 6-6 SEM micrographs of ball-milled alloy powders.
(a) NiSi powders. (b) FeSi-Si powders.

6.2.3 Electrochemical properties of NiSi and FeSi alloys electrode

Several Li/NiSi and Li/FeSi-Si coin cells were assembled to examine the lithium insertion properties of NiSi and FeSi-Si electrodes. Fig. 6-7 shows the discharge curves of two of these cells. The open-circuit potential of NiSi and FeSi-Si electrodes are in the range of 2.8-3.2 V vs. Li/Li^+ in the unlithiated state. As shown in Fig. 6-7 (a) for NiSi electrode, when discharged, the potential of the electrode quickly dropped to 2.0 V and then followed an approximately half parabolic curve until the cut-off voltage of 0 V. No obvious discharge plateau was observed. The first discharge capacity of 1180 mAh/g was achieved, corresponding to the insertion of 3.82 moles Li per mole of NiSi. If all of the Si in the NiSi compound reacts with Li to form $Li_{4.2}Si$, the theoretical capacity for NiSi alloy would be 1297 mAh/g. Here, the lithium storage capacity approached close to its theoretical value in the first discharge. However, after the first charge, only 80% of the lithium ions could be reversibility extracted. In the subsequent discharge/charge cycles, the capacity of the NiSi electrode gradually degraded. For the FeSi-Si electrode, in general, the shape of discharge curve is different from that of the NiSi electrode. When discharging, the voltage of FeSi-Si electrode dropped to 0.3 V more quickly, compared to the NiSi electrode. In the first discharge, there exists quite a large polarisation resistance. This is probably related to the presence of Si. Since Si still retained a coarse particle size after ball-milling (as shown in Fig. 1(b)), it could participate in the lithiation reaction. The kinetics of the reaction of coarse Si with Li are slow.

In the NiSi and FeSi-Si electrodes, the elements Ni and Fe are inactive to Li, and only Si can react with Li to form Li_xSi alloys. Thus, the following mechanism was proposed for the reaction of NiSi and FeSi with Li, based on the reaction mechanism of Sn and Sn-Sb with Li in lithium cells [202].

$$xLi^+ + xe^- + NiSi \longrightarrow Li_xSi + Ni \rightleftharpoons Ni + Si + xLi^+ + xe^- \quad (6.3)$$

$$xLi^+ + xe^- + FeSi \longrightarrow Li_xSi + Fe \rightleftharpoons Fe + Si + xLi^+ + xe^- \quad (6.4)$$

After the first discharge, when lithium was extracted from the alloy electrode, it is assumed that Ni or Fe and Si are kept in their elemental state. In that case, Ni or Fe will act as a buffering matrix for the formation of Li_xSi in the subsequent cycle.

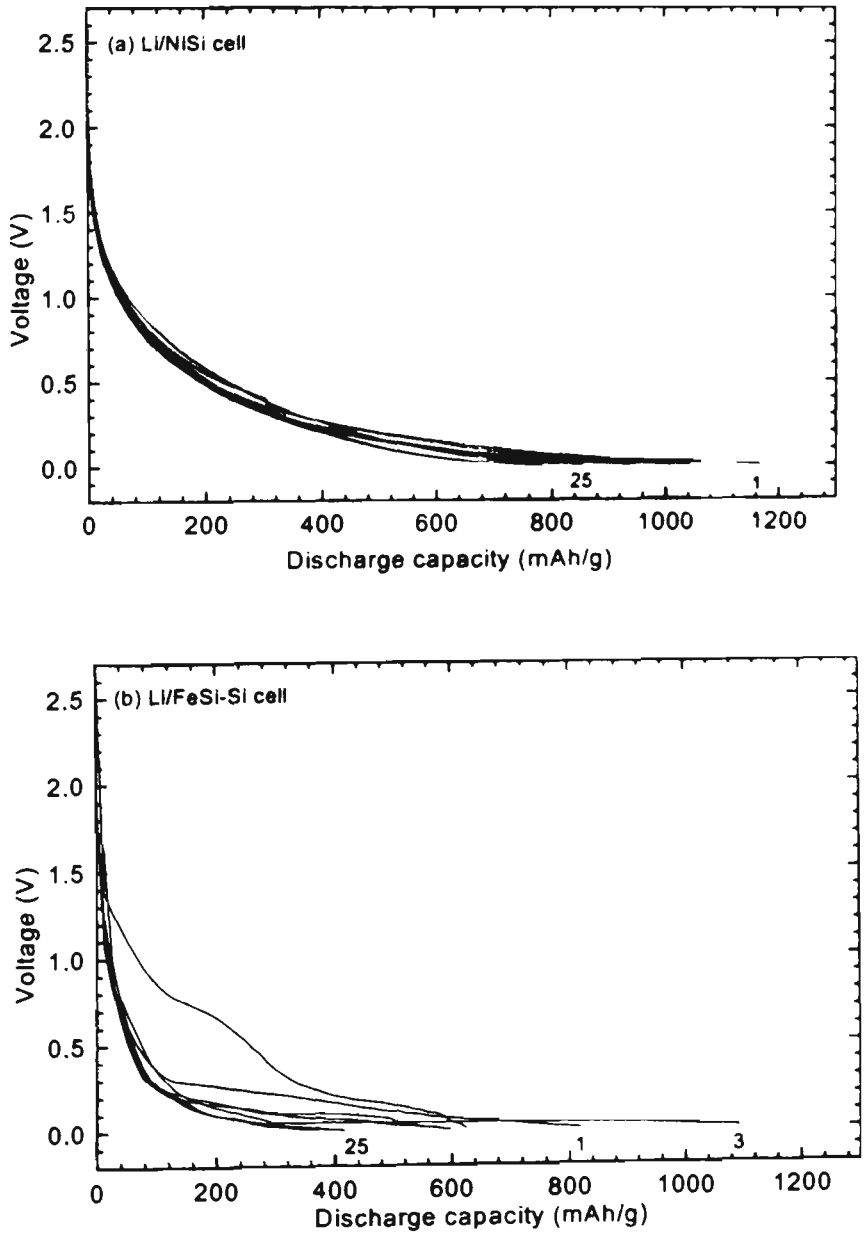

Fig. 6-7 The discharge curves of (a) Li/NiSi cell. (b) Li/FeSi-Si cell.

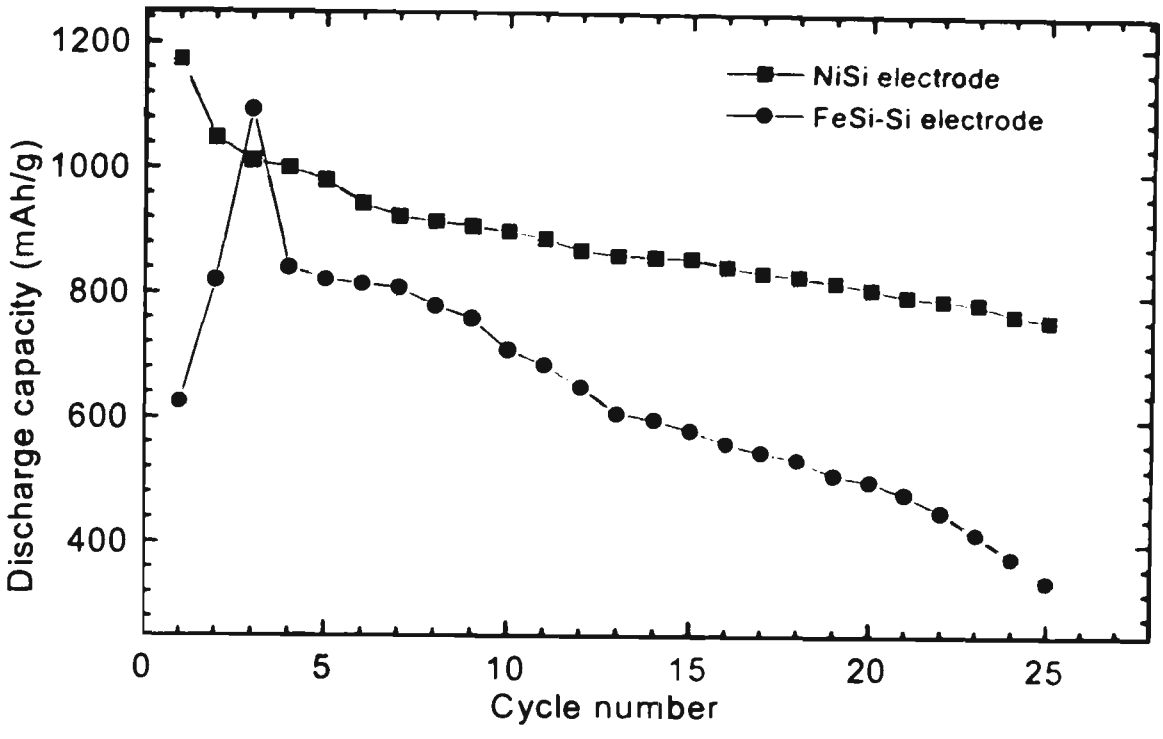

Fig. 6-8 The discharge capacity of NiSi and FeSi-Si electrodes.

Fig. 6-8 shows the degradation of the discharge capacity of NiSi and FeSi-Si electrodes with cycle number. FeSi-Si electrode reached its maximum capacity in the third cycle instead of in the first cycle for the NiSi electrode. The rate of capacity decrease for the FeSi-Si electrode is faster than that of the NiSi electrode, which could possibly relate to the presence of large particles of Si in the FeSi-Si electrode. The cycling behavior of the NiSi electrode seems relatively good, but it still can not compete with commercial carbon materials. During the charge/discharge cycle, some Li was trapped with Si in the electrode. It is very critical to utilise all of the Li source in the battery system. This could be realised through the optimisation of the crystal structure and morphology of the electrode materials in the future. In that case, nano NiSi or FeSi could be a choice as

an anodic materials for lithium ion batteries with double or even triple capacity of carbonaceous materials.

In summary, it can be seen that nanocrystalline NiSi and FeSi-Si powders can be synthesised via high energy ball-milling. When NiSi was used as electrode in lithium cells, it demonstrated a high lithium storage capacity of 1180 mAh/g in the initial discharge, in which Si acted as the active element to combine with Li to form Li_xSi. This reaction is partially reversible and its capacity degraded with each cycle. Further optimization of the synthesis of NiSi could lead to the improvement of the electrochemical performance of the NiSi electrode.

6.3 Graphite-Tin Composites as Anode Materials for Lithium-ion Batteries

The development of a new generation of lithium-ion batteries demands new cathode and anode materials with higher energy density than that of the existing systems. The new high capacity cathode materials will still need some time to develop. By contrast, the capacity of carbon anode materials has been improved greatly in the past few years from early types of soft carbons (200-240 mAh/g) to more recent MCMB graphites (300-340 mAh/g) [203, 204]. Some carbonaceous compounds (hard carbon) have demonstrated even higher capacity of about 700 mAh/g [205 - 208]. In addition to carbon materials, some binary or ternary lithium alloys, intermetallic alloys and tin oxide glass have recently attracted worldwide attention. In particular, tin was used as the active element because it can combine with Li to form $Li_{22}Sn_5$ alloy with a theoretical capacity of 990 mAh/g. The main shortcoming for Sn, MSn alloys and tin oxides is the volume expansion during the process of alloying with Li, which causes crumbling and cracking of the electrode, inducing a very short cycle life. Dahn et al

[198 – 200] have prepared a series of nano-crystalline Fe-Sn intermetallic alloys, which demonstrated high lithium storage capacity and reasonable cyclability.

The objective of this investigation is to combine the high lithium storage capacity of the element Sn and the stable cyclability of graphite. Graphite-tin composites with different content of tin were prepared by high energy ball milling. The physical properties and microstructure of the C-Sn composites were characterized by XRD, TEM and HREM. The electrochemical performance of the composites as anodes was examined using lithium test cells.

6.3.1 Preparation and Structural characterization of C-Sn composites

The ball-milled graphite and tin powders were produced by high energy ball-milling. The mixtures of pure graphite and tin with different atomic ratios (Sn:C = 0, 0.1, 0.2) were put into a stainless steel vial. The vial was evacuated and then purged with pure argon. The powders produced were characterised by x-ray diffraction and HREM. The morphology and microstructure of ball-milled powders were observed by high-resolution electron microscopy, using a JEOL 2010 high-resolution electron microscope.

The typical XRD patterns of ball milled graphite and graphite-tin composites are shown in Fig. 6-9. For comparison, the XRD pattern of the unmilled graphite is also shown. The unmilled graphite is a well-graphitized 2H graphite with strong (002) diffraction intensity. After ball milling, the diffraction lines (002) (100) and (101) of graphite became very broad and were shifted to lower angles. The (004) diffraction line was weak and indistinguishable. The interlayer distances (d_{002}) of graphite were 3.355 Å, 3.675 Å, 3.392 Å and 3.362 Å for unmilled graphite, ball milled graphite, $C_{0.8}Sn_{0.2}$ and $C_{0.9}Sn_{0.1}$ respectively. In general, the values of d_{002} for graphite increase after ball

milling. The d_{002} for ball-milled graphite in our investigation is the same as the result found by Shen and co-workers [209] (d_{002}=3.68Å). It has been reported that the increase in d_{002} by ball milling is attributed to the introduction of interstitial carbon atoms into the initial pristine graphite structure [210]. However, the d_{002} values in $C_{0.8}Sn_{0.2}$ and $C_{0.9}Sn_{0.1}$ composites are much smaller. This might mean that Sn could prevent the interstitial carbon atoms from entering into the pristine graphite structure during ball milling. As shown in Fig. 6-9 , the degree of diffraction peak broadening for Sn is much smaller than graphite on ball milling. Therefore, it follows that the effect of ball milling on reducing the particle size of tin is less than that on graphite.

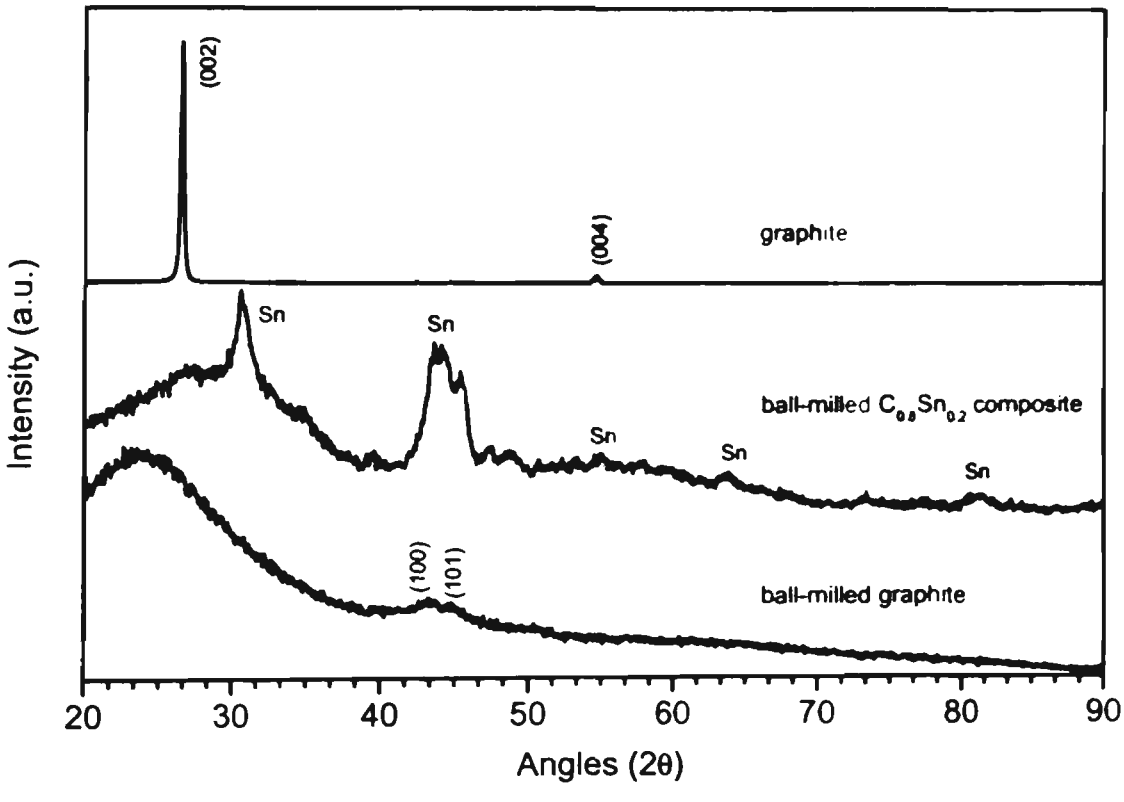

Fig. 6-9 Typical x-ray diffraction patterns of C-Sn composites.

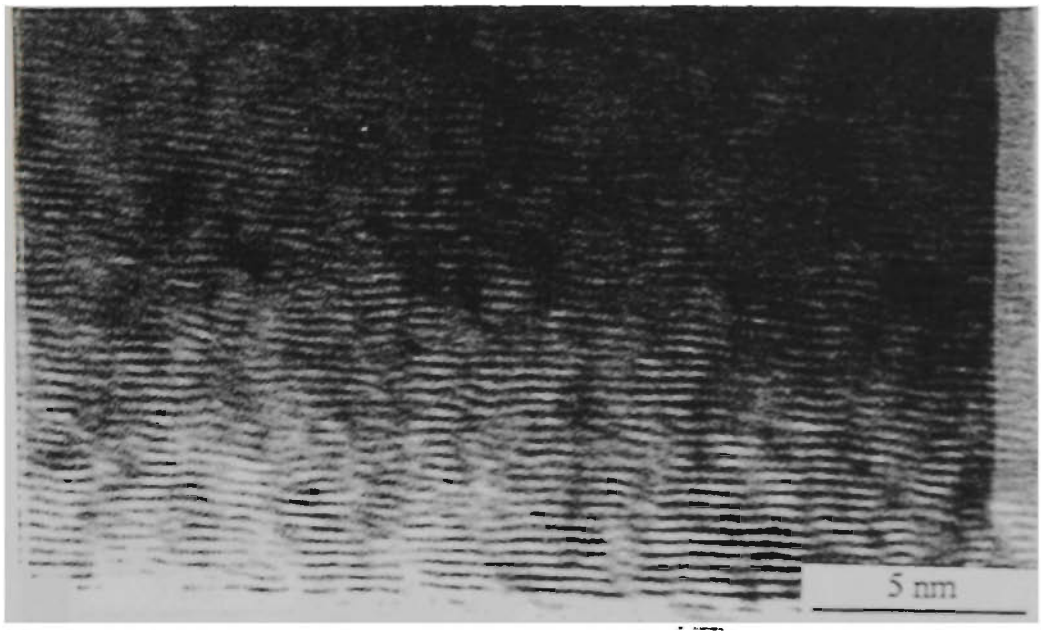

(a)

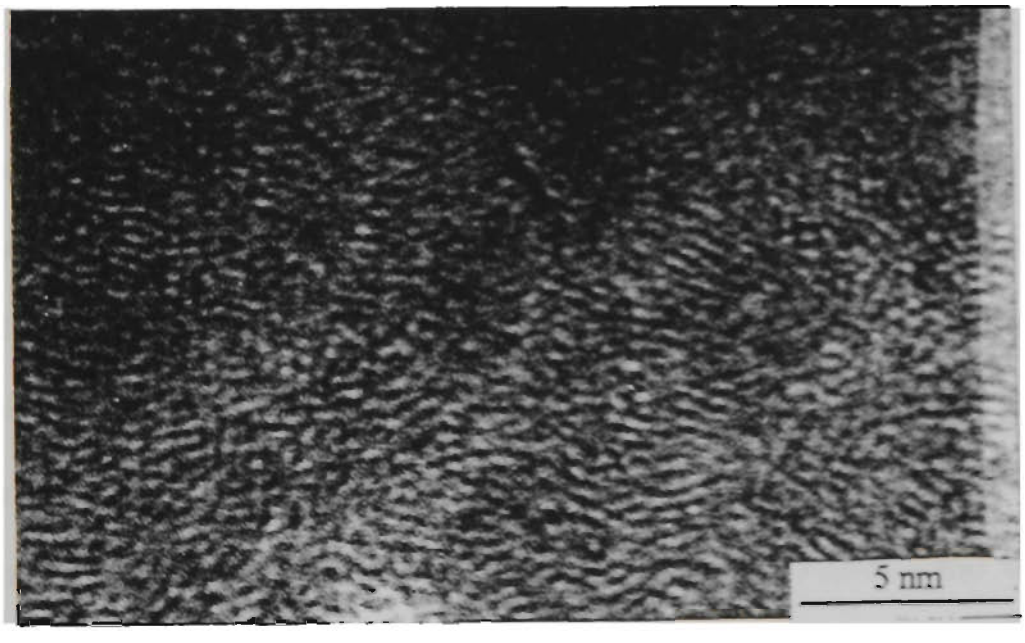

(b)

Fig. 6-10 HREM image of (a) pristine graphite (b) ball-milled graphite.

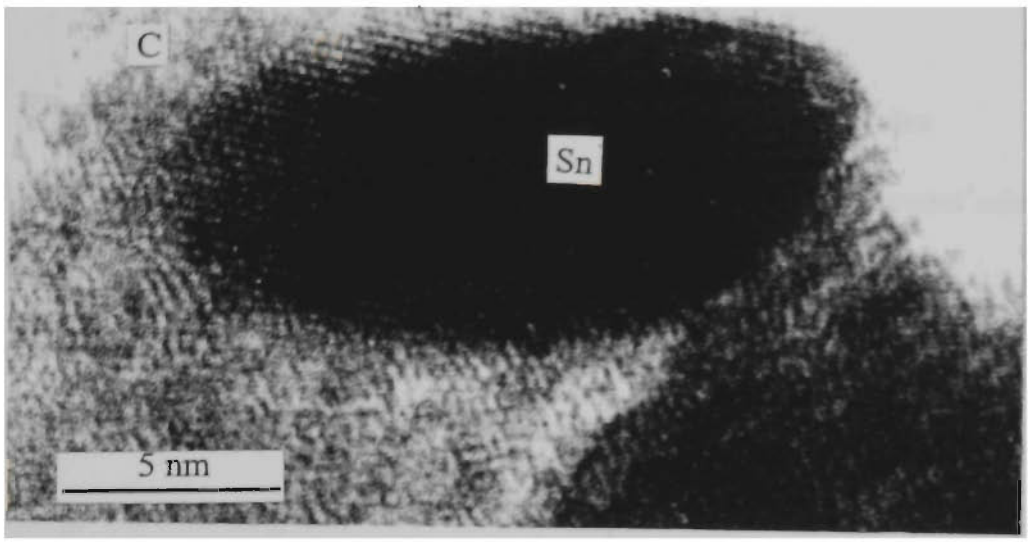

Fig. 6-11 HREM image of ball-milled $C_{0.8}Sn_{0.2}$ composite

The microstructure of ball milled graphite and graphite-tin composites were observed by HREM. Fig. 6-10 shows the HREM images of pristine graphite and ball-milled graphite. The pristine graphite is a well organized crystalline structure. After intensive ball milling, graphite became disordered and amorphous. The graphene layers are wrinkled and the interlayer spacings are irregular. Wang et al. [211] proposed that ball milled graphite consists of many basic structured units (BSU) and the wrinkled layers may be attributed to the interstitial atoms. Microcavities were observed on the edge of BSUs as shown in Fig. 6-10 (b). The HREM image of ball milled graphite-tin composite $C_{0.8}Sn_{0.2}$ is shown in Fig. 6-11. After ball milling, the Sn particles are broken down to 15-20 nm, but still attain an ordered crystalline state. Nanocrystalline Sn particles are embedded in a disordered or amorphous carbon matrix. The boundaries between Sn particles and C matrix are very smooth. This demonstrates that there is no

obvious gap between Sn particles and the C matrix, which should assist Li^+ ion diffusion and electron transfer between Sn particles and the amorphous graphite matrix.

6.3.2 Electrochemical characteristics of C-Sn composite electrodes

The electrochemical performance of $C_{1-x}Sn_x$ composites was measured using $C_{1-x}Sn_x$ as the working electrode and lithium metal as the counter electrode. Fig. 6-12 shows the discharge/charge profiles for ball-milled graphite and graphite-tin composite electrodes. The first discharge capacity for ball milled C, $C_{0.9}Sn_{0.1}$ and $C_{0.8}Sn_{0.2}$ electrodes were 820 mAh/g, 1250 mAh/g and 1070 mAh/g respectively. With the addition of Sn in graphite by ball milling, the specific capacity increased but not in proportion to the Sn content. The $C_{0.9}Sn_{0.1}$ composite electrode demonstrated the highest capacity. It has been reported that the electrochemical performance of ball milled C is related to the type of mixer and independent of the morphology and of the state of the starting materials [212]. As indicated from the XRD pattern after ball milling, graphite became disordered and amorphous, in which there were vacancies, microcavities and a disorganized region. The lithium can be inserted into these vacancies, microcavities, voids or the edges of BSU layers. Most of the reversible capacity is due to lithium storage in these regions [213, 214]. However a large irreversible capacity of 420 mAh/g in the first charge/discharge for ball milled C electrode was observed. This irreversible capacity, mainly between 1.2 V and 0.6 V, is supposed to be caused by the decomposition of the electrolyte and the formation of a passivation film on the surface of the electrode due to the larger surface area of ball milled graphite. The increased capacities for $C_{0.8}Sn_{0.2}$ and $C_{0.9}Sn_{0.1}$ electrodes should be attributed to the nano-dispersed Sn in the graphite matrix, because the ball milling condition was identical for all three samples. It is well known that Sn can react with Li to form $Li_{4.4}Sn$ alloy.

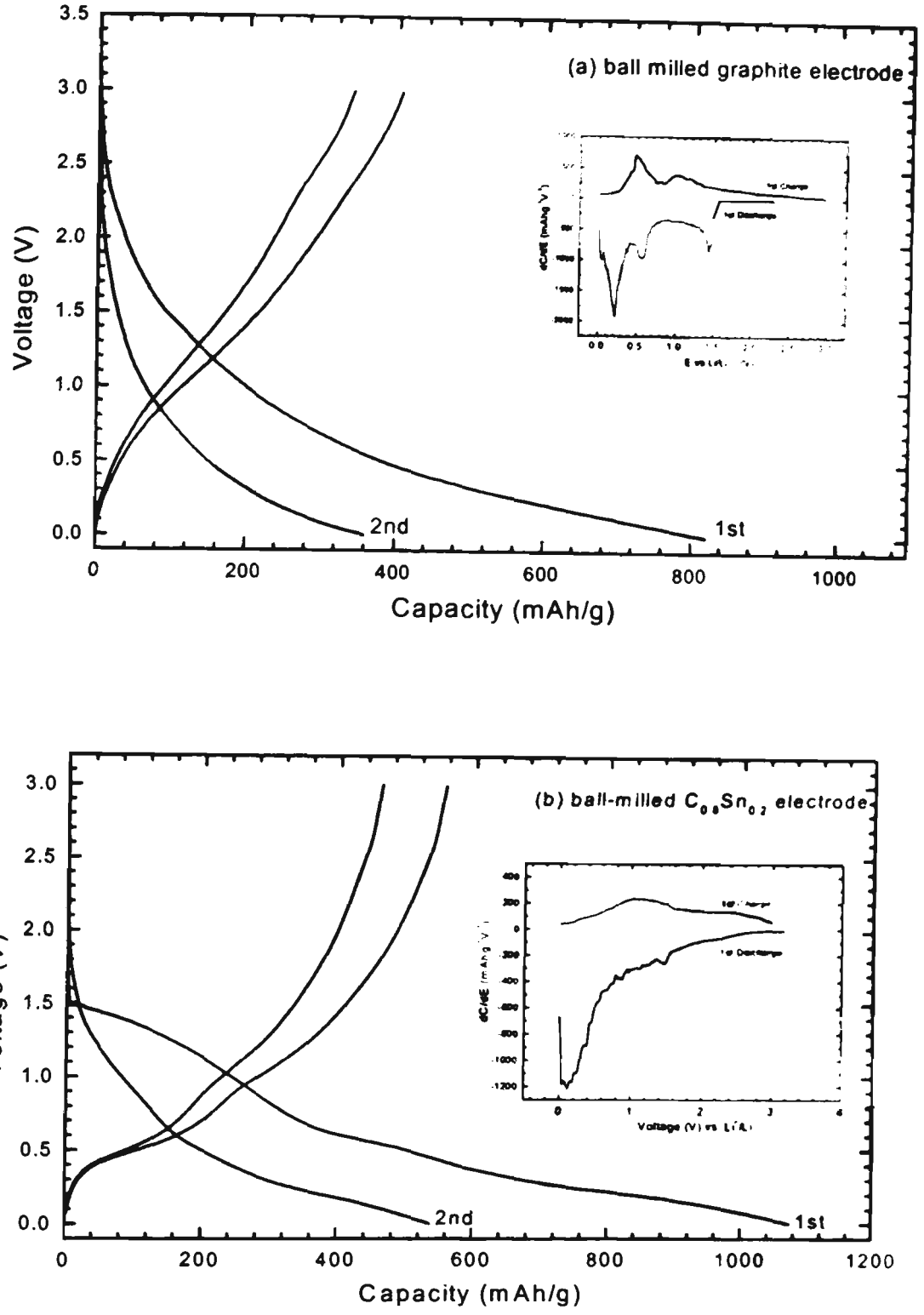

Fig. 6-12 Discharge and charge curves of (a) ball-milled graphite and (b) graphite-tin composite electrodes. The differential capacity vs. voltage are shown in inset.

The differential capacity plots of the first discharge/charge for ball-milled graphite and ball-milled $C_{0.8}Sn_{0.2}$ electrodes was present in the inset in Fig. 6-12 (a). In these plots, it was found that there were some differences between the ball-milled graphite and the $C_{0.8}Sn_{0.2}$ composite electrodes. In Fig. 6-12(a), there are three peaks at about 1.4 V 0.55 V, and 0.1 V respectively during the discharge process. The 1.4 V peak also appears in the differential capacity curves of $C_{0.8}Sn_{0.2}$ electrode during discharge. This is believed to originate from lithium insertion into vacancies in ball milled graphite, since lithium insertion into vacancies and disorganized regions is at a higher potential than that between interlayers [215]. In Fig. 12(b), the differential peaks between 0.5 and 0.6 V during charge and discharge are associated with the alloying reaction between Sn and Li. This means that Sn participated in the reaction. An attempt has been made to prove this mechanism by ex-situ x-ray diffraction. However, the Li-Sn alloy phase was not identified after the C-Sn composite electrodes were discharged. This is probably because the Li-Sn alloys formed are in a nanocrystalline or amorphous state. The lithium reaction with Sn to form Li_xSn alloys can result in a volume increase by 676%, which could induce serious cracking or crumbling of Li-Sn alloy. Any cracking of the Li-Sn alloys will cause the isolation of Sn, increase the impedance and eventually decrease the capacity of the electrode. However, Sn particles were reduced to the nanocrystalline state and dispersed in the graphite matrix after ball milling. Also, a ductile graphite matrix could buffer the expansion of the alloy volume. Therefore, the cyclability of the electrode can be improved. This is shown in Fig. 6-13. The $C_{0.8}Sn_{0.2}$ and $C_{0.9}Sn_{0.1}$ electrodes demonstrated a better rechargeability than that of the ball milled C electrode. From the previous reports [211, 216], ball milled graphite delivered a large initial lithium insertion capacity, but the capacity degraded with cycling quite quickly. This problem could be solved by optimizing the ball milling conditions to produce

carbon materials with appropriate crystal structure and microstructure. Furthermore, adding active Sn to the carbon matrix can improve the capacity, and if elementary Sn is dispersed properly, a good cyclability can be achieved.

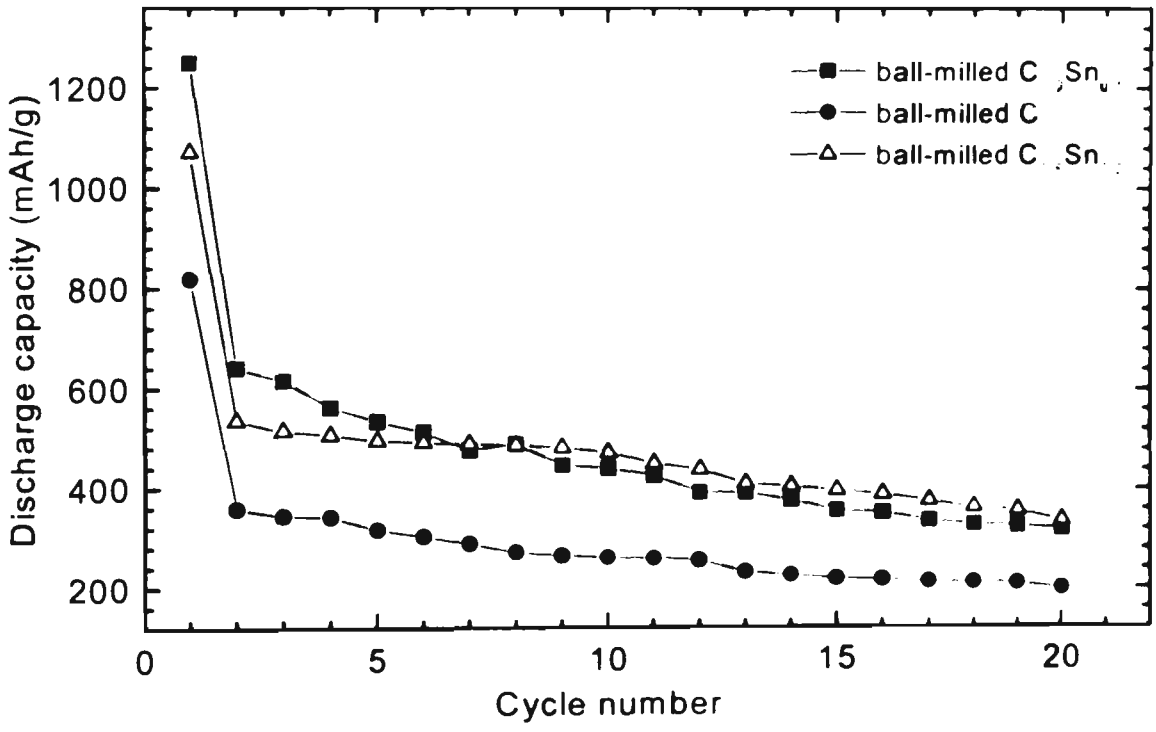

Fig. 6-13 The discharge capacities vs. cycle number for ball-milled graphite, $C_{0.8}Sn_{0.2}$ and $C_{0.9}Sn_{0.1}$ composite electrodes.

In summary, $C_{1-x}Sn_x$ composites can be prepared by mechanically ball-milling raw graphite and tin powders. Graphite was pulverized to a disorganized amorphous state. Sn became nanocrystalline and embedded in the graphite matrix. Electrochemical tests show that $C_{1-x}Sn_x$ composite electrodes can deliver a large lithium storage capacity of approximately 800-1250 mAh/g, which is 2-3 times that of graphite. However, a large irreversible capacity after the first cycle prevents their practical application. Optimization of conditions of materials preparation can probably overcome these

disadvantages. Therefore, graphite-tin composites appear to be a good candidate material for anodes in lithium-ion batteries.

Chapter 7 Identifying New Anode Materials for Li-ion Batteries Based on their Structural Characteristics

From a structural point of view, if there exists a two-dimensional channel or three-dimensional tunnel in the structure of a compound with vacancies, then, lithium ions could be reversibly inserted into and extracted from its structure. Ideally, the metal ion in the compound should be multivalent, so that it can accept or donate electrons. Many oxide compounds meet the above conditions.

7.1 Spinel $Li[Li_{1/3}Ti_{5/3}]O_4$ as an Anode Material for Lithium-ion Batteries

The main drawback for carbonaceous materials as anodes in the lithium-ion battery is the passivation film formed during the first charging, which consumes lithium from the cathode [217-219]. This passivation layer could decompose at higher temperature inducing failure of the cell and even ignition of the battery. The safety concern still exists.

Spinel materials of the type $Li[M_2]O_4$ have a cubic symmetry $Fd\bar{3}m$ which provides a three dimensional tunnel for lithium diffusion. The strong M-O bond maintains the $[M_2]O_4$ framework during lithium insertion and extraction. The defect spinels $Li[Li_{1/3}M_{5/3}]O_4$ (M=Mn, Ti) are extremely tolerant to cycling because the volume of the cubic unit cell changes less than 1%. $Li[Li_{1/3}Ti_{5/3}]O_4$ has been identified by Ohzuku et al. as a zero-strain insertion material with excellent cyclability [220]. However, there is no detailed report on the investigation of the kinetic process of the $Li[Li_{1/3}Ti_{5/3}]O_4$ electrode.

An investigation of the synthesis and electrochemical characteristics of the spinel $Li[Li_{1/3}Ti_{5/3}]O_4$ is described. Firstly, $Li[Li_{1/3}Ti_{5/3}]O_4$ was used as the cathode in a $Li/Li[Li_{1/3}Ti_{5/3}]O_4$ cell. In this system, AC impedance was employed to characterise the

$Li[Li_{1/3}Ti_{5/3}]O_4$ electrode. Secondly, $Li[Li_{1/3}Ti_{5/3}]O_4$ was used as anode coupled with high voltage insertion materials such as $LiCoO_2$ and $LiMn_2O_4$ to construct lithium ion cells.

7.1.1 Synthesis and structural characterization of $Li[Li_{1/3}Ti_{5/3}]O_4$ spinel

The spinel $Li[Li_{1/3}Ti_{5/3}]O_4$ was synthesised by two methods. The first required heating stoichiometric TiO_2 and $LiOH.H_2O$ at 850°C for 20 hours under an oxygen stream. The second involved heating precursors at 1000°C for 20 hours in air, providing 8 mol % excess Li to compensate for the loss of Li_2O at high temperature.

Fig. 7-1 shows the x-ray patterns of $Li[Li_{1/3}Ti_{5/3}]O_4$ synthesised by these two different methods. The $Li[Li_{1/3}Ti_{5/3}]O_4$ synthesised at 1000°C with 8 mol% excess Li contained an impurity phase which was identified to be Li_2TiO_3. The single phase $Li[Li_{1/3}Ti_{5/3}]O_4$ compound was obtained by heating stoichiometric precursor materials at 850°C under an oxygen stream. This sample was chosen to fabricate electrodes for lithium test cells. All diffraction peaks were indexed assuming a face-centered cubic system ($Fd\bar{3}m$ space group). Lithium ions are at 8a tetrahedral sites. Lithium ions and titanium ions are located at octahedral 16d sites with ratio Li:Ti=1:5, and oxygen ions are at 32e sites. Thus, $Li[Li_{1/3}Ti_{5/3}]O_4$ could be expressed as $[Li]_{8a}[Li_{1/3}Ti_{5/3}]_{16d}[O_4]_{32e}$ in space notation. The lattice constant was calculated to be a=8.364 Å, which is in agreement with previous work by Murphy et al [221]. Each formula $Li[Li_{1/3}Ti_{5/3}]O_4$ can accomodate 1 lithium ion. Ohzuku et al. [220] described the process of the insertion of Li ions into $Li[Li_{1/3}Ti_{5/3}]O_4$ spinel structure as follows:

$$[Li]_{8a}[Li_{1/3}Ti_{5/3}]_{16d}[O_4]_{32e} + e^- + xLi^+ \rightleftharpoons [Li_{1+x}]_{8a/16c}[Li_{1/3}Ti_{5/3}]_{16d}[O_4]_{32e} \rightleftharpoons [Li_2]_{16c}[Li_{1/3}Ti_{5/3}]_{16d}[O_4]_{32e} \quad (7.1)$$

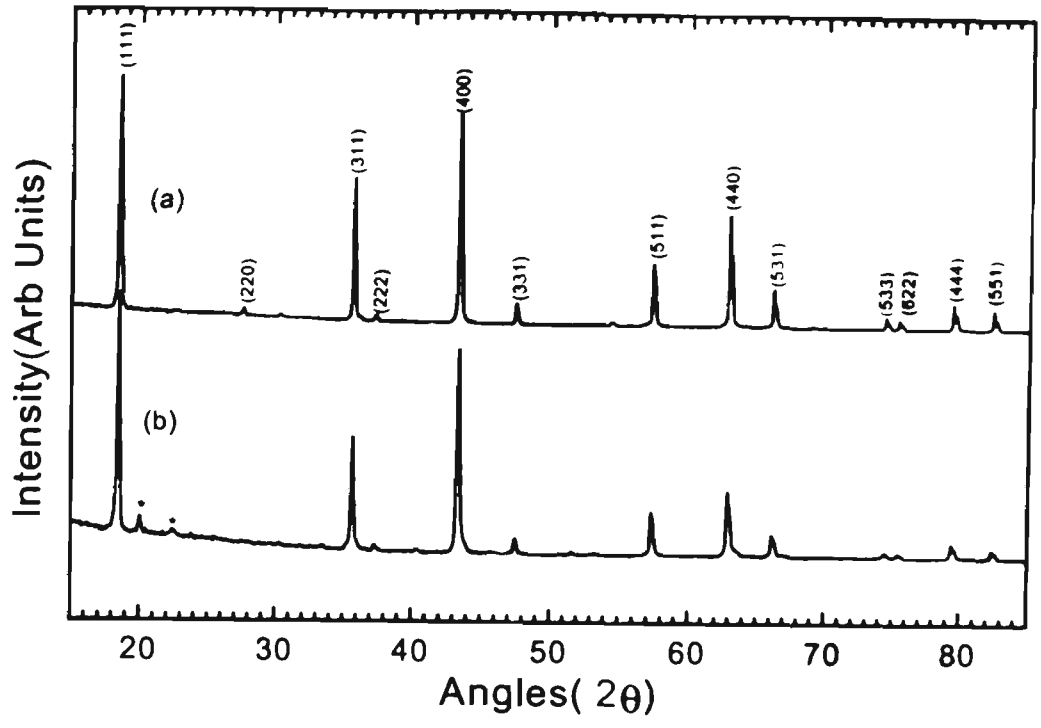

Fig. 7-1 x-ray diffraction patterns of $Li[Li_{1/3}Ti_{5/3}]O_4$.
(a) synthesised at 850°C under oxygen stream.
(b) synthesised at 1000° in air with 8 mol % Li in the precursors.
* impurity phase Li_2TiO_3

During the intercalation of Li ions into the $Li[Li_{1/3}Ti_{5/3}]O_4$ structure, Li ions begin to occupy 16c sites. Then Li ions in the tetrahedral 8a sites also migrate to 16c sites. Eventually, all 16c sites are occupied by Li ions. The insertion product $Li_2[Li_{1/3}Ti_{5/3}]O_4$ is still cubic spinel phase. In order to confirm this mechanism, chemical lithium intercalation into $Li[Li_{1/3}Ti_{5/3}]O_4$ was carried out by reacting $Li[Li_{1/3}Ti_{5/3}]O_4$ powders with 2.5 M n-butyllithium in a hexane solution in a glove-box filled with argon. The samples were immersed in butyllithium-hexane solution for different times, then filtered and washed with hexane. The x-ray diffraction was performed on these chemical insertion products which were sealed between two pieces of glass with wax in the glove-box. The content of lithium ions inserted into the sample was determined by

atomic absorption spectrophotometry. As shown in Fig. 7-2, the insertion products $Li_{1+x}[Li_{1/3}Ti_{5/3}]O_4$ retain the cubic phase. The impurity phase marked in Fig. 7-2 could be unfiltered butyllithium or other ternary Li-Ti-O phases, but they are difficult to identify by x-ray diffraction. After long term chemical insertion, the maximum amount of Li ions which can be inserted into the structure of the $Li[Li_{1/3}Ti_{5/3}]O_4$ is limited to about 1 Li ion per formula $Li[Li_{1/3}Ti_{5/3}]O_4$. This is because there are no vacant octahedral sites available to further accommodate Li ions. According to the reaction (1), the $Li[Li_{1/3}Ti_{5/3}]O_4$ compound has a theoretical capacity of 175 mAh/g.

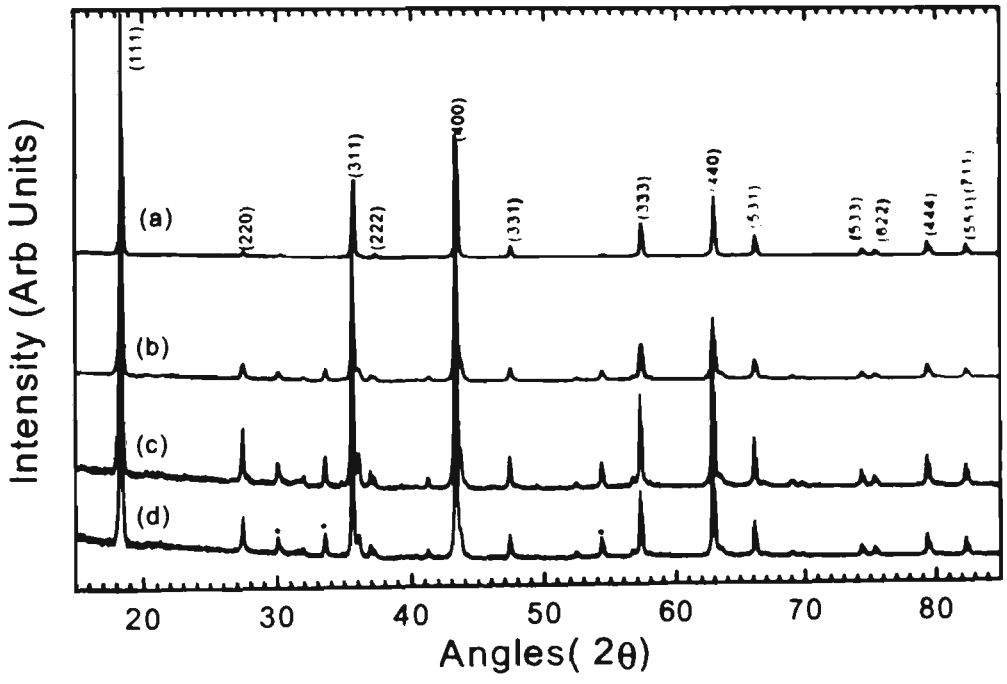

Fig. 7-2 X-ray diffraction patterns of the chemical insertion products $Li_{1+x}[Li_{1/3}Ti_{5/3}]O_4$

(a) x=0 (b) x=0.44 (c) x=0.71 (d) x=1.02
* impurity phases

7.1.2 Electrochemical test of the $Li[Li_{1/3}Ti_{5/3}]O_4$ electrode.

$Li/Li[Li_{1/3}Ti_{5/3}]O_4$ coin cells were constructed to examine the electrochemical performance of the $Li[Li_{1/3}Ti_{5/3}]O_4$ electrode in lithium cells. Fig. 7-3 shows the charge/discharge profiles of one of these cells. The cells were cycled between 1.2 V and

3.2 V. The average discharge voltage is around 1.5 V, while the charge plateau is around 1.54 V. There is about 40 mV hysteresis between the charge and discharge plateaus. A rechargeable capacity of approximately 150 mAh g was obtained, corresponding to 0.86 Li, which can be reversibly intercalated and de-intercalated in per formula $Li[Li_{1/3}Ti_{5/3}]O_4$. In the first hundred cycles, the capacity of $Li[Li_{1/3}Ti_{5/3}]O_4$ electrode was almost constant, indicating that the $Li[Li_{1/3}Ti_{5/3}]O_4$ structure is very stable for Li ion insertion and extraction. Fig. 7-4 shows the differential chronopotentiometric curves of dQ/dV vs. E for the first cycle and the hundredth cycle. The oxidation peak and reduction peak are at 1.55V and 1.50V respectively, which is in agreement with the data from the charge and discharge plateaus.

$Li[Li_{1/3}Ti_{5/3}]O_4$ demonstrated a stable discharge plateau at 1.5 V. It can be used therefore as an anode material and coupled with a high voltage cathode material such as $LiCoO_2$ or spinel $LiMn_2O_4$ to construct a lithium ion cell with a voltage range of 2.4V-2.5V. The $Li[Li_{1/3}Ti_{5/3}]O_4$ / $LiCoO_2$ and $Li[Li_{1/3}Ti_{5/3}]O_4$ / $LiMn_2O_4$ cells were constructed based on the following characteristics of the anode and cathode materials: (i) the anode $Li[Li_{1/3}Ti_{5/3}]O_4$ can be discharged to 150 mAh/g capacity, (ii) the cathode $LiMn_2O_4$ and $LiCoO_2$ can provide 120 mAh/g and 140 mAh/g charge capacity respectively. The ratio of the anode and cathode active materials were maintained as a slight excess of the anode active $Li[Li_{1/3}Ti_{5/3}]O_4$ in the cell configuration. The charge/discharge data for $Li[Li_{1/3}Ti_{5/3}]O_4/LiCoO_2$ and $Li[Li_{1/3}Ti_{5/3}]O_4/LiMn_2O_4$ cells are shown in Fig. 7-5. The voltages of the freshly assembled cell are in the range of 0.6-0.8 V. The average charge/discharge voltages for these two types of the cells are around 2.4 V-2.5 V. As shown in Fig. 7-5(b), the discharge capacity of the $Li[Li_{1/3}Ti_{5/3}]O_4/LiMn_2O_4$ cell fades quite quickly at an average rate of 0.34 mAh/g per cycle in the first fifty cycles. This is related to the degradation of the $LiMn_2O_4$ cathode.

However, the fading of the discharge capacity of the $Li[Li_{1/3}Ti_{5/3}]O_4$ / $LiCoO_2$ cell is much lower, with an average rate of only 0.06 mAh g per cycle. This suggests that the rechargeability of $LiCoO_2$ is better than that of $LiMn_2O_4$.

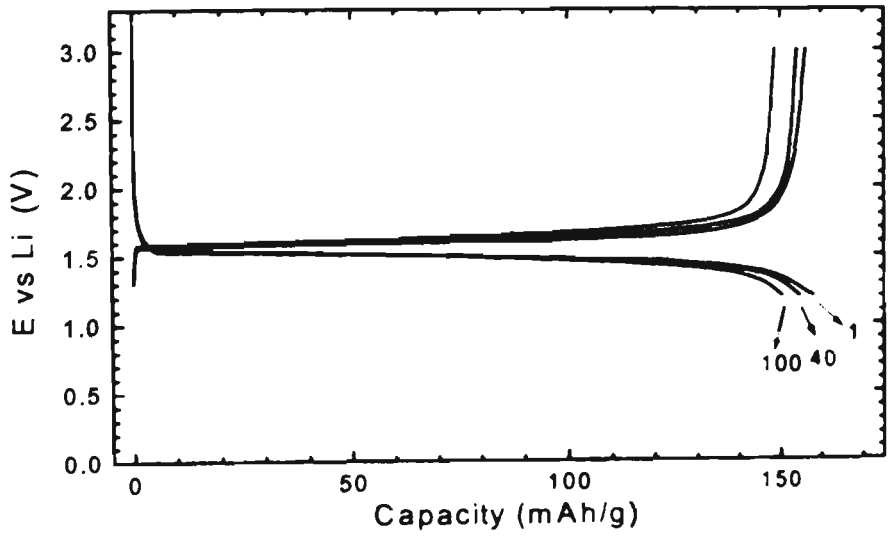

Fig. 7-3 The selected cycling profiles of Li/ for $Li[Li_{1/3}Ti_{5/3}]O_4$ cell. The cell was cycled between 1.2 V and 3.2 V at a rate of C/8.

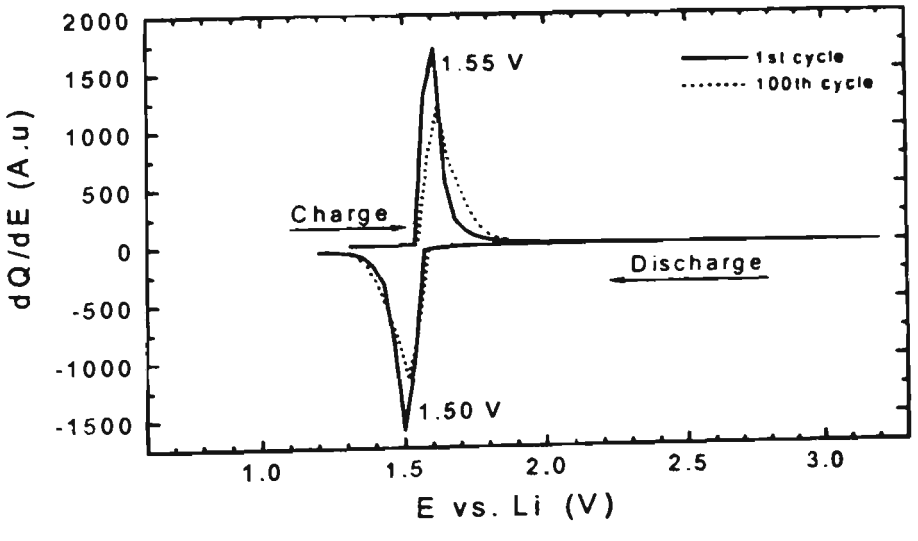

Fig. 7-4 Differential chronopotentiometric curves for Li / $Li[Li_{1/3}Ti_{5/3}]O_4$ cell in Fig. 7-3.

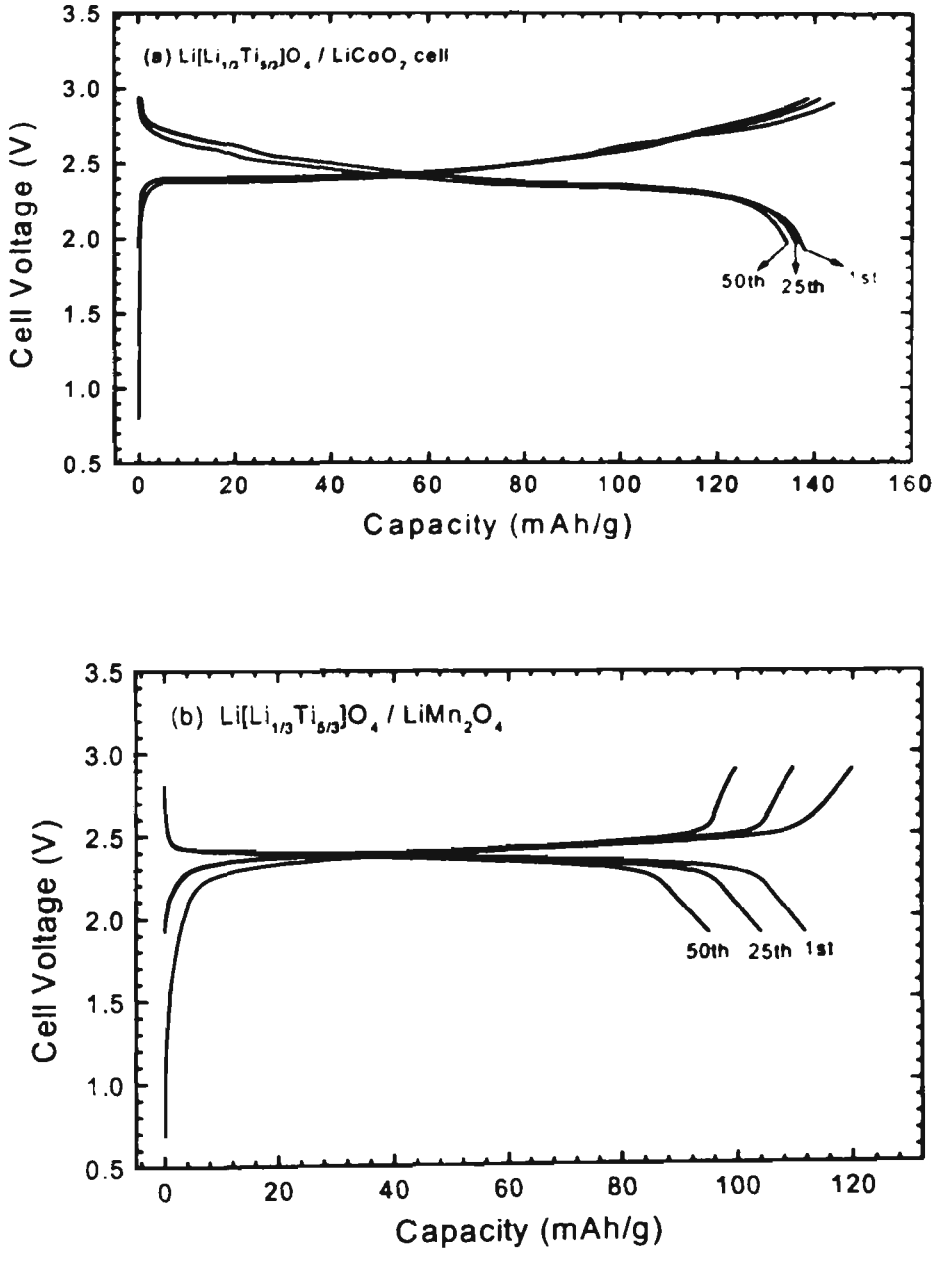

Fig. 7-5 The charge/discharge data of $Li[Li_{1/3}Ti_{5/3}]O_4$ / $LiCoO_2$ and $Li[Li_{1/3}Ti_{5/3}]O_4$ / $LiMn_2O_4$ cells. The cells were cycled between 1.9 V to 2.9 V at a rate of C/6. The capacities are based on the mass of the cathode active materials.

Therefore, the contribution to the decline of the capacity is mainly due to the degradation of the cathode, since the $Li[Li_{1/3}Ti_{5/3}]O_4$ anode is very stable upon cycling. Although the lithium ion cell with $Li[Li_{1/3}Ti_{5/3}]O_4$ as anode is structurally stable, its energy density is lower than that using a carbonaceous anode due to the relatively higher operating potential of the $Li[Li_{1/3}Ti_{5/3}]O_4$ anode (1.5 V vs. Li).

7.1.3 AC impedance determination of the $Li[Li_{1/3}Ti_{5/3}]O_4$ electrode

A.c. impedance spectra of the $Li/Li[Li_{1/3}Ti_{5/3}]O_4$ cell was obtained at different discharged states. The cell was potentiostatically discharged from OCV (3.0V) to 1.55V, 1.5V, and 1.2V respectively and then equilibrated for 10 hours. The a. c. impedance measurements were performed at these conditioned potentials. The Nyquist plots are presented in Fig. 7-6. A single semicircle is displayed along the real axis in the high frequency range. At lower frequencies, a straight line inclines to the real axis with an angle of 45°, corresponding to the Warburg impedance.

A second semicircle has been observed for AC impedance spectroscopy of the $Li/LiMn_2O_4$ system, which is attributed to the formation of a surface layer on the electrode due to the oxidation of the electrolyte on the surface of the highly charged $LiMn_2O_4$ electrode[19]. In the $Li/Li[Li_{1/3}Ti_{5/3}]O_4$ system, this second semicircle was not observed in the voltage range of OCV (3.0 V) - 1.2 V, which is in the voltage window of the cycling of the $Li[Li_{1/3}Ti_{5/3}]O_4$ electrode. The equivalent circuit for the $Li/Li[Li_{1/3}Ti_{5/3}]O_4$ system is also shown in Fig. 7-6 as an inset, which consists of (i) faradic components: the charge-transfer resistance R_{CT}; the electrolyte resistance R_{EL} and the Warburg resistance Z_W. (ii) a non-faradic component: double layer capacitance C_{DL}. The exchange current density can be calculated from the following equation: $i_o = RT/nFR_{CT}$.

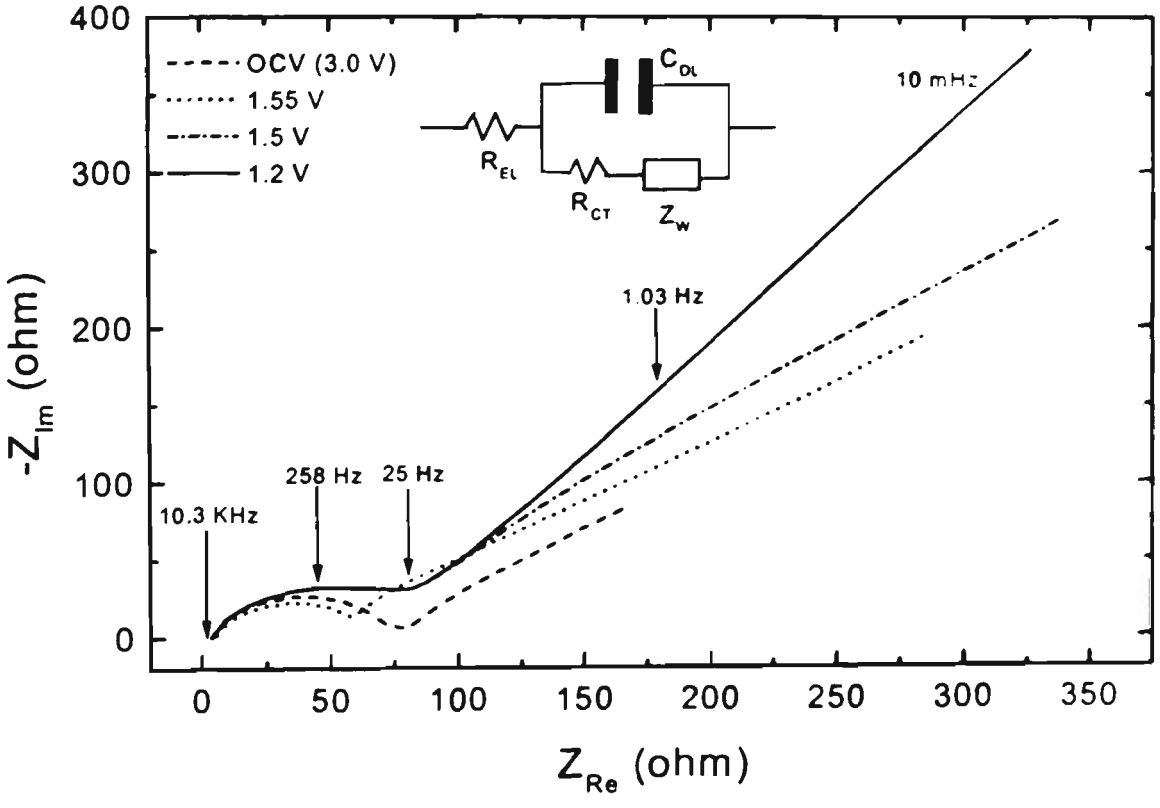

Fig. 7- 6 AC impedance spectra of a Li/Li[$Li_{1/3}Ti_{5/3}$]O_4 cell obtained at different conditioned potentials.

The double layer capacitance (C_{DL}) also could be deduced from this semicircle according to: $C_{DL} = 1/R_{CT} \times \omega_{max}$. The kinetic parameters of the Li[$Li_{1/3}Ti_{5/3}$]O_4 electrode are shown in Table 7-1. The charge-transfer resistance (R_{CT}) at 1.50 V (discharge plateau) and 1.20 V (deeply discharge state) are the same and higher than that at OCV and initial discharge state (1.55 V). The double-layer capacitance increases as lithium insertion proceeds and keeps constant from 1.50 V (discharge plateau) to 1.20 V (cut-off voltage), indicating no change of the double-layer of the Li[$Li_{1/3}Ti_{5/3}$]O_4 electrode during this discharging process.

It has been determined that a passivation film forms on the surface of an anode such as carbon at the potential of ~0.8 V vs. Li/Li^+, which is caused by the solvent decomposition reaction. The passivation film compounds are complicated and only known to contain Li_2CO_3, C-H bonds and COOH groups [218]. When the passivation film forms on the surface of the anode in lithium ion cells, lithium ions have to diffuse through it. During long term cycling, this passivation film could be blocked and consequently result in the formation of chemically unstable lithium powder or dendrites. From the result of the AC impedance spectra of $Li[Li_{1/3}Ti_{5/3}]O_4$ electrode, it seems that the $Li[Li_{1/3}Ti_{5/3}]O_4$ electrode is passivation free. From these results therefore, it appears that the passivation free $Li[Li_{1/3}Ti_{5/3}]O_4$ anode is much safer for battery operation than either lithium metal or carbonaceous anodes.

Table 1 The kinetic parameters of the $Li[Li_{1/3}Ti_{5/3}]O_4$ electrode at different discharge states

Discharge state / Kinetic parameters	OCV (3.0 V)	1.55 V	1.50 V	1.20 V
Charge-transfer resistance (R_{CT}, Ω/cm^2)	75.69	65.78	106	106
Exchange current density (i_o, A/cm^2)	3.39×10^{-4}	3.90×10^{-4}	2.42×10^{-4}	2.42×10^{-4}
Double-layer capacitance ($\mu F/cm^2$)	5.1	5.9	9.1	9.1

To summarize, the spinel $Li[Li_{1/3}Ti_{5/3}]O_4$ was synthesised and its electrochemical properties in lithium cells were tested. The maximum amount of Li ions which can be inserted into the $Li[Li_{1/3}Ti_{5/3}]O_4$ structure is limited to be about 1 Li ion per formula $Li[Li_{1/3}Ti_{5/3}]O_4$. $Li[Li_{1/3}Ti_{5/3}]O_4$ demonstrated a very stable characteristic for Li ion insertion and extraction without passivation. $Li[Li_{1/3}Ti_{5/3}]O_4$ / $LiCoO_2$ and

$Li[Li_{1/3}Ti_{5/3}]O_4$ /$LiMn_2O_4$ cells provide an average operating voltage of 2.4-2.5 V with no safety concerns.

7.2 Structure Characterisation and Lithium Insertion in $La_{0.33}NbO_3$ Perovskite

The ABO_3 perovskites contain a large number of compounds with a variety of special properties such as ionic conductivity [222-225], magnetism [226] and ferroelectricity [227, 228]. The A-site deficient ABO_3 compounds $La_{0.67-x}Li_xTiO_3$ [229-232] and $La_xLi_yNbO_3$ [233, 234] have demonstrated high lithium ionic conductivity, and have the potential to be used as the electrolyte for solid state lithium batteries and electrochromic devices. Since there are vacancies in their structure, it is possible for them to be used as lithium intercalation hosts. The materials with intercalation capability can be considered for use as electrode material for the lithium ion battery. Inaguma et al. first reported the intercalation of lithium into $La_{0.51}Li_{0.34}TiO_{2.94}$ [222]. Recently, $LiLaNb_2O_7$ perovskite was demonstrated to have an intercalation capacity of 1 lithium per formula [235].

From a structural point of view, if there exists a 2-dimensional channel or 3-dimensional tunnel in the structure of a compound with vacancies, then, lithium ions could be reversibly inserted into and extracted from the structure. Ideally, the metal ion in the compound should be multivalent, so that it can accept or donate electrons. $La_{0.33}NbO_3$ perovskite exactly meets the above conditions.

7.2.1 Preparation of $La_{0.33}NbO_3$ perovskite

The $La_{0.33}NbO_3$ perovskite was prepared from La_2O_3 and Nb_2O_5. The mixture of precursors was calcined at 1200°C for 8 hours. After that, the calcined powder was

ground and fired at 1350°C for 10 hours and cooled down. In order to improve the ordering of La^{3+} ions and vacancies in $La_{0.33}NbO_3$ perovskite, the sample was then heated at 800°C for 3 days and quenched in liquid nitrogen. The powder XRD pattern of $La_{0.33}NbO_3$ perovskite is shown in Fig. 7-7. All reflections were indexed as a cubic unit cell with the stacking of two perovskite subcells along the c-axis (called double primitive cell). The parameter for the primitive unit cell was calculated as a=3.928 Å. Superstructure lines were observed, which are generally considered to originate from the ordering of La^{3+} and vacancies in the A-sites. As shown in Fig. 7-8, Nb^{5+} ions occupy the octahedral interstitial and La^{3+} ions locate at the corner of the cubic unit cell. $La_{0.33}NbO_3$ perovskite is A- site deficient and 2/3 A-site vacancies exist in the structure. Due to the electrostatic interaction among the constituent ions, the ordering of A-site vacancies along c-axis occurs naturally. It is possible for deficient $La_{0.33}NbO_3$ to accommodate lithium in its structure because it contains vacancies. The ordering arrangement of vacancies provides a 2-dimensional channel for lithium insertion and extraction. Therefore, lithium ions could intercalate into and de-intercalate from $La_{0.33}NbO_3$ perovskite. Simultaneously, Nb^{5+} ions are reduced to Nb^{4+}. The materials possessing the above properties could be used as electrode materials for the lithium ion battery.

To determine the superlattice of $La_{0.33}NbO_3$, electron diffraction was performed on $La_{0.33}NbO_3$ powder. Fig. 7-9 shows the electron diffraction pattern of $La_{0.33}NbO_3$ along [010] zone axis. Extra reflections from superstructure are observed. The four superlattice diffraction spots appear together, indicating that unknown sub-superstructure exists associated with the ordering arrangement of vacancies.

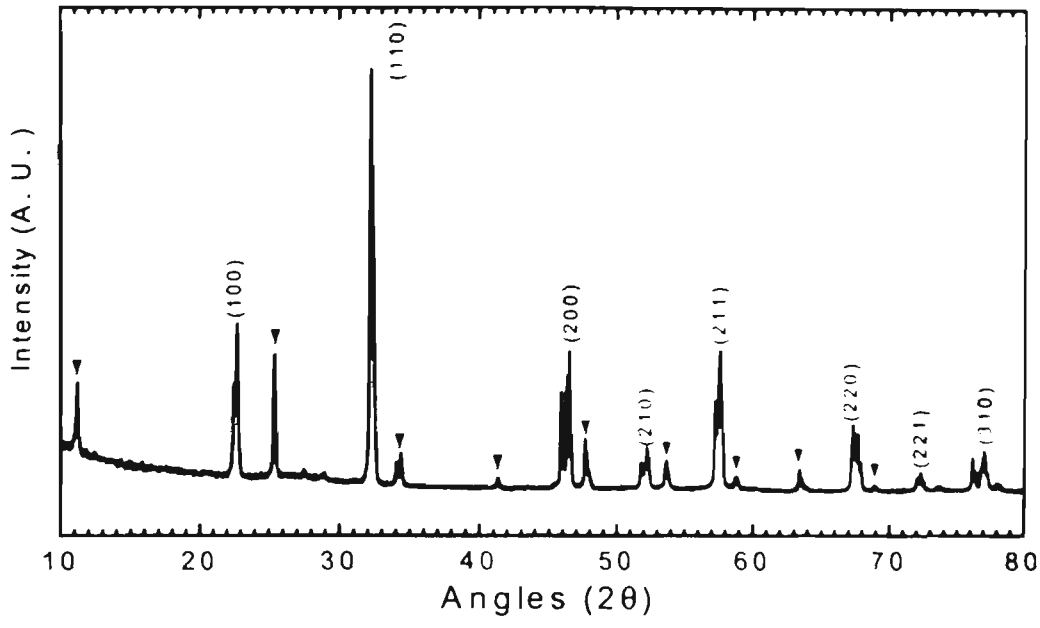

Fig.7-7. X-ray diffraction pattern of $La_{0.33}NbO_3$ perovskite.
▼ Superstructure lines

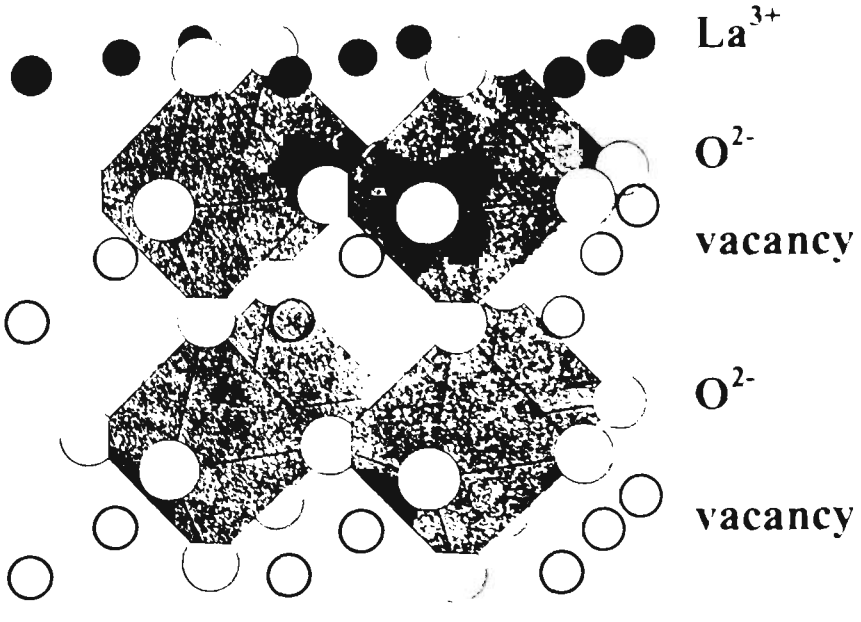

Fig. 7-8 The structure of $La_{0.33}NbO_3$ perovskite with the ordering of La^{3+} and vacancies along c-axis.

Fig. 7-9 The electron diffraction patterns of $La_{0.33}NbO_3$ along the [010] zone axis.

7-7.2 Electrochemical intercalation of Li^+ into $La_{0.33}NbO_3$ perovskite

The first discharge curve of lithium intercalation into a $La_{0.33}NbO_3$ electrode is shown in Fig. 7-10 The potentials for the $La_{0.33}NbO_3$ electrode at the OCV state are between 3.2 V to 3.4 V vs. Li/Li^+. When discharged, the potential of $La_{0.33}NbO_3$ electrode quickly dropped down to 2.0 V. Then, a descending discharging slope followed to 1.2 V. No obvious discharging plateau was observed, suggesting that there was no phase transformation during lithium intercalation. Consequently, we can deduce that lithium ions occupy A-vacancy sites in the perovskite structure. Theoretically, 0.67 lithium can be inserted per formula of $La_{0.33}NbO_3$. Under the constant current density of 40 $\mu A/cm^2$, approximately 0.63 lithium can be electrochemically inserted per formula of $La_{0.33}NbO_3$, corresponding to ~95% of theoretical capacity. Perhaps this is because the equilibration of the electrode was not reached under the condition of constant current of 40 $\mu A/cm^2$ discharging. Therefore, galvanostatic intermittent titration technique (GITT) was employed to measure the lithium intercalation process. The profile of the GITT measurement is shown in Fig. 7-11. The maximum lithium uptake reached 0.72 lithium

per formula $La_{0.33}NbO_3$. This means that all of the vacancies in $La_{0.33}NbO_3$ could be occupied by lithium. The additional 0.05 lithium was possibly consumed to form a passivation film on the surface of the electrode.

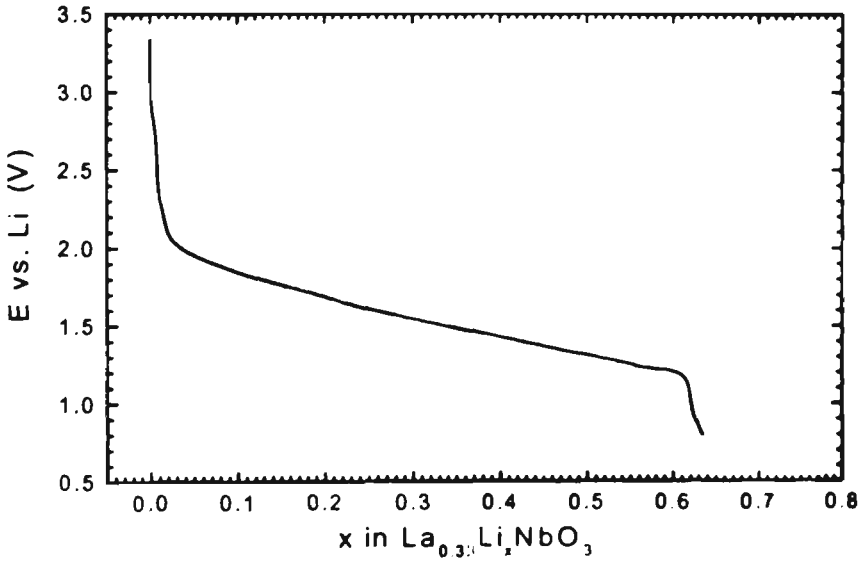

Fig. 7-10 The first discharge of lithium intercalation into $La_{0.33}NbO_3$ electrode. Current density: 40 μA/cm^2.

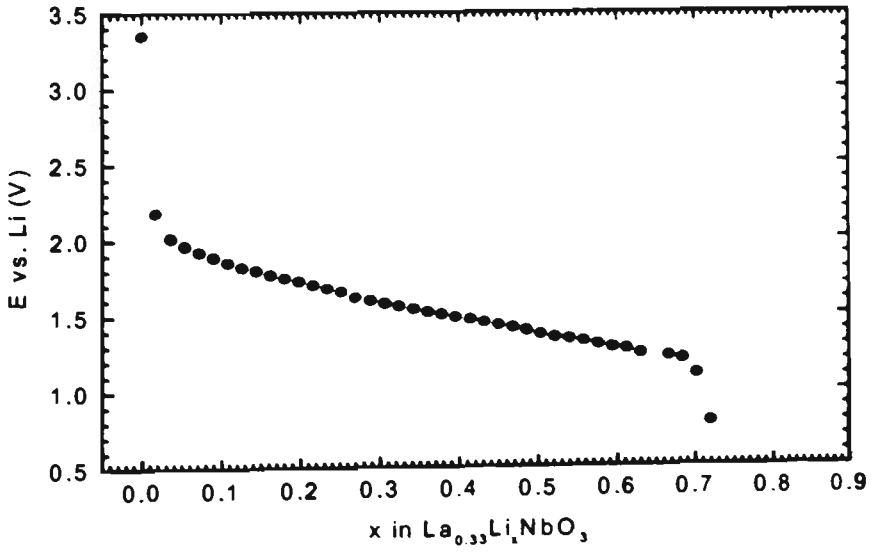

Fig.7-11 The discharge profile $La_{0.33}NbO_3$ electrode obtained by the galvanostatic intermittent titration technique (GITT). A discharge current of 10 μA/cm^2 was switched on for a certain time with a step of Δx=0.02, and then switched off for 10 hours for equilibration.

To determine the reversibility of $La_{0.33}NbO_3$ electrode for lithium insertion and extraction. Charge/discharge cycles for Li/ $La_{0.33}NbO_3$ cells were performed. The cycling data for one of these cells are presented in Fig. 7-12. During the first cycle, about 20% of the lithium was trapped in the $La_{0.33}NbO_3$ electrode. Then, lithium ions can reversibly intercalate into and de-intercalate from $La_{0.33}NbO_3$ perovskite structure with an efficiency of 99% after sixty cycles. From the structural analysis, it is known that La^{3+} ions and vacancies order along the c-axis, which provides positions and a diffusion tunnel for lithium ion insertion and extraction. The electrochemical cycling test confirms the above mechanism. Although $La_{0.33}NbO_3$ is not suitable as an electrode material for the lithium ion battery, with analysis and understanding of the structure of the material, more electrode materials may be identified or even designed for the lithium ion battery.

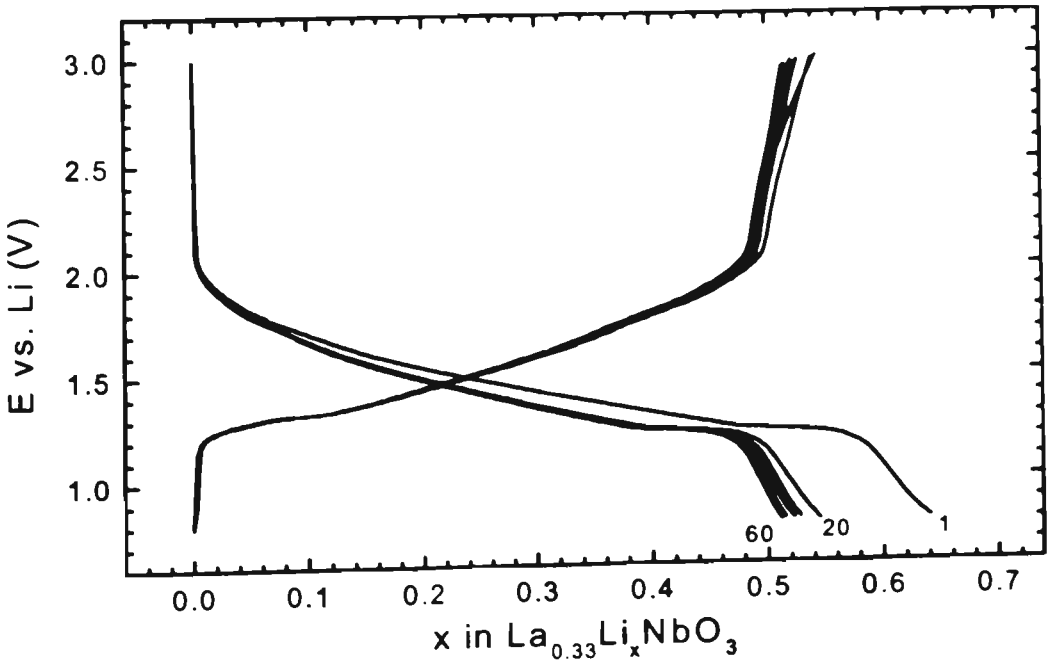

Fig. 7-12 The cycling data for a Li/$La_{0.33}NbO_3$ cell. Current density: 40 $\mu A/cm^2$.

7.2.3 Kinetic process of lithium insertion/extraction in the $La_{0.33}NbO_3$ electrode

Fig. 7-13 presents the AC impedance spectra of $La_{0.33}NbO_3$ electrode (Nyquist plots) at different discharge states. A semicircle was observed in the high frequency range, which corresponds to a charge-transfer reaction and a non-faradic process of the charging of the double-layer capacitance. The charge-transfer resistance (R_{CT}) and exchange current density (i_o) can be deduced from this semicircle. A straight line inclined to the real axis at 45° in the low frequency range is ascribed to a Warburg diffusion process. The chemical diffusion coefficient D_{Li} may be obtained from the Warburg's prefactor σ according the following equation:

$$\sigma = \frac{Vm}{\sqrt{2} \times nF \times S \times D} \times \frac{dE}{dx}$$

V_m is the molar volume of $La_{0.33}NbO_3$ (36.6 cm^3/mole), dE dx is the slope of the GITT curve at each x value and S is the apparent geometric area of the $La_{0.33}NbO_3$ electrode.

As shown in Fig. 7-14, the charge-transfer resistance (R_{CT}) decreases with the insertion of Li^+ ions into the $La_{0.33}NbO_3$ electrode. Consequently, the exchange current density (i_o) increases as lithium insertion proceeds. When Li^+ ions intercalate into the $La_{0.33}NbO_3$ structure, Nb^{5+} ions are reduced to Nb^{4+}. With the mixture of Nb^{4+} and Nb^{5+} ions in the perovskite structure, the electronic conductivity is improved, which could be responsible for the decrease of the charge-transfer resistance. A second semicircle was observed in the discharged state of x=0.28. The absorption surface layer formed on the surface of the $La_{0.33}NbO_3$ electrode could be the cause for this second semicircle. However, at more deeply discharged states, even in the fully discharged state, no second semicircle was observed in the a.c. impedance spectra. It is possibly due to the damage of the surface layer at low potential.

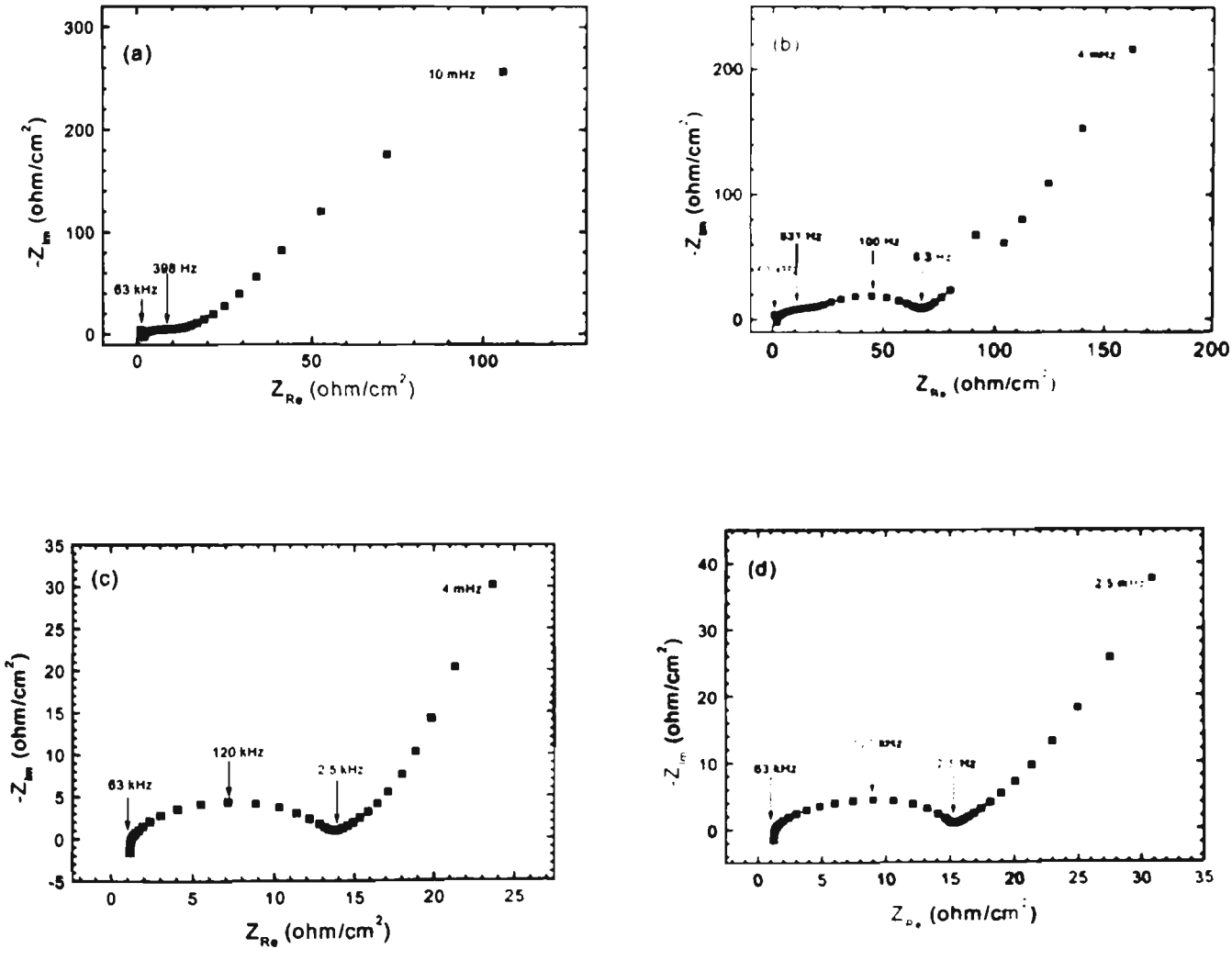

Fig. 7-13 A. c. impedance spectra (Nyquist plots) for the $La_{0.33}NbO_3$ electrode at different discharge state: (a) x=0 (b) x=0.28 (c) x=0.55 (d) x=0.67
* x is the amount of lithium in $La_{0.33}Li_xNbO_3$.

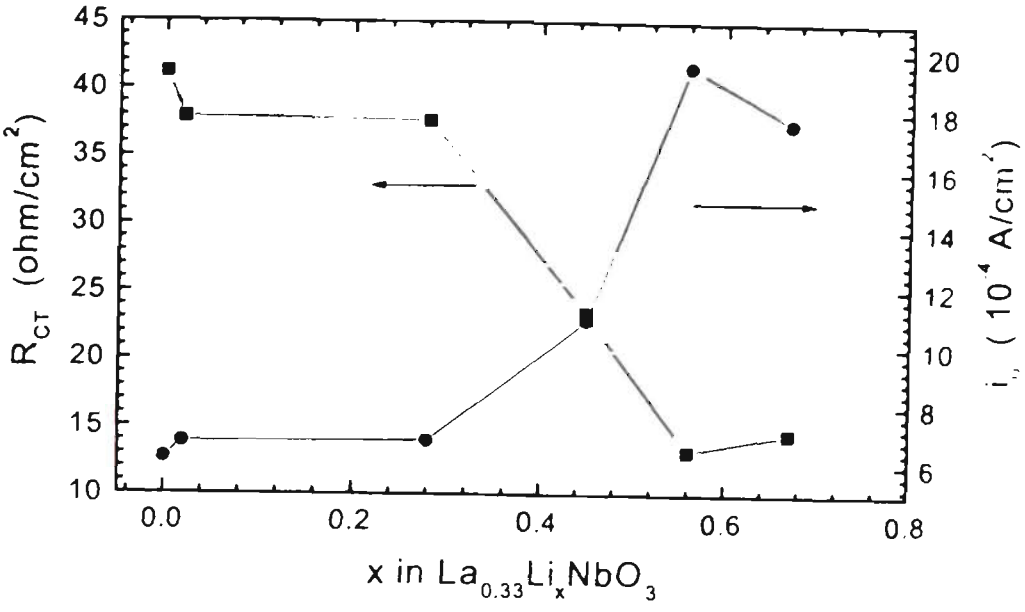

Fig. 7-14 The charge-transfer resistance (R_{CT}) and exchange current density (i_o) at different discharge states.

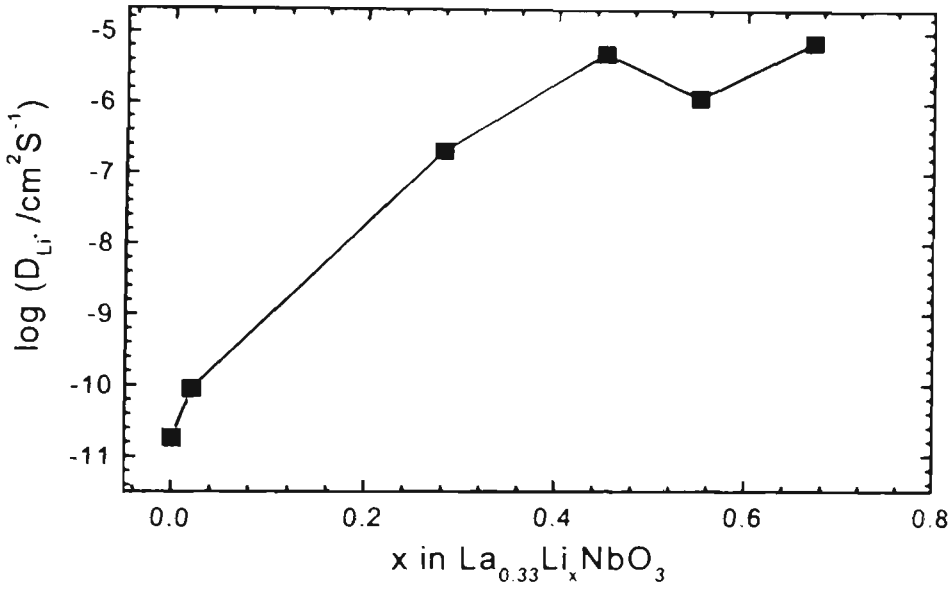

Fig. 7-15 The chemical diffusion coefficients (D_{Li}) of lithium ion within the $La_{0.33}NbO_3$ electrode.

Fig. 7-15 shows the chemical diffusion coefficients (D_{Li}) of lithium ions in the $La_{0.33}NbO_3$ electrode at different discharge states. The values of D_{Li} increase with the insertion of lithium. This behaviour is similar to the graphite electrode [236].

In conclusion, the A-site vacant $La_{0.33}NbO_3$ perovskite can be synthesised by a solid-state reaction. X-ray diffraction and electron diffraction confirmed the ordering arrangement of vacancies in the $La_{0.33}NbO_3$ perovskite structure, which provides diffusion tunnels for lithium insertion and extraction. The electrochemical tests demonstrate that lithium ions can reversibly intercalate into and de-intercalate from $La_{0.33}NbO_3$ perovskite electrode in a potential range of 2.0 V to 1.2 V vs. Li. The kinetic process of lithium insertion in the $La_{0.33}NbO_3$ perovskite electrode was characterised via AC impedance measurement. The charge-transfer resistance (R_{CT}) for $La_{0.33}NbO_3$ electrode decreases and the diffusion coefficient increases as lithium insertion into $La_{0.33}NbO_3$ structure.

7.3 $LiTi_2(PO_4)_3$ with NASICON-type Structure as Lithium Storage Materials

The Na^+ superionic conductor (NASICON) materials are good ionic conductors as solid state electrolytes. The crystal structure of NASICON $A_xM_2(XO_4)_3$ consists of a net work in which MO_6 octahedra share all their corners with XO_4 tetrahedra and XO_4 tetrahedra share all three corners with MO_6 octahedra. The interstitials and conduction channels are generated along the c-axis direction, in which alkali metal ions (Na^+ or Li^+) occupy the interstitial sites. Consequently, the diffusion of alkali metal ions along the conduction channel is possible [237-244]. The NASICON structure $A_xM_2(XO_4)_3$ can be chemically versatile. It can be stabilized with K^+, Na^+ or Li^+ in the A position, transition metal cations in the M position, P, Si or Mo in XO_4 polyanions. Therefore, NASICON materials can be used not only as solid-state electrolytes but also as lithium storage materials in rechargeable lithium batteries, based on their structural characteristics. The synthesis and electrochemical properties of $LiTi_2(PO_4)_3$ were investigated. It was

considered that it could be a candidate anodic material for lithium ion batteries because of the low potential of the Ti^{4+}/Ti^{3+} redox couple vs Li/Li^+.

The raw materials Li_2CO_3, TiO_2 and $(NH_4).H_2PO_4$ were thoroughly mixed. The mixtures were then pressed into pellets and pre-calcined at 900°C for 12 hours to decompose Li_2CO_3 and $(NH_4)H_2PO_4$. The pellets were then reground and fired at 1250°C for 24 hours. The overall reaction is as follow:

$$0.5Li_2CO_3 + 2TiO_2 + 3(NH_4)\,H_2PO_4 \rightarrow$$

$$LiTi_2(PO_4)_3 + 3NH_3 + 4.5H_2O + 0.5CO_2 \qquad (7.2)$$

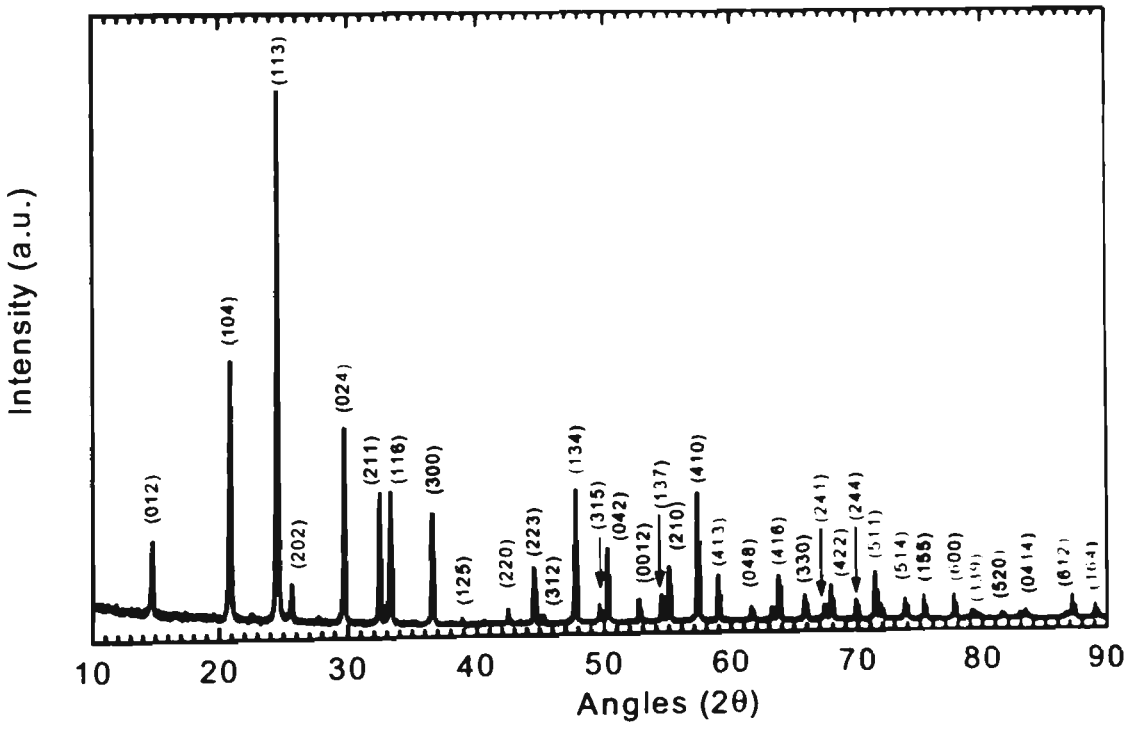

Fig. 7-16 X-ray diffraction pattern of $LiTi_2(PO_4)_3$ NASICON powders.

$LiTi_2(PO_4)_3$ has a rhombohedral (S.G: R-3c) structure with an open 3-D framework of TiO_6 octahedra sharing all corners with PO_4 tetrahedra and vice versa. Li^+ ions occupy the interstitial spaces, either 18e or 6b sites. Fig. 7-16 shows the x-ray diffraction pattern of $LiTi_2(PO_4)_3$. All diffraction lines are indexed based a rhombohedral structure with a space group of R-3c. The lattice constants were calculated to be a=8.5105 Å and c=20.8645 Å using a least square method by 25 diffraction lines. The calculated parameters of the unit cell are in good agreement with the literature value [245].

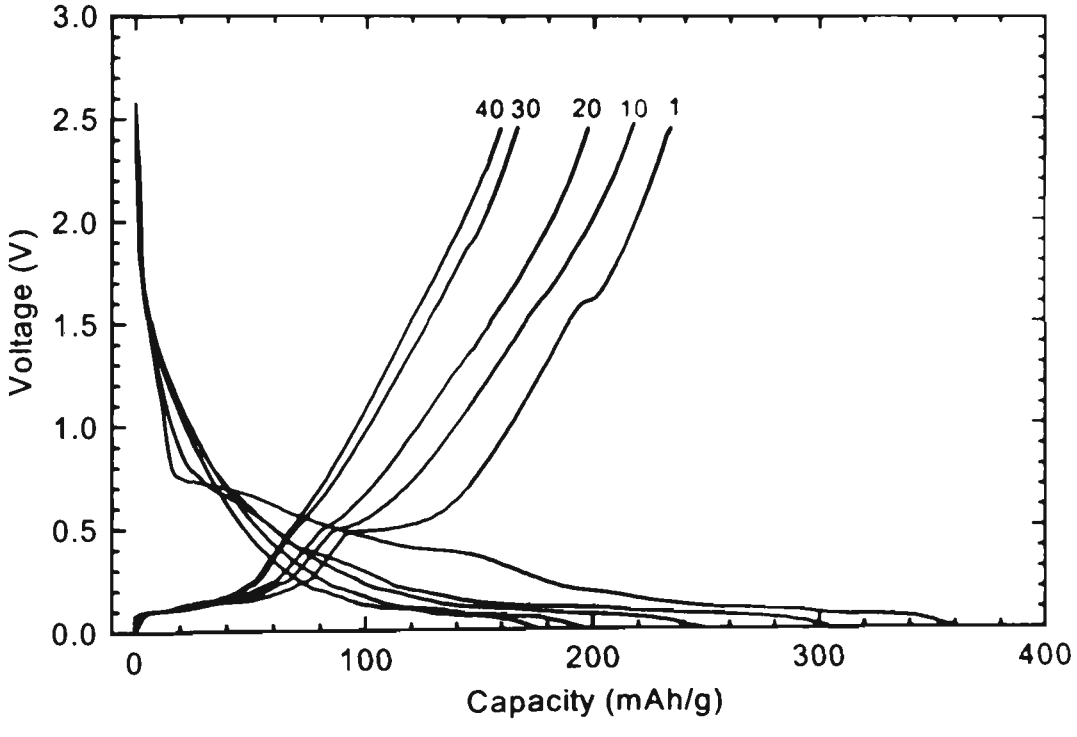

Fig. 7-17 The charge/discharge profiles of Li/LiPF6 (EC+DMC)/ $LiTi_2(PO_4)_3$ cell in the voltage range of 0-2.5 V. Current density i=0.1 mA cm^{-2}.

Li/ $LiTi_2(PO_4)_3$ cells were discharged and charged at a constant current density of 0.1 mA/cm^2 (20 mA/g). Lithium insertion into the $LiTi_2(PO_4)_3$ electrode corresponds to the discharge process and the extraction of lithium from the host as the charge process. Fig. 7-17 shows the discharge/charge profiles of one of the Li/ $LiTi_2(PO_4)_3$ cells in the voltage range of 0-2.5 V. The first lithiation for the $LiTi_2(PO_4)_3$ compound reached a capacity of 360 mAh/g, corresponding to 5.2 moles lithium insertion into per mole of $LiTi_2(PO_4)_3$. However, only 65% of the initially inserted lithium could be reversibly extracted in the first charge process. The capacity of the $LiTi_2(PO_4)_3$ faded quickly with cycling. The charge and discharge capacity of the $LiTi_2(PO_4)_3$ electrode was mainly concentrated within the voltage range of 0.1-0.8 V. This is different from $Li_4Ti_5O_{12}$ whose potential is around 1.5 V vs. Li/Li^+. If it is only the Ti^{4+}/Ti^{3+} redox couple which contributes to the redox reaction as lithium is inserted and extracted, then the operating potential should be almost the same for these two compounds. However, the experimental observation is the opposite. Furthermore, if only the Ti^{4+} ions in $LiTi_2(PO_4)_3$ accept electrons responding to the lithium insertion, the maximum lithium intake would be merely 2 moles of Li per mole of $LiTi_2(PO_4)_3$ to form $Li_3Ti_2(PO_4)_3$, whereas, approximate 5.2 moles of Li were electrochemically inserted into per mole of $LiTi_2(PO_4)_3$ in the first discharge process. Therefore, it is suggested that $[PO_4]$ tetrahedra possibly also take part in the redox reaction to accept and donate electrons when lithium ions intercalate and de-intercalate in the $LiTi_2(PO_4)_3$ structure, although at this stage, there is no direct physical evidence to confirm this proposal. However some support for the proposal is provided from a study by Ceder et al., which indicated that oxygen, rather than transition-metal ions, function as the electron acceptors upon insertion of Li into metal-oxides and metal-dichalcogenides [246, 247]. Also, data from Li nuclear magnetic resonance (NMR) measurements also demonstrated that there

is significant oxygen participation during the insertion of Li in TCO glass [248]. The situation for Li insertion in $LiTi_2(PO_4)_3$ NASICON is similar. The quasi-open-circuit potential (OCV)/ composition curve was obtained by the galvanostatic intermittent titration technique (GITT). The $Li/LiTi_2(PO_4)_3$ cell was discharged to a desired value of x in $Li_{1+x}Ti_2(PO_4)_3$ at a constant current density of 20 $\mu A/cm^2$ and then relaxed for 2 hours. The final voltage of the cell was recorded as the OCV for that composition. Fig. 7-18 shows the variation of OCVs vs. inserted lithium composition x in the $Li_{1+x}Ti_2(PO_4)_3$ electrode. The maximum inserted Li was still about 5.2 moles per mole $Li_{1+x}Ti_2(PO_4)_3$ even under quasi-equilibrium discharging condition.

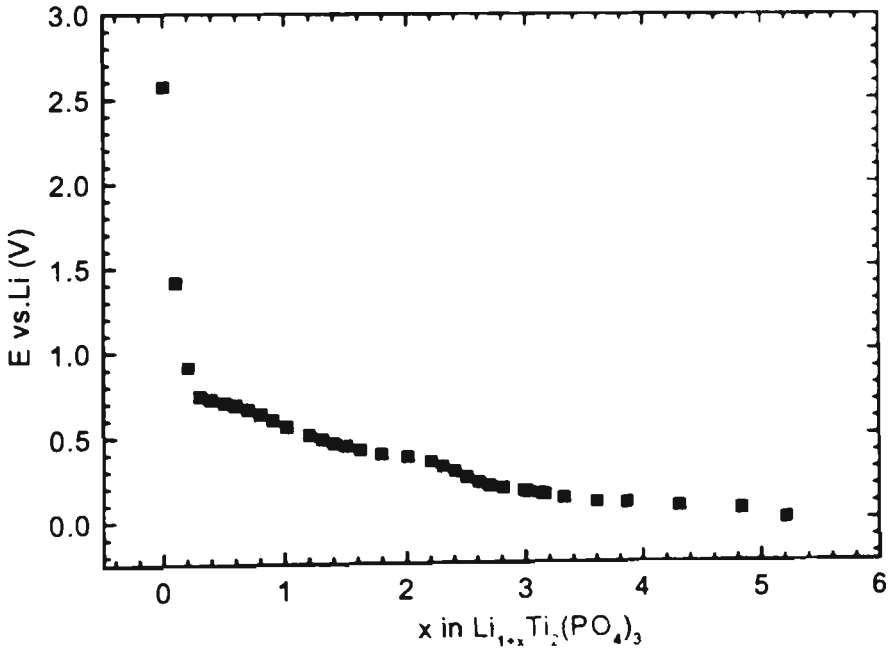

Fig. 7-18 Open-circuit potentials vs. inserted lithium compositions x in $LiTi_2(PO_4)_3$, obtained via GITT technique.

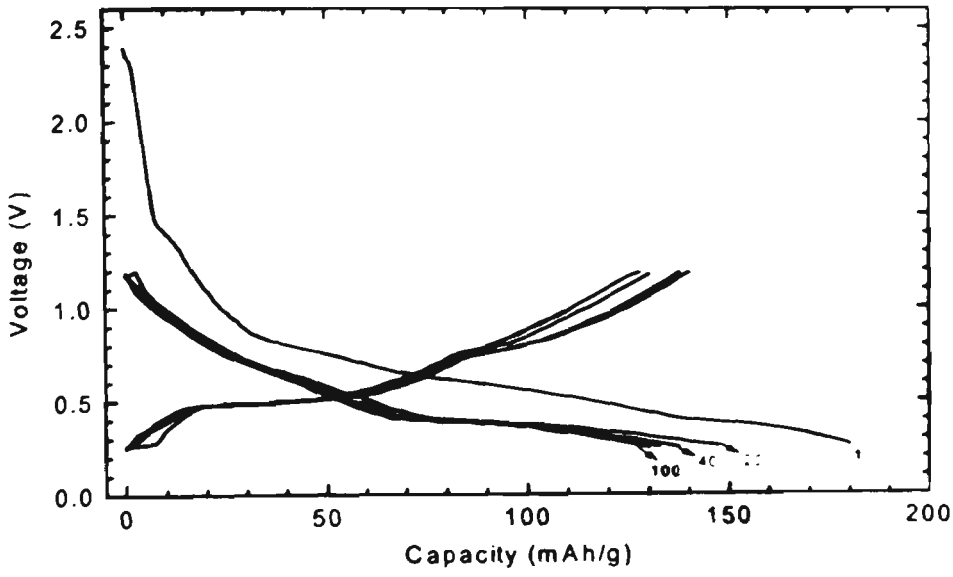

Fig. 7-19 The cycling profiles of Li/LiPF6 (EC+DMC) $LiTi_2(PO_4)_3$ cell with the voltage cut-off between 0.25 V to 1.2 V.

The capacity decay rate is related to the voltage range of cycling. Therefore, the cycling performance could be improved by limiting the voltage range of charge and discharge. Li/ $LiTi_2(PO_4)_3$ cells were cycled in a voltage range of 0.25-1.2 V. Surprisingly, they demonstrated excellent capacity retention (as shown in Fig. 7-19). During the first cycle, approximate 80% initial inserted lithium was reversibly extracted in the first charge. After the first cycle, the reversibility of the electrode was much better than that cycled between 0-2.5 V.

The kinetic process of lithium insertion into $LiTi_2(PO_4)_3$ NASICON can be determined by a. c. impedance measurement. A.c. impedance measurements were performed on the $LiTi_2(PO_4)_3$ electrode at different state of discharge (SoD). The impedance spectra are presented in Fig. 7-20. One semicircle was observed for the $LiTi_2(PO_4)_3$ electrode in OCV state (no Li insertion). After Li intercalation into the $LiTi_2(PO_4)_3$ electrode, two semicircles were observed. The first semicircle is generally

considered to contribute to the charge-transfer process and double layer capacitance. The second semicircle is caused by a surface layer formed on the electrode, which has been found on the carbonaceous material electrode. The surface layer was formed when discharging the electrode below the potential of ~ 0.8 V vs. Li/Li$^+$ due to the decomposition of the organic electrolyte. This has been confirmed by FTIR [218]. However, when Li insertion reaches $x > 2$ ($E \leq 0.2$ V vs. Li/Li$^+$) the second semicircle disappeared as shown in Fig. 7-20 (c). The damage of the surface layer at low potential could be responsible for that. The a. c. impedance spectra in SoDs of x=2.6 and x=5.2 are almost same. The charge-transfer resistance (R_{CT}) and exchange current density (i_o) in different SoDs were estimated from the EIS and are shown in Fig. 7-21. The values of R_{CT} and the exchange current density i_o were almost invariant regardless of the state of discharge. It is suggested that the reaction for lithium insertion in $LiTi_2(PO_4)_3$ proceeds as:

$$xLi^+ + xe + LiTi_2(PO_4)_3 \rightarrow Li_{1+x}Ti_2(PO_4)_3 \qquad (7.3)$$

The exchange current i_o for the above reaction can be expressed as [249]:

$$i_o = nFk_sC_1^{(1-\alpha)} \times C_2^{\alpha} \qquad (7.4)$$

where k_s is the reaction constants, C_1 and C_2 are the activities of Li^+ in the electrolyte and NASICON solid solution respectively. C_1 can be regarded to be constant during the insertion reaction. Since EIS tests showed i_o invariant with Li insertion, C_2 should keep constant according to equation (7.4). So, it is thought that the inserted Li^+ ions occupy the interstitials or conducting channels, which does not have an influence on the physical environment of Li^+ in $LiTi_2(PO_4)_3$. The unique structure characteristics of the NASICON skeleton with large numbers of interstitials and channels could contribute to this point.

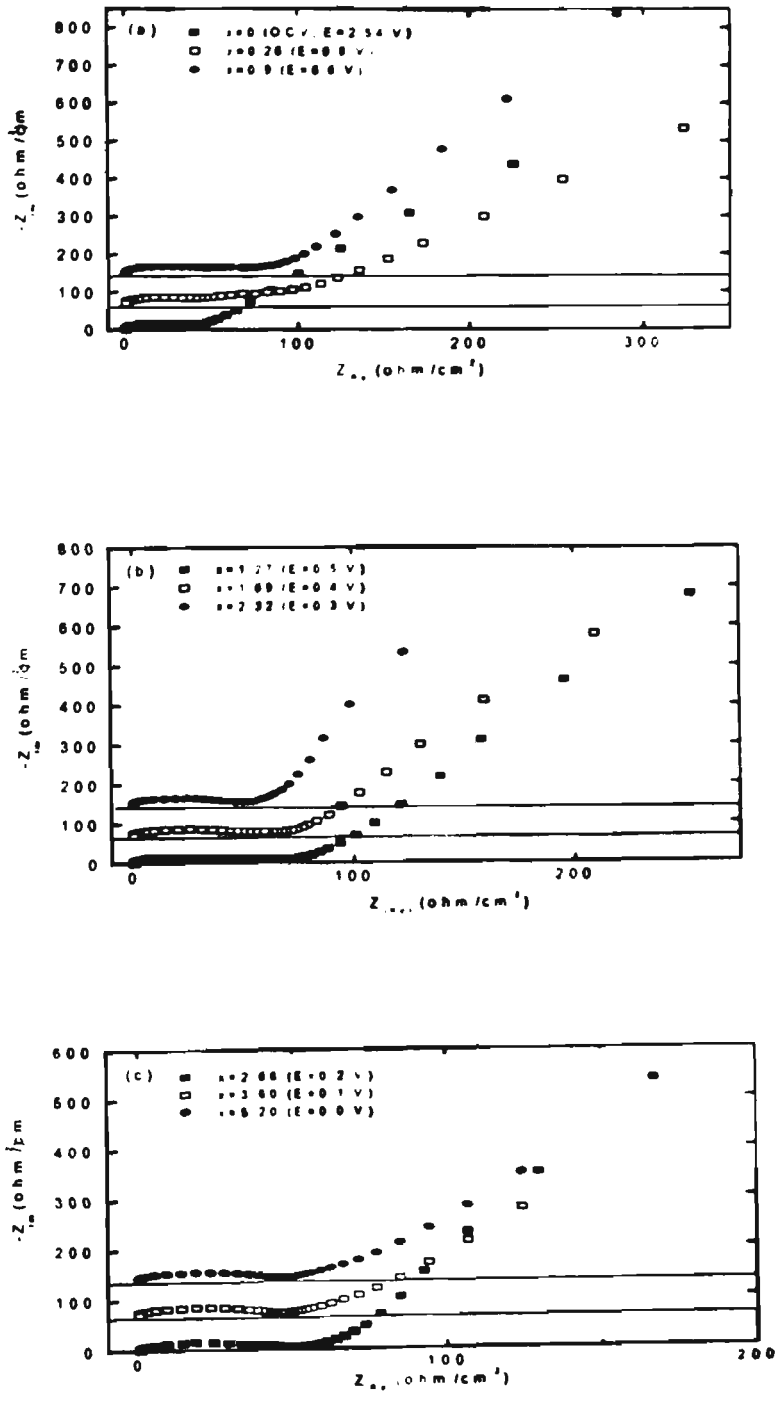

Fig. 7-20 A. c. impedance spectra for $LiTi_2(PO_4)_3$ electrode in different states of discharge (SoDs). The SoD is expressed as the amount of inserted Li in $Li_{1-x}Ti_2(PO_4)_3$. The potentials (E) refer to the potential of the $Li_{1+x}Ti_2(PO_4)_3$ electrode vs. Li reference electrode.

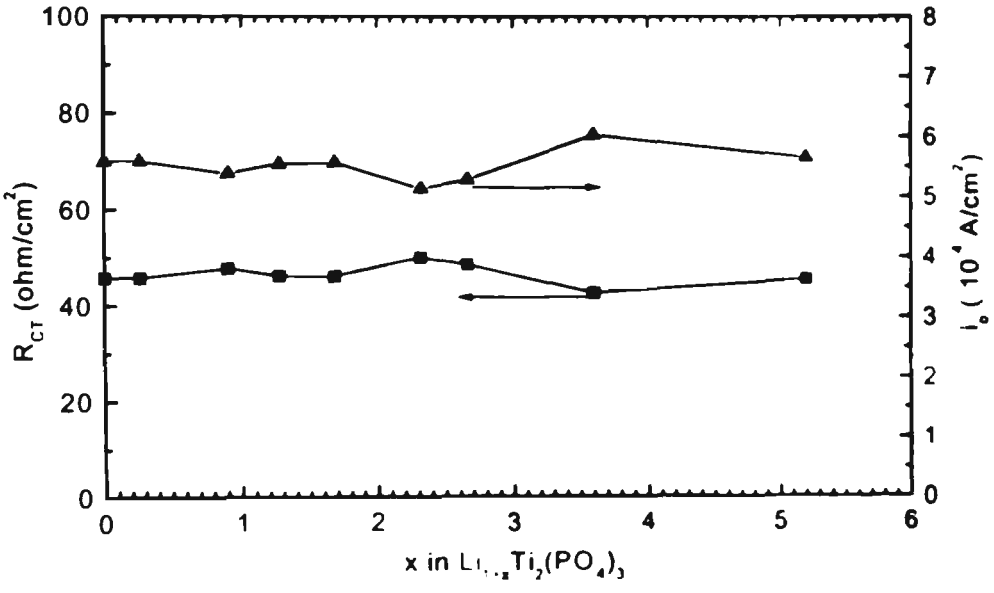

Fig. 7-21 The charge-transfer resistance (R_{CT}) and exchange current density (i_o) as a function of SoD for the $LiTi_2(PO_4)_3$ electrode.

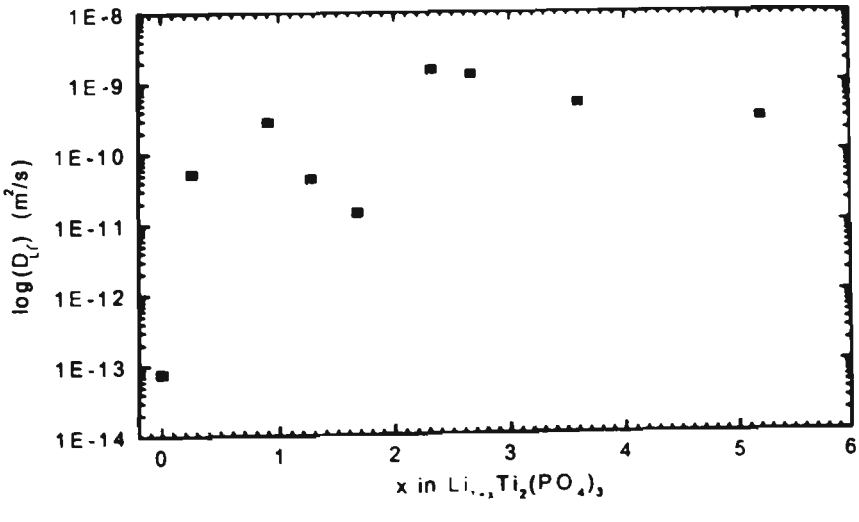

Fig. 7-22 The variation of Li^+ diffusion coefficient (D_{Li}) with SoDs in the $LiTi_2(PO_4)_3$ NASICON skeleton.

The kinetics for reaction (7.3) are limited by the Li diffusion in the host materials. The lithium diffusion coefficient D_{Li} in $LiTi_2(PO_4)_3$ electrode were calculated, and the Li diffusion coefficients D_{Li} in different SoDs are depicted in Fig. 7-22. The D_{Li} at OCV undischarged state is 7.6×10^{-14} m^2/s. After discharging, D_{Li} is in the range 1.4×10^{-11} to 1.2×10^{-9} m^2/s, which is much higher than those of other intercalation materials such as $LiCo_yMn_{2-y}O_4$ for which D_{Li} is in the range 9.20×10^{-14} - 2.6×10^{-12} cm^2 s and λ-MnO_2, where D_{Li} is between 1.9×10^{-12} to 3.1×10^{-11} cm^2 s [84, 154]. The conducting channels and interstitials in this NASICON structure could facilitate Li diffusion.

To summarize, it was found that a maximum of approximately 5.2 moles Li ions can be electrochemically intercalated into per mole of $LiTi_2(PO_4)_3$ structure. EIS measurements demonstrated that the Li diffusion coefficients D_{Li} in $LiTi_2(PO_4)_3$ are very high, which is related to the NASICON structure with interstitials and conducting channels. The exploration of similar NASICON materials could provide new electrode materials for lithium-ion batteries.

Chapter 8 Lithium Ionic Conductivity of $La_{(0.57-2x/3)}Sr_xLi_{0.3}TiO_3$ Solid-state Electrolyte

ABO_3 perovskites and NASICONs have been investigated and have demonstrated an ionic conductivity from 10^{-3} Scm^{-1} to 10^{-6} Scm^{-1} [250 – 253]. The best lithium ion conductors were found to be $La_{0.67-x}Li_{3x}TiO_3$ perovskites with a cation deficiency at A-sites [254]. The mechanism for ion conduction in ABO_3 perovskites is considered to originate from lithium ions hopping through the wide square planar bottlenecks between A-sites [255 -257]. Therefore, lithium ion conductivity depends on the concentration of the free volume, lithium ion and vacancy in the A-site. It has been reported that the substitution of ions with a large ionic radius such as Sr^{+} for La^{3+} ions in A-sites can increase the conductivity of ABO_3 perovskites [258, 259].

So, Sr^{2+} ion was chosen to partially substitute for La^{3+} in $La_{0.5}Li_{0.3}TiO_3$ perovskite according to the principle that one Sr^{2+} ion is equivalent to $\frac{2}{3}La^{3+}$ ion. A series of $La_{(0.57-2x/3)}Sr_xLi_{0.3}TiO_3$ perovskites were prepared and their structures and ionic conductivities were characterised.

The A-site deficient $La_{(0.57-2x/3)}Sr_xLi_{0.3}TiO_3$ perovskites (x=0, 0.04, 0.08, 0.12) were prepared using a solid-state reaction method. The starting materials of Li_2CO_3, La_2O_3, $SrCO_3$ and TiO_2 from were mixed using an agate pestle and mortar. The mixtures were calcined at 1100°C for 12 hours with several stages of intermediate grinding. The powders were pressed into pellets (diameter ϕ=10 mm) at a pressure of 300 MPa. The pellets were sintered at 1380°C for 2 hr in air. The ionic conductivity of the sample was measured by an AC impedance technique. The sintered samples were polished and gold was sputtered on both sides.

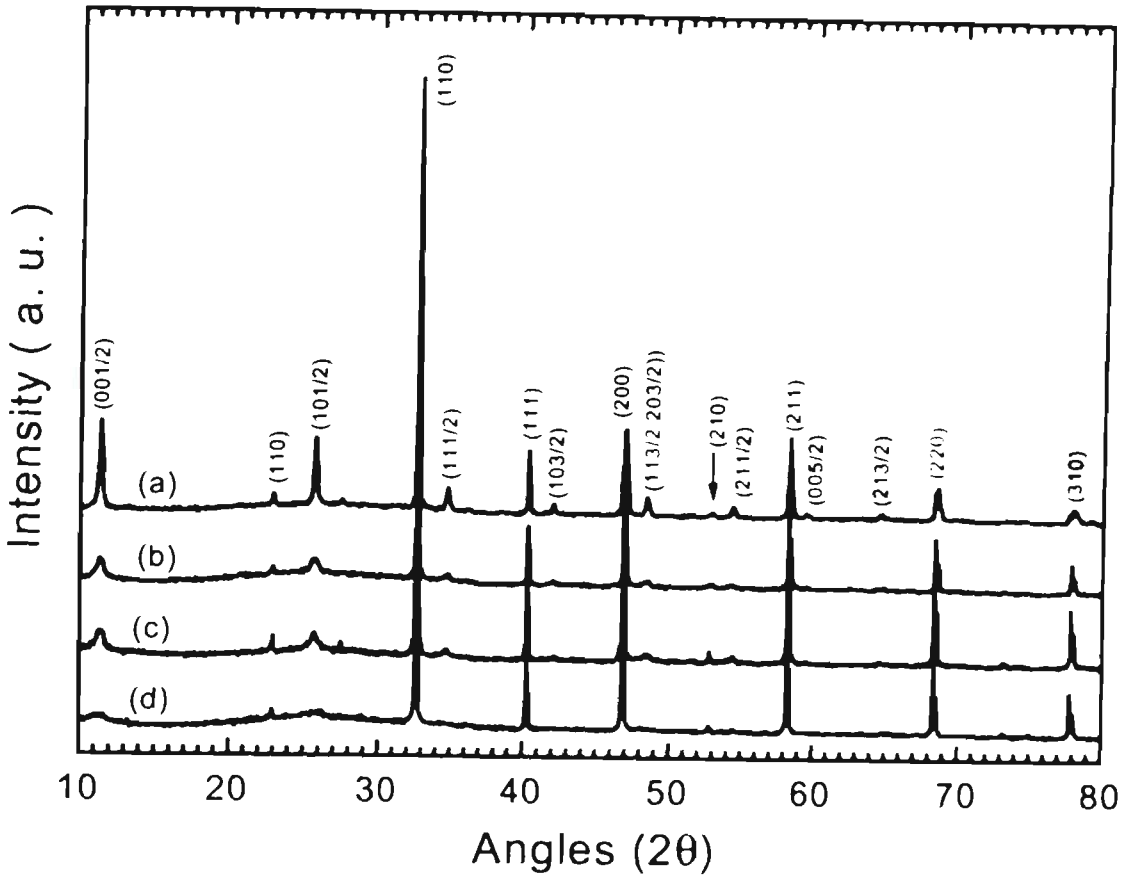

Fig. 8-1 XRD patterns of $La_{(0.57-2x/3)}Sr_xLi_{0.3}TiO_3$ perovskites.
(a) x=0 (b) x=0.04 (c) x=0.08 (d) x=0.12

The phases of the synthesised $La_{(0.57-2x/3)}Sr_xLi_{0.3}TiO_3$ were determined by powder x-ray diffraction. As shown in Fig. 8-1, well defined crystallities were obtained and no impurity phases were detected by the x-ray diffraction technique, which indicates that Sr ions entered into the perovskite structure. All reflections in four samples were indexed as a cubic unit cell (space group: P4/mmm; c=2a). Superstructure lines were observed and indexed as (h k l/2). These superstructure lines were generally considered to originate from the superlattice with the stacking of two perovskite subcells along the c axis and the ordering of La^{3+} (Sr^{2+}), Li^+ or vacancies. With the increase of Sr content in

the perovskite structure, all of the superstructure lines gradually become weak and broaden. When x=0.12, all superstructure lines almost disappear. This was the first indication that Sr additions disturbed the superstructure of the $La_xLi_yTiO_3$ perovskite. The ionic radii for Sr^{2+} and La^{3+} are 1.44Å and 1.36 Å respectively. In the perovskite structure, the A-site is tolerant to different sizes of ions. Therefore, the lattice distortion caused by the mismatch between Sr^{2+} and La^{3+} is probably the reason for the above observation. However, the disordering of La^{3+} (Sr^{2+}), Li^+ and vacancies in the A-sites could contribute to the decreasing and broadening of the superstructure lines (h k l/2) in the XRD patterns.

In order to observe the superlattice of $La_{(0.57-2x/3)}Sr_xLi_{0.3}TiO_3$ perovskites on microdomain, electron diffraction was performed on powders of the perovskites. Fig. 8-2 shows the electron diffraction patterns at x=0 and x=0.12 respectively. Surprisingly, the superstructure diffraction spots were still observed when the Sr addition was x=0.12. This is in contrast to the XRD observation, suggesting that a sub-superlattice still exists in the microdomain. In Fig. 8-2(b), the electron diffraction pattern of the superstructure is more complicated than that of $La_{0.57}Li_{0.3}TiO_3$, indicating that the addition of Sr does disturb the ordering structure of $La_{0.57}Li_{0.3}TiO_3$ perovskite.

At this stage, the exact position of La^{3+}, Sr^{2+}, Li^+ and vacancies in the perovskite structure can not be determined. Further identification needs to be done by neutron scattering. The lattice parameters of $La_{(0.57-2x/3)}Sr_xLi_{0.3}TiO_3$ perovskites were refined against an internal silicon standard using the least squares method. The lattice constant a for $La_{0.57}Li_{0.3}TiO_3$ is 3.8712 Å, which is in agreement with the literature value [252]. The lattice parameters and the volume of the unit cell increase slightly with the addition

of large Sr^{2+} ions (see Fig. 8-3). This effect should be beneficial for lithium ion diffusion.

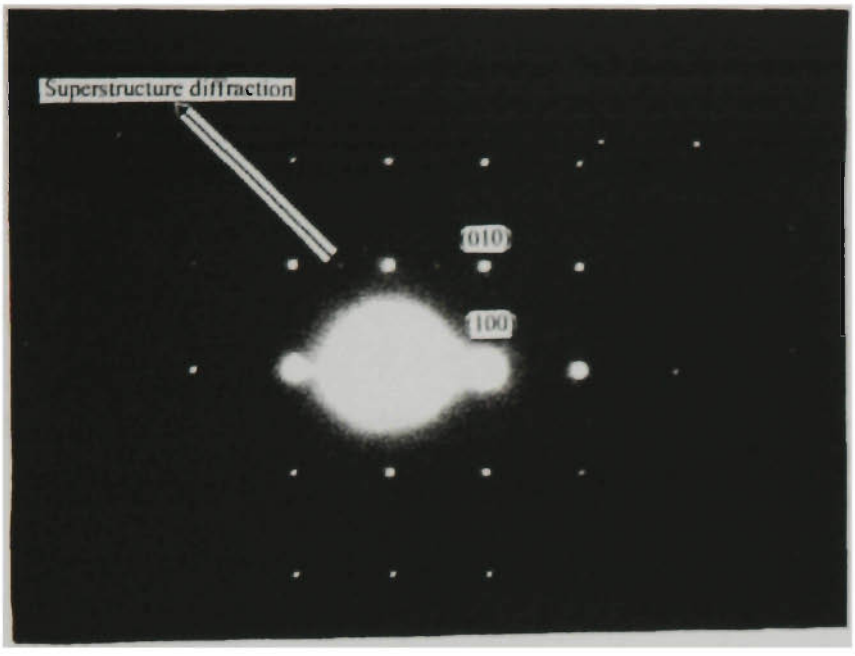

(a)

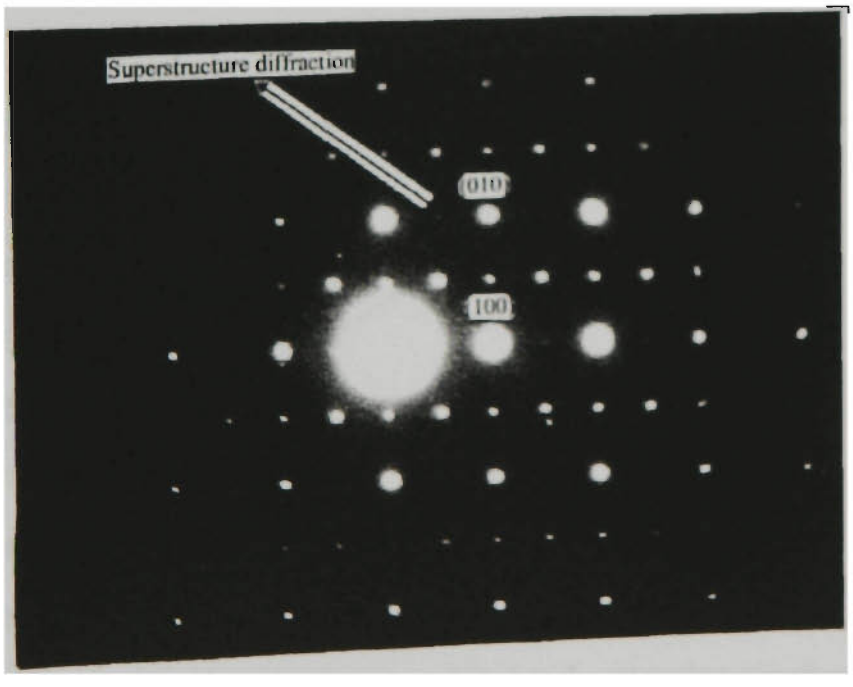

(b)

Fig. 8-2 Electron diffraction patterns of $La_{(0.57-2x/3)}Sr_xLi_{0.3}TiO_3$ perovskites indexed on the basis of the cubic perovskite phase.
(a) x=0, [001] zone axis. (b) x=0.12, [001] zone axis.

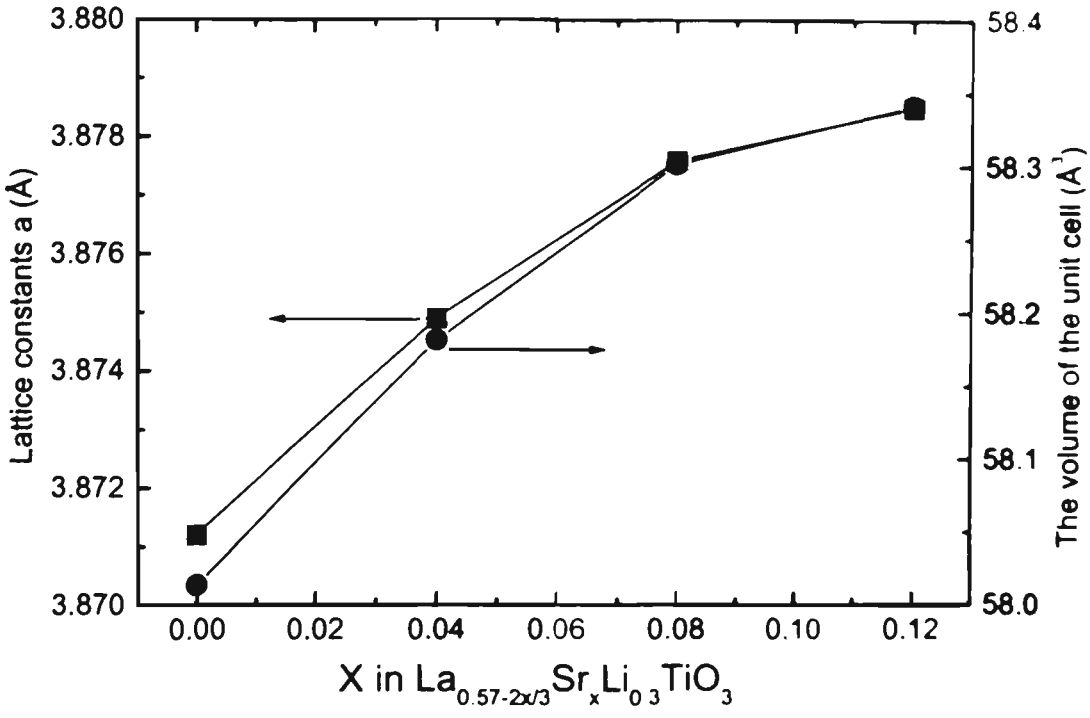

Fig. 8-3 The lattice parameters a and the volume of the unit cell for $La_{(0.57-2x/3)}Sr_xLi_{0.3}TiO_3$.

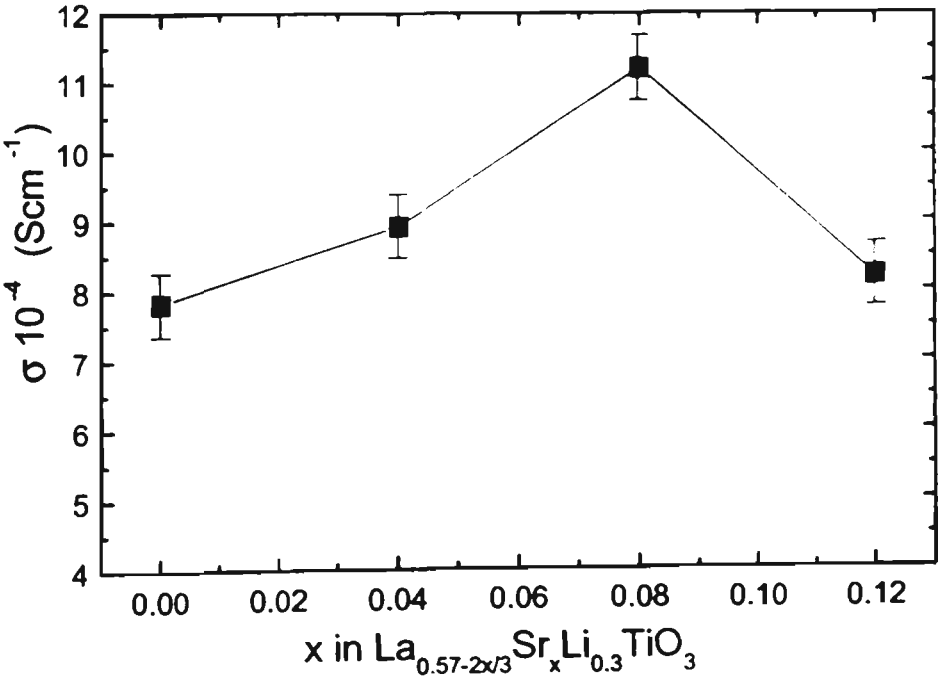

Fig. 8-4 Lithium ion conductivity of $La_{(0.57-2x/3)}Sr_xLi_{0.3}TiO_3$ perovskites at 25 °C.

Fig. 8-4 compares the lithium ion conductivity of $La_{(0.57-2/3x)}Sr_xLi_{0.3}TiO_3$ at 25°C. An improvement of the bulk ionic conductivity was observed with the Sr^{2+} doping effect. At x=0.08, the bulk conductivity reached a maximum of 1.12×10^{-3} Scm^{-1}.

The conductivity of the solid electrolyte is related to the carrier concentration as [254, 255]:

$$\sigma = Z_e \times C \times \mu \qquad (8.1)$$

where Z_e is the ionic charge (Z=1), C is the carrier concentration, and μ is the the mobility of lithium ions which is assumed to be constant in the certain composition range. In $La_{(0.57-2/3x)}Sr_xLi_{0.3}TiO_3$ solid solutions, the lithium ion concentration $N_{Li}=0.3/V_s$ and vacancies $N_v=(0.13-x/3)/V_s$ (V_s is the volume of the cubic unit cell). So, the concentration of all available A-sites for conduction is $N=N_{Li}+N_v$. Therefore, the bulk conductivity can be expressed as:

$$\sigma = Z_e \times N_{Li}N_v/N \times \mu = Z_e \times (0.117-0.3x)/(1.29-x)V_s \times \mu \qquad (8.2)$$

The vacancies decrease with the increase of x in $La_{(0.57-2/3x)}Sr_xLi_{0.3}TiO_3$ perovskite. The substitution must be limited to be $x\leq0.39$. In this range, according to the equation (2), the conductivity should decrease with the increase of the amount of Sr^{2+} ions. However, the experimental observation was opposite (as shown in Fig. 8-4). Two other factors could also contribute to the lithium ion conductivity. The increase of the unit cell volume is helpful for lithium ion diffusion. On the other hand, the disordering of La^{3+} (Sr^{2+}), Li^+ and vacancies in the A-site can also enhances lithium ion conductivity. Long-range, ionic conduction in perovskite compounds seems to involve Li ion migration through the whole bulk in three-dimensions. The ordered arrangement of La^{3+} (Sr^{2+}), Li^+ and vacancies in the A-site decreases the lithium ionic conductivity due to the blocking effect of large La^{3+} (Sr^{2+}) ions. In Fig. 8-1, the superstructure lines gradually diminish

with the increase in the amount of Sr^{2+} dopant. This phenomenon suggests that the degree of the ordering of La^{3+} (Sr^{2+}), Li^+ and vacancies in A-site decreases. Consequently, the ionic conductivity could be enhanced by this effect and would therefore not obey the equation (2).

In conclusion, single phase $La_{(0.57-2x/3)}Sr_xLi_{0.3}TiO_3$ solid solutions were obtained in the range of $x \leq 0.12$. It was found that the XRD diffraction peaks of the superstructure lines (h k l/2) decrease gradually with the addition of large Sr^{2+} ions, which is related to the disordering of La^{3+} (Sr^{2+}), Li^+ ions and vacancies in A-sites on macro domain. However, electron diffraction observation revealed that a sub-superlattice still existed on the micro domain level even when Sr addition reached x=0.12. The lithium conductivity could be improved by adding Sr^{2+} ions. The maximum conductivity at room temperature was 1.12×10^{-3} Scm^{-1} for x=0.08. This Sr^{2+} doped perovskite could be a candidate material as an electrolyte for solid state lithium batteries.

Chapter 9 Summary

Tn this investigation, extensive experimental work has been done on the lithium-ion battery system with the aim of improving the performance of both anode and cathode materials. A new solid-state electrolyte was also investigated. The major conclusions drawn from this investigation are summarized as follows.

9.1 Improvement of the $LiMn_2O_4$ Spinel Cathode Materials

$LiMn_2O_4$ spinel is a promising cathode material but it has some serious disadvantages such as capacity fading during cycling and fast self-discharge rate in the highly charged state. It was found that these problems can be improved by doping the $LiMn_2O_4$ spinel with other cations. Co^{3+} and Cr^{3+} ions were found to have the best dopant effects in improving the structural stability at high temperature as well as the electrochemical stability in the highly charged state and the cycle life. DTA TG analysis demonstrated that the $LiMnO_2$ spinel will decompose to oxygen deficient $LiMn_2O_{4-\delta}$ tetragonal phase at high temperature, which has poor electrochemical performance. The binding energies of CoO and CrO are higher than that of MnO. Therefore, the improvement of the overall properties of $LiMn_2O_4$ by the Co^{3+} and Cr^{3+} dopant effects could be attributed to the enhancement of the stability of the spinel skeleton structure. Low valence Co^{3+} and Cr^{3+} ions in the spinel also suppress Jahn-Teller distortion at the end of the 3 V discharge plateau to preserve the structural integrity of the spinel electrode during cycling. Some good results have been obtained for these Co and Cr doped spinel electrodes. The $LiCo_{0.03}Mn_{1.94}O_4$ electrode has 114 mAh/g capacity after fifty cycles and the $LiCr_{0.04}Mn_{1.96}O_4$ electrode maintains 115 mAh g capacity after fifty cycles. A. c. impedance measurements show that the influence of the dopant ions on the

kinetic processes of lithium ion intercalation and de-intercalation in spinel electrode is relatively small.

Rechargeable lithium-ion cells can be constructed with an aqueous electrolyte, using a spinel cathode and anode. The $Li_2Mn_4O_9/LiCoO_2$ and $Li_4Mn_5O_{12}/LiMn_2O_4$ aqueous Li-ion cells can be reversibly cycled with an average voltage of 1.2 V. The aqueous lithium-ion systems would provide a cost-effective technology for manufacturing.

9.2 Modification of Layered $LiNiO_2$ Compound and Electrochemical Performance of Orthorhombic $LiMnO_2$ Cathode Material

The layered $LiNiO_2$ compound is an attractive cathode material for the lithium-ion battery due to its low cost and non-toxicity. However, it is more difficult to synthesise and needs modification to improve its electrochemical properties.

It was found that the $LiNiO_2$ compound could decompose to $Li_{1-x}Ni_{1+x}O_2$ with poor electrochemical reactivity. Using an oxygen atmosphere for synthesis can suppress this decomposition. $LiAl_\delta Ni_{1-\delta}O_2$ compounds have been prepared in the range of $\delta = 0 - 0.25$. Doped $LiAl_\delta Ni_{1-\delta}O_2$ electrodes demonstrated lower capacity but better rechargeability than the $LiNiO_2$ electrode. The kinetic characterization showed that Al^{3+} dopant effects decreased the charge-transfer resistance and increased the exchange current density as well as the Li-ion diffusion coefficient (D_L) of the electrode. These are favourable changes for battery operation.

A wide range of $LiNi_xCo_{1-x}O_2$ solid solutions have been investigated. The thermal stability and electrochemical stability of $LiNi_xCo_{1-x}O_2$ increase with increasing amounts of Co in the structure. The measurements of the magnetic susceptibility of the $LiNi_xCo_{1-x}O_2$ powders demonstrated that an ordered layered structure can be obtained by an

appropriate synthesis process. The partial substitution of Co for Ni in the layered $LiNiO_2$ structure decreases the initial specific capacity but the cyclability is improved.

$LiNi_{0.8}Co_{0.2}O_2$ thin-film electrodes were deposited using a pulsed laser ablation technique. The thin-film electrode provides an ideal geometry for electrochemical characterization of the electrode materials.

A maximum capacity in the range of 180 – 190 mAh/g for the o-$LiMnO_2$ cathode can be reached with quite good cyclability. Orthorhombic $LiMnO_2$ gradually transfers to a spinel-like phase, which is more electrochemically active than the original o-$LiMnO_2$. The two discharge voltage plateaus at ~4.0 V and ~3.0 V respectively of o-$LiMnO_2$ is a problem for practical application.

9.3 Intermetallic Alloys as Lithium Storage Materials

Intermetallic alloys are new anode materials for lithium-ion batteries. In the current investigation, nano-crystalline η-Cu_6Sn_5, NiSi and FeSi alloys were studied. These nano-crystalline alloys demonstrated very high lithium storage capacity in the initial cycle, but with a large irreversible capacity. It is suggested that The mechanism of the reaction between lithium and these alloys is an alloying process in which lithium alloys with active elements such as Sn and Si to form Li_xSn or Li_xSi alloys. The optimization of the structure and morphology of the intermetallic alloys could improve their electrochemical performance.

Ball milled $C_{1-x}Sn$ composites electrodes can deliver a lithium storage capacity of 800 – 1250 mAh/g, which is 2 – 3 times that of graphite. Similar to nano-crystalline alloys, these composite anode materials also have a large irreversible capacity, which is a problem to be overcome.

9.4 Some New Anode Materials for Lithium-ion Batteries

It was found that the spinel $Li[Li_{1/3}Ti_{5/3}]O_4$ was very stable for lithium insertion at 1.5 V versus lithium reference electrode. The $Li[Li_{1/3}Ti_{5/3}]O_4$ / $LiCoO_2$ and $Li[Li_{1/3}Ti_{5/3}]O_4$ / $LiMn_2O_4$ cells can provide an average operating voltage of 2.4 – 2.5 V with no safety concerns.

$La_{0.33}NbO_3$ perovskite was found to have a capability for lithium insertion, because of the vacant sites in $La_{0.33}NbO_3$ perovskite. The vacancies have an ordering arrangement in the structure, which provides diffusion tunnels for Li-ion insertion and extraction.

The lithium storage capacity of $LiTi_2(PO_4)_3$ with NASICON-type structure was also explored. $LiTi_2(PO_4)_3$ has a high Li diffusion coefficient D_{Li}, which is related to the NASICON structure with interstitials and conducting channels. The exploration of NASICON type materials could provide new anode materials for Li-ion batteries.

9.5 A New Solid-state Electrolyte

A new solid-state electrolyte $La_{(0.57-2x/3)}Sr_xLi_{0.3}TiO_3$ perovskite has been investigated. By doping Sr with La in the perovskite structure, the Li-ion conductivity can be modified. Electron diffraction has shown that there is superstructure in the $La_{(0.57-2x/3)}Sr_xLi_{0.3}TiO_3$ perovskite micro domain. The maximum Li-ion conductivity at room temperature was measured to be about 1.12×10^{-3} Scm^{-1}. This perovskite could be an candidate electrolyte for all solid-state lithium-ion batteries.

9.6 Suggestions for Further Work

Through the whole investigation, it is suggested that modification of o-$LiMnO_2$ and m-$LiMnO_2$ by doping using a chemical synthesis approach can improve their electrochemical properties. Further research using this approach should lead to more economical cathode materials for lithium-ion batteries.

In terms of anode materials, the combination of high lithium storage elements such as Sn and Si with graphite-type carbon appears to be a very promising method for the preparation of anode materials with high capacity and good cyclability. The critical point is to distribute these active elements in the carbon matrix homogeneously, in particular on a nano meter scale. Much work needs to be done in this area.

References

[1] J. E Chilton Jr., G. M. Cook, Abstract of ECS Fall Meeting, Boston, 1962, pp. 90-91.

[2] T. Nagaura, K. Tozawa, Pro. Batt. Solar Cells **9** (1990)209.

[3] M. S. Whittingham, Science **192** (1976) 1126.

[4] A. N. Dey, J. Electrochem. Soc. **118** (1971) 1547.

[5] T. R. Jow and C. C. Liang, *ibid* **129** (1982) 1429.

[6] A. S. Baranski, W. R. Fawset, J. Electrochem. Soc. **129** (1982) 901.

[7] A. Anani, S. Crouch-Baker, R. A. Huggins, J. Electrochem. Soc. **134** (1987) 3098.

[8] A. Anani, S. Crouch-Baker and R. A. Huggins, J. Electrochem. Soc. **135** (1988) 2103.

[9] J. O. Besenhard, P. Komenda, A. Paxines, E. Wudy and M. Josowics, Solid State Ionics **18&19** (1986) 823.

[10] P. Sanchez, C. Belin, C. Crepy and A. De Guibert, J. Appl. Electrochem. **19** (1989) 421.

[11] R. Yazami, Ph. Touzain, J. Power Sources **9** (1983) 365-371.

[12] K. Mizushima, P. C. Jones, P.J. Wiseman and J. B. Goodenough, Mater. Res. Bull. **17** (1980) 783.

[13] G. Dutta, A. Manthiram, and J.B. Goodenough, J. Solid State Chem. **96** (1992) 123-131.

[14] J. L. Godman, R. M. Mank, J. H. Young, V. R. Koch, J. Electrochem. Soc. **127** (1980) 1461.

[15] D. Herbert and J. Ulam, US Patent 3, 043, 896, 1962.

[16] M. Armand, in: Materials for Advanced Batteries, eds. D. W. Murphy, J. Broadhead and B.C.H. Steele (Plenum Press, New York, 1980) p. 145.

[17] K.O. Hever, J. Electrochem. Soc. **115** (1968) 826.

[18] M. Lazzari and B. Scrosati, J. Electrochem. Soc. **127** (19800 773.

[19] B. di. Pietro, M. Patriarca and B. Scrosati, Synth. Met. 5 (1982) 1.

[20] S. Morzilli, B. Scrosati and F. Sgarlata, Electrochim. Acta **30** (1985) 1271.

[21] M.S. Whittingham, US Pat, 4,009,052, 1973.

[22] M.S. Whittingham, J. Electrochem. Soc. **123** (1976) 315.

[23] L. Campanella, G. Pistoia, J. Electrochem. Soc. **118** (1971) 1905.

[24] J.O. Besenhard, R. Shollhorn, J. Electrochem. Soc. **124** (1977) 968.

[25] D.W. Murphy, P.A. Christian, F.J. Disalvo, J.N. Carides, J. Electrochem. Soc. **126** (1979) 497.

[26] T. Ohzuku and A. Ueda, J. Electrochem. Soc. **141**(1994) 2972-2977.

[27] C. Delmas, Mater. Sci. Eng. **B3** (1989) 97.

[28] B. Garcia, J. Farcy, J.P. Pereira-Ramos, J. Perichon and N. Baffier, J. Power Sources **54** (1995) 373.

[29] R. Yazami, N. Lebrun, M. Bonneau and M. Molteni, J. Power Sources **54** (1995) 389.

[30] J.N. Reimers, E. Rossen, C.D. Jones and J.R. Dahn, Solid State Ionics **61** (1993) 335.

[31] M.G.S.R. Thomas, P.G. Bruce and J.B. Goodenough, Solid State Ionics **17** (1985) 13.

[32] Y. Ma, M.M. Doeff, S.J. Visco and L.C. De Jonghe, J. Electrochem. Soc. **140** (1993) 2726.

[33] K.W. Beard, W.A. Depalma and J.P. Buckley, Proc. 1992 IEEE 35th Intern. Power Sources Symp., IEEE, NJ. USA. 1992, P. 201.

[34] T. Ohzuku, A. Ueda and M. Nagayama, J. Electrochem. Soc. **140** (1993) 1862.

[35] J. R. Dahn, U. Von Sacken and C. A. Michal, Solid State Ionics, **44** (1990) 87.

[36] T. Ohzuku, H. Komori, M. Nagayama, K. Sawai and T. Hirai, Chem. Express, **6** (1991) 161.

[37] T. Ohzuku, A. Ueda, M. Nagayama, Y. Iwakoshi and K. Sawai, Chem. Express, 7 (1992) 689.

[38] M. Broussely, F. Perton, P. Biensan, J.M. Bodet, J. Labat, A. Lecerf, C. Delmas, A. Rougier, J.P. Peres, J. Power Sources **54** (1995) 109-114.

[39] Shuji Yamada, Masashi Fujiwara, Motoya Kanda, J. Power Sources **54** (1995) 209-213.

[40] R.V. Moshtev, P. Zlatilova, V. Manev, Atsushi Sato, J. Power Sources **54** (1995) 329-333.

[41] J.N. Reimers, W. Li, J.R. Dahn, Phy. Rev. B **47** (1993) 8486.

[42] A. Rougier, P. Graveau, C. Delmas, J. Electrochem. Soc. **143** (1996) 1168.

[43] J. Desilvestro, O. Hass, J. Electrochem. Soc. **137** (1990) 5C.

[44] G.T.K. Fey, M.C.Hsieh, H.K. Jaw and T.J. Lee, J. Power Sources **43–44** (1993) 673.

[45] K. Takeda, N. Aotani, K. Iwamoto and S. Kondo, Solid State Ionics **79** (1995) 284.

[46] M. Broussely, F. Perton and J. Labat, J. Power Sources **43–44** (1993) 209.

[47] R. Koksbang, I.I. Olsen and D. Shackle, Solid State Ionics **69** (1994) 320.

[48] B. Garcia, J. Farcy, J.P. Pereira-Ramos, J. Perichon and N. Baffier, J. Power Sources **54** (1995) 373.

[49] W. Li, J.N. Reimers, J.R. Dahn, Solid State Ionics **67** (1993) 123.

[50] R.V. Moshtev, P. Zlatilova, V. Manev and A. Sato, J. Power Sources **54** (1995) 329.

[51] A. Ueda and T. Ohzuku, J. Electrochem. Soc. **141** (1994) 2010.

[52] T. Ohzuku and A. Ueda, J. Electrochem. Soc. **144** (1997) 2780.

[53] W. Li and J.C. Currie, J. Electrochem. Soc. **144** (1997) 2773.

[54] Q. Zhong, U. von Sacken, J. Power Sources **54** (1995) 221-223.

[55] T. Ohzuku, A. Ueda and M. Kouguchi, J. Electrochem. Soc. **142** (1995) 4033-4039.

[56] T. Ohzuku, K. Nakura, T. Aoki, Electrochimica Acta **45** (1999) 151-160.

[57] Su-Il Pyun, J. Power Sources **81-82** (1999) 442-447.

[58] C.D.W. Jones, E. Rossen and J. R. Dahn, Solid State Ionics **68** (1994) 65.

[59] Y. Gao and M.V. Yakovleva, W.B. Ebner, Electrochem. Solid State Lett. **1** (1998) 117.

[60] T. Ohzuku, H. Konori, K. Sawai and T. Hirai, Chem. Express **5** (1990) 733.

[61] M. Antaya, J.R. Dahn, J.S. Preston, E. Rossen and J.N. Reimers, J. Electrochem. Soc. **140** (1993) 575.

[62] M. Yoshio, H. Noguchi, K. Tominaga and H. Tanaka, Progress in Batteries and Battery Materials, Vol. 11 (ITE-JECS Press Inc., OH, USA, 1992) P. 158.

[63] K. Mizushima, P.C. Jones, P.J. Wiseman and J.B. Goodenough, Solid State Ionics **3/4** (1981) 171.

[64] S. Miyazaki, S. Kikkawa and M. Koizami, Synth. Met. **6** (1983) 211.

[65] T. Nohma, H. Kurokawa, M. Uehara, M. Takahashi, K. Nishio and T. Saito, J. Power Sources **54** (1995) 522.

[66] R. Yazami, N. Lebrun, M. Bonneau and M. Molteni, J. Power Sources **54** (1995) 389.

[67] L. Xie, W. Ebner, D. Fouchard and S. Megahed, in: Proc. Symp. Rechargeable Lithium and Lithium-Ion Batteries Vol.94-28, eds. S. Megahed, B.M. Barnett and L. Xie (The Electrochemical Society, Inc., Pennington, NJ, 1995) P. 263.

[68] T. Miyashita, H. Noguchi, K. Yamamoto and M. Yoshio, J. Ceram. Soc. Japan **102** (1994) 258.

[69] C. Delmas and I. Saadoune, Solid State Ionics **53-56** (1992) 370.

[70] E. Rossen, C.D.W. Jones and J.R. Dahn, Solid State Ionics **57** (1992) 311.

[71] Q. Zhong and U. von Sacken, J. Power Sources **54** (1995) 221.

[72] M.M. Thackery, J. Electrochem. Soc. **142** (1995) 2558-2563.

[73] K.M. Colbow, J.R. Dahn and R.R. Haering, J. Power Sources **26** (1989) 397.

[74] M.M. Thackeray, A. de Kock, M.H. Rossouw, D.C. Liles, D. Hoge, and R. Bittchn, J. Electrochem. Soc. **139** (1992) 363.

[75] Isaac B. Bersuker, Electronic Structure and Properties of Transition Metal Compounds, John Wiley & Sons, Inc., 1996, USA, p78-89.

[76] F. Albert Cotton, Advanced Inorganic Chemistry, Fifth Edition, John Wiley & Sons, Inc., USA, 1988, P704.

[77] T. Tsumura, A. Shimizu and M. Inagaki, J. Mater. Chem. **3** (1993) 995.

[78] S. Bach, M. Henry, N. Baffier and J. Livage, J. Solid State Chem. 88 (1990) 325.

[79] J.P. Pereira-Ramos, J. Power Sources **54** (1995) 120.

[80] W. Liu, G.C. Farrington, F. Chapnt and B. Dunn, J. Electrochem. Soc. **143** (1996) 879-884.

[81] G.X. Wang, D.H. Bradhurst, H.K. Liu and S.X. Dou, Solid State Ionics **120** (1999) 95-101.

[82] A.D. Robertson, S.H. Lu, W.F. Averill and W.F. Howard, Jr., J. Electrochem. Soc., **144** (1997) 3500-3512.

[83] Li Guohua, H. Ikuta, T. Uchida and M. Wakihara, J. Electrochem. Soc. **143** (1996) 178-182.

[84] P. Arora, B.N. Popov and R.E. White, J. Electrochem. Soc. **145** (1998) 807-815.

[85] R.J. Gummow, A. de Kock, M. M. Thackeray, Solid State Ionics **69** (1994) 59.

[86] Y.Y. Xia, H. Takeshige, H. Noguchi, M. Yoshio, J. Power Sources **56** (1995) 61-67.

[87] D. Guyomard and J. M. Tarascon, ibid. **139** (1992) 937.

[88] J.M. Tarascon and D. Guyomard, ibid. **138** (1991) 2864.

[89] X.Q. Yang, X. Sun, S.J. Lee, J. McBreen, S. Mukerjee, M.L. Daroux, and X.K. Xing, Electrochemical and Solid-State Letters **2** (4) 1999.

[90] M.H. Rossouw, D.C. Liles, & M.M. Thackeray, J. Solid St. Chem. **104** (1993) 464-466.

[91] F. Leroux, D. Guyomard, & Y. Piffard, Solid State Ionics **80** (1995) 299-306.

[92] A. R. Armstrong and P.G. Bruce, Nature Vol. 381 6 June, 1996.

[93] Yet-Ming Chiang, D.R. Sadoway, Young-II Jang, Biying Huang and HaiFeng Wang, Electrochemical and Solid-State Letters **2** (1999) 107-110.

[94] L. Croguennec, P. Deniard, R. Brec and A. Lercerf, J. Mater. Chem. **7** (1997) 511-516.

[95] L. Croguennec, P. Deniard, and R. Brec, J. Electrochem. Soc. **144** (1997)3323.

[96] G. Vitins and K. West, J. Electrochem. Soc. **144** (1997) 2587.

[97] E. Levi, E. Zinigard, H. Teller, M.D. Levi, and D. Aurbach, J. Electrochem. Soc., **144** (4133).

[98] J.N. Reimers, Eric W. Fuller, Erik Rossen, and J.R. Dajn. J. Electrochem. Soc. **140** (1993) 3396.

[99] I.M. Kötschan and J.R. Dahn, J. Electrochem. Soc. **145** (1998) 2672-2677.

[100] B. Ammundsen, J. Desilvesto, R. Steiner and P. Pickering, 10th International Meeting on Lithium Batteries, Abstract No. 17, Como, Italy, May 28 – Jun 2, 2000.

[101] J. Kim and A. Manthiram, NATURE Vol 390, 20 November, 1997.

[102] J. Kim and A. Manthiram, Electrochemical and Solid-State Letters **2** (1999) 55-57.

[103] A.D. Wadsley, Acta Cryst. **10** (1957) 261.

[104] J.O. Besenhard, R. Schöllhorn, J. Power Sources **1** 1976/1977) 267.

[105] S. Panero, M. Pusquali, G. Pistoia, J. Electrochem. Soc. **130** (1983) 1225.

[106] G. Pistoia, M. Pasquali, G. Wang, Li Li, J. Electrochem. Soc. **137** (1990) 2365.

[107] K. Nassau, D.W. Murphy, J. Non-Cryst. Solids **44** (1981) 297.

[108] J. Kawakita, T. Kato, Y. Katayama, T. Miura, T. Kishi, J. Power Sources **81-82** (1999) 448-453.

[109] N. Kumagai, A.H. Yu, J. Electrochem. Soc. **144** (1997) 830.

[110] K. Kawashima, K. Kosuge, and S. Kachi, Chem. Letter. **1131** (1975).

[111] D.W. Murphy, P.A. Christian, F.J. Disalvo, J.N. Carides, and J.V. Waszczak, J. Electrochem. Soc. **128** (1981) 2053-2060.

[112] B.B. Owens, S, Passerini, Williem, H. Smyrl, Electrochemica Acta **45** (1999) 215-224.

[113] R. Kanno, Y. Takeda, T. Ichikawa, K. Nakamishi, O. Yamamoto, J. Power Sources **26** (1989) 534.

[114] D. Billaud, F.X. Henry, P. Willmann, Mat. Res. Bull. **28** (1993) 477.

[115] H. Zabel, S.A. Solin (Eds.), Graphite Intercalation Compounds I, Springer-Verlag Berlin Heidelberg 1990, New York, P6.

[116] J.R. Dahn, T. Zheng, Y. Liu, J.S. Xue, Science, Vol. 270 (1995) 290-293.

[117] Michio Inagaki, Solid State Ionics **86-88** (1996) 833-839.

[118] Sid Megahed and Bruno Scrosati, J. Power Sources **51** (1994) 79-104.

[119] J.R. Dahn, A.K. Sleigh, H. Shi, B.M. Way, W.J. Wegdanz, J.N. Reimers, Q. Gong and U. von Sacken, in G. Pistoia (ed.), Lithium Batteries, Elsevier Science, Amsterdam, 1994.

[120] T. Zheng et. al., J. Electrochem. Soc. **142** (1995) 2581.

[121] T. Enoki, S. Miyajima, M. Sano, H. Inokuchi, J. Mater. Res. **5** (1990) 435.

[122] G.T.-K. Fey and C.L. Chen, 10th International Meeting on Lithium Batteries, Abstract No. 17, Como, Italy, May 28 – Jun 2, 2000.

[123] C.S. Wang, G. T. Wu, X.B. Zhang, Z.F. Qi and W.Z. Li, J. Electrochem. Soc. **145** (1998) 2751.

[124] F. Salrer-Disma, C. Lenair, B. Beaudoin, L. Aymard, J-M. Tarascon, Solid State Ionics **98** (1997) 145-158.

[125] Y. Idota, T. Kubota, A. Matsufuji, Y. Maekawa, T. Miyasaka, Science vol. **276** (1997) 1395.

[126] US patent 5, 478, 671 (1995).

[127] Ian A. Courtney and J.R. Dahn, J. Electrochem. Soc. **144** (1997) 2045.

[128] J. Morales and L. Sanchez, J. Electrochem. Soc. **146** (1999) 1640-1642.

[129] G.R. Goward, F. Leroux, W.P. Power, G. Ouvrard, W. Dmowski, T. Egami, and L.F. Nazar, Electrochemical and Solid-State Letters **2** (1999) 367-370.

[130] J.O. Besenhard, J. Yang and M. Winter, J. Power Sources **68** (1997) 87-90.

[131] J. Wolfenstine, J. Power Sources **79** (1999) 111-113.

[132] K.D. Kepler, John T. Vaughey, and M.M. Thackeray, Electrochemical and Solid-State Letters **2** (1999) 3070309.

[133] O. Mao, R.A. Dunlap, and J.R. Dahn, J. Electrochem. Soc. **146** (1999) 405-423.

[134] B. Dipietro, M. Patriarca, B. Scrosati, J. Power Sources **8** (1982) 289.

[135] T. Ohzuku, A. Ueda, N. Yamamoto, J. Electrochem. Soc. **142** (1995) 1431-1435.

[136] G.H. Newman, R.W. Francis, L.H. Grains, and B.M.L. Rao, J. Electrochem. Soc. **127** (1980) 2025.

[137] T.C. Ehlet and M.M. Hsia, J. Chem. Eng. Data. **17** (1972)18.

[138] D. Aurbach, A. Zaban, Y. Gofer, Y. E. Ely, I. Weissman, O. Chusid, O. Abramson, J. Power Sources **54** (1995) 76-84.

[139] D.E. Fenton, J.M. Parker, P.V. Wright, Polymer **14** (1973) 589.

[140] G.B. Apetecchi, F. Croce, B. Scrosatti, J. Power Cources **66** (1997) 77.

[141] M. Watanabe, M. Kanba, K. Nagaoka, J. Appl. Electrochem. **27** (1982) 4191.

[142] O. Bohnke, C. Rousselot, P.A. Gillet, C. Truche, J. Electrochem. Soc. **139** (1992) 1862.

[143] Atso Yamada, Kaoru Miura, Koichro Hinokuma and Masahiro Tanaka, J. Electrochem. Soc. **142** (1996) 2149.

[144] J. M. Tarascon, W.R. McKinnon, F. Coowar, T.N. Bowmer, G. Amatucci and D. Guyomard, J. Electrochem. Soc. **141** (1994) 1421.

[145] Y. Xia, H. Takeshige, H. Noguchi, M. Yoshio, J. Power Sources **56** (1995) 61-67.

[146] R. Bittihn, R. Herr and D. Hoge, J. Power Sources **43-44** (1993) 223.

[147] M. Wakihara, Li Guoha, H. Ikuta, T. Uchida, Solid State Ionics **86-88** (1996) 907-909.

[148] Atsuo Yamada, Kaoru Miura, Koichiro Hinokuma, and Masahiro Tanaka, J. Electrochem. Soc. **142** (1995) 2149-2156.

[149] C. J. Howard and S. J. Kennedy, Materials Forum **18** (1994) 155-176.

[150] R. J. Hill and C. J. Howard, Australian Atomic Energy Commission Report, AAEC/M112.

[151] E. H. Kisi, Materials Forum **18** (1994) 135-153.

[152]] G. Pistoia, A. Autonini, R. Rosatti, and D. Zane, Electrochim. Acta, **41** (1996) 2683.

[153] D. Guyomard and J. M. Tarascon, *ibid.* **140** (1993) 3071.

[154] Hirofumi Kanoh, Qi Feng, Takahiro Hirotsu, and Kenta Ooi, J. Electrochem. Soc. **143** (1996) 2610 – 2614.

[155] K.Sekai, H. Azuma, A. Omaru, S. Fujita, H. Imoto, T. Endo, K. Yamaura and Y. Nishi, J. Power Sources **43-44** (1993) 241-244.

[156] D. Guyomard and J.M. Tarascon, J. Electrochem. Soc. **139** (1992) 937-947.

[157] W. Ebner, D. Fouchard, L. Xie, Solid State Ionics **69** (1994) 238-256.

[158] Sid Megahed, Bruno Scrosati, J. Power Sources **51** (1994) 79-104.

[159] W. Li, W.R. McKinnon, and J.R. Dahn, J. Electrochem. Soc. **141** (1994) 2310-2315.

[160] R.L.Deutscher, T.M.Florence, R.Woods, J. Power Sources. **55** (1995) 41-46.

[161] Wu Li, J.R. Dahn, D.S. Wainwright, Science, vol.264 (1994) 1115.

[162] Wu Li, J.R. Dahn, J. Electrochem. Soc. **142** (1995) 1742-1746.

[163] L. Sanchez, J.L. Tirado, J. Electrochem. Soc. **144** (1997) 1939.

[164] George Ting-Kuo Fey, Wu Li and J.R. Dahn, J. Electrochem. Soc. **141** (1994) 2279.

[165] George Ting-Kuo Fey, and Chi-sun Wu, 192nd Meeting Abstracts, The Electrochemical Society, Paris, France, 1997. P96.

[166] Joint Commission on Powder Diffraction Standards (JCPDS) Card No. 38-1395, International Center for Diffraction Data, Newtown Square, PA 19073, Wong-Ng, H. McMurdies, B. Paretzkin, C. Hubbard, and A. Dragoo, Powder Diffraction, 2, 262(1987).

[167] R. Moshtev, P. Zlatiova, S. Vasilev, I. Bakalova, K. Tagawa and A. Sato, Progress in Batteries & Battery Materials, Vol. 16 (1997) 268-283.

[168] J. Morales, C. Peres-Vicente and J. Tirado, Mater. Res. Bull. **25** (1990) 623.

[169] B. Garcia, J. Farcy and J. P. Perira-Ramos, J. Electrochem. Soc. **144** (1997) 1179-1184.

[170] Atsushi Funabiki, Minoru Inaba, and Zempachi Ogumi, J. Electrochem. Soc. **145** (1998) 172-178.

[171] I.D. Raistrick, Solid State Ionics **9/10** (1983) 425.

[172] J.R. Dahn, U. Von Sacken, M.W. Jazkow, H. Al-Janaby, J. Electrochem. Soc. **139** (1991) 2207-2211.

[173] S. Yamada, M. Fujiwaru, M. Kanda, J. Power Sources **54** (1995) 209-213.

[174] B. Garcia, J. Farcy, J.P. Pereira-Ramos, J. Electrochem. Soc. **144** (1997) 1179-1184.

[175] W. Ebner, D. Fouehard, L. Xie, Solid State Ionics **69** (1992) 238-256.

[176] M.E. Spahr, P. Novak, B. Schnyder, O. Hass, R. Nesper, J. Electrochem. Soc. **145** (1998) 113.

[177] K. Hirota, Y. Nakazawa, M. Ishikawa, J. Phys. Condens. Mater. **3** (1991) 4721.

[178] A. Ott, P. Endres, V. Klein, B. Fuchs, A. Jäger, H. A. Mayer, S. Kemmler-Sack, H.-W. Praas, K. Brandt, G. Filoti, V. Kunczer, M. Rosenberg, J. Power Sources **72** (1998) 1-8.

[179] K. Yamaura, M. Takano, A. Hirano, R. Kanno, J. Solid State Chem. **127** (1996) 109.

[180] J. B. Bates, N.J. Dudney, D.C. Lubben, G.R. Gruzalski, B.S. Kwak, Xiaohua Yu, R.A. Zuhr, J. Power Sources **54** (1995) 58-62.

[181] K.A. Striebel, C.Z. Deng, S.J. Wen, and E.J. Cairns, J. Electrochem. Soc. **143** (1996) 1821-1827.

[182] Steven D. Jones, James R. Akridge, Solid State Ionics **69** (1994) 357-368.

[183] T. Brousse, R. Retoux, U. Herterich, and D. M. Schleich, J. Electrochem. Soc. **145** (1998) 1-4.

[184] C. Bohnke, O. Bohnke and J. L. Fourquet, J. Electrochem. Soc. **144** (1997) 1151.

[185] R. J. Gummow and M.M. Thackeray, J. Electrochem. Soc. **141** (1994) 1176-1182.

[186] I. Kötschau, M.N. Richard, and J.R. Dahn, J. Electrochem. Soc. **142** (1995) 2906-2910.

[187] E. Levi, E. Zinigrad, H. Teller, M.D. Levi, and D. Aurbach, J. Electrochem. Soc. **144** (1997) 4133-4141.

[188] I. J. Davidson, R.S. McMillan, J.J. Murray and J.E. Greedan, J. Power Sources **54** (1995) 232.

[189] L. Croguennec, P. Deniard, R. Brec, P. Biensan, and M. Broussely, Solid State Ionics **89** (1996) 127.

[190] A. Lecerf, P. Biensan and S. Baudry, French Patent 9308484 (1993) and US Patent US 5561006.

[191] L. Croguennec, P. Deniard, and R. Brec, J. Electrochem. Soc. **144** (1997) 3323-3330.

[192] Laurence Croguennec, Philippe Deniard, Raymond Brec and André Lecerf, J. Mater. Chem. **7** (1997) 511-516.

[193] M. Winter, J.O. Besenhard, M.E. Spahr, P. Novak, Adv. Mater. **10** (1998) 725.

[194] R.A. Huggins, J. Power Sources **22** (1998) 341.

[195] Keith D. Kepler, John T. Vaughey and M. Thackeray, Electrochemical and Solid-State Letters **2** (1999) 307-309.

[196] O. Mao, R.L. Turner, L.A. Courtney, B.D. Fredericksen, M.J. Buckett, LJ. Krause and J.R. Dahn, Electrochemical and Solid-State Letters **2** (1999) 3-5.

[197] W. Liu, X. Huang, Z. Wang, H. Li, L. Chen, J. Electrochem. Soc. **145** (1998) 59.

[198] O. Mao, R.A. Dunlap, J.R. Dahn, J. Electrochem. Soc. **146** (1999) 405-413.

[199] O. Mao, J.R. Dahn, J. Electrochem. Soc. **146** (1999) 414-422.

[200] O. Mao, J.R. Dahn, J. Electrochem. Soc. **146** (1999) 423-427.

[201] H. Li, X. Huang, L. Chen, Z.G. Wu, Y. Liang, Electrochem. Solid-State Lett. **2** (1999) 547.

[202] M. Winter, J.O. Besenhard, J.H. Albering, J. Yang, M. Wachtler, Prog. Batteries & Battery Mater. **17** (1998) 208.

[203] I. Kuribayashi, M. Yokoyama, M. Yamashita, J. Power Sources **54** (1995) 1-5.

[204] N. Takami, A. Satoh, M. Hara, and T. Ohsaki, J. Electrochem. Soc. **142** (1995) 2564-2571.

[205] Agnès Claye, John E. Fisher, Electrochimica Acta **45** (1999) 107-120.

[206] K. Sato, M. Noguchi, A. Demachi, N. Oki, M. Endo, Science **264** (1994) 556-558.

[207] T. Zheng, Y. Liu, E. W. Fuller, S. Tseng, U. Von Sacken, J. R. Dahn, J. Electrochem. Soc. **142** (1995)2581.

[208] Young-Soo Han, Ji-Sang Yu, Gyeong-Su Park and Jai-Young Lee, J. Electrochem. Soc. **146** (1999) 3999-4004.

[209] T. D. Shen, W. Q. Ge, K. Y. Wang, M.X. Quan, J.T. Wang, W.D. Wei, C.C. Koch, Nanostructured Materials **7** (1996) 393.

[210] J. B. Aladekomo, R. H. Bragg, Carbon **28** (1990) 897.

[211] C.S. Wang, G.T. Wu, X.B. Zhang, Z.F. Qi and W.Z. Li, J. Electrochem. Soc. **145** (1998) 2751-2758.

[212] F. Salver-Disma, C. Lenain, B. Beaudoin, L. Aymard, J.-M. Tarascon, Solid State Ionics **98** (1997) 145-158.

[213] A. Mabuchi, K. Tokumitsu, H. Fujimoto, T. Kasuh, J. Electrochem. Soc. **142** (1995) 1041.

[214] K. Tokumitsu, A. Mabuchi, H. Fujimoto, T. Kasuh, J. Electrochem. Soc. **143** (1996) 2235.

[215] M. Inaba, H. Yoshido, Z. Ogumi, J. Electrochem. Soc. **143** (1996) 2572.

[216] C.S. Wang, G.T. Wu, W.Z. Li, J. Power Sources **76** (1998) 1-10.

[217] K. Tokumitsu, A. Mabuchi, H. Fujimoto, T. Kasuh, J. Power Sources **54** (1995) 444-447.

[218] Y. Matsumura, S. Wang, and J. Mondori, J. Electrochem. Soc., 142 (1995) 2914-2918.

[219] N. Imanishi, S. Ohashi, T. Ichikawa, Y. Takeda and O. Yamamoto, J. Power Sources **39** (1992) 185-191.

[220] Tsutomu Ohzuku, Atsushi Ueda and Norihiro Yamamoto, J. Electrochem. Soc. **142** (1995) 1431-1435.

[221] D.W. Murphy, R.J. Cava, S.M. Zahurak and A. Santoro., Solid Satae Ionics **9&10** (1983) 413.

[222] Y. Inaguma, L. Chen, M. Itoh and T. Nakamura, Solid State Communications **86** (113) 689-693.

[223] M. Morales, A.R. West, Solid State Ionics **91** (1996) 33-43.

[224] K. Nomura, S. Tanase, Solid State Ionics **98** (1997) 229-236.

[225] A.G. Belous, Solid State Ionics **90** (1996) 193-196.

[226] W. J. Merz, Phys. Rev. **76** (1949) 1221.

[227] M.A. Subramanian et al., Science **273** (1996)81.

[228] A.P. Ramirez, R.J. Cava, and J. Krajewski, Nature (London) **386** (1997) 156.

[229] Hiroo Kawai and Jun Kuwano, J. Electrochem. Soc. **142** (1995) L8.

[230] Y. Inaguma, J. Yu, Y. Shan, M. Itoh and T. Nakamura, J. Electrochem. Soc. **142** (1995) L8.

[231] Y. Harada, T. Ishigaki, H. Kawai, J. Kawano, Solid State Ionics **108** (1998) 407-413.

[232] O. Bohnke, J. Emery, A. Veron, J.L. Fourquet, J.Y. Buzare, P. Florian, D. Massiot, Solid State Ionics **109** (1998) 25-34.

[233] Y. Shan, N. Sinozaki, T. Nakamura, Solid State Ionics **108** (1998) 403-406.

[234] Y. Kawakami, M. Fukuda, H. Ikata, M. Wakihara, Solid State Ionics **110** (1998) 187-192.

[235] C. Bohnke, and J.L. Fourquet, J. Electrochem. Soc. **144** (1997) 1151-1158.

[236] A. Funabiki, M. Inaba, and Z. Ogumi, J. Electrochem. Soc. **145** (1998) 172.

[237] Heinz Kohler, Heinz Schulz and Oleg Melnikov, Mat. Res. Bull. **18** (1983) 1143-1152.

[238] B.V.R. Chowdari, K. Radhakrishna, K. A. Thomas and G. V. Subba Rao, Mat. Res. Bull. **24** (1989) 221-229.

[239] A. Leclaire, M.M. Borel, A. Grandin and B. Raveau, Mat. Res. Bull. **26** (1991) 207-221.

[240] Y. Miyajima, Y. Saito, M. Matsuoka and Y. Yamamoto, Solid State Ionics **84** (1996) 61-64.

[241] Hiromichi Eisuku Sugimoto, Nobuhito Imanaka and Gin-ya Adachi, J. Electrochem. Soc. **137** (1990) 1023.

[242] Carla Verissimo, Francisco. M.S. Garrido, Oswaldo L. Alves, Paloma Calle, Ana Martinez-Juarez, Juan E. Iglesias, Jose M. Rojo, Solid State Ionics **100** (1997) 127-134.

[243] Enrique R. Losilla, Sebastian Bruque, Miguel A.G. Aranda, Laureano Moreno-Real, E. Morin, M. Quarton, Solid State Ionics **112** (1998) 53-62.

[244] K.Kasthuri Rangan and J. Gopalakrishnan, Journal of Solid State Chemistry **109** (1994) 116-121.

[245] Joint Commission on Powder Diffraction Standards (JCPDS) Card No. 35-754, International Center for Diffraction Data, Newtown Square, PA 19073, USA.

[246] M. K. Aydinol, A. F. Kohan, G. Ceder, K. Cho and J. Joannopoulos, Phys. Rev. B **56** (1997) 1354-1365.

[247] G. Ceder, Y.-M. Chiang, D. R. Sadoway, M. K. Aydinol, Y.-I. Jiang and B. Huang, Nature **392** (1998) 694.

[248] G. R. Goward, F. Leroux, W. P. Power, G. Ourrard, W. Dmowski, T. Egami and L. F. Nazar, Electrochemical and Solid-State Letters **2** (1999) 367-370.

[249] Z. Galus, Fundamentals of Electrochemical Analysis, John Wilsey and Sons Inc., p67, 1976.

[250] Y. Inaguma, L. Chen, M. Itoh and T. Nakamura, Solid State Communications **86** (1993) 689.

[251] M. Morales, A. R. West, Solid State Ionics **91** (1996) 33-43.

[252] Y. Harada, T. Ishigaki, H. Kawai, J. Kuwano, Solid State Ionics **108** (1998) 407.

[253] A. G. Belous, Solid State Ionics **90** (1996) 193.

[254] H. Kawai and J. Kuwano, J. Electrochem. Soc. **141** (1994) 178.

[255] Y. Inaguma, M. Itoh, Solid State Ionics **86-88** (1996) 257.

[256] O. Bohnk, C. Bohnke, J.L. Fourquet, Solid State Ionics **91** (1996) 21-31.

[257] O. Bohnke, J. Emery, A. Veron, J.L. Fourquet, J.Y. Buzare, P. Florian and D. Massiot, Solid State Ionics **109** (1998) 25-34.

[258] K. Nomura, S. Tanase, Solid State Ionics **98** (1997) 229-236.

[259] Y. Kawakami, M. Fukuda, H. Ikuta, M. Wakihara, Solid State Ionics **110** (1998) 187-192.

[258] U. S. Patent 3,330,697 (1967).

Publications

1. Journal Papers

1. G.X. Wang, S. Zhong, D.H. Bradhurst, S.X. Dou and H.K. Liu. "Secondary aqueous lithium-ion batteries with spinel anodes and cathodes", Journal of Power Sources, **74** (1998) 198-201.

2. G.X. Wang, S. Zhong, D.H. Bradhurst, S.X. Dou and H.K. Liu, "Synthesis and Characterization of $LiNiO_2$ Compounds as Cathodes for Rechargeable Lithium Batteries", Journal of Power sources 76, (1998) 141-146, 1998.

3. G. X. Wang, S. Zhong, D. H. Bradhurst, S. X. Dou, H. K. Liu, "$LiAl_\delta Ni_{1-\delta}O_2$ Solid Solutions as Cathodic Materials for Rechargeable Lithium Batteries", Solid State Ionics **116** (1999) 271-277.

4. G. X. Wang, D. H. Bradhurst, S. X. Dou, H. K. Liu, "Improvement of Electrochemical Properties of the Spinel $LiMn_2O_4$ using a Cr Dopant Effect", Solid State Ionics **120** (1999) 95-101.

5. G. X. Wang, P. Yao, D. H. Bradhurst, S. X. Dou, H. K. Liu, "Structure Characterization and Lithium Insertion in $La_{0.33}NbO_3$ Perovskite", Solid State Ionics **124** (1999) 37-43.

6. G. X. Wang, D. H. Bradhurst, S. X. Dou, H. K. Liu, "Spinel $Li[Li_{1/3}Ti_{5/3}]O_4$ as an Anode Material for Lithium Ion Batteries", J. Power Sources **83/1-2** (1999) 156-161.

7. G. X. Wang, P. Yao, S. Zhong, D. H. Bradhurst, S. X. Dou, H. K. Liu, "Electrochemical Study on Orthorhombic $LiMnO_2$ as Cathode in Rechargeable Lithium Batteries", Journal of Applied Electrochemistry **29** (1999) 1423-1426.

8. G. X. Wang, J. Horvat, D. H. Bradhurst, S. X. Dou, H. K. Liu, "Structural, Physical and Electrochemical Characterization of $LiNi_xCo_{1-x}O_2$ Solid Solutions", J. Power Sources **85/2** (2000) 279-283.

9. G. X. Wang, S. Zhong, P. Yao, D. H. Bradhurst, S. X. Dou, H. K. Liu, "Electrochemical performance of Orthorhombic $LiMnO_2$ as Cathode in Lithium Ion Batteries", Journal of New Materials for Electrochemical Systems **2** (1999) 215-219.

10. G. X. Wang, S. Zhong, D. H. Bradhurst, S. X. Dou, H. K. Liu, "Rare Earth Element (La) Doped $LiNiVO_4$ as a Cathode Material for Secondary Lithium Ion Cells", Materials Science Forum **315-317** (1999) 105-112.

11. G. X. Wang, L. Sun, D. H. Bradhurst, S. X. Dou and H. K. Liu, "Lithium Storage Properties of Nanocrystalline eta-Cu_6Sn_5 Alloys prepared by ball-milling", Journal of Alloys And Compounds **299/1-2** (2000) L12-L15.

12. G. X. Wang, L. Sun. D. H. Bradhurst, H. K. Liu and S. X. Dou, "Innovative Nanosize Lithium Storage Alloys with Silica as Active Center", J. Power Sources **88** (2000) 278-281.

13. G. X. Wang, L. Sun, D. H. Bradhurst, S. Zhong, H. K. Liu and S. X. Dou, "Nanocrystalline NiSi Alloy as an Anode Material for Lithium-ion Batteries", Journal of Alloys and Compounds **306** (2000) 249-252.

14. G. X. Wang, P. Yao, D. H. Bradhurst, S. X. Dou and H. K. Liu, "Structure Characteristics and Lithium Ionic Conductivity of $La_{(0.57-2x/3)}Sr_xLi_{0.3}TiO_3$ Perovskites", Journal of Materials Science **35** (2000) 1-3..

15. L. Sun, G. X. Wang, H. K. Liu, D. H. Bradhurst and S. X. Dou, "The Effect of Co Addition on Mg_2Ni Alloy Hybride Electrodes prepared by Sintering and Followed by Ball Milling", Journal of New Materials for Electrochemical System, **2** (1999) 211-214.

16. L. Sun, G. X. Wang, H. K. Liu, D. H. Bradhurst and S. X. Dou, "Synthesis of Nonstoichiometric Amorphous Mg-Based Alloy Electrodes by Mechanical Milling", Electrochemical and Solid-State Letters, **3** (2000) 121-124.

17. S. Zhong, G. X. Wang, J. Wang, H. K. Liu, D.H. Bradhurst and S. X. Dou, "An Anode Material with Perovskite structure for Rechargeable Li-ion Batteries", Journal of New Materials for Electrochemical Systems **3** (2000) 9-12.

18. S. Zhong, P. Yao, G. X. Wang, H. K. Liu, D.H. Bradhurst and S. X. Dou, "Effect of Pre-lithiation Treatment on Amorphous Carbon Materials for the Li-ion Battery", Journal of New Materials for Electrochemical Systems (in Press).

2. International Conference papers

19. G. X. Wang, D. H. Bradhurst, S. X. Dou, and H. K. Liu, "Structural and Electrochemical Characteristics of $Li_{1+x}Mn_{2-x}O_4$ and $LiMn_2O_{4-\delta}$ for Secondary Lithium Batteries", Proceedings of the 13th Annual Battery Conference on Applications and Advances, IEEE 98TH 8299, pp 375-380, 1998.

20. G.X. Wang, S. Zhong, D.H. Bradhurst, S.X. Dou and H.K. Liu, "Intercalation materials as electrodes for rechargeable lithium ion batteries", Proceedings of Materials 98, Biennial Conference of Institute of Materials Engineering, Australasia Ltd, pp 705-710, 1998.

21. S. Zhong, G. X. Wang, J. Wang, D. H. Bradhurst, H. K. Liu and S. X. Dou, " A Solid Hydrogen-ion Battery", International Symposium Metal Hydrogen System, Fundamentals and Applications, HangZhou, China, Page: A2 13-pOct. 4-9, 1998.

22. L. Sun, G.X. Wang, H.K. Liu, D.H. Bradhurst and S.X. Dou, "Preparation of nanocrystalline and amorphous FeTi hydrogen storage alloys", 24th annual

condensed matter meeting of the Australian and New Zealand Institutes of Physics, February 1-4, 2000. Wagga Wagga, Australia.

23. L. Sun, G.X. Wang, H.K. Liu, D.H. Bradhurst and S.X. Dou, "High Energy Storage Mg-based Amorphous Alloys for Nickel-Metal Hydride Battery", 24th annual condensed matter meeting of the Australian and New Zealand Institutes of Physics, February 1-4, 2000. Wagga Wagga, Australia.

24. G. X. Wang, Jung-Ho Ahn, M.J. Lindsay, L. Sun, D.H. Bradhurst, S. X. Dou and H. K. Liu, " Graphite-tin Composites as Anode Materials for Lithium-ion Batteries", 10th International Meeting on Lithium Batteries, Como, Italy, May 28 – June 2, 2000.

25. G. X. Wang, M.J. Lindsay, M. Ionescu, D. H. Bradhurst, S. X. Dou and H. K. Liu, " Physical and Electrochemical Characterization of $LiNi_{0.8}Co_{0.2}O_2$ Thin Film Electrodes Deposited by Laser Ablation", 10th International Meeting on Lithium Batteries, Como, Italy, May 28 – June 2, 2000.

26. J.-H. Ahn, G.X. Wang, M.J. Lindsay, S. X. Dou and H.K. Liu, "Mechanically Milled Nanocrystalline Ni3Sn4 and FeSi2 Alloys as an Anode Material for Li-ion Batteries", International Symposium on Metastable, Mechanically Alloyed & Nanocrystalline Materials (ISMANAM-2000), July 9-14, 2000, Oxford, UK.

List of Symbols

CV	Cyclic voltammetry
PITT	Potentiostatic intermittent titration
GITT	Galvanostatic intermittent titration
A.c. impedance	Alternative current impedance spectroscopy
E_F	Fermi energy
TCO	Tin-based composite oxide
DTA	Differential thermal analysis
TG	Thermo gravimetric analysis
SEI	Solid electrolyte interface
SoC	State of Charge
SoD	State of Discharge
i_o	Exchange current density
D_{Li}	Lithium chemical diffusion efficient
R_Ω	Ohmbic resistance
R_{CT}	Charge transfer resistance
C_{dl}	Double capacitance
Z_w	Warburg diffusion impedance
OCV	Open circuit voltage

R_s	surface layer resistance
BSC	Basic structure units
NASICON	Na super ionic conductor